1-1-1982

Small angle scattering studies of isotactic and atactic polystyrene blends.

Martin Paul Wai
University of Massachusetts Amherst

SMALL ANGLE SCATTERING STUDIES OF ISOTACTIC AND ATACTIC POLYSTYRENE BLENDS

A Dissertation Presented

By

MARTIN PAUL WAI

Submitted to the Graduate School of the
University of Massachusetts in partial fulfillment
of the requirements for the degree of

DOCTOR OF PHILOSOPHY

February 1982

Polymer Science and Engineering

SMALL ANGLE SCATTERING STUDIES OF ISOTACTIC AND ATACTIC POLYSTYRENE BLENDS

A Dissertation Presented

By

MARTIN PAUL WAI

Approved as to style and content by:

Richard S. Stein

Richard S. Stein, Chairman of Committee

William J. MacKnight

William J. MacKnight, Member

Otto Vogl

Otto Vogl, Member

Roger S. Porter

Roger S. Porter, Member

William J. MacKnight

William J. MacKnight, Head
Polymer Science & Engineering

Dedicated to my

Parents and Lei

for their endless support, understanding

and love.

Acknowledgments

My deepest gratitude is extended to Dr. Richard S. Stein, my dissertation director, for his patience, understanding, guidance and advice throughout the course of my graduate study. It has been a real honor knowing this man.

I am also grateful for the stimulating discussions and assistance of other members of my committee: Dr. William J. MacKnight, Dr. Otto Vogl and Dr. Roger S. Porter. It has been a pleasure working with them.

I wish to acknowledge Dr. Robert L. Laurence for his insights concerning the diffusion of polymers in the melt. I am particularly grateful to Dr. Paul D. Calvert of Sussex University in England for the invaluable discussion concerning the morphology of semi-crystalline blends. My appreciation is extended to Dr. Edwin L. Thomas at the University of Massachusetts and Dr. George D. Wignall of Oak Ridge National Laboratory for their collaborations and discussions concerning small angle neutron scattering.

I am deeply indebted to Dr. Thomas P. Russell and Dr. Georges Hadziioannou for the long hours of stimulating discussions on polymers and scattering, and for their friendship.

I am thankful for the valuable discussions with Drs. J. Koberstein, B.S. Morra and W.L. Wu concerning x-ray scattering.

I am particularly indebted to Messrs. Ronald J. Tabar, Dale Handlin and W. Wade Adams for their discussions on polymer research, and especially their friendship throughout the course of my graduate

career. A special note must go to the pinball machines for their endurance when I release my frustrations on them.

The technical assistances of Messrs. D. Keedy, C. Napikoski, N. Page and J. Domain is greatly appreciated. Special note of thanks must go to Mrs. Judith Allardice for her typographical assistance.

To all of these individuals and to the entire Polymer Science Department for creating an atmosphere of exciting research, I am extremely grateful for making this work so enjoyable.

Finally, the financial support of the Materials Research Laboratory of the University of Massachusetts is appreciated.

ABSTRACT

Small Angle Scattering Studies Of Isotactic and Atactic Polystyrene Blends

(February 1982)

Martin Paul Wai

B.S. Worcester Polytechnic Institute

M.S., University of Massachusetts

Ph.D., University of Massachusetts

Directed by Professor Richard S. Stein

Small angle neutron scattering (SANS) from melt blends of isotactic polystyrene (IPS) and atactic polystyrene (APS) of various compositions have been studied. By incorporating deuterium-labelled atactic polystyrene chains, the radius of gyrations, molecular weights and the apparent second virial coefficient, A_2, were calculated. SANS results indicated that the polymer chains remained in their unperturbed dimensions, the experimental determined molecular weights remained within experimental error of the true molecular weight. The values of χ, Flory's interaction parameter, were calculated from A_2 values. The values of χ were found to be less than the critical value of χ, χ_c, for all blend compositions indicating compatibility on a molecular level.

Small angle x-ray scattering from the melt crystallized blends, incorporating up to 30% APS, were also studied. The SAXS intensity

profiles were analyzed using the Vonk and Hosemann techniques. It was found that segregation of the atactic component occurs during crystallization within the growing spherulite of the isotactic component. Despite the high molecular weight of the atactic component ($\bar{M}w$ up to 1.11×10^6), the interlamellar distance did not increase with atactic content. This was further supported by the constancy of the experimental invariant calculation. These results were found for crystallization temperatures of 140, 180 and 200°C. The resulting morphologies are interpreted by a rejection parameter which relates the diffusion rate of the non-crystalline component away from the growth front of the crystallizable component.

TABLE OF CONTENTS

SECTION II

APPENDIX

LIST OF TABLES

LIST OF FIGURES

SECTION I

SEMI-CRYSTALLINE MORPHOLOGY OF ISOTACTIC AND ATACTIC POLYSTYRENE BLENDS BY SMALL ANGLE X-RAY SCATTERING

C H A P T E R I

INTRODUCTION

The subject area of polymer blends has received considerable attention. Many excellent books and review articles can be found in the literature dealing with this broad general area [1-10]. However, if one only considers that the blend be a mixture of only two pure homopolymers, then it is possible to divide these blends into three general catagories [10]:

1. Polymer A and polymer B are both amorphous
2. Polymer A is crystalline and polymer B is amorphous, or vice versa
3. Both polymer A and polymer B are crystalline

Polymer A and Polymer B are Both Amorphous. Blends in which both components are amorphous include such systems as poly(ε-coprolactone) (PCL) and poly(vinyl chloride) (PVC) with PVC being the dominant component [11-15], polystyrene (PS) with poly(o-chlorostyrene)(PoClS) [15,16,17], polystyrene with poly(vinyl methylether)((PVME) [23-25] to name a few. Also included in this blend area are the very important industrial polymers such as styrene-butadine-styrene (SBS) block copolymers [2,9,21,22] and polystyrene blend with poly (2,6 dimethyl phenylene oxide) (PPO) [18-20].

Blends in which both components are amorphous can exibit compatibility, partial compatibility or non-compatibility. Many techniques have been developed to study the degree of compatibility and the

morphology of these blends and they will be discussed later in this dissertation.

Polymer A is Crystalline and Polymer B is Amorphous. Blends in this category include PVC/PCL [13-15], in which the PCL is the crystalline components, poly(vinylidiene flouride)(PVF_2) with poly (methyl methacrylate)(PMMA) [26-28], isotactic polypropylene (IPP) with atactic polypropylene (aPP) [29], and isotactic polystyrene (IPS) blended with poly(phenylene oxide) (PPO) [30], to name a few systems. These blends can also exhibit many types of morphologies and these morphologies will be discussed later.

Both Polymer A and Polymer B Can Crystallize. Blends in this area include poly(butylene terephthalate)(PBT) with poly(ethylene terephthalate) (PET) [4,10,31], high density polyethylene (HDPE) with low density polyethylene (LDPE) [32-34], Nylon 6,6 with PET [35], to name a few. These blends can also exhibit various morphologies depending upon the crystallization conditions. These morphologies and their degree of compatibility in the amorphous phase will also be discussed later.

The final properties of any blend will ultimately depend upon its degree of compatibility and its morphology. A compatible blend is one in which both homopolymers are miscible with each other on a molecular level and there is no phase distinction. A non-compatible blend is one in which the medium consists of phases of pure homopolymer. In between these two extremes are the partially compatible blends where

the medium consists of phases that are not pure homopolymer. Schematic illustrations by Stein et al. [10], of the possible morphologies that could occur, are shown in Figures 1, 2, and 3, respectively. A polymer blend can exhibit any or all of these morphologies depending in which fashion the blend is prepared. Among the factors that influence compatibility and ultimately its morphology are: temperature, solvent, pressure and molecular weight.

Many methods have been developed to determine the degree of compatibility of a blend. The easiest and most frequently employed method is the determination of the glass transition temperature, Tg. For a completely compatible system, a single Tg will be found. One such formulation is given by Nielsen [36] as:

$$Tg = v_1 Tg_1 + v_2 Tg_2 \qquad (1)$$

where Tg_1 and Tg_2 are the glass temperatures of pure homopolymers 1 and 2, respectively. The corresponding volume fractions of components 1 and 2 are v_1 and v_2. One the other hand, for a completely phase separated system, two distinct Tg's, each corresponding to its homopolymer will be observed. Many techniques have been developed to measure the Tg of the blend; among these are: differential scanning calorimetry [2,11,27,37], dynamic mechanical testing [38-40], diffusion study [41], and free volume distribution [39,42]. Unfortunately for equation (1), measurement of Tg as a criteria for compatibility cannot be used if the Tg of the two homopolymers are very close to one another or if one homopolymer is a very dominant

component. Optical clarity can also be used to determine compatibility if the refractive indicies of the two homopolymers are significantly different. Masse [43] used this technique to probe the compatibility of polystyrene with poly(methyl methacrylate). However, if the phases are small, then this test will be insensitive [44,45]. Recently, the use of excimer fluorescence has been employed to probe polymer miscibility [46,47]. However this technique requires that there are aromatic groups present in the blend. Nevertheless, excimer fluorescence allows one to experimentally calculate the interaction parameter between the two species in the blend [47]. These are only a few of the many methods employed to examine the compatibility and to analyze the morphology of a polymer blend. At this point, I'd like to introduce the technique of scattering, whether it be neutron, x-ray or light, to analyze a polymer blend.

Stein [48] and Stein et al, [10,49] gave a series of symposia to summarize the use of scattering in the morphology and compatibility studies of polymer blends. Nishi and Kwei [24] use optical microscopy to study the phase separation of polystyrene with poly(vinyl methyl ether) (PVME). Their results indicated that for this blend system, phase separation occurred by spinodal decomposition [50-53]. Keith and Padden [29] and Yeh and Lambert [54] used optical microscopy to study crystallization morphology of blends of isotactic and atactic polystyrene. Both results indicated a fibrillous structure in the morphology of the blend upon addition of the non-crystallizing component, atactic polystyrene. Unpublished results of Goldstein and

Gilmer [55] indicated phase separation of polystyrene and poly(orthochlorostyrene) (PoClS) when analyzed by small angle light scattering (SALS). The measured variation of the SALS invariant [56] with time indicates phase separation occurring in two stages, the first where compositions and amounts of phases are changing followed by a second constant stage, believed to be domain ripening where the phases grow bigger, but remaining constant in amount and composition.

If there are significant electron density differences between the two homopolymers of a blend, then it is possible to study compatability and the morphology by small angle x-ray scattering (SAXS). SAXS has been employed by numerous authors to study a blend system. Russell [15] studied the compatibility situation of numerous blends by SAXS; Krigbaum and Godwin [57] and Hayashi et al. [58] studied the bulk conformation of polystyrene by incorporating a dilute amount of iodinated polystyrene to supply the contrast. Stein et al. [10,14] and Russell [15] studied the crystalline morphology of blends of PVC and PCL. Their results indicated that the non-crystalline component PVC resided in the inter-lamellae region of the crystalline PCL. Similar study by Morra [26] in PVF_2 with PMMA led to similar results. In this case, the non-crystalline PMMA resided in the interlamellae region of the crystalline PVF_2. However, a different result was found by Warner et al. [85] for isotactic polystyrene blended with atactic polystyrene. In their case, the noncrystalline component resided in the inter-fibrillar region. The morphology of these semi-crystalline blends is qualitively described by the delta "δ" parameter of Keith and Padden

[29], which relates the diffusion rate of the rejected specie and the growth rate of the crystal growth front.

Recently, a very new and powerful technique has been applied to study polymer in the solid state, this being small angle neutron scattering (SANS). Unlike SAXS, which depends on electron density differences, SANS depends upon the neutron scattering length. SANS is particularly useful when one wishes to study the conformation of a polymer. Whereas, SAXS requires heavy labeling which may alter the chemical nature of the polymer, SANS alleviates this problem by the use of deuteration which only changes the neutron cross sectional area, but in most cases, not its chemical nature. Benoit and others [57-60] employed SANS to study the conformation of polymers in the bulk amorphous state. Other workers [61-65] used SANS to study morphology of polymers, which are crystalline, while others [65-68] employed SANS to study the morphology and conformation of blends of polymers.

Each method of small angle scattering has its unique characteristics, namely the contrast factor necessary for excess intensity. However, each scattering method complements the others and the combination of these techniques is a very powerful and useful tool to study polymers in the solid state. It is with this goal in mind that this dissertation was initiated to study the radius of gyration, molecular weight, interaction parameter and morphology of blends of isotactic polystyrene (IPS) and atactic polystyrene (APS) in both the melt and crystalline state.

BACKGROUND

The crystallization studies of isotactic polystyrene [69] were first reported by Kenyon, et al. [70], who observed spherulites of IPS under optical microscope by annealing at various temperatures above the Tg of isotactic polystyrene. They showed that when the rate of the free growing spherulites was plotted as a function of temperature, a uniform Gaussian-type bell curve was formed with a maximum growth rate at about 175°C. They were able to fit their growth kinetics to the Turnbull-Fischer [71] expression for spherulitic growth:

$$G = G_0 (T) \exp (^{-E}D/kT) \exp (-\Delta F^*/kT) \qquad (2)$$

where G is the spherulite growth rate and G_0 is a constant. E_D is the energy of activation necessary for the transport process at the interface. The term $G_0 \exp (^{-E}D/kT)$ may be represented as the jump rate for the molecular rearrangement necessary for adding a crystallizing unit to the crystal. The quantity ΔF^*, which is proportional to $(T_m-T_c)^{-1}$ the extent of supercooling, is the work required to form a nucleus of a critical size. In this case T_m is the melting temperature and T_c is the temperature of crystallization. This free energy term was given by Burneth and McDevil [72] as

$$\Delta F^* = [\pi \ell \sigma_s^2/(\Delta Hi)] T_M/\Delta T \qquad (3)$$

where ΔHi is the heat of fusion per unit volume of repeating unit, σ_s is the interfacial free energy of fusion per unit area for a cylindrical surface, ΔT is the extent of supercooling and ℓ is the distance between

adjacent chains.

Conversely, when Boon et al. [73] tried to fit their experimental growth rate of IPS with the Turnbull-Fischer theory, they were not able to achieve a good fit. Consequently, they were able to fit their growth rate with the Hoffman-Weeks [74] expression of crystallization of supercooled liquid based upon the empirical relation derived by Williams, Landel and Ferry (WLF) for viscous flow.

$$G = G_0 \exp\left(-C_1/R(C_2 + T - Tg)\right) \exp\left(-\Delta F^*/kT\right) \qquad (4)$$

where C_1 and C_2 are arbitraty constants. If the growth rate is controlled by two dimensional nucleation, the free energy term is given as

$$\Delta F^* = [4\ell\sigma\ \sigma_e/\Delta H_i](T_M)/\Delta T \qquad (5)$$

where σ and σ_e are the interfacial free energy per unit area parallel and perpendicular to the molecular chain direction. By utilizing this equation, Boon et al. were able to fit theoretical results with experimental results for rate of growth versus temperature. Furthermore, they concluded that the bulkiness of the phenyl group of the polystyrene chain accounted for the slow growth of IPS.

One of the predictions of secondary nucleation is that lamellae thickness is inversely proportional to the degree of supercooling. In the case of IPS, this was shown to be the case by Blais and Manley [75]. Edward and Phillip [76] used electron microscopy to show the morphology of IPS. They incorporated models that showed the formation of lamellae by "reeling" in of the chain from entanglement of the melt. More

discussion of the morphology of melt crystallized IPS will follow later.

Hay [77] examined the isothermal crystallization of IPS from the melt in terms of the Avrami equation. From all cases considered by him, 179°C $<T_c<$210°C, he found that the Avrami constant changes over the period of crystallization. If the Avrami constant has any real significance, then the crystallization kinetics must change from homogeneous nucleation to heterogeneous nucleation or from a homogeneous nucleation growing in three dimensions to that of two dimensions. However, if the average values of the Avrami constant were used, then at all temperature regions studied, the Avrami constant did not vary to any significant extent. Rate constants followed the typical Gaussian bell shape from the growth rate as previously discussed. Furthermore, Hay found that the limiting number of nuclei increases with increasing degree of supercooling.

Boon et al. [78] extended this study of nuclei formation. They deduced that nucleation appears to be heterogeneous. Moreover, they made a distinction between nuclei still present above the melting point (existent nuclei) and nuclei created by severe supercooling to T_c of 75-100°C (induced nuclei). The crystallization kinetics from the melt are governed by resistant nuclei while crystallization be annealing from the glassy state is completely caused by induced nuclei. Heating the IPS above its melting temperature completely destroys its induced nuclei while only diminishing the number of resistant nuclei, with a greater amount destroyed at higher temperatures. Furthermore, the process is irreversible. However, upon supercooling only induced nuclei

are created.

Secondary crystallization was also studied in detail by both Lemstra et al [79,80] and Overbergh et al. [81]. Both studies indicated that lamellae thickness is inversely proportional to degree of supercooling. However, melting studies by DSC lead to similar results by different explanations. DSC melting studies can lead to either two or three exothermic peaks depending upon crystallization conditions and heating rates. If the temperature of crystallization was greater than 190°C, double melting peaks were observed. Lemstra et al. attributed this phenomenon to melting and recrystallization while Overbergh et al. attributed this to solid state reorganization. In Overbergh et al. subsequent paper [82] they showed, via SAXS analysis, that lamellar thickness increases as they annealed the IPS up to its melting point. Thus they concluded that the melting peak increases were due to increase in lamellar thickness, fold surface perfection and internal perfection of the crystallites.

If the IPS was crystallized below 190°C, a third exothermic peak was observed by both parties, which occurred about 20°C lower than the first melting peak. Again, both parties gave different explanations for the observation. Lemstra et al. [80] attributed this to melting of intercrystalline links which consisted of a small number of molecules. They deduced this conclusion from observations made by electron microscope of the surface replica of the polymer. On the other hand, Overbergh et al. attributed this phenomenon to crystallized fraction of "impurities" of sterically inhomogeneous

species.

Despite these conflicts explanation of the same results, Petermann and Gohil [83] showed, via transmission electron microscopy, that both explanations proposed by Lemstra et al. and Overbergh et al. are valid. Petermann and Gohil showed that for IPS crystallized at 130°C and subsequently reheated toward the melting point, the lamellae do thicken provided that the heating rate is slow, thus the observation made by Overbergh et al. However, if the heating rate is fast, then the lamellae first melt and then recrystallize. This recrystallized morphology is similar to the morphology observed from crystallization from the melt at that particular temperature, completely unlike the morphology obtained by lamellae thickening. This accounts for the conclusions reached by Lemstra et al.

To explain the various morphologies observed on crystallization from the melt at various temperatures, Keith and Padden [84] introduced the parameter δ, a characteristic length. The δ parameter is defined as $\delta = D/G$, where D is the diffusion coefficient of the non-crystalline component away from the growth front of the crystallizing component and where G is its growth rate. The δ parameter is then the thickness of the "impurity-rich" layer. This dimension then should determine the lateral dimension of the fibers. At low degree of supercooling where D, in the case of pure IPS the self diffusion rate, is high and the growth rate G is low, a more open or compact spherulite is observed. The δ parameter as will be discussed later is on the order of interfibrillar length or less if the spherulites are

volume filling. However, at the crystallization temperature of the highest growth rate, a more coarse or fine spherulite is observed due to the decrease in δ. In their subsequent papers, Keith and Padden [29] performed a series of remarkable controlled experiments to show the effect of varying δ to the observed morphologies. In one specific case, they blended IPS with the non-crystalline atactic polystyrene to show the effect of D and G. They were able to show that the behavior of the spherulites is described remarkably well by the parameter δ as they varied experimental conditions. They showed that the molecular weight of the non-crystalline component has a pronounced effect on the diffusion coefficient, with D being inversely related to the molecular weight. Furthermore, increasing the concentration of the atactic component also depressed the growth rate, although the general bell shape of growth rate versus (crystallization) temperature stayed the same. They were able to show that crystallization temperature, concentration of non-crystalline component and molecular weight are all intertwined with one another and the spherulites behaved according to how each parameter affected δ.

Yeh and Lambert [54] extended Keith and Padden's studies to incorporate various molecular weights of the APS. They found a melting point depression with increasing concentration of the APS component. However, this was limited to molecular weight of the APS below 20,000. Furthermore, they noticed a jump in the maximum growth rate beyond a certain concentration of the APS component at a particular molecular weight when the molecular weight of the APS is varied. They explained

this phenomenon by accumulation of impurities of the non-crystalline APS component at the growth front and the resulting openness of the spherulite when the impurity rich region reached too high. In such a case the trapped impurity probably resides between the spherulitic fibrils.

Stein and Warner [85] examined the profiles of SAXS intensities of various blends of IPS with APS crystallizing from the melt. Using various models (to be discussed in experimental section), they concluded that the lamellae spacing did not change with increasing concentration up to 30% of the APS.

Since the non-crystalline component was not between the lamellae and the spherulites were volume filling when viewed under optical microscope, it was deduced that the atactic component resides in the interfibrillar region. The Keith and Padden parameter δ is believed to be on the order of interfibrillar length.

Guenet [86] employed SANS to study the chain conformation of the atactic component in annealed samples of IPS/APS blends. By using a three component system, tagged atactic chains with blends of hydrogenated atactic and isotactic polystyrene, he was able to show that the atactic components were located interfibrillarly. Furthermore, when the molecular weight of the atactic component is high ($MW = 5.5 \times 10^5$), the chains are globally extended by the crystalline fibers. However, if the molecular weight of the atactic component is much lower ($MW = 1.4 \times 10^5$), the chains are more Gaussian like than the higher molecular weights under annealing at identical conditions. Despite Guenet's

results, his experimental conditions are very much different from those of Warner and Stein. Guenet's samples were annealed from the glassy state at 180°C for an annealing time of 70 minutes, while Warner and Stein crystallized their samples from the melt at 200°C until the spherulites were volume filling, generally greater than 48 hours.

One of the purposes of this research is to extend the studies of Warner and Stein to incorporate different molecular weights of the non-crystalline component and to incorporate the effect of crystalization temperature. It has been shown that both parameters will affect the diffusion rate and the growth rate. If the crystallization morphology could be described by the Kieth and Padden parameter δ, then when δ is in the order of lamellae thickness, then we expect an increase in amorphous thickness due to entrapment.

C H A P T E R I I

GENERAL THEORY OF SCATTERING

Many books and articles [87-91] have been written and published dealing with the general theory of scattering, whether it be light, x-ray or neutron. Very generally speaking, scattering is the Fourier transform of the structure that is being irradiated by an electromagnetic wave.

Consider the diagram below for a coherent scattering by a single particle of arbitrary origin O:

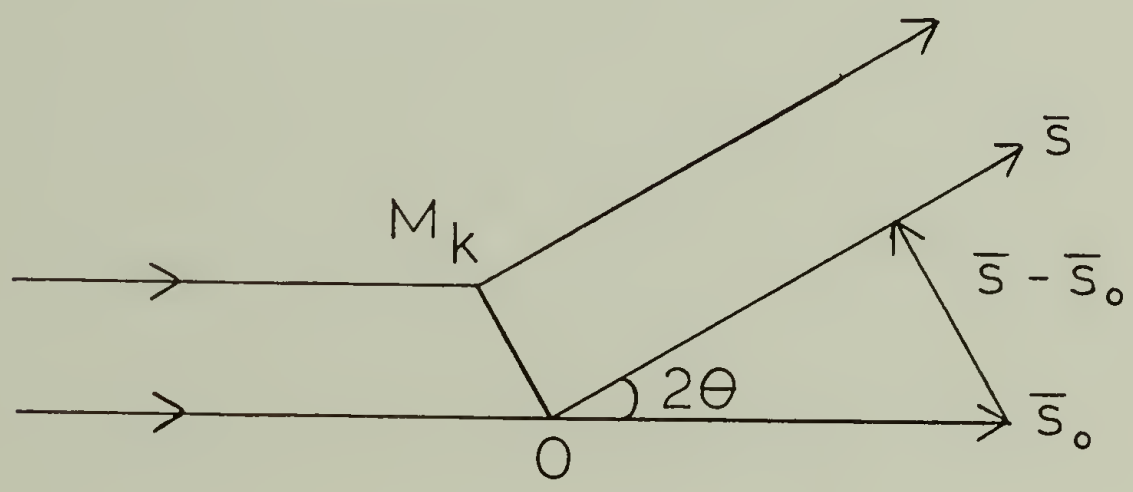

The classical formula for the scattering amplitude of radiation scattered by the point M_k (of scattering factor f_k) in the direction defined by the unit vector $\bar{S}$ is given as:

$$A_k = A_o f_k e^{-i \frac{2\pi}{\lambda}(\bar{S}-\bar{S}_o)\cdot\overline{OM_k}} \qquad (6)$$

where A_o designates the amplitude of the incident field strength; O, an arbitrary origin served to describe the path difference between

unit vector describing the scattered ray. If 2θ is the scattered angle and $\bar{h}$ is the vector $\frac{2\pi}{\lambda}(\bar{S}-\bar{S}_o)$, then the magnitude of $\bar{h}$ is $\frac{4\pi}{\lambda}$ sin θ, f_k is the scattering factor of the k^{th} particle. It is this scattering factor f_k that serves to distinguish the nature of the scattering. For neutron scattering, this is associated with the nature of the scattering nucleus, for x-ray scattering with electron densities and for light with polarizabilities or refractive indices.

The total amplitude scattered is then the sum over all k particles:

$$A(\bar{h}) = \sum_k A_k = A_o(\bar{h}) \sum_k f_k \, e^{-i\bar{h}\cdot\overline{OM}_k} \qquad (7)$$

The scattered intensity is the product of amplitude A and its complex conjugate A^*:

$$I(\bar{h}) = A(\bar{h}) \cdot A^*(\bar{h}) = A_o^2(h) \sum_k \sum_j f_k \, f_j \, e^{-i(\bar{h}\cdot\overline{OM}_k)} \, e^{i(\bar{h}\cdot\overline{OM}_j)} \qquad (8a)$$

and taking its real part:

$$I(h) = A_o^2(h) \sum_k \sum_j f_k \, f_j \cos(\bar{h}\cdot\bar{R}_{kj}) \qquad (8b)$$

where $\bar{R}_{kj}$ is the vector between the k^{th} and j^{th} particle. Recognizing that $\sum_k f_k = V_s \sum_k \rho_k$ where V_s is the volume of the scattering system and ρ_k is the characteristic property of the k^{th} particle, and expressing A_o^2 as:

$$A_o^2(h) = \frac{KI_o}{x^2} \tag{9}$$

where I_o is the incident intensity, x is the sample to detector distance and K is a constant whose value depends upon the type of radiation employed, we can write equation (8) as:

$$I(h) = \frac{K\ I_o\ V_s}{x^2} \sum_k \sum_j \rho_k\ \rho_j \cos\ (\bar{h} \cdot \bar{R}_{kj}) \tag{10}$$

The intensity is generally expressed in terms of the Rayleigh factor defined as:

$$R(h) = \frac{I(h)x^2}{I_o V_s} \tag{11}$$

Thus equation (10) becomes:

$$R(h) = K \sum_k \sum_j \rho_k \rho_j \cos\ (\bar{h} \cdot \bar{R}_{kj}) \tag{12}$$

Defining a structure factor F(h) as:

$$F(h) = \sum_k \rho_k\ e^{-i\bar{h} \cdot \overline{OM}_k} \tag{13}$$

Equation (12) can also be written as:

$$R(h) = \overline{KF^2(h)} \tag{14}$$

Equation (12) and (14) are identical, the former describes the scattering system as a summation over all k and j particles while the

latter describes the scattering as the square of the structure factor. Equation (14) is generally applied if the structure factor is known, usually based upon a model. However, if the scattering system is ill-defined or concentrated, then a statistical approach using equation (12) is employed.

For scattering from a polymeric material, the scattering profile can be divided into four regions, depending upon the dimensions one wishes to analyze. They are called the very small angle region, also known as the Guinier region, which deals with the intra-particle interference, the particle interference region, which is generally applicable to the study of semi-crystalline polymers, the Porod law region, which arises from the interfacial boundary of the material, and finally the wide angle or background region, which arises from thermal fluctuation within the phase.

The structure factor approach is discussed first followed by the statistical approach to describe the scattering system. Rewriting equation (13) in terms of a trigometric function:

$$F(h) = \sum_k \rho_k \cos (\bar{h} \cdot \bar{O}M_k) \tag{15}$$

If the scattered particle in the solution is dilute and spherical symmetric, then we can write equation (15) as:

$$F(h) = \sum_k \rho_k \frac{\sin hr}{hr} \tag{16}$$

where r is the distance from the origin to the k^{th} particle. The

squared of the structure factor is then:

$$\overline{F^2(h)} = \sum_k \sum_j \rho_k \rho_j \frac{\sin h |\bar{R}_{kj}|}{h |\bar{R}_{kj}|} \tag{17}$$

Rewriting equation (17) by expanding the sine function into a power series yield:

$$\overline{F^2(h)} = \sum_k \sum_j \rho_k \rho_j \{ 1 - \frac{h^2}{6} |\bar{R}_{kj}|^2 + ...\} \tag{18}$$

noting that:

$$|\bar{R}_{kj}| = |\bar{R}_k|^2 + |\bar{R}_j|^2 - 2|\bar{R}_k||\bar{R}_j| \cos \phi_{kj} \tag{19}$$

and since the system is spherical symmetric such that $\sum_k \rho_k \bar{R}_k = 0$, and contribution from $\sum_k \rho_k |\bar{R}_k|^2$ is the same as $\sum_j \rho_j |\bar{R}_j|^2$, then in the region of small h, equation (18) becomes:

$$\overline{F^2(h)} = (\sum_k \rho_k)^2 \{ 1 - \frac{h^2 \overline{R_g^2}}{3} \} \tag{20a}$$

$$\text{where } \overline{R_g^2} = \frac{\sum_k \rho_k |\bar{R}_k|^2}{\sum_k \rho_k} \tag{20b}$$

Equation (20) is then approximated by Guinier [90] as:

$$\overline{F^2(h)} = (\sum_k \rho_k)^2 e^{(-h^2 \overline{R_g^2}/3)} \tag{21a}$$

$$R(h) = K\overline{F^2(h)} = K\left(\sum_k \rho_k\right)^2 e^{(-h^2\overline{R_g^2}/3)} \qquad (21b)$$

Thus a plot of ln [R(h)] vs. h^2 would yield a limiting slope of $\overline{R_g^2}/3$. Equation (21) is commonly called the law of Guinier and is applicable only in the regime $h^2\overline{R_g^2} < 1$, due to the approximation made in the derivation.

The square of the structure factor is also known as the interference function or the intensity distribution function. Interference function for particles of various shapes, taken overall orientation of equal probability, have been determined by various workers and are listed below.

a) Sphere of radius R (Rayleigh [92]):

$$\overline{F^2(h)} = \left[\frac{3}{h^3R^3}\ \{\sinh R - hR\cosh R\}\right]^2 = \frac{9\pi}{2}\left[\frac{J_{3/2}(hR)}{(hR)^{3/2}}\right]^2 \qquad (22)$$

b) Cylinder of revolution of diameter 2R and height 2H (Fournet [93]):

$$\overline{F^2(h)} = \int_0^{\pi/2} \frac{\sin^2(hH\cos\theta)}{h^2H^2\cos^2\theta} \times \frac{4J_1^2(hR\sin\theta)}{h^2R^2\sin^2\theta} \sin\theta d\theta \qquad (23)$$

c) Rod of infinitesimal transverse dimensions and length 2H (Neugebauer [94]):

$$\overline{F^2(h)} = \frac{Si(2hH)}{hH} - \frac{\sin^2(hH)}{h^2H^2} \qquad (24a)$$

where

$$Si(x) = \int_0^x \frac{\sin t}{t}\, dt \qquad (24b)$$

d) Flat disc of infintensimal thickness and diameter 2R (Kratky and Porod [95]):

$$\overline{F^2(h)} = \frac{2}{h^2R^2}\left[1 - \frac{1}{hR} J_1 (2hR)\right] \qquad (25)$$

e) Random coil of Gaussian distribution with a mean square radius of gyration $\overline{R_g^2}$ (Debye [96]):

$$\overline{F^2(h)} = \frac{2}{h^4R_g^4}\left[e^{-h^2\overline{R_g^2}} - (1 - h^2\overline{R_g^2})\right] \qquad (26)$$

If $h^2\overline{R_g^2}$ is small, this equation reduced to equation (20) simply by expanding the exponential.

The statistical approach is to consider that the scattering arises from fluctuations in the characteristics property ρ_j throughout the material. The local charcteristic property (for x-ray this is electron density) for the j^{th} volume element is expressed from the average as:

$$\rho_j = \bar{\rho} + \Delta\eta_j$$

where $\bar{\rho}$ is the average value of the characteristic property and $\Delta\eta_j$ is the deviation from the average for the j^{th} volume element. Substitution

into equation (12) yields:

$$R(h) = K \{ \sum_k (\bar{\rho} + \Delta\eta_k) \sum_j (\bar{\rho} + \Delta\eta_j) \cos(\bar{h}\cdot\bar{R}_{jk})\} \tag{27a}$$

$$= K \{ \sum_j \sum_k \Delta\eta_j\Delta\eta_k \cos(\bar{h}\cdot\bar{R}_{jk}) + \bar{\rho}^2 \sum_j \sum_k \cos(\bar{h}\cdot\bar{R}_{jk}) +$$

$$\bar{\rho} \sum_j \sum_k (\Delta\eta_j + \Delta\eta_k) \cos(\bar{h}\cdot\bar{R}_{jk})\} \tag{27b}$$

$$= K \sum_j \sum_k \Delta\eta_j\Delta\eta_k \cos(\bar{h}\cdot\bar{R}_{jk}) \tag{27c}$$

The second term of equation (29b) is zero since it arises from a homogeneous medium and the last term is also zero since η_j and η_k are not correlated and their sum will average to zero. The product $\Delta\eta_j\Delta\eta_k$ depends only on the vector $\bar{R}_{jk}$. A correlation function is defined to describe the size and shape of the heterogeneities as:

$$\gamma(\bar{R}_{jk}) = \frac{\langle\Delta\eta_j\Delta\eta_k\rangle_{\bar{R}_{jk}}}{\overline{\eta^2}} \tag{28}$$

where $\langle\Delta\eta_j\Delta\eta_k\rangle_{\bar{R}_{jk}}$ represents the average product of fluctuation of the pair of volume element separated by the vector $\bar{R}_{jk}$ and $\overline{\Delta\eta^2}$ is the mean square fluctuation. It is this mean square fluctuation or the contrast factor that gives rise to scattering. For a two phase system with infinite sharp boundaries, $\overline{\eta^2}$ is

$$\overline{\eta^2} = \phi_1\phi_2 \, (\rho_1-\rho_2)^2 \tag{29}$$

where ϕ_1 and ϕ_2 are the volume fraction of the two phases with its corresponding characteristic property ρ_1 and ρ_2, respectively.

Substitution of the correlation function and replacement of the summations by integrals by integrating over $\bar{R}_{jk}$, equation (27c) becomes:

$$R(h) = K \, \overline{\eta^2} \int_0^\infty \gamma \, (\bar{R}_{jk}) \cos \, (\bar{R}_{jk} \cdot \bar{h}) \, d\bar{R}_{jk} \tag{30}$$

For a spherically symmetric system and integration over $\bar{R}_{jk}$ into a scalar yield the familiar Debye and Bueche [97] results:

$$R(h) = K \, \overline{\eta^2} \int_0^\infty \gamma(r) \, \frac{\sin \, hr}{hr} \, 4\pi r^2 dr \tag{31}$$

where $r = \left| \bar{R}_{jk} \right|$ and $\gamma(r) = \dfrac{\langle \Delta\eta_j \Delta\eta_k \rangle_r}{\overline{\eta^2}}$

The scattering is now totally defined in terms of the correlation function. The correlation function simply represents that given a distance r, what is the probability $\Delta\eta_j$ and $\Delta\eta_k$ will be equal to each other. Thus at $r = 0$, $\gamma(r) = 1$ for total probability and $\gamma(r)$ approaches zero as $r \to \infty$ for no correlation. Various correlations can be used to describe a scattering system. For example, the correlation function for a sphere of radius R is given as [90]:

$$\gamma(r) = 1 - \frac{3}{4}\left(\frac{r}{R}\right) + \frac{1}{16}\left(\frac{r}{R}\right)^3 \qquad (32)$$

The experimental correlation function is obtained by Fourier transform of equation (31):

$$\gamma(r) = \frac{K'}{2\pi^2\eta^2} \int_0^\infty R(h)h^2 \frac{\sin hr}{hr}\, dh \qquad (33)$$

Thus any maximum in the plot of the correlation function vs r would correspond to the maximum probability of the separation of the volume elements.

A. Guinier Region. The Guinier region, also known as the intra-particle interference region, describes the scattering from a dilute solution at very small angle. As was previously described, this is best approached from the structure factor.

B. Particle Interference Region. The particle interference region is also known as the intermediate angular region of the scattering profile. The scattering here is due to particles possessing some sort of structure. Quite often, a structural model is employed to characterize the size and shape of the scattering particle. Thus the correlation function approach is often used if the appropriate function can be chosen. For a random two phase system, Debye, Anderson and Brumberger [97] have chosen an correlation function of

$$\gamma\,(r) = e^{-r/a} \qquad (34)$$

where a is a correlation distance that serves to characterize the heterogeneties of the medium. Substitution of equation (34) into (31) yields:

$$R(h) = K\overline{\eta^2} \int_0^\infty e^{-r/a} \frac{\sin hr}{hr} 4\pi r^2 dr \qquad (35)$$

Solving for equation (35) yields:

$$R(h) = K\overline{\eta^2} \frac{2a^3}{(1 + h^2a^2)^2} \qquad (36)$$

Inversion of equation (36) and taking the square root yields:

$$\frac{1}{R(h)^{1/2}} = \frac{1 + h^2a^2}{(2K\overline{\eta^2}\, a^3)^{1/2}}$$

Thus a plot of $1/R(h)^{1/2}$ vs h^2, also known as the Debye-Bueche plot, yields a slope/intercept value of a^2 if this correlation function is obeyed.

Kratky and Porod [98] has related this correlation distance to the chord length ℓ of a two phase system. If one is to draw random lines through a two phase system, as shown in figure 4, then the average chord length is given as:

$$\bar{\ell}_1 = \frac{a}{\phi_2} \qquad (37a)$$

$$\bar{\ell}_2 = \frac{a}{\phi_1} \qquad (37b)$$

where ϕ_1 and ϕ_2 are the volume fraction of phase 1 and 2 respectively.

Porod [99] related this correlation distance a to the surface area S_{12} of the two phase system by:

$$\frac{S_{12}}{V_S} = \frac{4\phi_1\phi_2}{a} \tag{38}$$

Furthermore, the derivative of the correlation function is given by Porod as:

$$\left(\frac{d\gamma(r)}{dr} \right)_{r=o} = - \frac{S_{12}}{V_S} \frac{\gamma(r)}{4\phi_1\phi_2} \tag{39a}$$

$$\frac{d\gamma(r)}{dr} = \frac{d(e^{-r/a})}{dr} = - \frac{1}{a} e^{-r/a} \tag{39b}$$

Combining (39a) and (39b) gives:

$$\left(\frac{d\gamma(r)}{dr} \right)_{r\to o} = - \frac{S_{12}}{V_S} \frac{1}{4\phi_1\phi_2} \tag{39c}$$

Thus the initial slope of the experimental correlation function described by this type of model will yield a slope relating the surface area of the system. Russell [14,15] used this approach to characterize the phase in the case of the amorphous blend of PVC/PCL. Many polymeric materials such as semicrystalline polymers and block copolymers could be represented by a lamellar model.

There are presently several models available to describe the scattering from a lamellar structure. Two of these, Tsvankin-Buchanan

(100) and the Vonk (101) model incorporate a one-dimensional infinite lattice with alternating layers of crystalline and amorphous regions. The Tsvankin-Buchnan model is based upon a distorted one-dimensional infinite lattice of crystalline and amorphous phases separated by a linear transition zone. A series of calibration curves are then calculated based upon thickness distribution to obtain the crystallinity and model parameters. The Tsvankin-Buchanan model is simple, however, poor fit is obtained for many common polymer systems [15,85].

The Vonk model (101), on the other hand, calculates the correlation function from the experimental scattering curve via a Fourier transform of the scattered curve. This experimental correlation function is then compared to a theoretical correlation function curve derived from a one dimensional disordered lattice model.

The normalized one-dimensional correlation function is derived by Vonk as:

$$\gamma(r) = \frac{\gamma'(r)}{\gamma'(o)_{r=0}} = \frac{\int_0^\infty I(h)h^2\cos(hr)dh}{\int_0^\infty I(h)h^2dh} \qquad (40)$$

The experimental intensity I(h) is multiplied by h^2 to correct for the fact the scattering is due to a three-dimensional system. This type of correction is commonly known as Lorentz correction [87,102]. For a semi-crystalline blend, the first maximum of the correlation function corresponds to the long period of the system.

In the derivation of the model correlation function, one identified a crystal of thickness r_c with a thickness distribution function $P_c(r_c)$ with a mean thickness C. The amorphous layer is identified in an identical manner. The average volume fraction of crystallinity is therefore:

$$\phi_c = \frac{C}{C+A} \tag{41}$$

Now if a rod of length r is placed in such a system of alternating crystalline and amorphous region, the probability that both ends will be in the crystalline phase is P_{cc}. The probability that both ends of the rod is the same crystalline phase is q_C, whereas the probability that one end is in another crystalline phase separated by only one amorphous region is q_{CAC}. This can be extended to the probability that the rod's ends are in different crystalline regions, q_{CACAC}, and so forth to infinity. Thus P_{cc} is the sum of all these probabilities:

$$P_{cc} = q_C + q_{CAC} + q_{CACAC} + ... \tag{42}$$

$q_C(r)$ is then derived by Vonk as:

$$q_C(r) = \frac{1}{\phi_c(C+A)} \int_r^\infty (r_c-r)\, P_c(r_c)dr_c \tag{43}$$

Calculation of $q_{CAC}(r)$ involves the thickness distribution for the crystal amorphous-crystal stack and is obtained by convolution of the individual distribution:

$$q_{CAC}(r) = \phi_c\ (C+A)\ Q(r_1)\ P_a(r_a)\ Q(r_2) \tag{44}$$

where

$$Q(r_1) = Q(r_2) = Q_c = \frac{1}{\phi_c(C+A)} \int_{r_1}^{\infty} P_c(r_c)dr_c \tag{44b}$$

Subscripts refer to the layer number in the stack. This relationship can be extended to:

$$q_{CACAC} = \phi_c(C+A)\ P_{CACAC} \tag{45a}$$

where

$$P_{CACAC} = \overbrace{Q_c P_a P_c P_a Q_c} \tag{45b}$$

where $\frown$ means the convolution of the distribution. Values of additional probabilities, q, can be extended in this fashion. Vonk defined the correlation function as:

$$\gamma(r) = \frac{P_{cc}(r) - \phi_c}{1 - \phi_c} \tag{46}$$

Substituting equation (42) and rearranging yields:

$$\gamma(r) = \frac{\phi_c}{1-\phi_c}\left[\frac{1}{\phi_c^2}\int_{r}^{\infty}(r_c-r)\ P_c(r_c)dr_c + P_{CAC} + P_{CACAC} + \ldots -1\right] \tag{47}$$

Consequently, calculation of the theoretical correlation function can be calculated by assuming a crystallinity and the distribution function to any desired slope and width.

The Vonk correlation function does have several drawdacks, as pointed out by various workers [15,103,104]. The values of the distribution function must be assumed with care due to the fact that a broad distribution value will lead to a high probability of very thin lamellae. In addition, the correlation function is fitted to the experimental correlation function. The low value of r corresponds to the tail of the scattering curve where the experimental error is inherently high. Furthermore, the model assumes infinite height lattice which may not truly describe some polymer systems. Nevertheless, the Vonk correlation function has been used successfully to describe several polymer systems [15,26,101,105,106].

The Hosemann paracrystalline lattice model [88] is a refinement of the Tsvankin-Buchanan model in which the infinite lattice is replaced by a finite stack of N parallel lamellae. The crystalline and amorphous layers are arranged in a paracrystalline statitics thus the term paracrystalline model.

In general, the Hosemann paracrystalline model fits various parameters, crystal and amorphous thickness and its respective distribution functions, a transition zone thickness and N, the number of parallel lamallae in a stack.

Hosemann derived the theoretical intensity as:

$$I(s) = \frac{K}{s^2} R_e \left[\frac{N(1-F_a)(1-F_c)}{(1-F_d)} + F_c \left(\frac{1-F_a}{1-F_d} \right)^2 (1-F_o^N) \right] Z(s) \qquad (48)$$

where K is a normalization factor, F_a and F_c are the Fourier transform

of the amorphous and crystalline thickness distribution factor, respectively, where F_i is defined as:

$$F_i = \int_0^\infty H_i\,(x)\exp\,(-2\pi\ i\ s\ x)\ dx \qquad (49)$$

and $F_o = F_a - F_c$

H_i is generally taken to be Gaussian shape thickness distribution expressed as:

$$H_i(x) = \frac{1}{2\pi i\overline{(\Delta x_i)^2}} \quad \exp\left[\frac{-(\bar{x}-x_i)^2}{2\overline{(\Delta x_i)^2}}\right] \qquad (50)$$

where $\bar{x}$ is the average thickness. The transition zone thickness E is incorporated in the Z (s) term by:

$$Z(s) = \frac{1}{(2\pi\ i\ s)^2\ E}\ \left|1\ -\ \exp\,(-2\pi\ i\ s\ E)\right|^2 \qquad (51)$$

The Hosemann model has two important drawbacks. The first is the fitting of multiparameters to the scattering curve. A good fit of multiparameters does not necessarily insure the physical reality of the system. Hendricks [127] has emphasized this point in his article on fitting the scattering curve due to tilting of lamellar stack. The second important drawback of the Hosemann model is based upon the value of N used to fit the scattered curve. Many workers [15,30,85,107] have found N to be a very low number of 4 or less. Physically, it is quite difficult to envision stack of lamallae less than 4. Baczek [107] suggested that N corresponds rather to the

number of perfectly parallel stack of lamellae while Wenig et al. [30] considered N as a measure of the degree of angular disorder in a lamellar stack.

The Ruland interface distribution approach [128] is similar to Vonk, but it utilizes the derivative of the electron density profile. Instead of looking at the crystal and amorphous distribution, the interface distribution is calculated. This approach emphasizes the lower order distance distribution and demands considerable accuracy in the tail region of the experimental curve. Furthermore, this method is extremely sensitive to background or fluctuation correction. Since this method involves working with the Fourier transform of the scattered curve, any small error will lead to significant deviation upon transformation.

C. Porod's Law and the Invariant. The Porod's law region deals with the tail of the scattering curve. Porod [99], from investigation of a wide variety of systems, found that regardless of the morphology, and assuming a rectangular electron density profile, i.e. no transition or interface zone, that the limiting intensity is given by:

$$\lim_{h\to\infty} \left[I(h)\right] = \frac{K_p}{h^4} \tag{52}$$

where K_p is the constant relating to the specific inner surface of the system S/V as:

$$K_p = \left(\frac{S}{V}\right) \frac{Q}{8\pi^3 \phi_1 \phi_2} \tag{53}$$

where ϕ_1 and ϕ_2 are the volume fraction of phase 1 and phase 2, respectively. Q is the invariant of the system and is obtained by use of the correlation function. Recalling equation (31):

$$R(h) = K\overline{\eta^2} \int_0^\infty \gamma(r) \frac{\sin hr}{hr} 4\pi r^2 dr$$

Recalling Fourier transform of equation (31) yields equation (33) as:

$$\gamma(r) = \frac{K'}{2\pi^2 \overline{\eta^2}} \int_0^\infty R(h)\, h^2 \frac{\sin hr}{hr}\, dh$$

at $r = 0$, $\gamma(r) = 1$ and $\frac{\sin h(o)}{h(o)} = 1$

$$1 = \frac{K'}{2\pi^2 \overline{\eta^2}} \int_0^\infty R(h)h^2 dh \qquad (54)$$

The invariant Q is defined as:

$$Q = \int_0^\infty R(h)h^2 dh \qquad (55)$$

To evaluate Q (experimentally), the integral of equation (55) is determined by:

$$Q = \int_0^\infty R(h)h^2 dh = \int_0^{h_{pp}} I(h)h^2 dh + \int_{h_{pp}}^\infty I(h)h^2 dh \qquad (56)$$

The first integral is determined from h = 0 to the value of h where Porod's Law is obeyed designated as h_{pp}. The second integral is determined numerically. Utilizing equation (52) in the limit of $h \to \infty$:

$$\int_{h_{pp}}^{\infty} \frac{K_p}{h^4} h^2 dh = -\frac{K_p}{h}\Big|_{h_{pp}}^{\infty} = \frac{K_p}{h_{pp}}$$

K_p can be determined from a plot of intensity versus $1/h^4$. These relationships are based upon a sharp interface. However, rarely does a polymer system exhibit a sharp interface. The effect of the transition zone is treated in the following section.

D. Effect of Fluctuation and Deviation from Porod's Law. The tail end of the scattering profile is due to transition zone and thermal fluctuation of the sample. Thermal fluctuation or background causes a positive deviation of the scattering profile while the effect of a transition zone leads to negative deviation. Both effects have been discussed in an excellent article by Koberstain et al. [109]. Only the main points will be offered here.

In general, the intensity of a system is due to the auto convolution of the electron density profile:

$$I_{obs}(h) = \mathcal{F}(\Delta q^{*2}_{obs})$$

where $\mathcal{F}$ is the three dimensional Fourier transform of the auto convolution (*2) of the difference (Δq_{obs}) between the observed local electron density and the average. However, due to the presence of an

interface Δq_{obs} must be modified by a smoothing function h(r) (Figure 5). Ruland [110] and subsequently modified by other authors [111,112] represented h(r) as a Gaussian model while Vonk [113] represented h(r) as a box function.

$$\text{Ruland's:} \quad h(r) = 2\pi s^2 \exp(-r^2/2\sigma^2) \tag{56a}$$

when σ = standard deviation of the Gaussian smoothing function related to the transition zone thickness.

$$\text{Vonk's:} \quad h(r) = \begin{cases} 1/E & \bar{\rho}_1 \leq r \leq \bar{\rho}_2 \\ 0 & \text{everywhere else} \end{cases} \tag{56b}$$

where E is the transition zone thickness and $\bar{\rho}_1$ and $\bar{\rho}_2$ are the average electron densities of phase 1 and 2, respectively. Thus Δq_{obs} is given as:

$$\Delta q_{obs}(r) = \Delta q(r) * h(r) \tag{57}$$

The intensity is given as:

$$I_{obs}(h) = \mathcal{F}\{\Delta q^{*2}(r)\}\,\mathcal{F}\{h^{*2}(r)\} \tag{58a}$$

$$\lim_{h \to \infty} \left[I_{obs}(h) \right] = I_{ideal}(h)\, H^2(h) \tag{58b}$$

where $I_{ideal}(h)$ is the Porod law intensity and $H^2(h)$ is the Fourier transform of the autocorrelation of the smoothing function. The $H^2(h)$ term contributes to negative deviation from Porod's law due to a diffuse interface. However, before correction can be made for negative deviation, the fluctuation within a phase must be corrected.

Fluctuation within a phase gives rise to a positive deviation from Porod's law, giving rise to a background scattering:

$$\lim_{h \to \infty} \left[I_{obs}(h) \right] = I_{ideal}(h)\, H^2(h) + I_B(h) \qquad (59)$$

where $I_B(h)$ is the background scattering. Various workers have developed various expressions to express this background intensity. Vonk [113] expressed the background as:

$$I_B(h) = Fl + b_1 h^n \qquad (60)$$

where b_1, is a constant and n is an even integer. Fl is the intensity extrapolated to zero angle.

Ruland [110] and subsequently treated further by Rathje and Ruland [114] and Wiegand and Ruland [115] express this background as:

$$I_B(h) = Fl \exp(b_2 h^2) \qquad (61)$$

where b_2 is a constant. The background can also be represented as a constant [109,110,111] as:

$$I_{obs}(h) = \frac{K_p}{h^4} H^2(h) + Fl \qquad (62)$$

This expression is valid only if in a plot of $I(h)h^4$ vs h^4 yield a constant slope of Fl and an intercept of zero provided at large h, $H^2(h)$ goes to zero. If this is so, then a plot of I(h) vs $1/h^4$ will also yield a value of Fl as the intercept of the plot. However, various workers [111] have found a non-zero intercept. Koberstein [109] argued this by the reason that $H^2(h)$ is still of significant

magnitude in the region being used. Nevertheless Vonk [113] has shown that the final value obtained for the interface width varies less than 10% for various background substraction.

After correction for background, then the negative deviation from Porod's law must be corrected. As pointed out by equation (58), the negative deviation is due to the $H^2(h)$ term, the Fourier transform of the auto-correlation of the h(r) given by equation (56):

$$\text{Vonk:} \quad H^2(h) = \frac{\sin^2 \pi Eh}{(\pi Eh)^2} = 1 - 2\pi^2 E^2 h^2/3 + \ldots \tag{63a}$$

$$\text{Ruland:} \quad H^2(h) = \exp\,(-4\pi^2 \sigma^2 h^2) \tag{63b}$$

Substituting equation (63) into equation (58) yields:

$$\text{Vonk:} \quad I_{obs}(h) = \frac{K_p}{h^4}\,(1 - 2\pi^2 E^2 h^2/3 + \ldots) \tag{64a}$$

$$\text{Ruland:} \quad I_{obs}(h) = \frac{K_p}{h^4} \exp\,(-4\pi^2 \sigma^2 h^2) \tag{64b}$$

Koberstein [109] developed these equations further to include a range of applicibility as well as an empirical relationship.

An alternative method to determine the linear transition zone is derived by Vonk [113] by using the correlation function. In this manner a quantity R is calculated:

$$R = 4\pi^2 \frac{\int h^4 I(h) dh}{\int h^2 I(h) dh} \tag{65}$$

Evaluation of the three dimensional correlation function at r=E gives:

$$E = -\frac{4}{R}\left(\frac{d\gamma^1(r)}{dr}\right)_{r=E} \tag{66}$$

Existance of a finite transition zone modifies equation (29) [113] as:

$$\overline{\eta^2} = (\phi_1\phi_2 - \frac{E}{6}\frac{S}{V})\ (\rho_1 - \rho_2)^2 \tag{67}$$

For a one-dimensional lamellae model of average periodicity L, equation (67) can be expressed as:

$$\overline{\eta^2} = (\phi_1\phi_2 - \frac{E}{3L})\ (\rho_1 - \rho_2)^2 \tag{68}$$

Thus the effect of an interface is to reduce the value of the invariant.

E. Absolute Intensity. Recalling equation (11) that the Rayleigh ratio is defined as:

$$R(h) = \frac{I(h)\ x^2}{I_0 V_s}$$

Placing the intensity on this level of $I(h)/I_0$ is called absolute intensity. Evaluation of the absolute intensity requires the measurement of the main beam intensity I_0. This can be accomplished by the use of beam monitors, well calibrated beam alternators or by use of a secondary standard. In this work, a Lupolen standard (designated

17/4) kindly supplied by Professor O. Kratky [116-117] was employed. The sample attenuated intensity ($I_S A_S$) of the Lupolen (17/4) standard is measured at $2\theta = 0.59$ degree. The incident intensity is calibrated by

$$I_o = \frac{(I_S A_S)x}{KA} \tag{69}$$

where x is the sample to detector distance, A is the illuminated area of the sample, A_S is the Lupolen (17/4) attenuation factor and K is the calibration constant equal to 68.7 for this work.

The Rayleigh ratio is therefore:

$$R(h) = \frac{I(s)xK}{(I_S A_S)t} \tag{70}$$

where t is the sample thickness.

Hendricks [119] has pointed out that the use of the Lupolen standard is valid only when the infinite height geometry (to be discussed shortly) is assumed, otherwise a weighting function correction must be used. Furthermore Pilz [120] found a significant temperature dependence of the Lupolen scattering. The correction for this Lupolen (17/4) standard is:

$$I_S = \frac{I_{S,meas.}}{[1 + 0.0077\ (T_{meas} - 21.0°C)]} \tag{71}$$

where $T_{meas.}$ is the temperature of measurement.

F. Smearing Effect. The theoretical analysis presented so far has been based upon a pinhole collimation of radiation source. For small angle light scattering and small angle neutron scattering, this does not present a difficulty as both laser and neutron flux can be generated at a sufficient flux. However, the pinhole collimation does present a major problem for small angle x-ray scattering. Essentially there are two major obstacles to overcome: the effect of parasatic scattering and the lack of sufficient flux. Both of these effects can be overcome by increasing the sample to detector distance and using a more powerful generator. Such is the case for the Oak Ridge National Laboratory 10-meter rotating anode SAXS apparatus [121-122]. However a more common technique is to use a slit-collimation to decrease the parasatic scattering and increase the intensity. The main drawback of slit-collimation is that the scattering is smeared. Two approaches can be used to correct this effect. The experimental scattering can be desmeared or the theory can be smeared.

Guinier has shown that the slit intensity can be considered as a linear array of pinhole intensity, the smeared intensity J(h) for a slit or arbitrary height but of negligible width is:

$$J(h) = 2 \int_0^\infty \omega_\ell(u)\ I\sqrt{(h^2+u^2)}\ du \qquad (72)$$

where $\omega_\ell(u)$ is a weighting function describing the shape of the incident beam and u is a variable of integration. The weighting function is normalized so that

$$\int_0^\infty \omega_\ell(u)\, du = 1 \tag{73}$$

Different cameras have different weighting functions. For a Kratky camera, the weighting function could be considered constant if the beam is of infinite height. In order to illustrate this in a physical manner, consider the system where the width of the receiving slit is ℓ_C and the width of the beam at the receiving slit is ℓ_B. If the entire scattering profile occurs within the angular range corresponding to ℓ_B-ℓ_C, then a beam of infinite length would yield identical results; hence the term infinite height. For other cameras, such as a Rigaku-Denki or a Beeman camera, the weighting function is assumed to be Gaussian.

Applying the smearing integral to Porod's law for a constant weighting function (infinite height), equation (52) becomes

$$\lim_{h\to\infty} J(h) = K \int_0^\infty \frac{1}{(h^2+u^2)^2}\, du = \frac{\pi K_p}{2h^3} \tag{74}$$

Thus the smeared intensity for a system with infinite sharp interface, the limiting intensity is proportional to h^{-3}. Similarly the smeared invariant is given by, from equation (55):

$$Q_{SM} = \int_0^\infty R(h)h^2dh = \int_0^\infty \int_0^\infty R\left(\sqrt{h^2+u^2}\right) h^2 dh du \tag{75a}$$

$$Q_{SM} = 2\int_0^\infty R(h)h^2dh = 2Q \tag{75b}$$

The smeared invariant is equal to twice the desmeared invariant. Furthermore equation (62) becomes:

$$J_{obs}(h) = \frac{\pi H^2(h) K_p}{2h^3} + Fl \qquad (76)$$

The corresponding correction for transition zone becomes [109]:

$$\text{Vonk:} \quad J_{obs}(h) \simeq \frac{K'_p}{h^3}\left(1 - \frac{2\pi^2 E^2}{3}\right) \qquad (77a)$$

$$\text{Ruland:} \quad J_{obs}(h) \simeq \frac{K'_p}{h^3} \exp\left(-4\pi^2\sigma^2 h^2\right) \qquad (77b)$$

Thus far the theory has been smeared or modified because of a slit beam profile. However the experimental scattering can be desmeared. Guinier [123] has shown for infinite height assumption, the desmeared intensity is given as:

$$I(h) = \frac{-1}{\pi c}\int_o^\infty \frac{dJ\left(\sqrt{h^2+u^2}\right)}{d\left(\sqrt{h^2+u^2}\right)} \frac{du}{\sqrt{h^2+u^2}} \qquad (78)$$

Procedures for treating beam of finite width, employing the weighting function has been treated extensively by Hendricks [124-126]. When the exact weighting function is determined the resulting intensity is generally desmeared by numerical procedure. Many workers [127-134] have given various procedures to perform the desmearing operation. They all involve the use of a function to obtain the

desmeared intensity. The desmeared intensity is then smeared and compared to the experimental intensity. Generally, iterations are performed until a convergence is reached.

C H A P T E R I I I

EXPERIMENTAL

Both isotactic polystyrene (IPS) and atactic polystyrene (APS) were obtained from Polymer Laboratories of Shrewsbury, England. Purification of the isotactic polystyrene was done in the following fashion. The IPS was initially melted at 260°C under nitrogen atmosphere and quenched in ice water. The quenched isotactic polystyrene was then Soxhlet extracted with spectro-grade toluene for 96 hours. The IPS was then recovered by reprecipitating the extracted solution into vigorously stirred methanol in a 15:1 volume ratio of methanol/toluene solution. The resulting IPS was vacuum dried at 60°C for 3 days. The IPS was then Soxhlet extracted with methyl ethyl ketone for 96 hours to extract out the atactic polystyrene. The raffinate IPS was then vacuum dried at 60°C for 3 days prior to use. C-13 NMR spectrum of the purified IPS in deuterated chloroform was performed and is shown in Figure 6. The chemical shift 147 ppm is due to the isotactic polystyrene C^1 carbon while the chemical shift at 145-146 ppm due to the atactic polystyrene C^1 carbon [135]. Integration of the area under intensity peaks and taking its ratio leads to > 95% isotacticity.

Gel permeation chromotography (GPC) [137] was done on the purified IPS to determine its molecular weight. The solvent was GPC grade tetrahydrofuran. GPC spectrum of the IPS is shown in Figure 7. The calibration curve based upon atactic PS for this sample is shown in

Figure 8. Calculation of the molecular weight was based upon the method of Benoit et al. [136]. The equation used for this case is:

$$\log M_{IPS} = - 0.33 + 1.056 \log M_{APS} \quad (79)$$

where M_{IPS} is the equivalent molecular weight of the atactic polystyrene, M_{APS}. Based upon these values, the calculation yields a weight averaged molecular weight for IPS as 3.89×10^5 and a number average molecular weight of 1.22×10^5. This yields a polydispersity of 3.2.

The atactic polystyrenes (APS) were also obtained from Polymer Laboratories. Two ranges of APS molecular weight were studied. One has a weight averaged molecular weight of 1.11×10^6 with a polydispersity of less than 1.1 and the other has a weight averaged molecular weight of 5.22×10^5 with a polydispersity also less than 1.1. The atactic polystyrenes were purified by dissolving in toluene and reprecipitating into excess methanol and then vacuum dried at 60°C for 3 days.

The IPS/APS blends were prepared by dissolving the weight fractions of each polymer in boiling toluene at a 2% concentration, then coprecipitating into a large excess (20:1 volume ratio) of vigorously stirred methanol by drop wise addition. The blends were then vacuum dried at 60°C for 3 days prior to use.

In order to be sure that no fractionation occurs in these blends, a representative blend with a ratio of 80/20 IPS/APS with an APS molecular weight of 1.11×10^6 was prepared to determine its viscosity

before and after coprecipitation.

The viscosity data of this sample is given in Figures 9. As can be seen, the intrinsic viscosity remains the same before and after coprecipitating. Thus, it was felt confident that there was no fractionation of either component nor fractionation of molecular weights since either of these two effects would have drastically changed the intrinsic viscosity.

The dried blends and the pure IPS were compression molded at 6000 psi and 260°C in a 14 mm thick mold between aluminium foil and then quenched in water at 25°C. The samples were then remelted at 260°C for 20 minutes and then transferred to the crystallization bath set at the desired temperature (200°C, 180°C or 140°C).

Crystallization was allowed to continue undisturbed for 76 hours and then quenched in water at 25°C. Many workers [29,54,85] have shown this is sufficient time to ensure complete crystallization, i.e. volume filling spherulites. Crystallization at 200°C was done in a sand bath regulated to within $\pm$ 1.0°C. Crystallization at 180°C and 140°C was done in an oil bath regulated to within $\pm$ 0.5°C. A list of the samples prepared and studied is given in Table 1.

SAXS EXPERIMENTS

The blends were prepared at three different crystallization temperatures: 200°C, 180°C and 140°C. These temperatures were chosen because they represented the ranges of growth rate of the isotactic polystyrene. Various workers have measured the growth rate for the

Table 1

Samples Prepared for Small Angle X-Ray Scattering Studies

Sample Designation	Crystallization Temperature	$\bar{M}w$ (APS	%Isotactic Polystyrene[1]
A10000	200°C ± 1.0°C	——	100
A91111	"	1.11×10^6	90
A82111	"	"	80
A73111	"	"	70
A91522	"	5.22×10^5	90
A82522	"	"	80
A73522	"	"	70
B10000	180°C ± 0.5°C	——	100
B91111	"	1.11×10^6	90
B82111	"	"	80
B73111	"	"	70
B91522	"	5.22×10^5	90
B82522	"	"	80
B73522	"	"	70
C10000	140°C ± 0.5°C	——	100
C91111	"	1.11×10^6	90
C82111	"	"	80
C73111	"	"	70

[1]weight averaged molecular weight of isotactic polystyrene is 3.89×10^5, DP < 3.2

samples studied and is plotted in Figure 10. It can be seen that at each crystallization temperature, the growth rate of the IPS in the blend decreases as more atactic polystyrene is added.

Yeh and Lambert [54] studied the effect of molecular weight of the non-crystalline component on the growth rate. It was concluded by them that above a critical molecular weight of 50,000, the molecular weight of APS has a slight effect in the growth rate. Molecular weight used in this study are above the critical molecular weight as determined by Yeh and Lambert.

The effect of variation of the concentration of the APS is to alter the growth rate of the isotactic polystyrene at each crystallization temperature. Effect of variation of the molecular weight is to vary the diffusion rate of the APS away from the growth front of the crystallizing component. Diffusion of polymer has been shown by many workers to be an activated process that can be represented by an Arrhenius type equation:

$$D = D_0 \exp(-E_A/RT) \tag{80}$$

where D_0 is the diffusion coefficient at a reference temperature, E_A is the activation energy for self diffusion, R is the gas constant and T is the temperature. Self diffusion of atactic polystyrene have been determined by Kumagai et al. [138] for various molecular weights and is plotted in Figure 11. Employing an activation energy as given by Keith and Padden [29] for self diffusion of polystyrene as 35 kcal $mole^{-1}$ (147 kJ/mole), a plot of the diffusion rate versus temperature

can be constructed for each of our molecular weights studied and is plotted in Figure 12. These values are in qualitative agreement with the values obtained by Laurence et al. [139] on polyvinyl chloride at equivalent molecular weights.

All of the SAXS samples were analyzed in the same fashion using the Vonk FFSAXS version 3 computer program [140]. The raw scattering data were corrected for detector's sensitivity and electronic noise. The parasatic or main beam scattering was then subtracted from the sample scattering. The resulting scattering data were then corrected for thermal fluctuation by assuming a constant value, which was determined by the use of equation (76). After correction for thermal fluctuation, the interfacial thickness was determined by assuming a linear electron density gradient across the interface. The corresponding equation used was (77a). The smeared invariant was then obtained by use of equation (75a). Desmearing of the scattered intensity was done according to Vonk's procedure [134], using a trapezoid weighting function. The resulting desmeared data was then Lorentz corrected and then fitted by the use of 2 different particle interference models; Hosemann paracrystalline model [85] and the Vonk's theoretical correlation function (TCF) [101] model to fit the Fourier transform of the experimental desmeared intensity data.

SAXS studies were carried out using a Kratky camera assuming infinite slit-height geometry. Nickel filtered CuKα radiation was used. Detection was done by employing either a Tennelec or TEC one dimensional position sensitive detective (1DPSD). A complete description

of the University of Massachusetts one dimensional position sensitive detector, and the vacuum flight path chamber as constructed and designed by the author and various helpers, is given in Appendix I.

C H A P T E R I V

RESULTS

As was forementioned, a computer program kindly supplied by G.C.G. Vonk [140] was used to perform many of the calculations.

The infinite slit height assumption is often applied to data from a Kratky system. For the angular range scanned in the present study, up to $2\theta = 4°$, this assumption is valid according to the criteria defined by Kratky [141].

Measurements of both sample scattering intensities and the parasatic scattering, obtained with no sample, were made by dividing the detector wire into 512 or 1024 channels. Calibration of the detector wire at each of the channels was accomplished using a radioactive iron 55 source which gave a constant incident intensity at all angles. Both the sample data and the parasatic scattering were corrected by this calibration to eliminate effects due to deviations in the wire.

The sample and parasatic scattering were each independent smoothed using a 4-points interval. The parasatic scattering was then scaled to the sample scattering, using the sample attenuation factor, and subtracted from it.

The attenuation factor of the samples were measured with the use of a solid scintillation detector set at an arbitrary angle. The intensity scattered from a reference sample (in our case polyethylene) was measured at this set angle. The intensity was then measured with

the sample placed directly in front of the detector. The ratio of the intensity with the sample to that without is the attenuation factor. These are presented along with the sample thickness in Table 2.

The parasatic scattering was extremely small in comparison to the sample scattering in all cases studied. Figure 13 shows comparison of a typical sample scattering to the parasatic scattering. The correction for both the parasatic scattering and the detector wire sensitivity did not alter any of the sample curves appreciably.

Figures 14 to 31 show the corrected smeared intensities for all of the samples studied. On a qualitative scale, it can be seen that at each crystallization temperature, the pure IPS has a scattering maximum. However, upon addition of more APS, is can be inferred that the peak maximum stays at the same angular position, but becoming more spread out, until at a 30% concentration of APS, the scattering maximum is like a shoulder on the scattered curve. Thus qualitatively speaking, the long periodicity does not change upon addition of the non-crystalline component, but rather there is becoming a greater distribution of crystal and amorphous sizes.

To perform quantitative analyses on this type of scattering, which arises from lamellar interferences, scattering due to fluctuation in the amorphous phase or the background scattering must first be removed.

In this study, the assumption was made that the background scattering was constant, with no dependence on a power series of the scattering angle h. Through the use of equation (76) for smeared

Table 2

SAXS Sample Thicknesses and Attenuation Factors

Sample	Thicknesses(cm)	Attenuation Factors
A10000	0.135	0.627
A91111	0.132	0.610
A82111	0.140	0.617
A73111	0.142	0.593
A91522	0.135	0.603
A82522	0.135	0.618
A73522	0.135	0.610
B10000	0.135	0.748
B91111	0.135	0.757
B82111	0.132	0.747
B73111	0.127	0.740
B91522	0.132	0.744
B82522	0.132	0.735
B73522	0.130	0.750
C10000	0.132	0.741
C91111	0.165	0.590
C82111	0.160	0.610
C73111	0.173	0.580

intensity, plots of $J(h)h^3$ vs h^3 were made for sample studied at the crystallization temperature of 100°C and 140°C. Representative samples are plotted in Figures 32 to 35.

As can be seen from these plots, a reasonable fit of a straight line can be made through all scattered intensity values. The scatter of the data at the high h regime is large due to the inherent low signal/noise ratio, which is magnified in this type of plot. Nevertheless, a constant slope can be obtained with an intercept that is very close to zero. For samples crystallized at 180°C, plots of $J(h)h^3$ vs h^3 yielded very similar results. Because no power series dependence can be seen and because a constant slope was obtained along with a zero intercept, plot of $J(h)$ vs. $1/h^3$ was performed on these samples to obtain the fluctuation by the intercept in these plots. Plots of this type are shown in Figures 36 to 38. It can be seen that a straight line can be drawn through the points at the high h values. The increase in intensity at high h values are due to the onset of wide angle scattering and can be seen quite clearly in this type of plot. This is very encouraging since this indicates that the intensity gathered for the samples studied are well beyond the Porod's law regime.

The values obtained for the fluctuation are given in Tables 3, 4 and 5. Constant values are seen in all cases for each series of temperature and molecular weights. The values were then subtracted from its respective scattering curve to remove the liquid scattering.

The question now arises whether the use of a constant background

Table 3

Values of Background Fluctuation for T(C) = 200°C

Sample	Fluctuation (e.u./cc) x 10^{-24}
A10000	1.325
A91111	1.221
A82111	1.282
A73111	1.383
A91522	1.295
A82522	1.339
A73522	1.408

Table 4

Values of Background Fluctuation for T(C) = 180°C

Sample	Fluctuation (e.u./cc) x 10^{-24}
B10000	1.95
B91111	1.72
B82111	1.81
B73111	1.98
B91522	1.84
B82522	2.03
B73522	1.83

Table 5

Values of Background Fluctuation for T(C) = 140°C

Sample	Fluctuation (e.u./cc) x 10^{-24}
C10000	1.467
C91111	1.146
C82111	1.119
C73111	1.219

is valid in these samples. Vonk et al. [101] have shown that for polyethylene, the background can be represented in an even power series of s. Nevertheless, they concluded that the use of a constant background gives almost the same result as a background obeying a power series. Similar conclusions were also reached by Vonk [113] in polypropylene. However, in Wendorff [142] small angle scattering study on blends of PVF_2 and PMMA, a large anglular dependence of the backgound intensity was observed. This was divided into s-independent and s-dependent terms. As Morra [26] elucidated, the former corresponded to the value of pure components using simple mixing rules and was attributed to the density fluctuation at constant concentration. The latter term arises from the concentration fluc-turation at constant particle number density and was strongly dependent upon composition. This term becomes more important when there is interaction between the two components in the amorphous state. As Morra [26] showed, there was an increase in the background intensity as more PMMA was added to the blend.

From present study by this author (see Section II) on the melt condition of blends of IPS and APS , it was concluded there was no specific interaction between IPS and APS, as deduced by small angle neutron scattering with deuterium labelling of the APS chain. Thus it was safe to assume that there are no interactions between chains in the amorphous phase in these semicrytalline blends. Since the background scattering arose from the thermal fluctuation in the amorphous phase, the use of a constant background in this study was

justified.

Nevertheless, preliminary calculation was made on various samples with a constant backgound and a power series dependence backgound. it was found that there was negligible differences on the values of the interfacial thickness and invariant obtained by the two different methods of substraction. Therefore, a constant backgound subtraction was employed in all samples studied.

Vonk [113] and Todo, Hashimoto and Kawai [143] have shown that the final value of interfacial width is only moderately sensitive to the method of background subtraction, in that the variation about the average value is less than 10%. However, as pointed out by Koberstein [109], representation of the backgound contribution as a constant will always lead to an overestimation of the interfacial thickness. The overestimation of the background causes the intensity to damp off faster thus leading to a larger interfacial thickness. Vonk [113] has shown this overestimation to be only 10%.

In order to obtain an interfacial thickness, a linear transition zone of thickness E was assumed to exist between the crystalline and amorphous phases. The electron density profile and its smoothing function was shown in Figure 5, as described by Vonk [113]. The smoothing function h(r) is a box function and its Fourier transform, H(s) was given by:

$$H(h) = \frac{(\sin \pi Eh)}{(\pi Eh)} \qquad (63a)$$

The Porod's intensity for this model is then, given previously by equation (64) as:

$$I(h) = \frac{K_p}{h^4} \left(1 - \frac{\pi^2 E^2 h^2}{3}\right)$$

For smeared intensity, this is given by equation (77a) as:

$$J(h) = \frac{K'_p}{h^3} \left(1 - \frac{2\pi^2 E^2 h^2}{3}\right) \qquad (77a)$$

A plot of $J(h)h$ vs. $1/h^2$ should then be a straight line with a negative intercept proportional to E. Representative plots of samples studied for each crystallization temperature and molecular weight are given in Figures 39 to 45. As can be seen from these representative figures, the sample had straight line portions with negative intercepts. The question now arises over which portion of the scattering profile to fit the straight line. Ruland [144] stated that the Porod's law should not be applied until s ($s = \frac{2}{\lambda} \sin \frac{2\theta}{2}$) is larger than the position at which a second maximum should appear. However, Koberstein [109] has shown that for the case of linear transition zone, the linear portion is applicable only if $Es < 0.10$, for slit smeared data with infinite slit height assumption. Furthermore, with a value of $Es < 0.10$, the transition zone calculated is within 5% of the actual value. In this study, the procedure of Koberstein was utilized to calculate the transition zone thickness. The straight

line thus drawn on these plots represents the linear region where Es < 0.10.

An alternate way to calculate the transition zone thickness is by use of the one-dimensional correlation function as described by Vonk [113] using equations (65) and (66). Both procedures were utilized to calculate the transition zone thickness and are given in Table 6 for each series of temperature. E_1 is the value calculated by plots of $J(h)h$ vs $1/h^2$ and E_2 is the value obtained by use of the one-dimensional correlation function. As can be seen, there is a consistency at each series of temperature although the values of E_2 is less than the values of E_1 in all cases. This may be due to the fact that both values are obtained in the high angular region where the S/N ratio is inherently low. Furthermore, Fourier transform of the scattering curve was used to obtain the values of E_2 which could lead to additional mathematical error in the transformation.

It can be seen that there is a difference in the transition zone thickness, depending upon the temperture of crystallization. At the crystallization temperature of 180°C there is a much lower transition zone thickness than either 140°C or 200°C. This indicates that there is less phase mixing. It is interesting to note that there was no molecular weight nor concentration of the non-crystalline component dependence upon the interface thickness for each series of temperature. Similar results were reached by Russell [15] on blends of PVC/PCL. This is in contrast to the results of Morra [26] on blends of PVF_2/PMMA, where it was found that the transition zone thickness

Table 6

Transition Zone Thickness

Sample	E_1(nm)[1]	E_2(nm)[2]
A10000	1.66	1.12
A91111	1.67	1.12
A82111	1.42	0.99
A73111	1.69	1.35
A91522	1.62	1.09
A82522	1.52	1.20
A73522	1.44	1.12
B10000	0.80	0.55
B91111	0.67	0.46
B82111	0.57	0.39
B73111	0.93	0.50
B91522	0.79	0.58
B82522	0.88	0.47
B76522	0.86	0.44
C10000	1.78	1.11
C91111	1.69	1.06
C82111	1.72	0.97
C73111	1.82	0.97

1) By equation (77a)

2) By equation (66)

increases as more PMMA was added to the blend.

After correction for the negative deviation due to an interface, the experimental data were extrapolated to $s \to \infty$. This was done to ensure accurate calculation of the invariant and calculation of the correlation function upon Fourier transform of the scattering data. To accomplish the extrapolation, the data for the straight line portion of $J(s)$vs $1/s^2$ curve were fitted, by method of Vonk [113], by the equation:

$$J(s) = \frac{C_1}{s} + \frac{C_2}{s^3} \qquad (81)$$

where C_1 and C_2 are constants. The first term represents the intensity change caused by a finite transition zone ($C_1 = 0$ for a sharp interface) and the second term represents Porod's law for the infinite slit case. To avoid negative values of $J(s)$, at very large values of s (as determined by the computer program) the intensity values were replaced by C_3/s^5. Vonk [113] attributed this effect to the neglection of the third and higher order term in the series expression of the sine function of equation (63).

1) Desmearing of the scattering curves were performed according to Vonk [113] using the measured slit intensity profile as given in Figure 46. Plots of the comparison between all of the smeared and desmeared data were shown in Figures 14 to 31.

2) Lorentz correction, as discussed previously, amounts to multiplying the intensities by h^2. Plots of this type are given in

Figures 47 to 51 for each series of temperatures and molecular weights. Using Bragg's Law [87], the long periods were calculated from the peak position and they shall be designated as L_B and are given in Table 7. As can be seen, the peak position stays at the same position for each series of temperatures, but is becoming broader as more APS is added. This is especially true when the molecular weight of the APS is high.

Two types of models used to describe scattering from a lamellar structure were employed in this study; the Hosemann paracrystalline model and the theoretical Vonk correlation function (TCF). Both of these models were discussed eariler and only their results in the application to this study will be shown.

The Hosemann paracrystalline model, with Gaussian distribution for both the amorphous and crystalline phases, was fitted to the Lorentz corrected desmeared data. Comparison of the theoretical and experimental scattering curves are shown for all samples in Figures 47 to 51. The symbols represent the experimental points while the lines represent the theoretical best fit values.

Due to the nature of the computer fitting program, a very large number of theoretical curves, greater than 10^5 in some cases, were generated. Each theoretical curve $I(s)_T$, was normalized to the experimental curve $I(s)_E$, on a total integral basis and minimizing the deviation Δ, where

$$\Delta = \int_{s_{min}}^{s_{max}} \frac{|I(s)_T - I(s)_E|}{I(s)_E} \qquad (82)$$

Table 7

Values of Long Periodicity as Determined by Various Methods

Sample	Bragg's Law (L_B)	Hosemann's (L_H)	Correction Function (L_C)
		(all values in nm)	
A10000	17.0	15.9	16.5
A91111	17.0	15.7	16.0
A82111	16.5	15.2	16.5
A73111	16.0	15.7	15.0
A91522	16.1	15.5	17.0
A82522	15.5	14.9	16.5
A73522	16.5	15.1	16.5
B10000	14.5	13.7	13.5
B91111	14.9	13.6	13.5
B82111	15.5	13.8	14.5
B73111	16.8	14.2	14.0
B91522	15.0	13.7	14.0
B82522	15.5	13.5	14.0
B73522	15.5	13.1	13.5
C10000	15.0	13.8	14.0
C91111	13.7	13.5	14.0
C82111	15.3	13.9	14.0
C73111	15.3	14.0	14.0

The deviation for all cases studied was below 6%. The fitting parameters for the theoretical curves having the smallest deviation are listed in Tables 8, 9 and 10. Keys for the fitted parameters are given in Table 11. The various fitted parameters are plotted as a function of composition are given in Figures 52 to 58. The Hosemann long periodicity, L_H, is the summation of crystal and amorphous thicknesses and are given in Table 7 for all samples.

It can be seen immediately that the periodicity stays the same throughout all composition regimes for each series of crystallization temperatures. Both the crystal thicknesses and amorphous thicknesses are within experimental error of each other at each series of crystallization temperature, with no dependence upon molecular weight of the APS nor upon concentration of APS. This indicates that the APS is not residing in the interlamellar regime of the crystalline IPS. Further evidence of this case is the lack of variation of the linear crystallinity (C/(C+A)). If the APS is residing in the interlamellar regime, the linear crystallinity must decrease due to the increase of the amorphous thickness. The bulk crystalline, as determined by DSC of these ISP/APS blends decreases down to 19% at a 70/30 ratio of IPS to APS [85]. The fact that we are not seeing this decrease in the SAXS crystallinity further indicates that the APS is not residing in the interlamellar regime.

These results are in excellent agreeement with those reached by Warner et al. [85] in blends of IPS/APS with much lower molecular weight of the APS. However, they are in contrast to the blends of

Table 8

Best Fit Parameters for Hosemann Paracrystalline Model

T(C) = 200°C

Sample	Δ(%)	ϕ_c(%)	C(nm)	A(nm)	g_c	g_a	N	E(nm)
A10000	3.79	28	4.4	11.5	0.32	0.30	2.9	1.66
A91111	2.83	30	4.7	11.0	0.42	0.36	3.2	1.67
A82111	4.92	30	4.6	10.6	0.57	0.39	3.1	1.42
A73111	4.10	28	4.3	11.4	0.58	0.32	1.4	1.69
A91522	3.48	32	4.9	10.5	0.41	0.41	3.0	1.62
A82522	4.45	31	4.7	10.2	0.48	0.42	3.4	1.52
A73522	4.05	30	4.5	10.6	0.53	0.41	2.8	1.44

Table 9

Best Fit Parameters for Hosemann Paracrystalline Model

T(C) = 180°C

Sample	Δ(%)	ϕ_c(%)	C(nm)	A(nm)	g_c	g_a	N	E(nm)
B10000	3.85	27	3.7	10.0	0.32	0.32	4.0	0.80
B91111	4.52	29	4.0	9.6	0.46	0.40	3.2	0.67
B82111	5.10	32	4.4	9.4	0.51	0.47	3.2	0.57
B73111	3.89	32	4.5	9.7	0.64	0.55	3.0	0.92
B91522	4.28	31	4.3	9.4	0.40	0.39	3.1	0.92
B82522	4.93	31	4.2	9.3	0.50	0.46	3.1	0.88
B73522	4.31	31	4.0	9.1	0.57	0.48	3.0	0.86

Table 10

Best Fit Parameters for Hosemann Paracrystalline Model

T(C) = 140°C

Sample	Δ(%)	ϕ_c(%)	C(nm)	A(nm)	g_c	g_a	N	E(nm)
C10000	5.71	15	2.0	11.8	0.03	0.26	4.4	1.78
C91111	5.17	16	2.1	11.4	0.05	0.30	4.5	1.69
C82111	4.65	17	2.4	11.5	0.17	0.38	3.7	1.72
C73111	4.72	21	3.0	11.0	0.24	0.42	3.2	1.82

Table 11

Keys for Fitting Parameters of Hosemann Paracrystalline Model

Symbols	Meaning
Δ	Deviation between experimental and model
ϕ_c	Linear crystallinity
C	Mean crystal (lamellae) thickness
A	Mean amorphous thickness
g_c	Crystal thickness distribution
g_a	Amorphous thickness distribution
N	Hosemann's parameter for lamellae stack
E	Transition zone thickness (predetermined)

PVF_2/PMMA and PVC/PCL, where the non-crystalline component was found in the interlamellae region [14,26].

The greatest noticable effects are seen in the crystal and amorphous distribution sizes, especially the crystal size distribution. As more APS is added there is an increase in the distribution of both phases, especially if the molecular weight of the APS is high (comparison made only in the 180°C and 200°C cases). This manifestation indicates that there is a significant amount of thin lamellae as one goes up in concentration of APS and molecular weight. It is very hard to visualize a polymer system composed of very thin and very thick lamellae. This broad distribution could also arise from a less uniform lamellae stack and this is represented by parameter N. The value of N, i.e., the number of lamellae per stack as proposed by Hosemann, remains low yet quite constant. Baczek attributed the value of N to the number of lamellae that are perfectly aligned with one another. In this case, the discussion of N will be delayed until the Vonk's theoretical correlation function fit is discussed.

A theoretical calculation can be made to predict what the long period of these blends would be if all of the amorphous component added were to be included between the lamellae of the semi-crystalline component. To accomplish this, simple addivity of the volume is assumed. Letting the long periods of the homopolymer and blends be L_o and L respectively, using a one-dimensional model of alternating crystalline and amorphous phase with no transition zone, the volume fraction of the semi-crystalline component in the blend, V_2, can be

given by:

$$V_2 = \frac{L_o}{L} \tag{83}$$

From this equation, values of L as a function of V_2 can be calculated and compared to experimental results. This is done and is shown in Table 12.

From this exercise, it can be seen that the experimental value stays constant while the long period from the theoretical calculation increases by as much as 70%. This further indicates that the APS is not residing in the interlamellar region.

The Vonk's theoretical one-dimensional correlation function was also used to fit the Lorentz corrected data. In this case the computer program allows the user various options on how to describe the crystal and amorphous distribution. The use of various distributions will lead to vastly different results on the fitting parameters [106,145]. Because of the large numbers of theoretical curves generated by the computer, and the fact that we are using the results for comparative studies, only a particular distribution is chosen for each phase. In this case, a Gaussian distribution was employed for the crystal phase while a log-normal distribution was employed for the amorphous phase. Comparison of the experimental and best fit theoretical curves are presented in Figures 59 to 76 for all samples studied. The best fit parameters are given in Table 13, along with its long periodicity. This long periodicity, Lc, is also given in Table 7.

Table 12

Comparison of Long Periods From Hosemann's Model to Values Calculated Assuming All of the APS to be Interlamellar

Sample	Long Period (nm) Hosemann	Calculated
A10000	15.9	15.9
A91111	15.7	17.6
A82111	15.2	19.9
A73111	15.7	22.7
A91522	15.5	17.6
A82522	14.9	19.9
A73522	15.1	22.7
B10000	13.7	13.7
B91111	13.6	15.2
B82111	13.8	17.1
B73111	14.2	19.6
B91522	13.7	15.2
B82522	13.5	17.1
B73522	13.1	19.6
C10000	13.8	13.8
C91111	13.5	15.3
C82111	13.9	17.3
C73111	14.0	19.7

One aspect to notice in these correlation functions plots is that they are rather shallow in their depth. This indicates that the values to be obtained for both its crystallinity and the thickness distribution will be low and broad, respectively. Indeed this is noticed in Tables 13. The values obtained can only be used on a comparative level due to the assumption made in its distribution. As Wetton et al. [106] pointed out, the values of the fitting parameters obtained on the Vonk's TCF will vary significantly depending on the distribution assumed.

The long periodicity, however, is obtained from the experimental data and does not depend on the distribution assumed. A comparison of the long periodicity obtained from the correlation function and from Hosemann's paracrystalline model is given in Figures 77 to 79. As can be seen, there is an excellent agreement between the two methods.

Comparisons of the fitting parameters between the Hosemann's paracrystalline model and Vonk's TCF model are given in Figures 80 to 83.

Like the Hosemann's analysis, the Vonk's TCF gives a broad distribution of the crystalline thickness as the concentration of the APS is increased, especially if the molecular weight of the APS is high. However, the amorphous thickness distribution by the Vonk's TCF is generally greater than that obtained by Hosemann's fit. This may be due to the type of distribution assumed, but nevertheless, it can be concluded that on a comparative scale, the addition of the APS serves to increase both the distribution of the amorphous and crystalline

Table 13

Best Fit Parameters for Vonk Theoretical Correlation Function

Sample	Long Period (nm)	ϕ_c (%)	g_c	g_a
A10000	16.5	24	0.40	0.36
A91111	16.0	14	0.30	0.45
A82111	16.5	30	0.54	0.50
A73111	15.0	34	0.74	0.74
A91522	17.0	15	0.40	0.40
A82522	16.5	16	0.46	0.37
A73522	16.5	10	0.62	0.36
B10000	13.5	20	0.30	0.30
B91111	13.5	10	0.30	0.30
B82111	14.5	12	0.50	0.40
B73111	14.0	16	0.68	0.76
B91522	14.0	10	0.30	0.30
B82522	14.0	4	0.56	0.48
B73522	13.5	10	0.72	0.56
C10000	14.0	32	0.24	0.20
C91111	14.0	32	0.24	0.28
C82111	14.0	30	0.36	0.32
C73111	14.0	30	0.40	0.36

thicknesses.

One of the main differences between the Hosemann fit and the Vonk's TCF is the values of the crystallinity obtained. Wereas the Hosemann crystallinities remain at approximatly 30%, the Vonk's crystallinities are quite low, some as low as 4%, except for a few samples. These low values further reflect a high percentage of thin lamellae, despite the fact that the long periodicity of both models are in excellent agreement. The low values of crystallinities and broad distributions are in agreement with those results obtained by Warner et al. [85]. As elucidated by Warner et al., this is understandable by the fact that the depth of the minimum in the correlation function is strongly dependent upon three factors:

i) decrease in crystallinity below 50%

ii) broad phase distribution

iii) stacking disorder such as angular branching of lamellae or lamellar stack of limited size

The third effect can be interpreted in terms of the Hosemann parameter N. A low value of N would give a much shallower depth than a high value of N. Thus if there is a disorder stacking of lamellae, as emplified by low values of N, fitting a theoretical correlation function based on Vonk's model will give an artifically low crystallinity.

The use of Vonk's TCF in the application to this study only serves as a comparative basis for the samples studied. The Vonk's TCF does not accurately describe this system for the various reasons:

i) the assumption of infinite stack is questionable due to the broadness of the correlation function. Crist [145] indicated that the ratio of peak position to peak width should be less than 0.5 in order for the infinite stack to be valid.

ii) the very broad fitting parameter, coupled with the low crystallinity would give an extremely broad melting point, especially with increasing concentration of the APS. However, many workers [29,54,147] have shown that this is not the case, that the melting point range observed from DSC peak width and optical technique, remains unchanged with increasing APS content.

In light of the results of these two models, it is felt that the Hosemann paracrystalline model describes this blend system more accurately. The fact that the lamellae thickness stays constant would lead to a constant melting point, as observed by various workers [29, 54,37].

A point should be made here regarding the values of the invariant, the mean squares of the electron density fluctuation. The theoretical invariant is given as:

$$\overline{\eta_I^2} = \phi_c (1 - \phi_c) (\rho_c - \rho_a)^2 \qquad (84)$$

where ϕ_c is the volume fraction of crystallinity, ρ_c and ρ_a are the electron densities of the crystalline and amorphous phases respectively. When a finite transition zone is present, this will

reduce the value of the invariant according to:

$$\overline{\eta_E^2} = [\phi_c (1-\phi_c) - (\frac{E}{3L})] (\rho_c - \rho_a)^2 \qquad (85)$$

where E is the transition zone thickness and L is the long periodicity.

In the calculation of the one-dimensional invariant, ϕ_c was taken from the Hosemann's data. The value of E was that obtained by the plot of J(h)h vs $1/h^2$. The crystal and amorphous density are given by Warner [85] as 1.112 and 1.04 g/cm^3, respectively. The values of $\overline{\eta_I^2}$ and $\overline{\eta_E^2}$ as calculated from equations (84) and (85) respectively are given in Tables 14. The experimental values, $\overline{\eta^2}$, are also given. Comparisons of $\overline{\eta_I^2}$, $\overline{\eta_E^2}$ and $\overline{\eta^2}$ are plotted in Figures 84 and 85. Fairly good agreement can be seen between the experimental and theoretical results lending further support that the APS is not in the interlamellar region, since if it was, the value of the invariant would decrease slightly due to a decrease in crystallinity. However, these invariant results must be interpreted with caution. The maximum crystallinity is only about 30%. If we assume that all the APS is included between the lamellae, the minimum crystallinity, corresponding to a 70% vol. IPS, would be 19%. This would affect the invariant calculation by only 25%, assuming the amorphous density is the same as the bulk APS density.

Thus it can be concluded that based upon all these results, that the molecular weight and concentration of the APS have no effect on the interlamellar distance. The non-crystalline component is rejected

Table 14

Mean Square Electron Density Fluctuation

Sample	$(\text{mole } e^-/cm^3)^2 \times 10^3$ $\overline{\eta^2}$ [a]	$\overline{\eta_I^2}$ [b]	$\overline{\eta_E^2}$ [c]
A10000	0.212	0.223	0.186
A91111	0.263	0.233	0.194
A82111	0.231	0.235	0.201
A73111	0.320	0.222	0.182
A91522	0.238	0.243	0.217
A82522	0.212	0.241	0.203
A73522	0.247	0.233	0.198
B10000	0.210	0.220	0.198
B91111	0.230	0.231	0.213
B82111	0.240	0.242	0.227
B73111	0.280	0.241	0.217
B91522	0.230	0.240	0.219
B82522	0.227	0.240	0.215
B73522	0.220	0.236	0.212
C10000	0.240	0.138	0.090
C91111	0.300	0.148	0.100
C82111	0.257	0.160	0.114
C73111	0.280	0.188	0.139

[a] Experimental values

[b] $\overline{\eta_I^2} = \phi_c(1-\phi_c)\,(\rho_c - \rho_a)^2$

[c] $\overline{\eta_E^2} = \left[\phi_c(1-\phi_c) - \left(\frac{E}{3L}\right)\right](\rho_c-\rho_a)^2$

from the growth front at all temperatures of crystallization studied.

Both the Hosemann's paracrystalline model and Vonk's TCF model can be used to describe the scattering system, although the Vonk's model would be less accurate.

In the next section, discussion is made on why the APS is not residing in the interlamellar region, contrary to other blend systems, despite such high molecular weight and high degree of supercooling.

C H A P T E R V

DISCUSSION

To describe the morphology of a semi-crystalline blend crystallized from the melt state, Keith and Padden [84] defined a parameter called delta (δ). δ is defined as D/G, where D is the diffusion rate of the non-crystalline component (or impurity) away from the growth front of the crystallizing component, and G is the growth rate of the crystallizing component. Keith and Padden viewed the non-crystallizable polymer in a blend as an impurity added to the crystallizable polymer. The location of this "impurity" is then related to δ, which has a unit of length. Qualitatively, if δ is large, the impurity has time to diffuse away from the growth front and be excluded from the interlamellar regions, whereas a small value of δ (δ being less than the width of the interlamellar region) would imply that the impurity is trapped between the lamellae. Morra [26] postulated a very qualitative relationship between δ and the interaction parameter between the polymer. A favorable interaction between the two polymers would decrease D and prevent the impurities from being segregated into large domain.

Past studies [14,26] have shown that for blends of PVF_2/PMMA and PVC/PCL, the non-crystalline component was found to reside in the interlamellar region. In both cases, there was favorable interaction between the polymers. Carter et al. [146], studied the morphology of blends of cis and trans-polyisoprene. They found that only at very high cis content (>70%), was these any change in the small angle

scattering long periodicity, and even at very high cis content, the increase was only less than 10%. Furthermore, optical microscopy showed that the spherulites are volume filled in all compositions of blends studied. However, there was an increase in the coarsening of the spherulites. They concluded that the non-crystallizable cis-polyisoprene segregates increasingly into the interfibrillar regions and this region increases in size as the cis content of the blend increases. Only a limited amount of interlamellar segregation occurs and this only is seen at very high cis content. It is expected that these blends of cis- and trans polyisoprene do not have any kind of specific interaction, i.e. χ (Flory interaction parameter) is very close to zero, through this need to be proved by further experiments such as melting point depression, or SANS.

On studies that have been done on blends of atactic and isotactic polystyrene, Warner et al. [85] has found that the non-crystallizable atactic polystyrene resided in the interfibrillar region, since the SAXS periodicity did not vary and the spherulitic remained volume filling at all compositions of IPS and APS.

It is interesting to note at this time that SAXS studies [30] of isotactic polystyrene with the non-crystallizable poly(phenylene oxide) (PPO) yield results from which it was concluded that the PPO was distributed between individual lamellae. Melting point depression studies by Neira [149] and Runt [147] showed that there was favorable interaction between the two species.

Runt [147] did a thermal study on blends of IPS and APS. He was able to calculate a polymer-polymer interaction parameter (χ_{12}) value

based upon melting point depression. Employing the theory of Flory-Huggins [148], the equilibrium melting point of the crystalline material in the blend (Tm') is related to the χ_{12} parameter by the relation:

$$\frac{1}{T_{m1}} - \frac{1}{T_m^\circ} = \frac{-R\bar{V}_2}{\Delta H_f^\circ \bar{V}_1}\left[\frac{\ln\phi_2}{M_2} + \left(\frac{1}{M_2} - \frac{1}{M_1}\right)\phi_1\right] + \frac{-R\bar{V}_2}{\Delta H_f^\circ \bar{V}_1}(\chi_{12}\phi_1^2) \qquad (86)$$

where $\bar{V}$ is the molar volume of the polymer repeat unit, ϕ the volume fraction of the component in the blend, ΔH_f° the perfect crystal heat of fusion of the crystallizable component, R the universal gas constant, M the degree of polymerization, and T_m° the equilibrium melting point of the pure crystallizable component. The first term on the right hand side represents the entropy of mixing, which is negligible for polymer of high molecular weights. The second term reflects the enthalpy of mixing which is dependent primarily on χ_{12} and ϕ_1. Employing equation (86), Runt, using melting point depression data, calculated an χ_{12} value for IPS/APS blends as -.003 for molecular weights of APS being 50,000.

The interaction parameter of a polymer-polymer system can also be calculated from SANS data. This author (Section II) has obtained a value of the interaction parameter between the IPS and APS for blends of various concentrations. These results are shown in Table 19.

Quite clearly, it can be seen that the χ_{12} value is very close to zero in all compositions studies, and in the melt state, these blends do form an "ideal" mixture [150].

Self diffusion rate data for the APS as a function of molecular weight and temperature were calculated previously and was plotted in

Figure 12. The growth rate for these blends was obtained from Keith and Padden [29] and Yeh and Lambert [54]. Calculation of the δ values from these diffusion and growth rate are given in Tables 15 and 16 and are plotted in Figure 86.

From this qualitative analysis, it can be seen that at the crystallization temperature of 190°C and below, the δ values are less than the interlamellar distance. Thus if the δ parameter truly describes the morphology, then at the crystallization temperature of 180°C and 140°C, we would expect the width of the interlamellar distance in these blends to increase in order to accommodate the entrapped atactic polystyrene. However, the opposite result was found. In all cases studied, the interlamellar distance did not vary at each temperature of crystallization as more of the non-crystallizable component is added. This is seen even at 140°C crystallization temperature where the diffusion rate is very slow.

There are two possible explanations to explain this observed deviation from the Keith-Padden postulation:

1) The diffusion rate of the non-crystallizable component, in this case the APS, is much higher than what was calculated. The diffusion rate calculated were the self diffusion rates of APS in APS. Maybe it is possible that in the crystallization of these blends, the diffusion rate of the APS is much higher than the self diffusion rate calculated in its homopolymer. An increase in the diffusion rate would increase the value of δ. However, despite this simple reasoning, it is hard to

Table 15

Values of δ ($\delta = D_{self}/G$)[a] for $\bar{M}w$ (APS) = 1.11×10^6

$T = 200°C$ $D_{self} = 4.90 \times 10^{-13}$ cm^2/sec

Composition ISP/APS	δ (nm)
90/10	32.6
80/20	42.0
70/30	58.8

$T = 180°C$ $D_{self} = 9.46 \times 10^{-14}$ cm^2/sec

Composition ISP/APS	δ (nm)
90/10	2.27
80/20	2.58
70/30	2.99

$T = 160°C$ $D_{self} = 1.57 \times 10^{-14}$ cm^2/sec

Composition ISP/APS	δ (nm)
90/10	0.51
80/20	0.57
70/30	0.73

$T = 140°C$ $D_{self} = 2.19 \times 10^{-15}$ cm^2/sec

Composition ISP/APS	δ (nm)
90/10	0.15
80/20	0.19
70/30	0.26

[a] D_{self} is the self diffusion coefficient of polysytrene

Table 16

Values of δ ($\delta = D_{self}/G$)[a] for $\bar{M}w$ (APS) = 5.22×10^5

T = 200°C $D_{self} = 4.90 \times 10^{-13}$ cm²/sec

Composition ISP/APS	δ (nm)
90/10	70.7
80/20	90.0
70/30	127.4

T = 180°C $D_{self} = 9.46 \times 10^{-14}$ cm²/sec

Composition ISP/APS	δ (nm)
90/10	4.92
80/20	5.59
70/30	6.47

T = 160°C $D_{self} = 1.57 \times 10^{-14}$ cm²/sec

Composition ISP/APS	δ (nm)
90/10	1.10
80/20	1.24
70/30	1.57

T = 140°C $D_{self} = 2.19 \times 10^{-15}$ cm²/sec

Composition ISP/APS	δ (nm)
90/10	0.22
80/20	0.26
70/30	0.32

[a] D_{self} is the self diffusion coefficient of polysytrene

visualize that at low crystallization temperature of the blend (i.e. 140°C), that the diffusion rate will have over a hundred fold increase.

2) The second possible explanation is that the diffusion rate of the impurity is not constant. The δ parameter assumes a constant diffusion rate. A constant diffusion rate can only be represented by steady state, and the concentration dependence term is removed. However, in a real situation, the concentration dependence term may become significant, as there is a concentration build-up of impurity at the interface.

It is with this in mind, that an expression is developed to express the growth rate at a function of impurity gathered at the interface.

The Keith-Padden δ parameter is actually based upon the growth kinetic of metallurgy, where the rejected specie accumulates at the growth front. Consider the diagram below for a steady state composition diagram for the impurity:

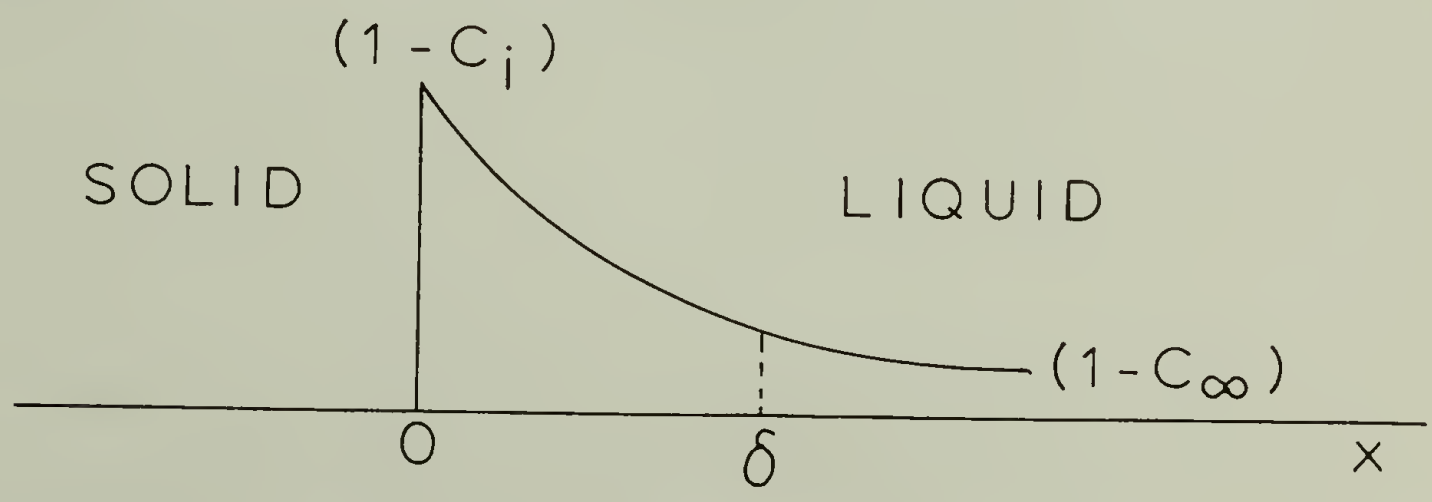

δ is defined as the width of the segregation length [84]. Now instead of considering the impurity concentration, consider the effect of the impurity layer (δ) on the growth kinetics of the isotactic polystyrene.

If we assume that:

C_∞ = volume fraction of bulk crystallizable component in the blend

C_i = volume fraction of crystallizable component at the interface

$1-C_\infty$ = volume fraction of impurity in the blend

Thus we can write the following postulations:

a) The overall growth rate is:

$$G = G_o\, C_i \tag{87a}$$

G_o = growth rate with no impurity present

C_i = 1, when there is no impurity

b) The growth front will advance δ in time Δt with no impurity present:

$$\delta = G_o\, \Delta t \tag{87b}$$

c) Due to the presence of impurity, we must modify equation (87b). Thus the modified growth front can be represented as:

$$\delta = G_o\, \Delta t\, C_i \tag{87c}$$

This equation assumes that the decrease of the growth front is a product of only C_i, the volume fraction of crystallizable component at the interface.

d) The amount of impurity diffusing out at any distance x in time Δt is:

$$\delta = D\left(\frac{\partial C}{\partial x}\right) \Delta t \tag{87d}$$

Assuming a linear slope over the segregation value δ (i.e. $\frac{\partial C}{\partial x}$ = constant over δ)

$$\delta = D\left(\frac{(1-C_i) - (1-C_\infty)}{\delta}\right) \Delta t \tag{87e}$$

Now equating equation (87c) and (87e) to achieve an overall mass balance as:

$$G_o \Delta t \, C_i = \frac{D}{\delta} (C_\infty - C_i) \Delta t \qquad (87f)$$

Simplifying equation (87f) and expressed in term of C_i as:

$$C_i = \frac{C_\infty}{1 + \frac{G_o}{D} \delta} \qquad (87g)$$

e) Substituting C_i into equation (87a), we can write the growth rate of the crystalline component due to the presence of impurity as:

$$G = G_o \left(\frac{C_\infty}{1 + \frac{G_o}{D} \delta}\right) \qquad (87h)$$

The derivation of equation (87h) assumes several key factors which may not hold for the real system. They are:

a) The assumption that the overall volume fraction of crystallizable component stays constant in the liquid phase is not valid at the latter stages of crystallization. In the early stages, this assumption holds since crystallization is occurring from the melt state.

b) The assumption that the volume fraction of impurity present in the liquid phase is staying constant is not valid if the degree of crystallinity is high. This is especially true during the latter part of crystallization, since the volume

fraction of build-up of impurity would increase during the latter stages.

c) The assumption of a linear gradient of impurity concentration over the segregation distance is not truly valid. Realisticly, this should be exponential, but for simplifing the calculation, we are assuming a linear profile.

Nevertheless, despite these assumptions made, we can qualitatively assume that equation (87h) can describe the growth of the crystalline component. If there was no impurity present, C_i would be one and the growth rate would be the growth rate of pure component. Equation (87h) essentially allows us to look at the effect of segregation value δ on the growth rate. In other words, given a segregation value δ, what would be the growth rate necessary to achieve this segregation due to the presence of impurity. For example, for the case of the 90/10 blends of IPS and APS ($Mw = 1.11 \times 10^6$) at a crystallization temperature of 180°C, the value of $\frac{D}{\overline{G}}$ would be approximately 50 Å.

This gives a volume fraction of crystalline component as $C_\infty = 0.9$. Now for rejection by lamellae as 50 Å (i.e. $\delta = 50$ Å), we can calculate G as:

$$G = G_0 \left(\frac{0.9}{1 + \frac{1}{50}(50)} \right)$$

$$= \frac{0.9}{2} = 0.450\ G_0$$

Thus if the growth rate can be described by equation (87h), the growth

rate should be about half of the value of its impurity-free condition. If the growth rate is much higher, than the crystallizable component will overtake the impurity layer and it will be trapped by the lamellae. For example, for rejection by the fibril, δ would be about 1000 Å. Employing the same conditions as before, we can calculate a growth rate as:

$$G = G_o \left(\frac{0.9}{1 + \frac{1}{50}(1000)}\right)$$

$$= \frac{0.9}{201} = 0.0045\ G_o$$

Thus if the impurity is to be rejected by the interfibrillar region, then the growth rate must be slower. If it is much faster, the impurity will be trapped by the fibers. Judging from the growth rate data for this condition, it can be seen that the growth rate is about the right order of magnitude for this at this temperature, but it is much faster than the growth rate necessary for fibrillar rejection. Thus the impurity is not trapped by the lamellae, but rather by the fibrils.

The Keith-Padden δ parameter is a segregation parameter, but caution has to be used if it is to predict an impurity layer. The impurity layer affects the growth rate of the crystallizable component, but only when the growth rate is fast enough, will the growth front overtake the impurity layer.

DeGennes [159,160] presented an elegant theory relating the diffusion coefficient with the Flory interaction parameter χ. He considered a polymer melt blend (two types of polymer chain) near the critical point to investigate the dynamics of fluctuation. DeGennes developed his equation as [160]

$$D_C(\chi,T) = D_1(T)N^{-2}\left(\frac{\chi_c-\chi}{\chi_c}\right) \tag{88}$$

where D_1 is a microscopic constant, N is the degree of polymerization of the blend and χ_c is the critical value of χ. Krause [7] presented χ_c as:

$$\chi_c = \frac{1}{2}\left(\frac{1}{N_1^{1/2}} + \frac{1}{N_2^{1/2}}\right)^2 \tag{89}$$

where N_1 and N_2 are the degree of polymerization of component 1 and 2, respectively. For a polymer blend of high molecular weight, χ_c would be very close to zero.

Equation (88) states that when $\chi = 0$, the diffusion coefficient is inversely proportional to the square of the degree of polymerization, which is the reptation result for an ideal mixture. However as $\chi \to \chi_c$, the diffusion coefficient approaches zero. This factor $(\chi_c-\chi)/\chi_c$ is postulated by DeGennes to reflect the law of "thermodynamic slowing down" near a critical point [161,162]. The diffusion described by equation (88) is extremely slow, because of this fator plus the N^{-2} dependence of D_{rep}.

In a truly compatible system, i.e. value of $\chi < \chi_c$, the diffusion rate as described by equation (88) would increase. Remembering that

diffusion occurs down a concentration gradient, this means that there is more tendency towards phase mixing of the components. By this argument, it is shown that for a blend exhibiting favorable interaction parameter ($\chi < \chi_c$), that there is much tendency towards mixing of the component in the amorphous phase.

Qualitatively, this would seem to support the postulation put forward by Morra [26] that if there is interaction, then the non-crystalline component will be found between the lamellae. If there is no interaction, the non-crystalline component will be rejected by the lamellae and accumulated in the interfibrillar or interspherulitic region. On semi-crystalline blend systems studied thus far, PVC/PCL, PMMA/PVF_2, IPS/APS, CIS/TRANS polyisoprene, this postulation holds quite well. More detailed studies on other blend systems will be needed to further elucidate this postulation.

CHAPTER VI

SUGGESTION FOR FUTURE STUDIES

The diffusion coefficients used in this study were based upon the self-diffusion value. However, during the crystallization kinetics of a semi-crystalline blend, the value of the self-diffusion coefficient may not be valid, since there is concentration gradient being formed. In such a case, the diffusion coefficient may be concentration dependent. Thus the most important criteria that remain to be measured in these semi-crystalline is the diffusion rate of the non-crystalline component.

Several methods have been developed to measure the bulk diffusion rate. Perhaps the most widely used method is radioactive labelling [138,151-152]. Other methods include: infrared microdensitrometry [153,154], proton nuclear magnetic resonance (NMR) [155], scanning electron microscopy equipped with energy-dispersive x-ray analysis [139], and laser fluorescence photobleaching recovery [156-158].

Whatever method is employed, one has to be sure that the chemical nature of the polymers is not changed, as it will have drastic effects on the diffusion rate.

Further work on other semi-crystalline blends must be done to study if there is a correlation between χ and the morphology of the semi-crystalline blend. Since crystallization is occurring from the melt state, one has to be certain that there is no segregation between the components in the melt state. This could easily be checked by various methods as outlined in the Introduction.

One particular interesting system would be blends of isotactic polystyrene with poly(vinylmethyl ether) (PVME). Schmidt et al. [163] have done an experiment on deuterated atactic polystyrene with hydrogenated PVME. Using SANS technique he has shown the variation of χ_{12} as a function of temperature. As one goes from 20°C to 100°C the value of χ_{12} changes from negative to positive. It would be interesting to study this blend with IPS. If there is a variation of χ_{12} with temperature for IPS and PMVE, then it might be possible to see different kinds of morphology depending on what temperature it is crystallizing at.

Very recently, VanderHart [164] has developed a novel technique using C-13 NMR with magic angle spinning (MAS) and cross-polarized (CP) to locate the atactic polystyrene specie in the blend of IPS/APS. This technique takes into the account that if the APS is segregated into the interfibrillar region, the probability of nearest neighbor IPS chain surrounding the APS would be much lower than if the components are mixed with one another. The use of MAS coupled with CP can distinbuish between protonated and deuterated chain carbon. Furthermore, the SP process is capable of cross-polarizing carbons within a radius of 0.5 nm from a neighboring proton. Thus if the APS is fully deuterated, then a decrease in normalized cross-polarized intensity for the deuterated chain, relative to that of the fully amorphous mixture, could be interpreted as vertification of segregation of the IPS and APS within the amorphous phase.

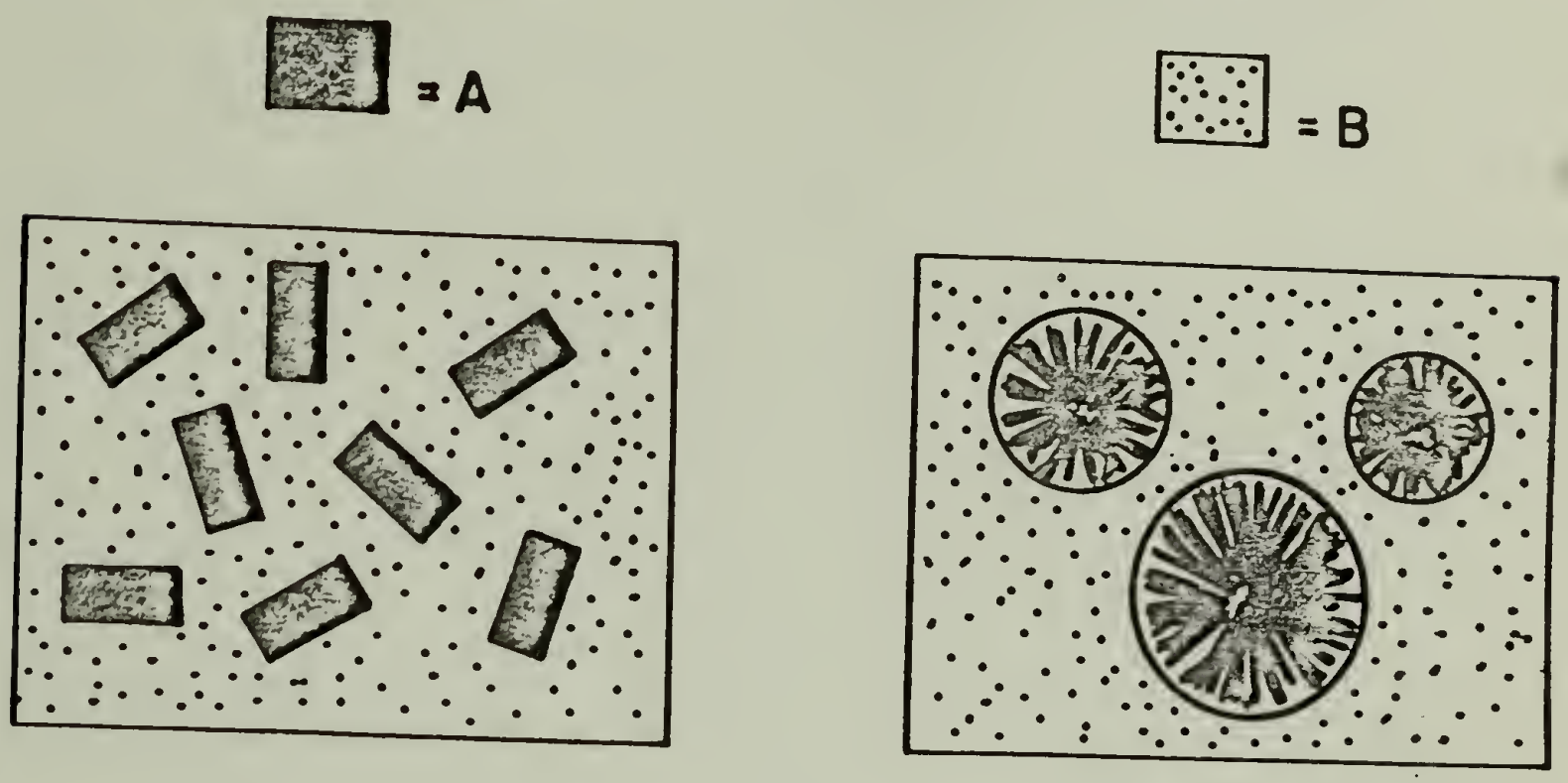

Figure 1. Schematic illustration of possible morphologies of a binary blend having one crystallizable component (reference 10).

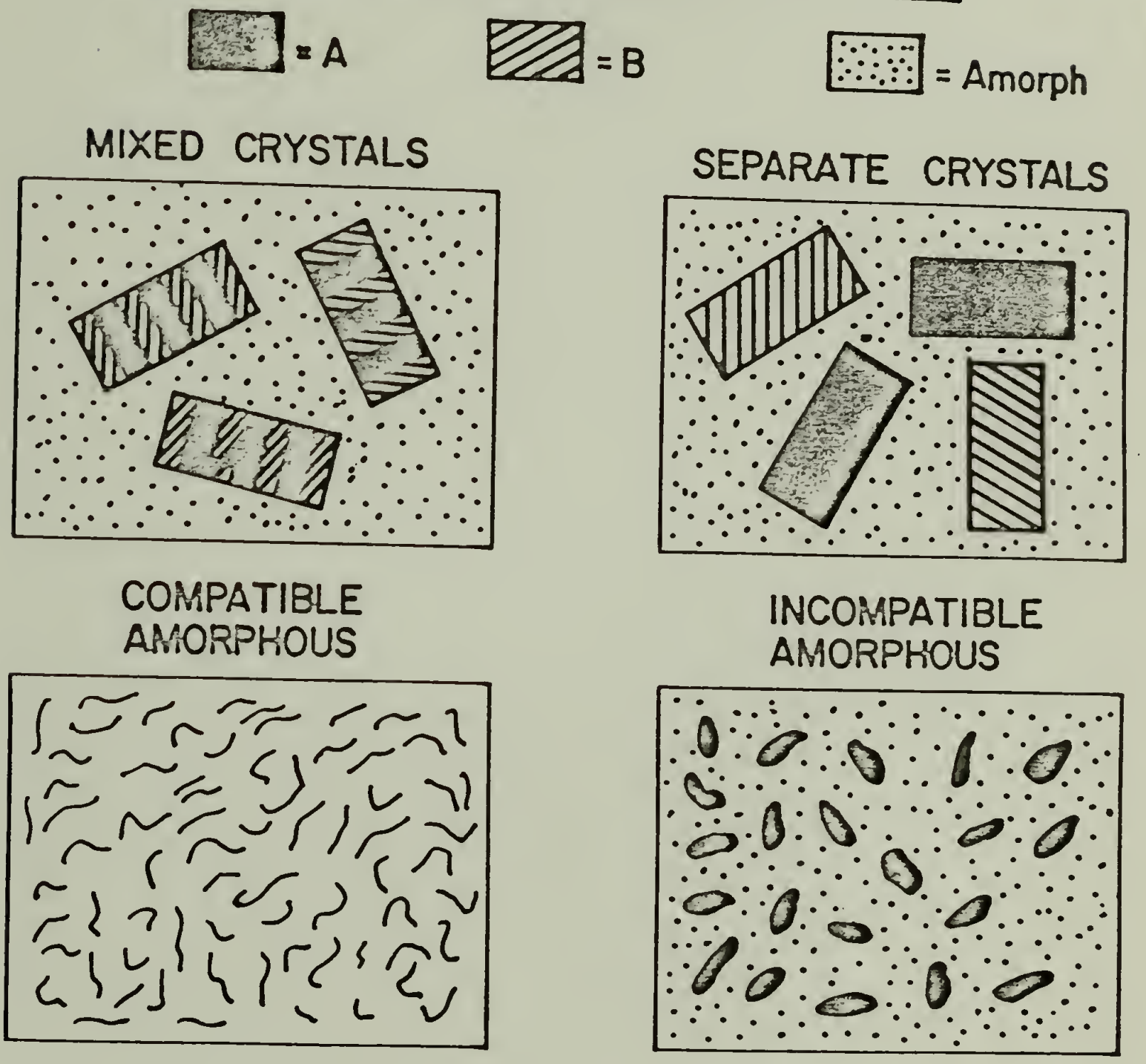

Figure 2. Schematic illustration of possible structures in a binary blend where both components are crystallizable (reference 10).

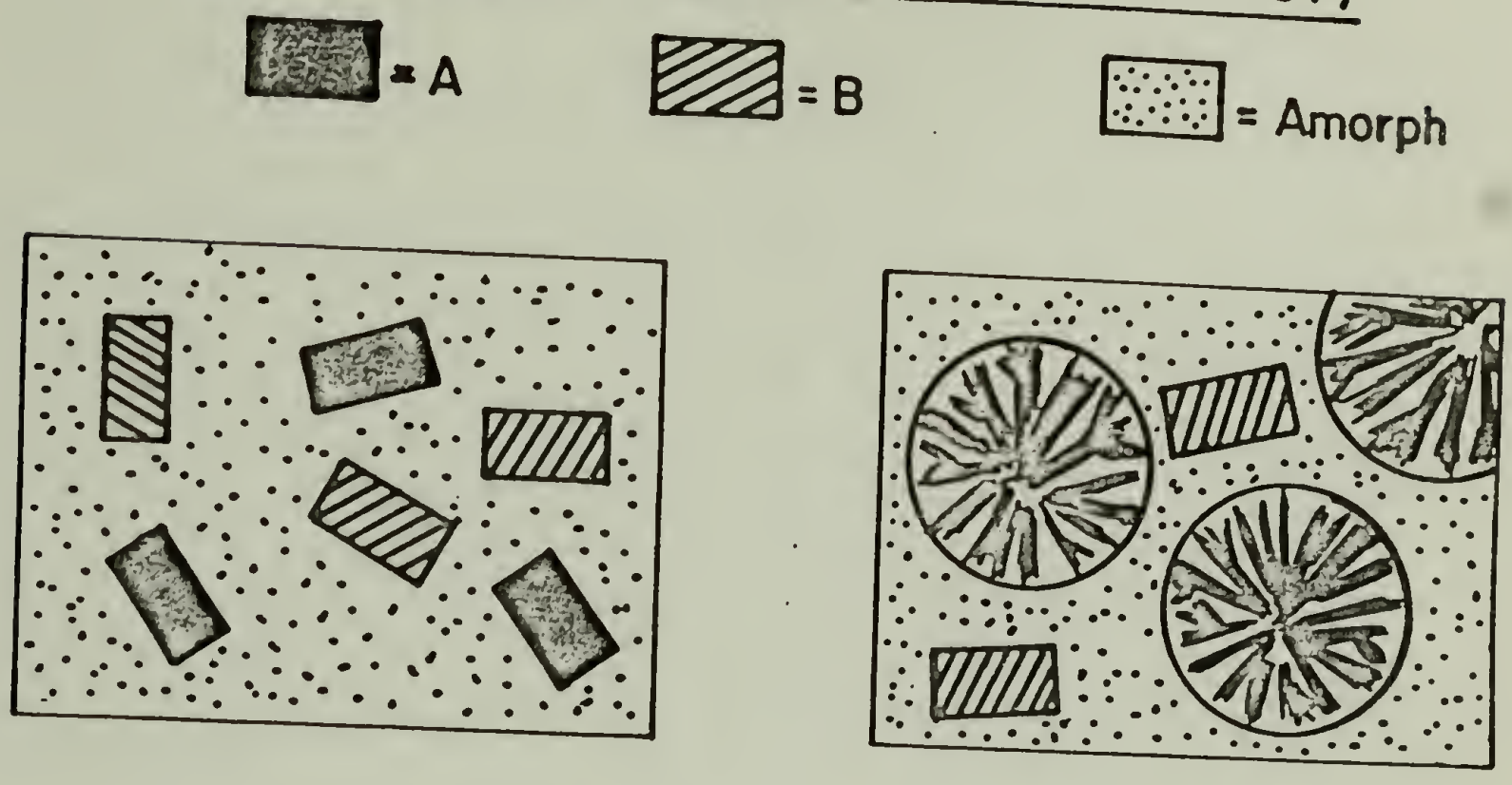

Figure 3. Schematic illustration of various morphologies that might be encountered with a binary blend of two crystallizable components (reference 10).

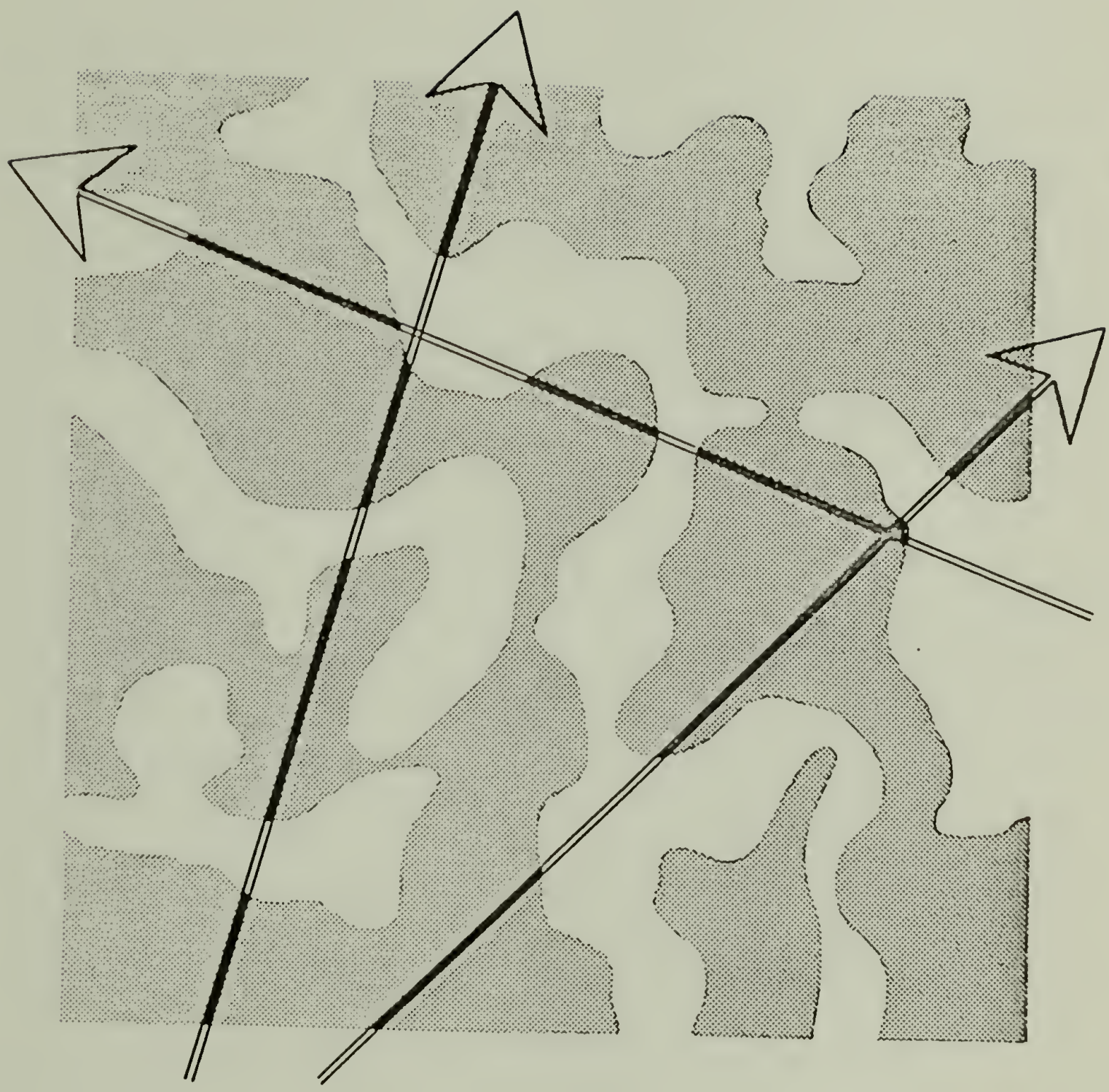

Figure 4. Chord length of a random two phase system. The average chord lenghts are the average length of randomly drawn vectors passing through the two phases (reference 98).

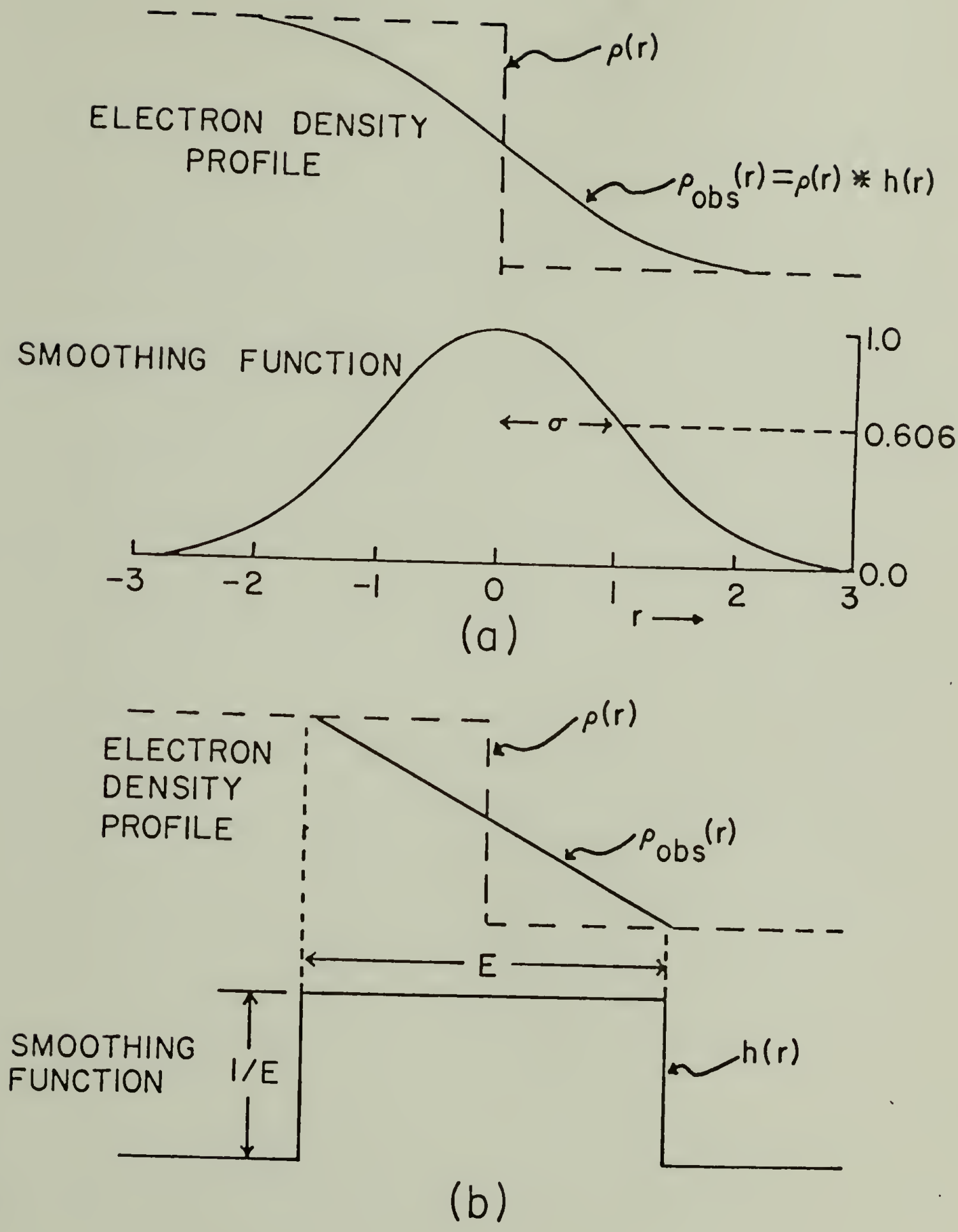

Figure 5. Electron-density profile, ρ(r), and smoothiing function, h(r), for (a) sigmoidal-gradient model, (b) linear-gradient model (reference 109).

ISOTACTIC POLYSTYRENE in $CDCl_3$

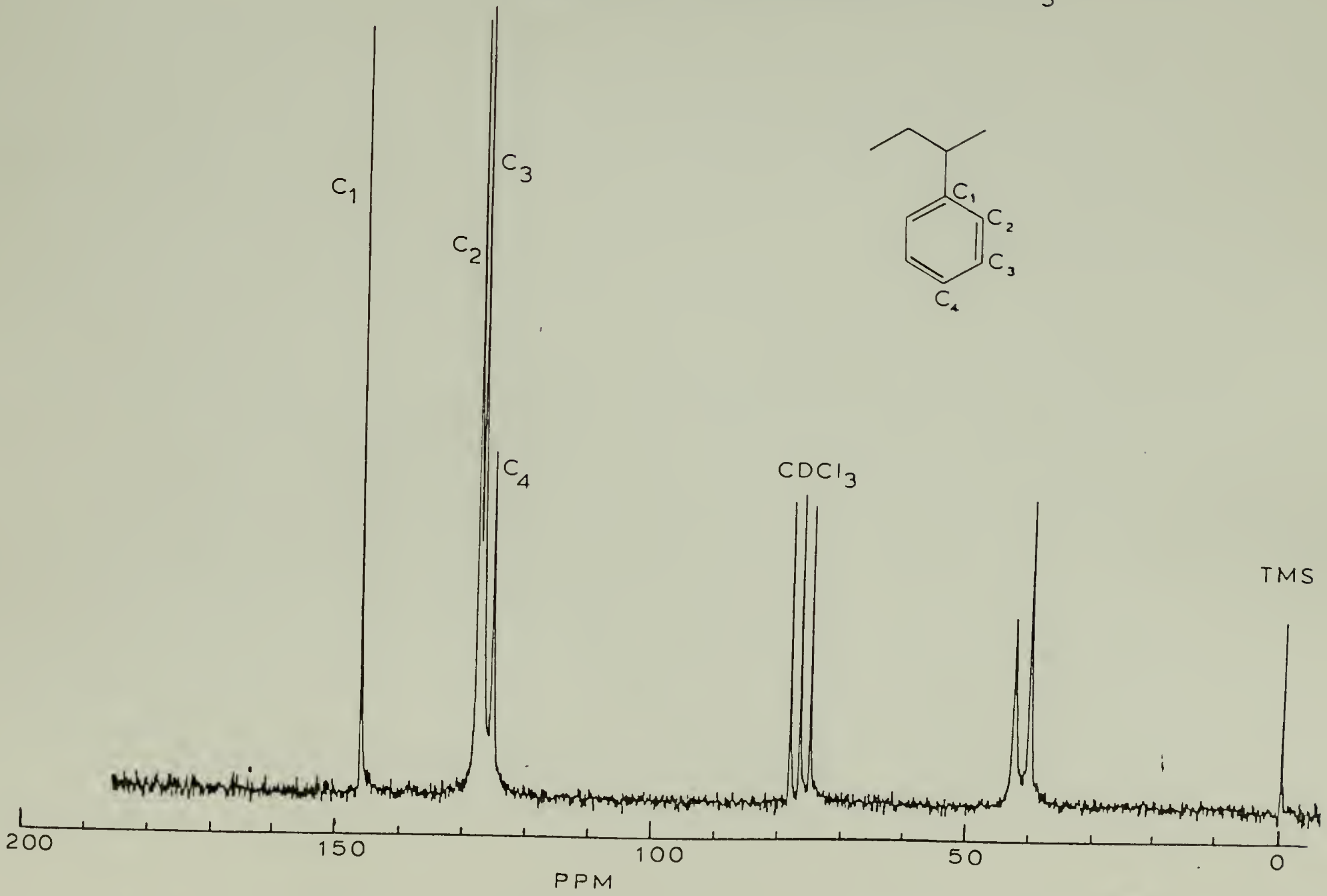

Figure 6. C-13 NMR spectrum of purified isotactic polystyrene in $CDCl_3$.

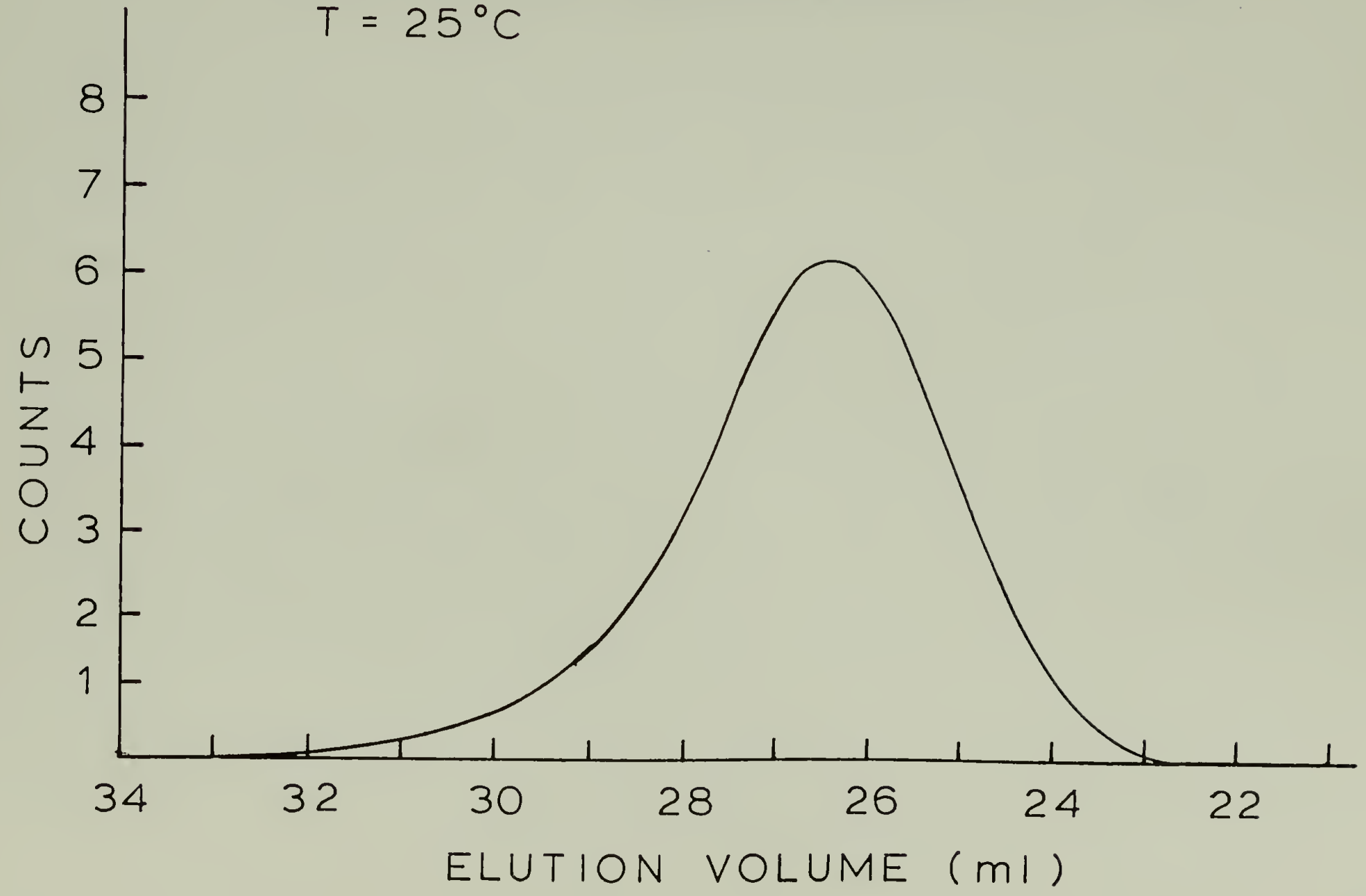

Figure 7. GPC spectrum of purified isotactic polystyrene in THF at 25°C.

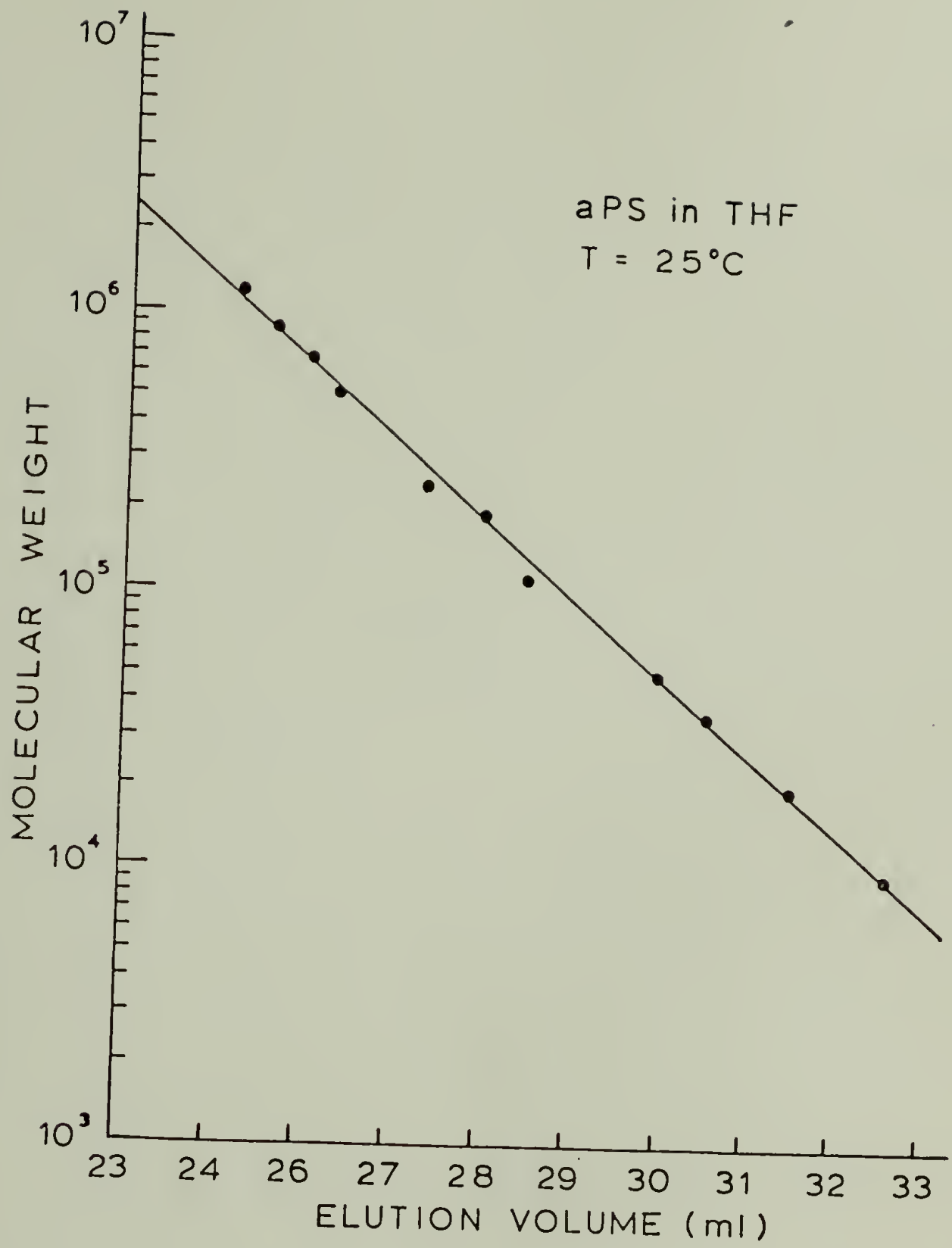

Figure 8. GPC calibration curve of atactic polystyrene in THF at 25°C.

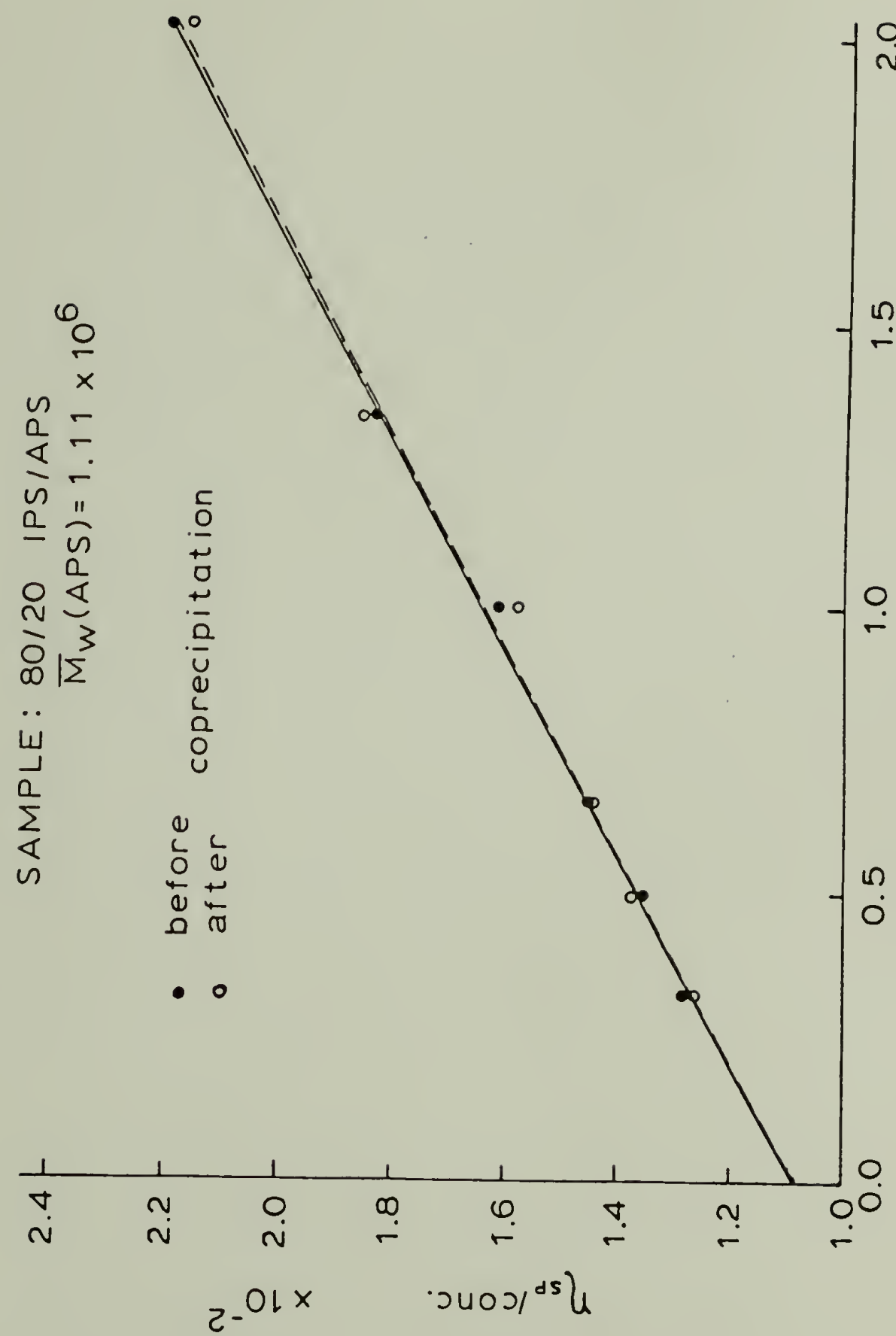

Figure 9. Viscosity measurement of a representative blend sample in toluene before and after coprecipitation into methanol. Measurement done at 30°C ±0.05°C.

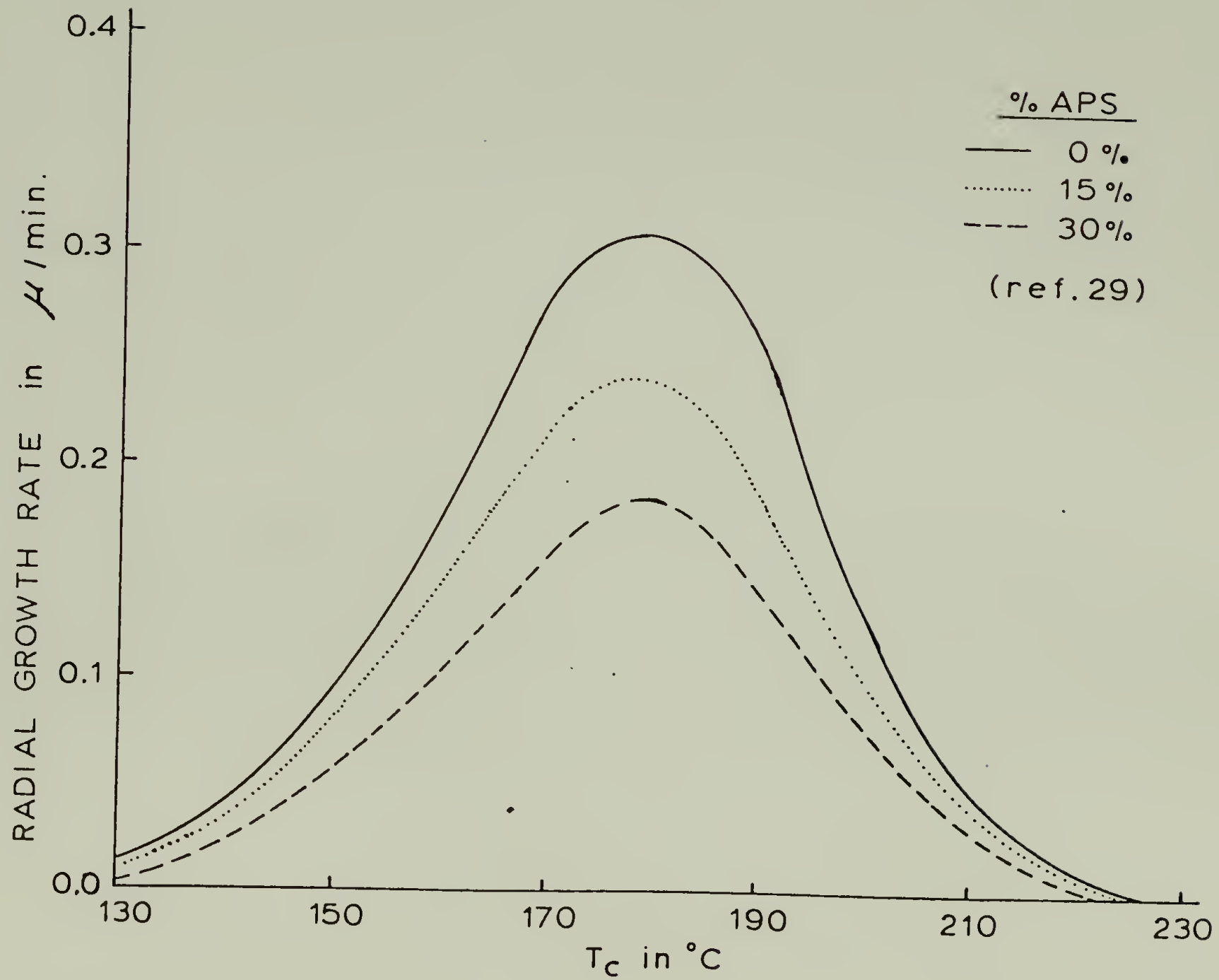

Figure 10. Isotactic polystyrene radial growth rate with various concentration of atactic polystyrene (reference 29).

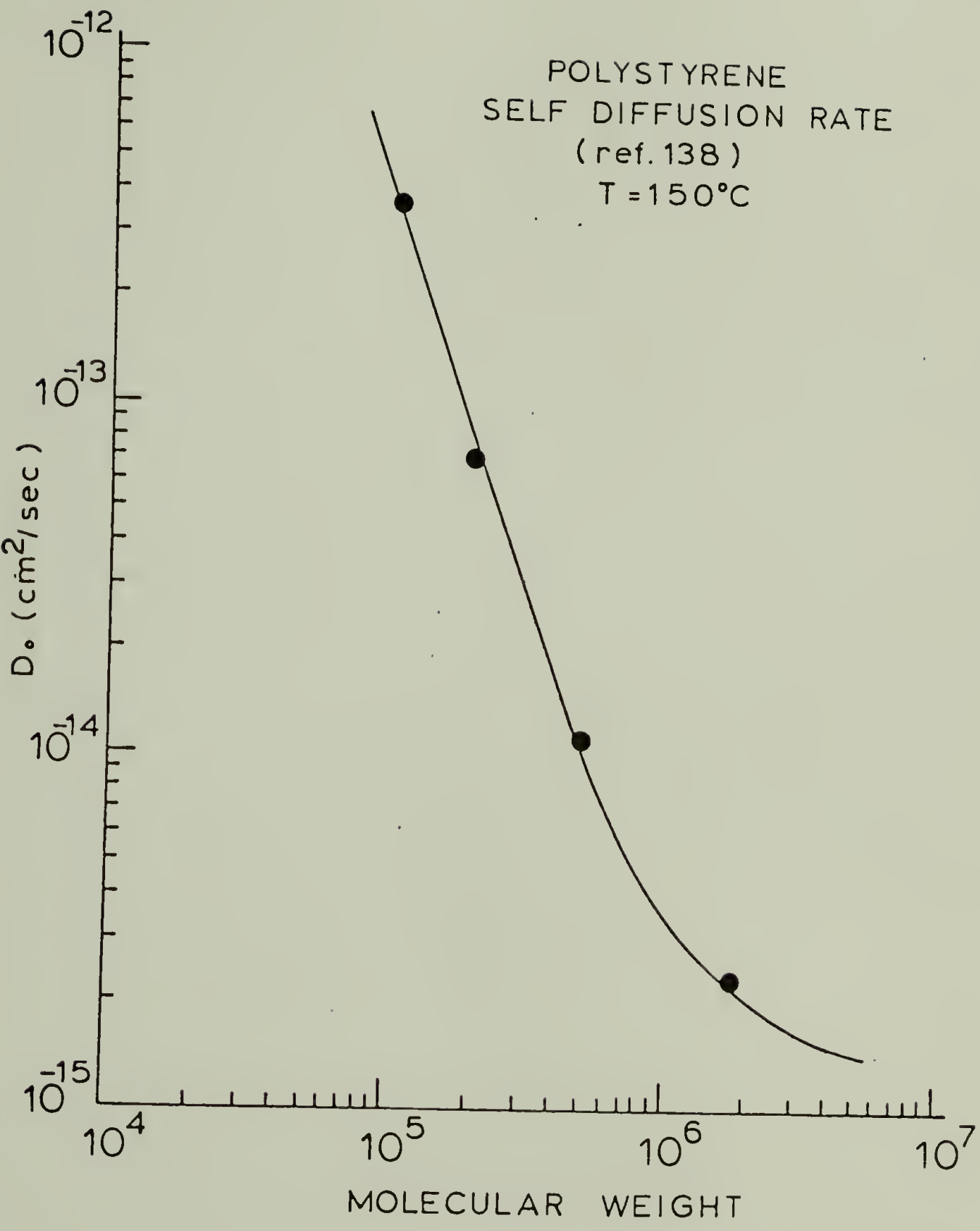

Figure 11. Self diffusion coefficient of polystyrene of various molecular weight (reference 138).

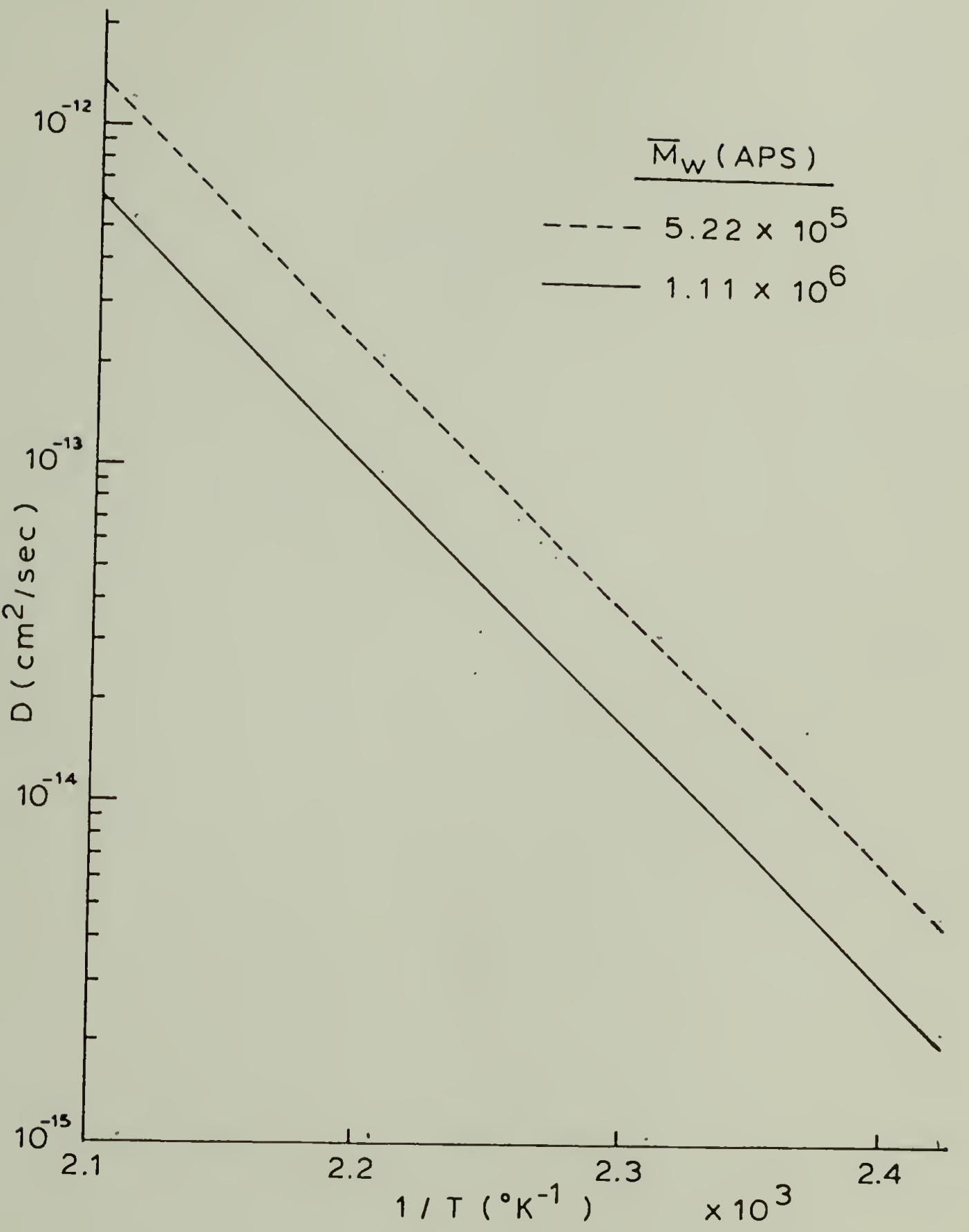

Figure 12. Calculated self diffusion coefficient of polystryene at other temperatures.

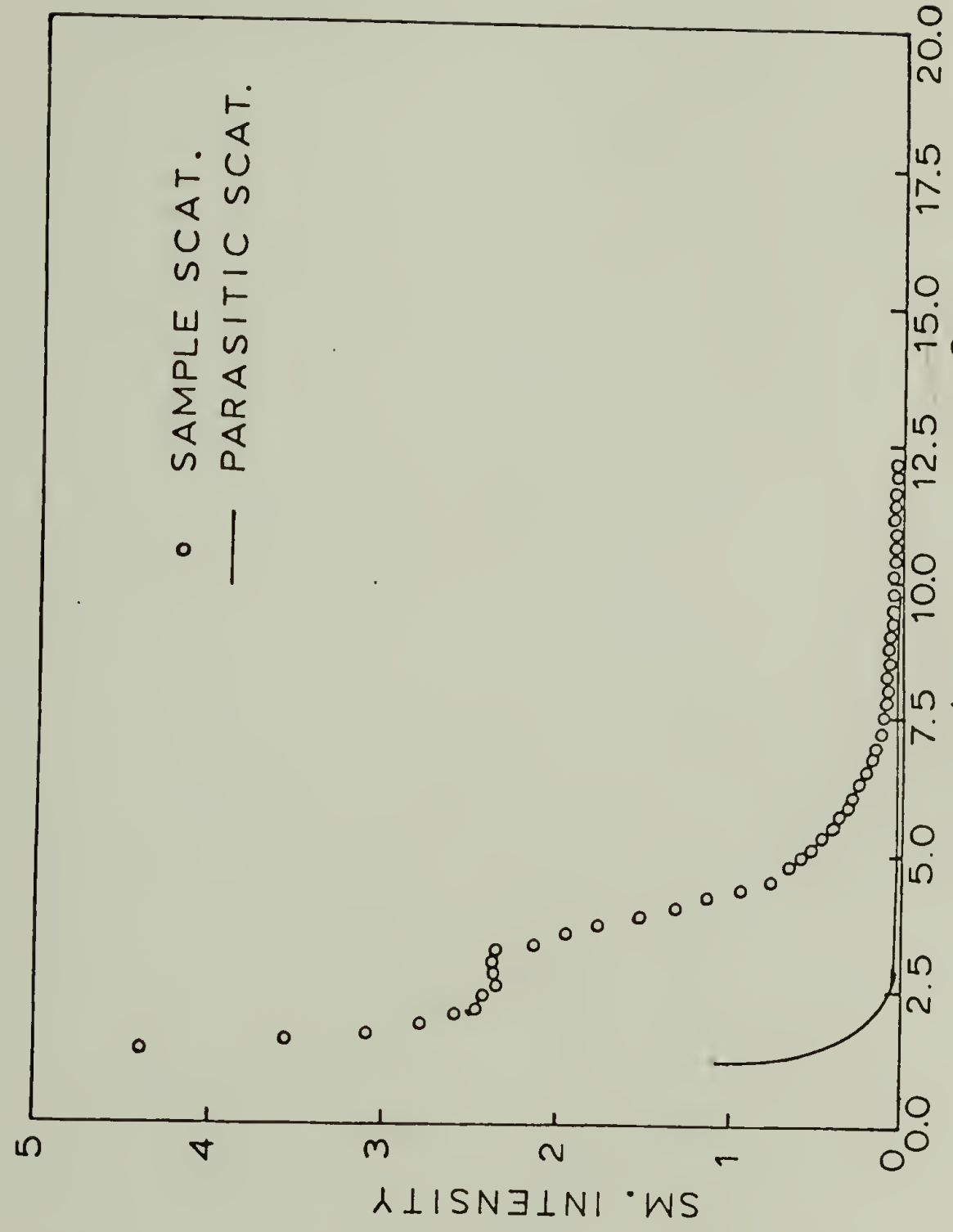

Figure 13. Comparison of a typical sample scattering to that of a parasatic scattering.

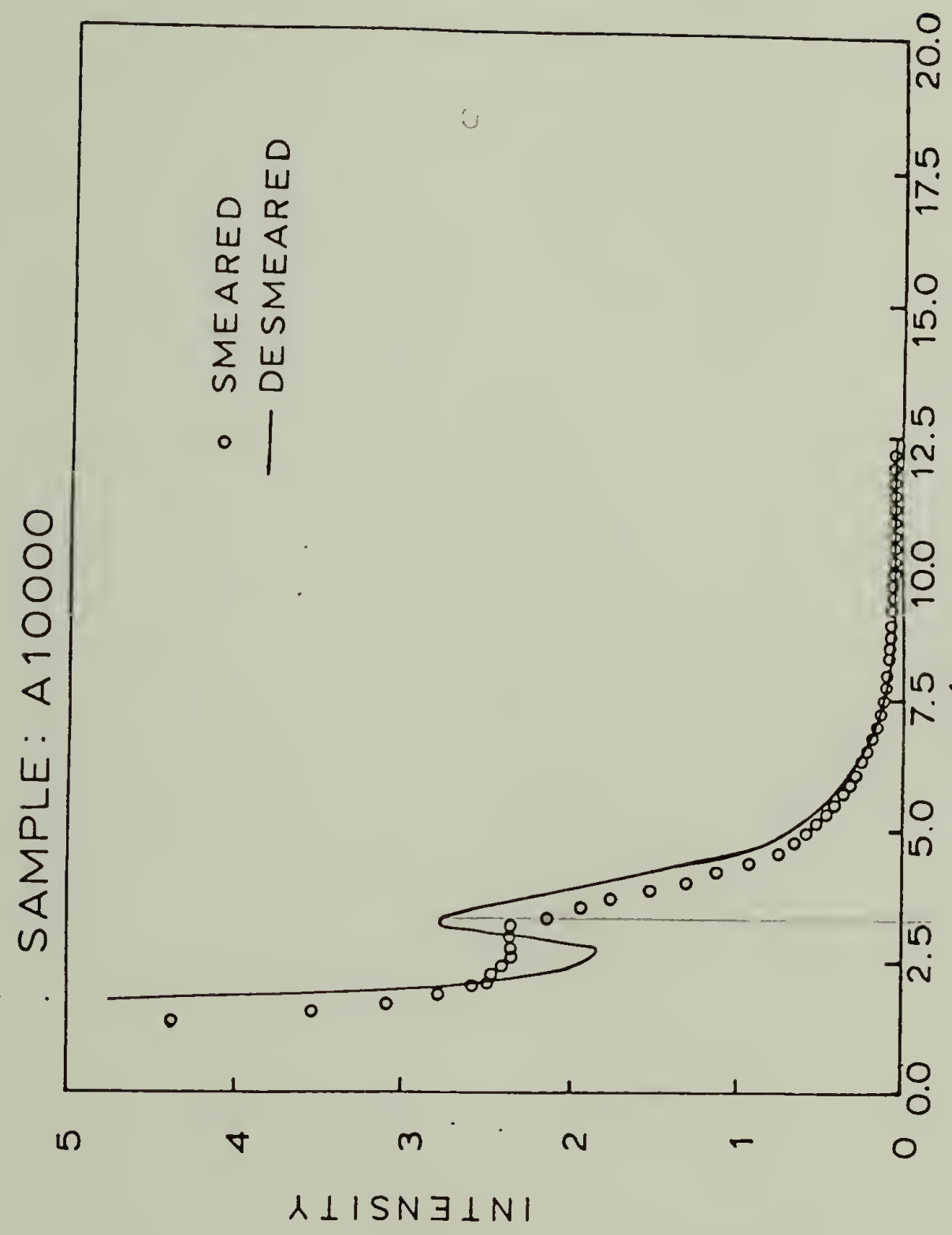

Figure 14. Comparison of slit smeared and desmeared intensity values for sample A10000. The intensity values are on a relative basis.

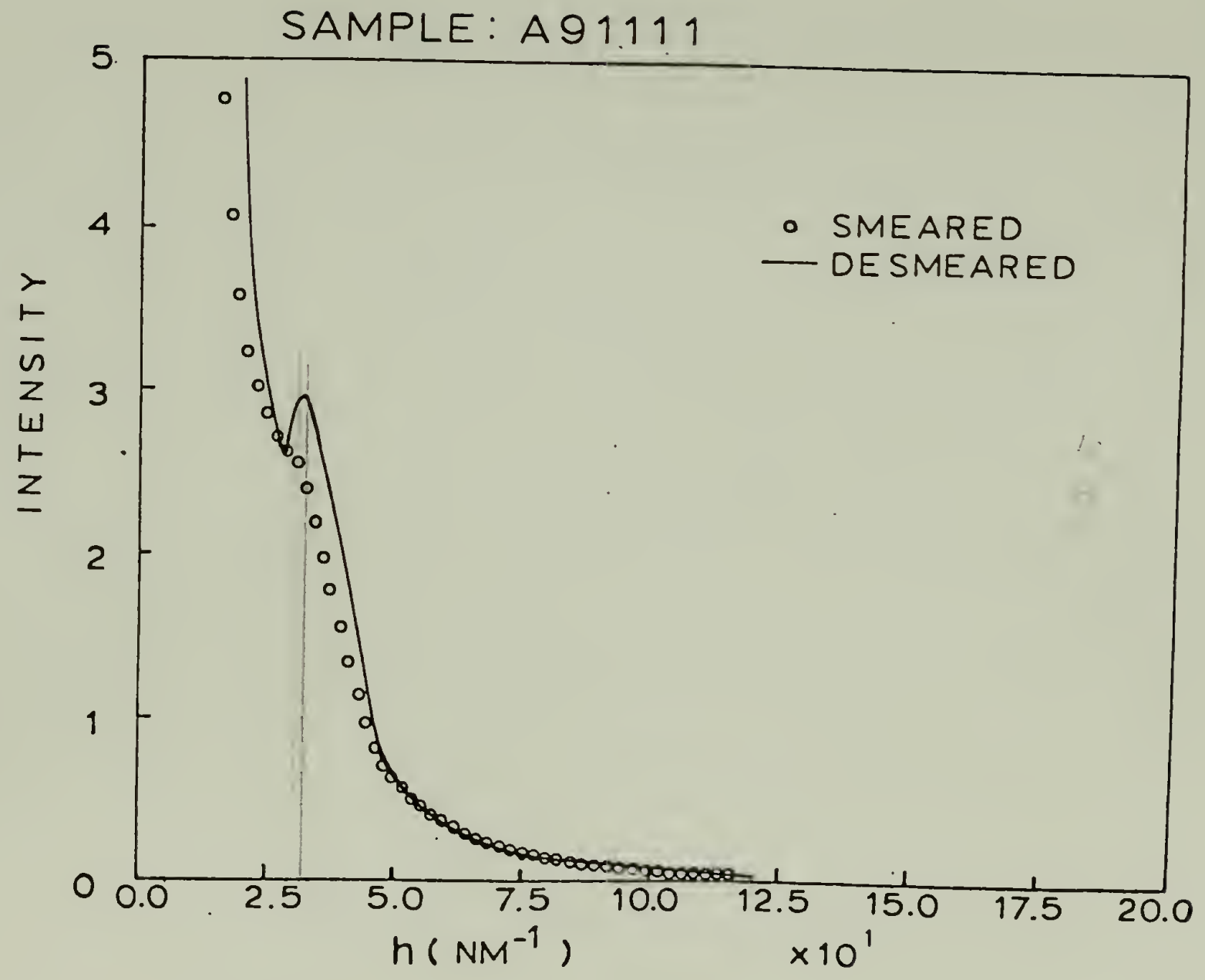

Figure 15. Comparison of slit smeared and desmeared intensity values for sample A91111. The intensity values are on a relative basis.

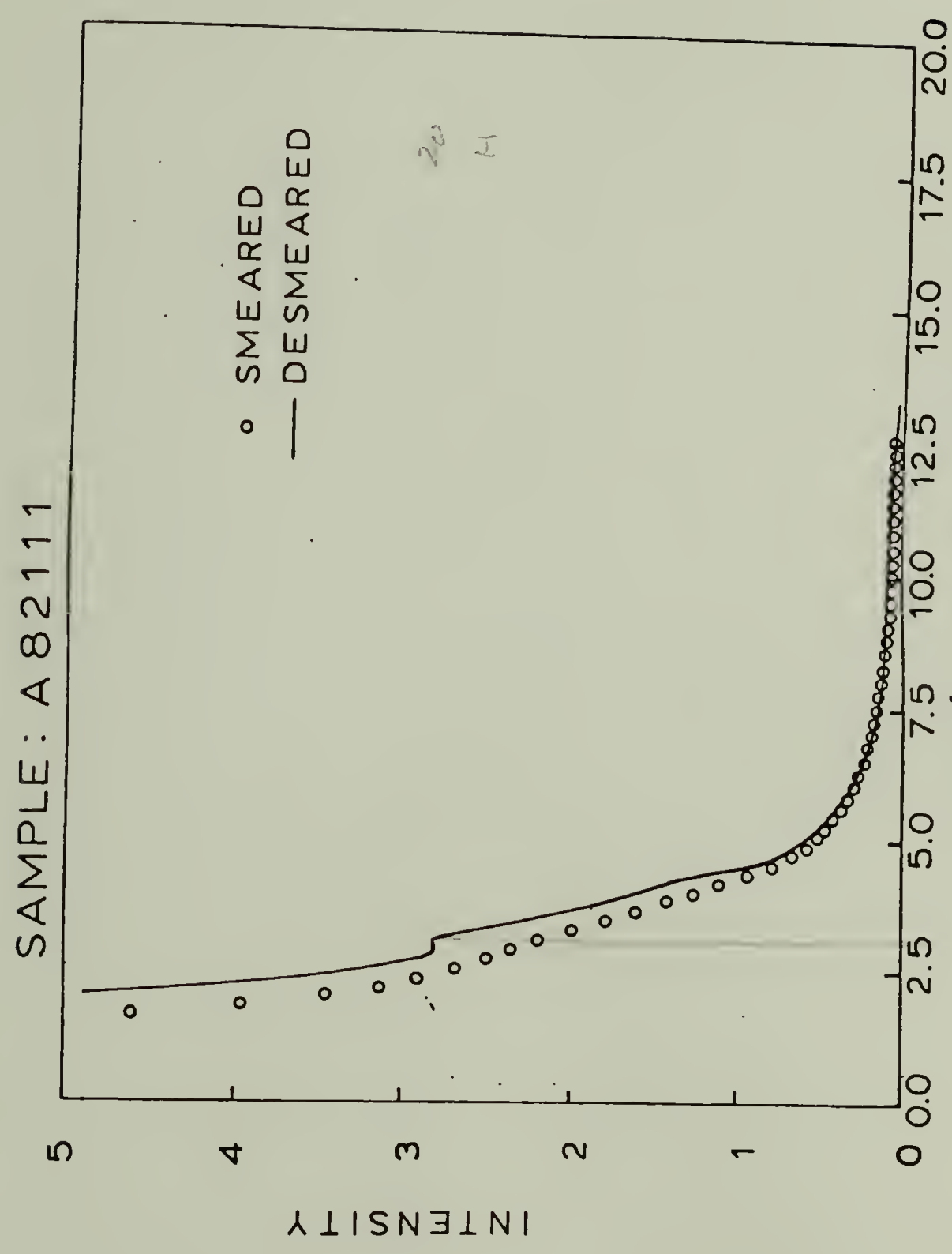

Figure 16. Comparison of slit smeared and desmeared intensity values for sample A82111. The intensity values are on a relative basis.

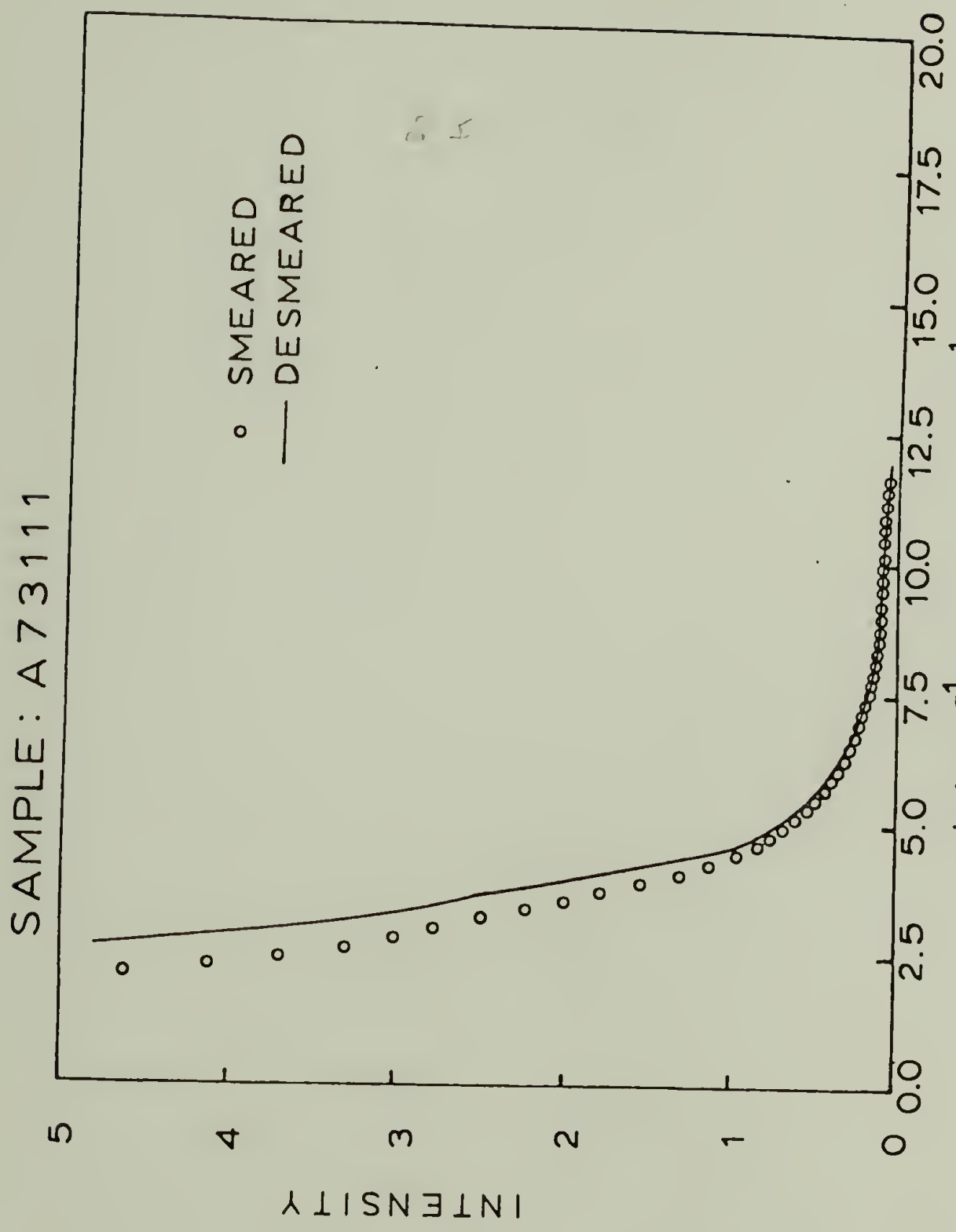

Figure 17. Comparison of slit smeared and desmeared intensity values for sample A7311. The intensity values are on a relative basis.

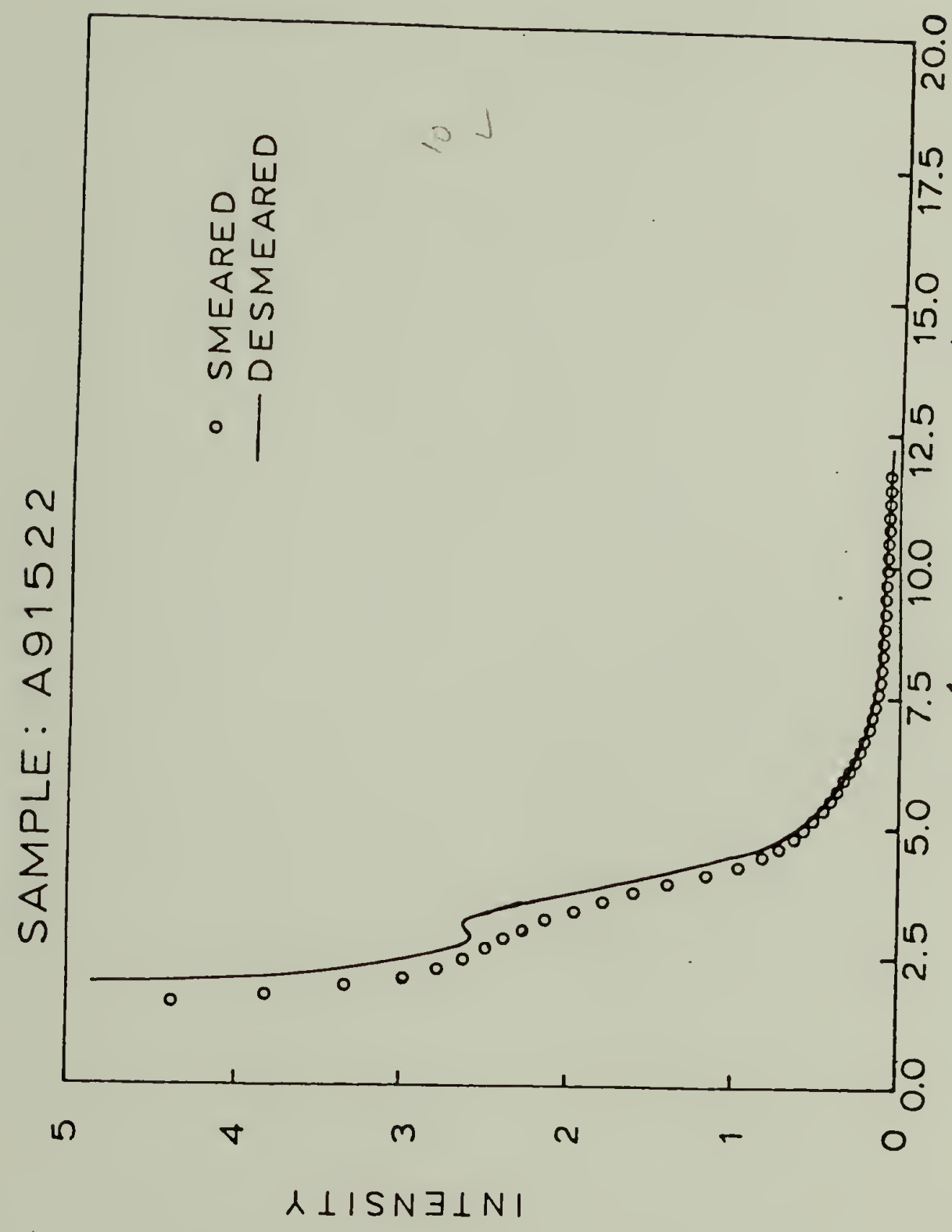

Figure 18. Comparison of slit smeared and desmeared intensity values for sample A91522. The intensity values are on a relative basis.

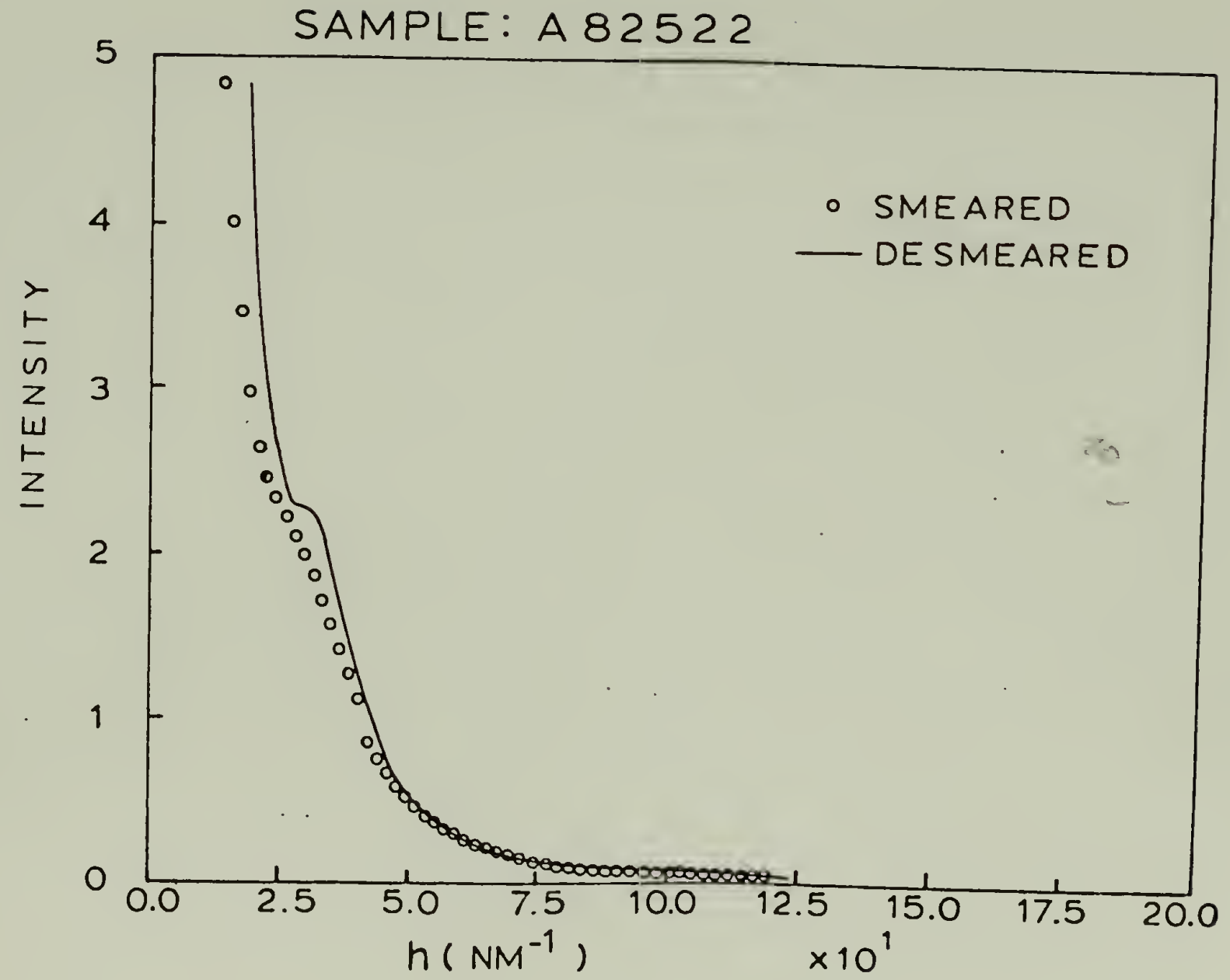

Figure 19. Comparison of slit smeared and desmeared intensity values for sample A82522. The intensity values are on a relative basis.

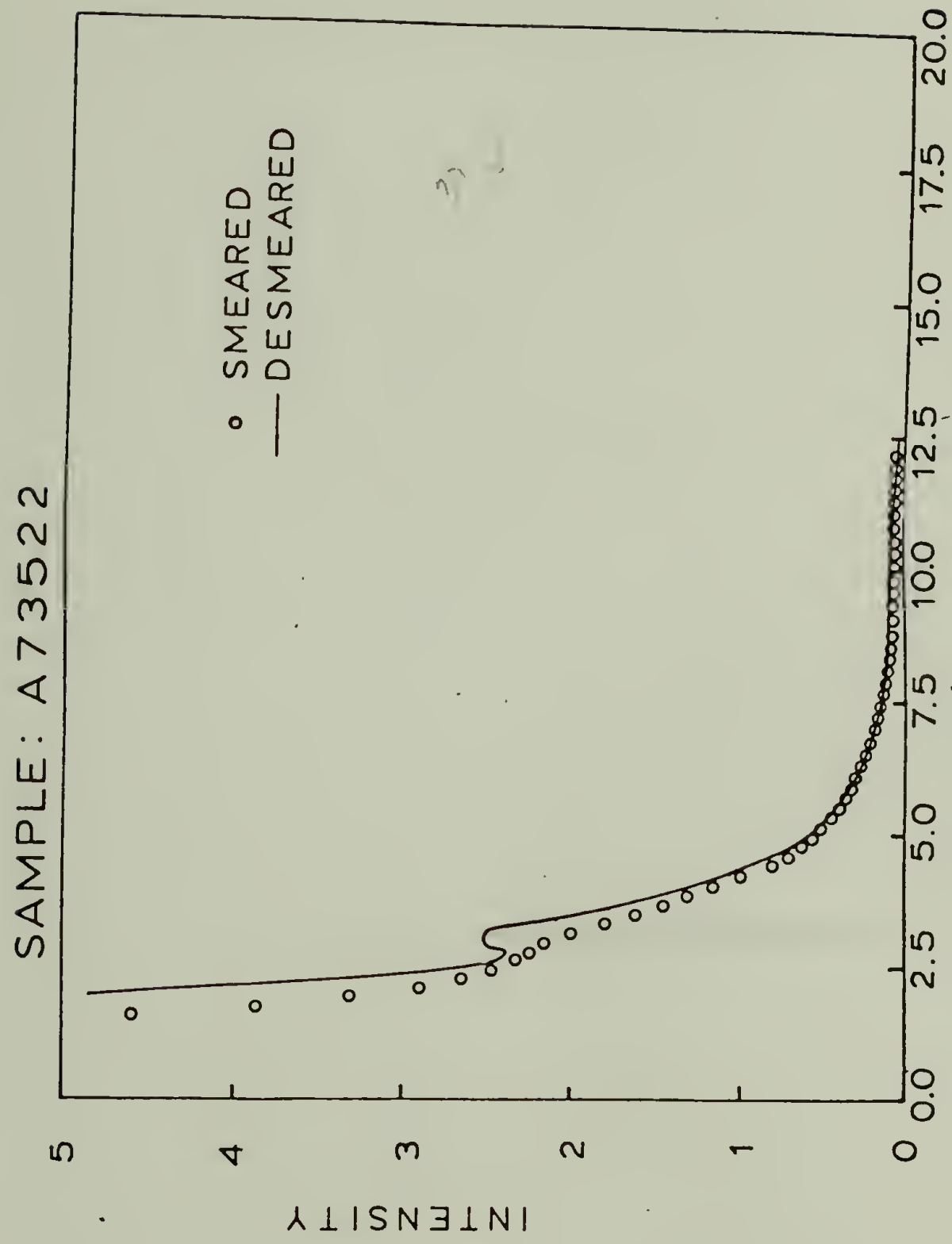

Figure 20. Comparison of slit smeared and desmeared intensity values for sample A73522. The intensity values are on a relative basis.

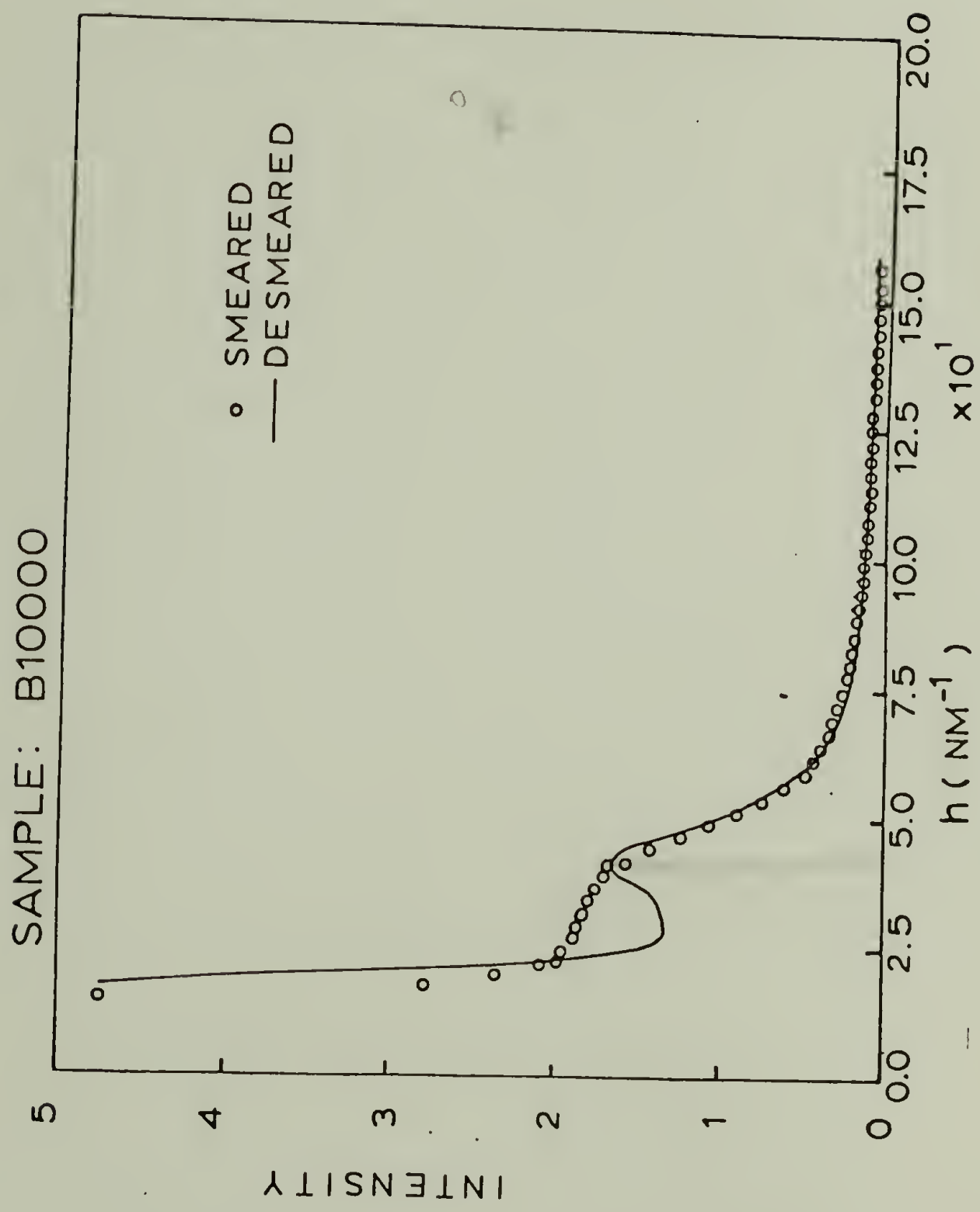

Figure 21. Comparison of slit smeared and desmeared intensity values for sample B10000. The intensity values are on a relative basis.

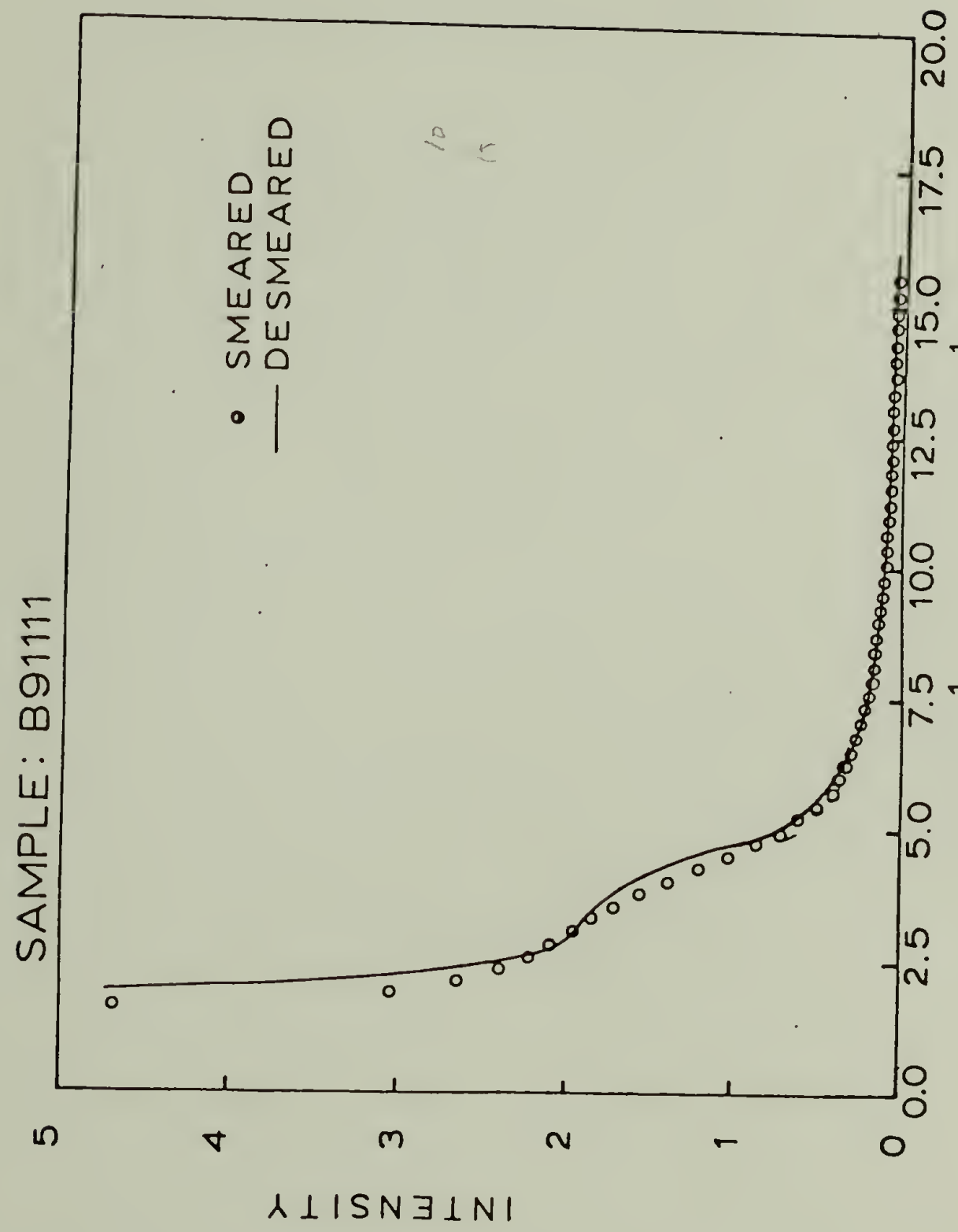

Figure 22. Comparison of slit smeared and desmeared intensity values for sample B91111. The intensity values are on a relative basis.

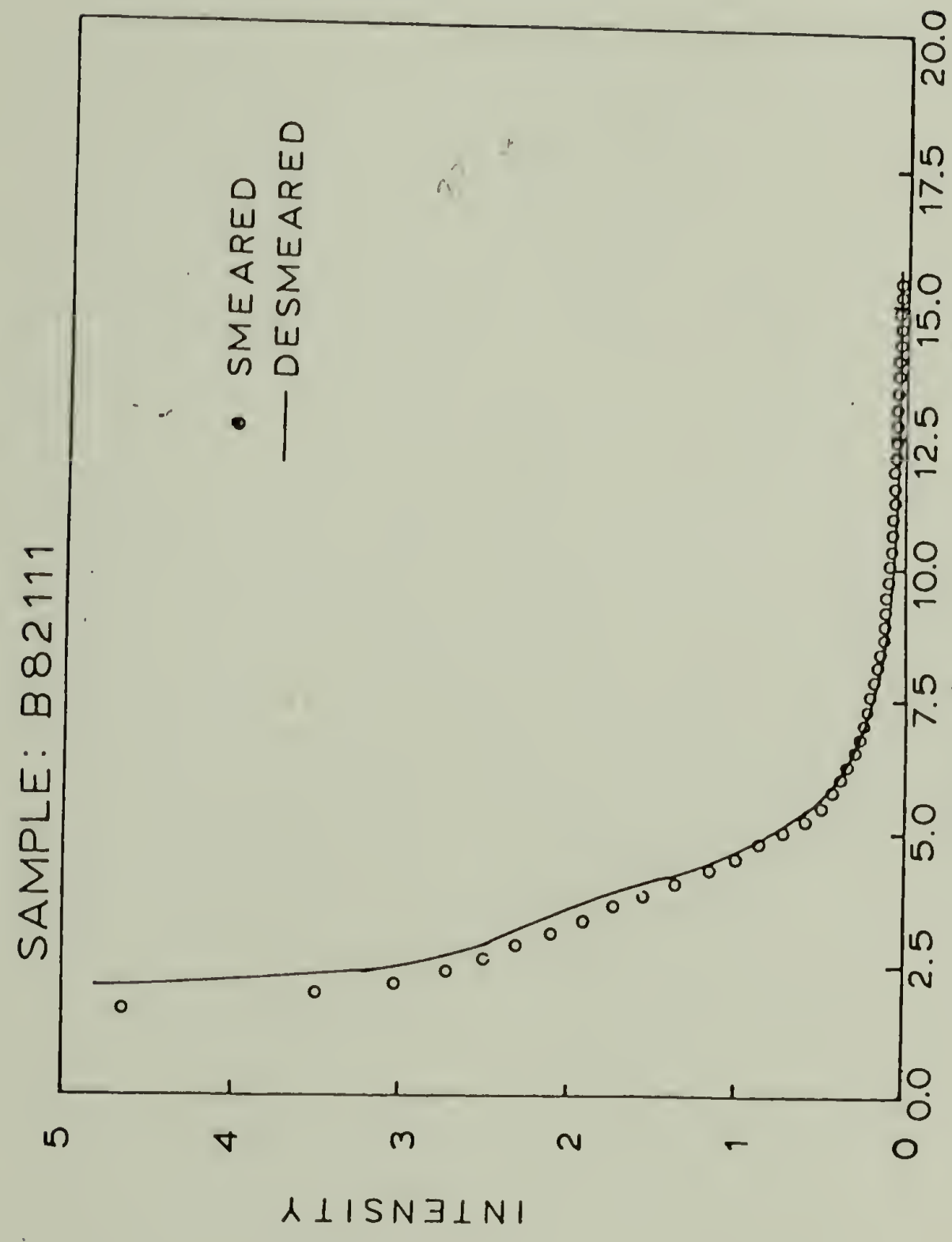

Figure 23. Comparison of slit smeared and desmeared intensity values for sample B8211. The intensity values are on a relative basis.

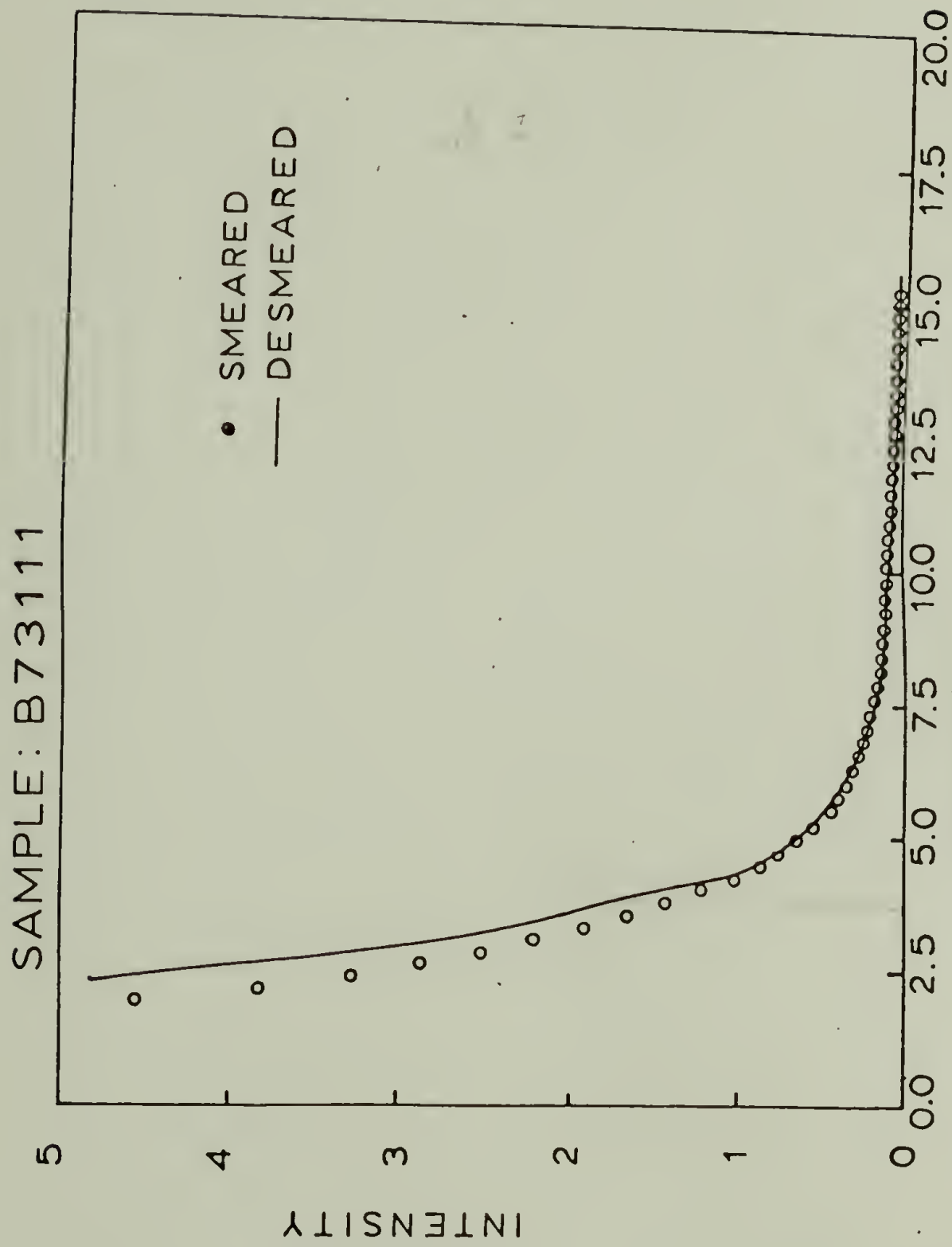

Figure 24. Comparison of slit smeared and desmeared intensity values for sample B73111. The intensity values are on a relative basis.

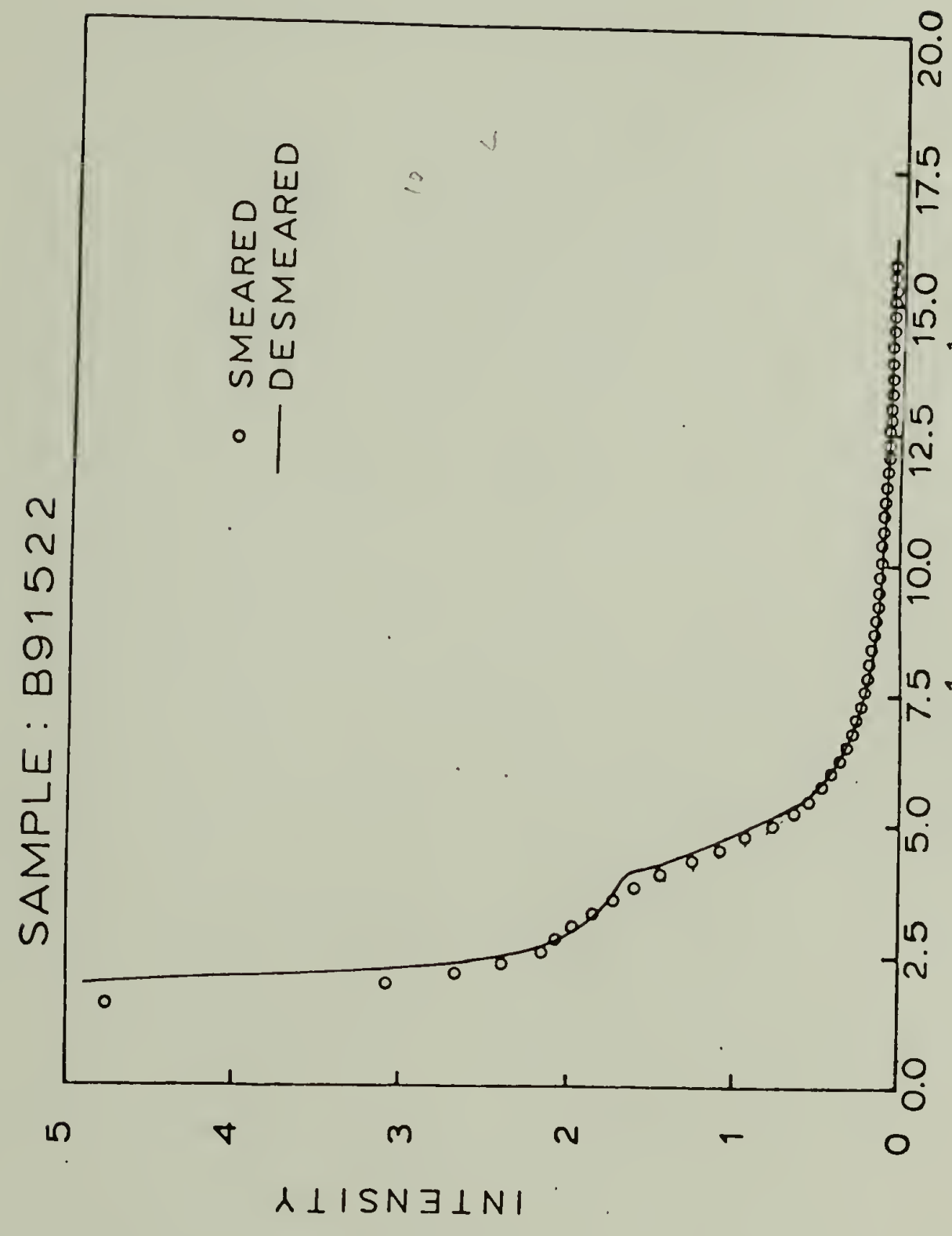

Figure 25. Comparison of slit smeared and desmeared intensity values for sample B91522. The intensity values are on a relative basis.

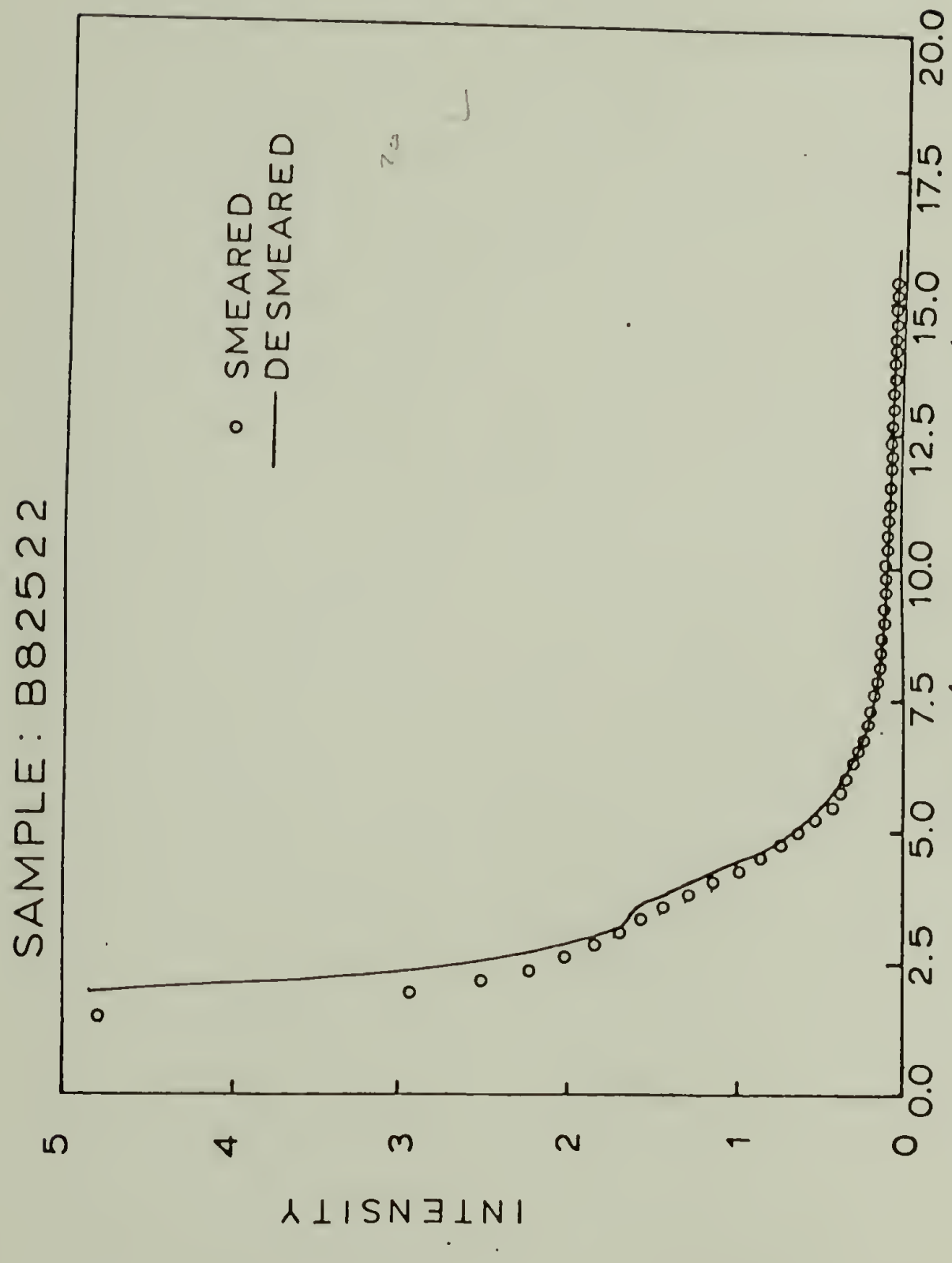

Figure 26. Comparison of slit smeared and desmeared intensity values for sample B82522. The intensity values are on a relative basis.

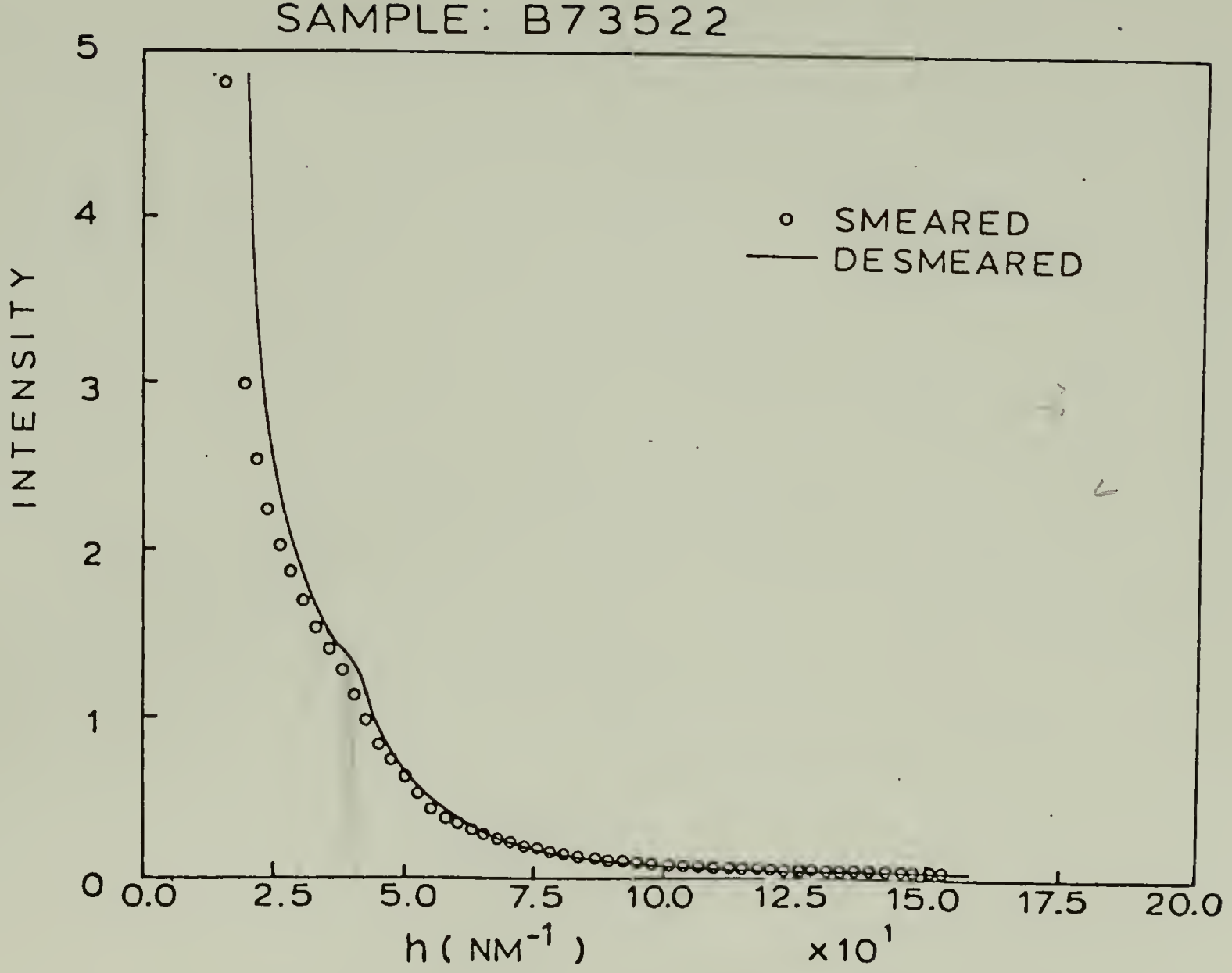

Figure 27. Comparison of slit smeared and desmeared intensity values for sample B73522. The intensity values are on a relative basis.

Figure 28. Comparison of slit smeared and desmeared intensity values for sample C10000. The intensity values are on a relative basis.

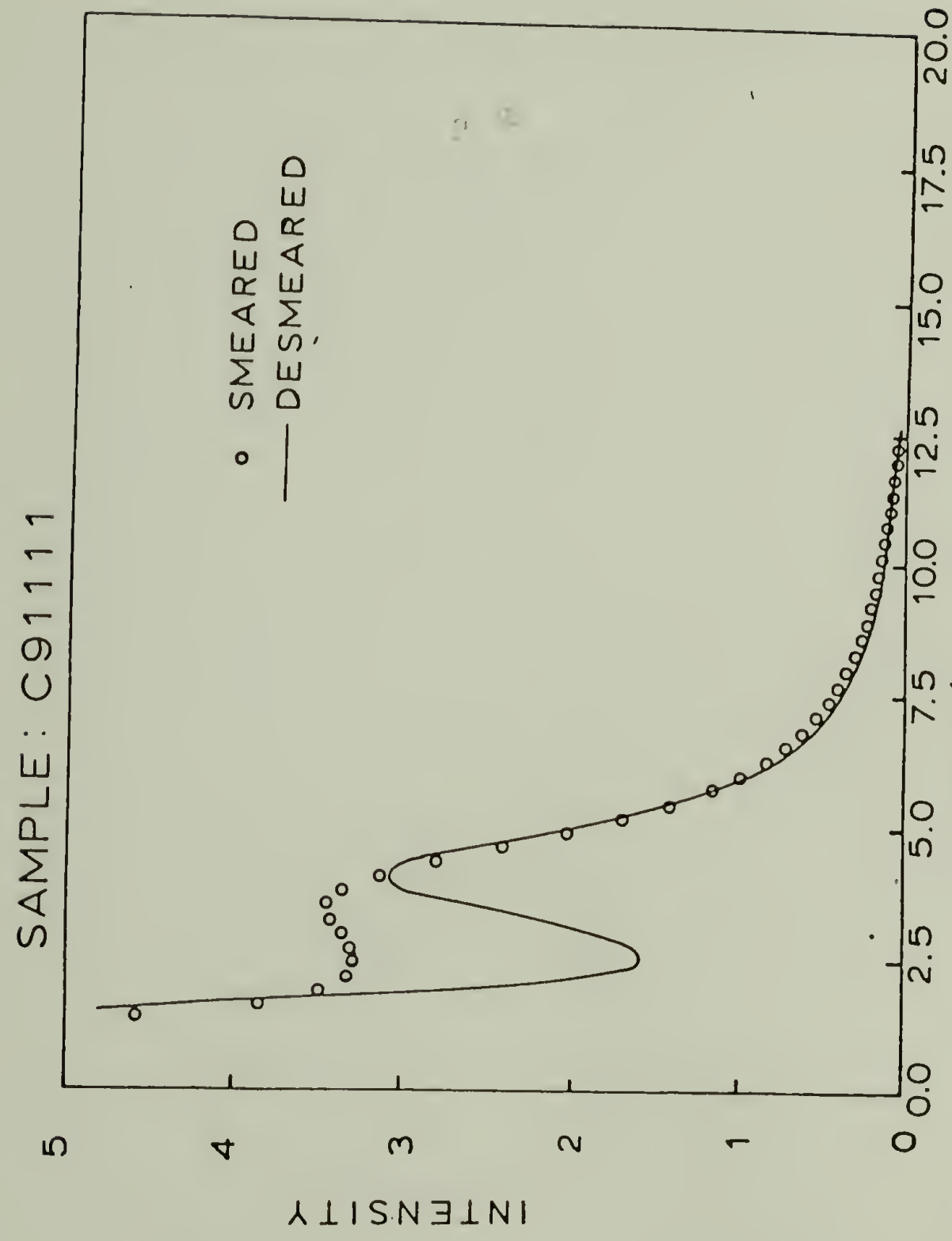

Figure 29. Comparison of slit smeared and desmeared intensity values for sample C91111. The intensity values are on a relative basis.

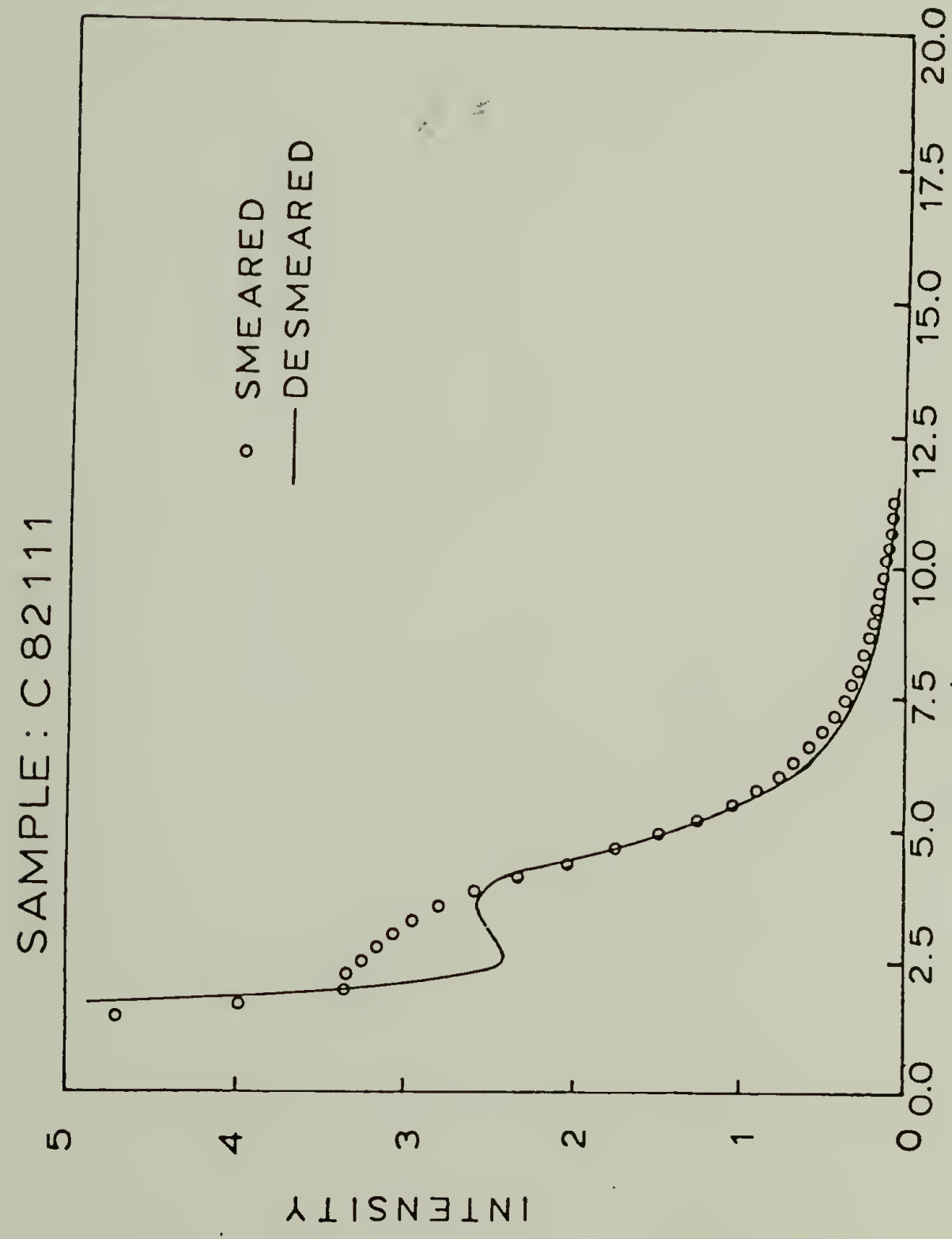

Figure 30. Comparison of slit smeared and desmeared intensity values for sample C82111. The intensity values are on a relative basis.

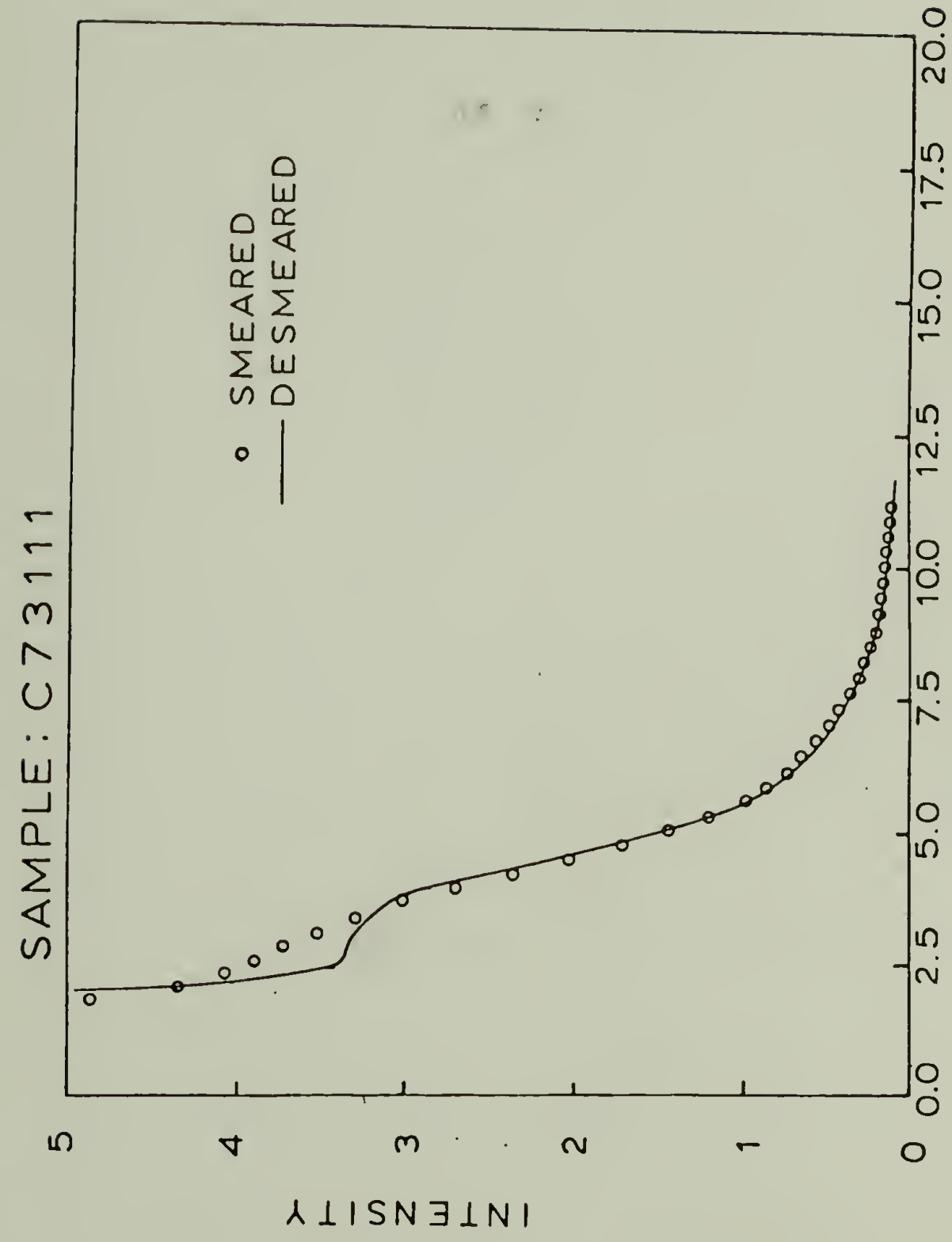

Figure 31. Comparison of slit smeared and desmeared intensity values for sample C7311. The intensity values are on a relative basis.

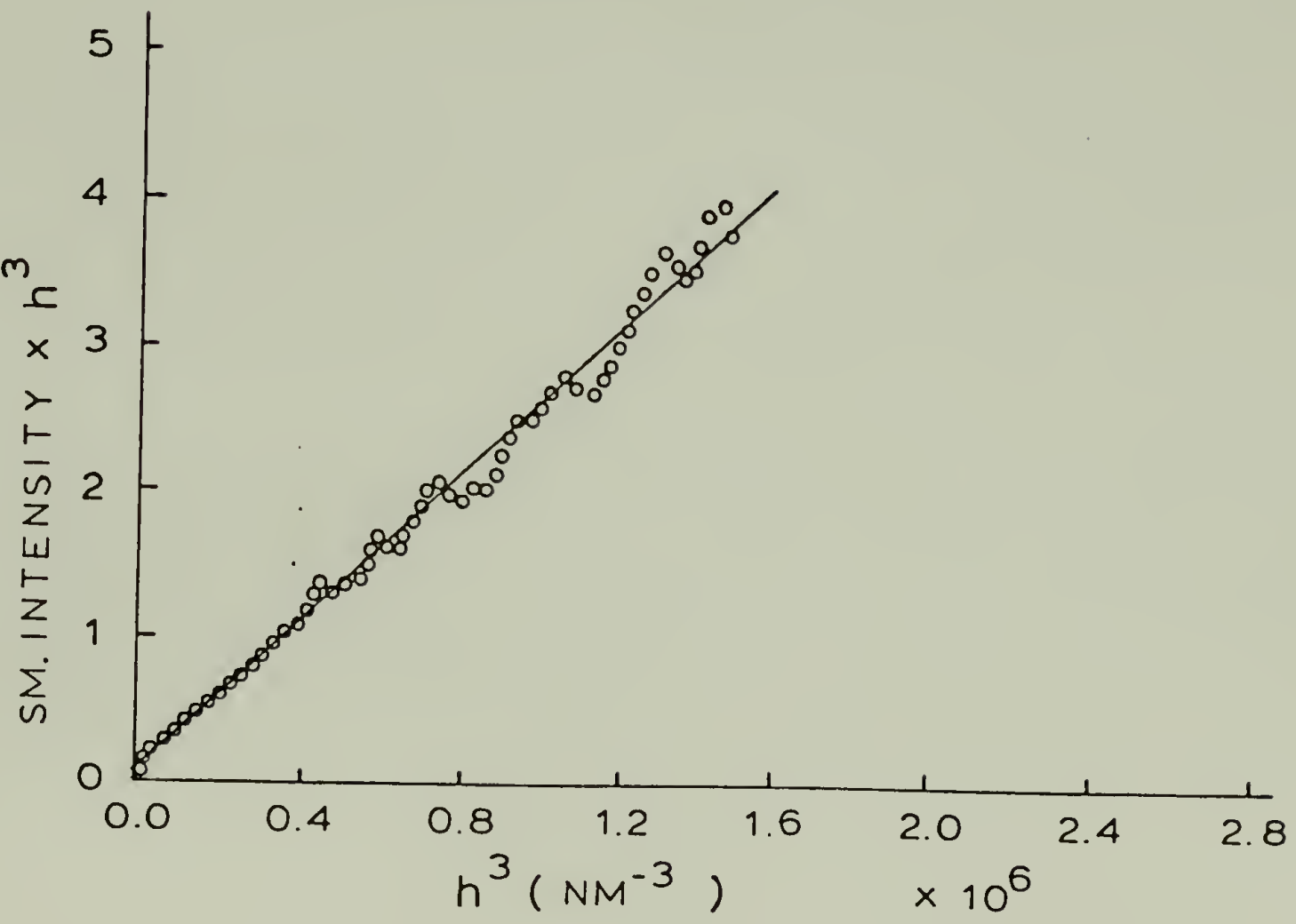

Figure 32. Plot of $J(h)h^3$ vs. h^3 to obtain the background fluctuation for representative sample A10000.

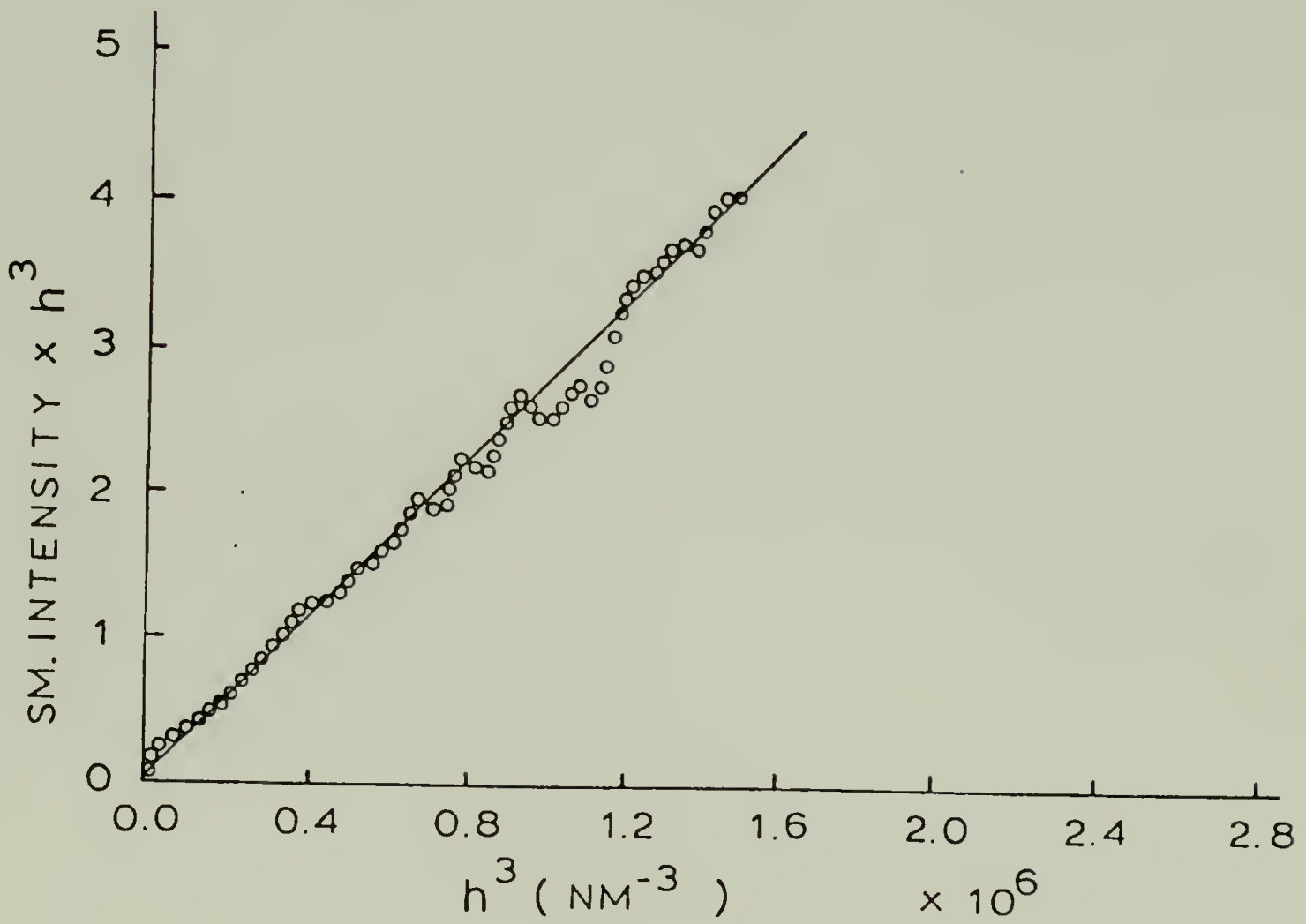

Figure 33. Plot of $J(h)h^3$ vs. h^3 to obtain the background fluctuation for representative sample A73111.

SAMPLE: A91522

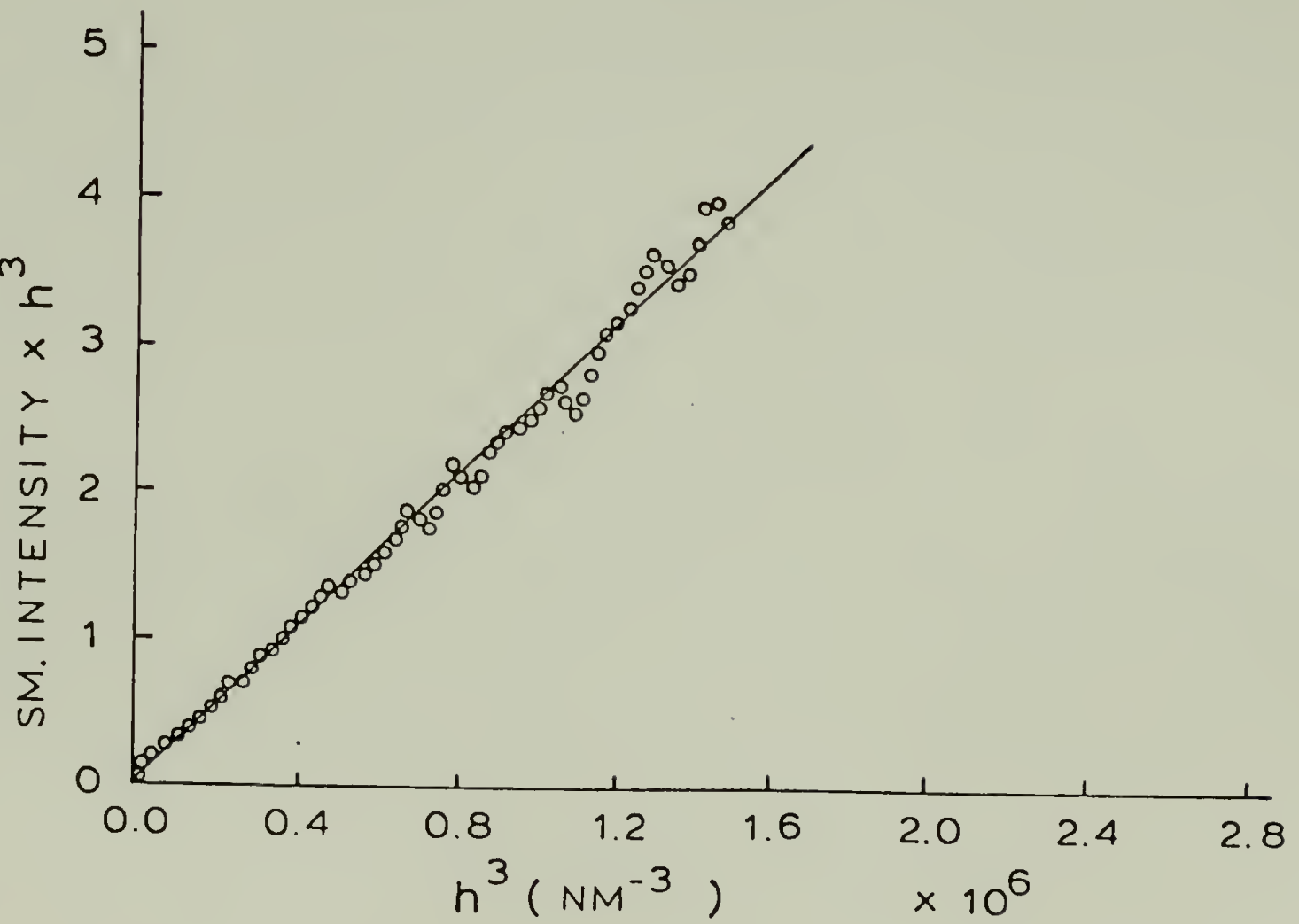

Figure 34. Plot of $J(h)h^3$ vs. h^3 to obtain the background fluctuation for representative sample A91522.

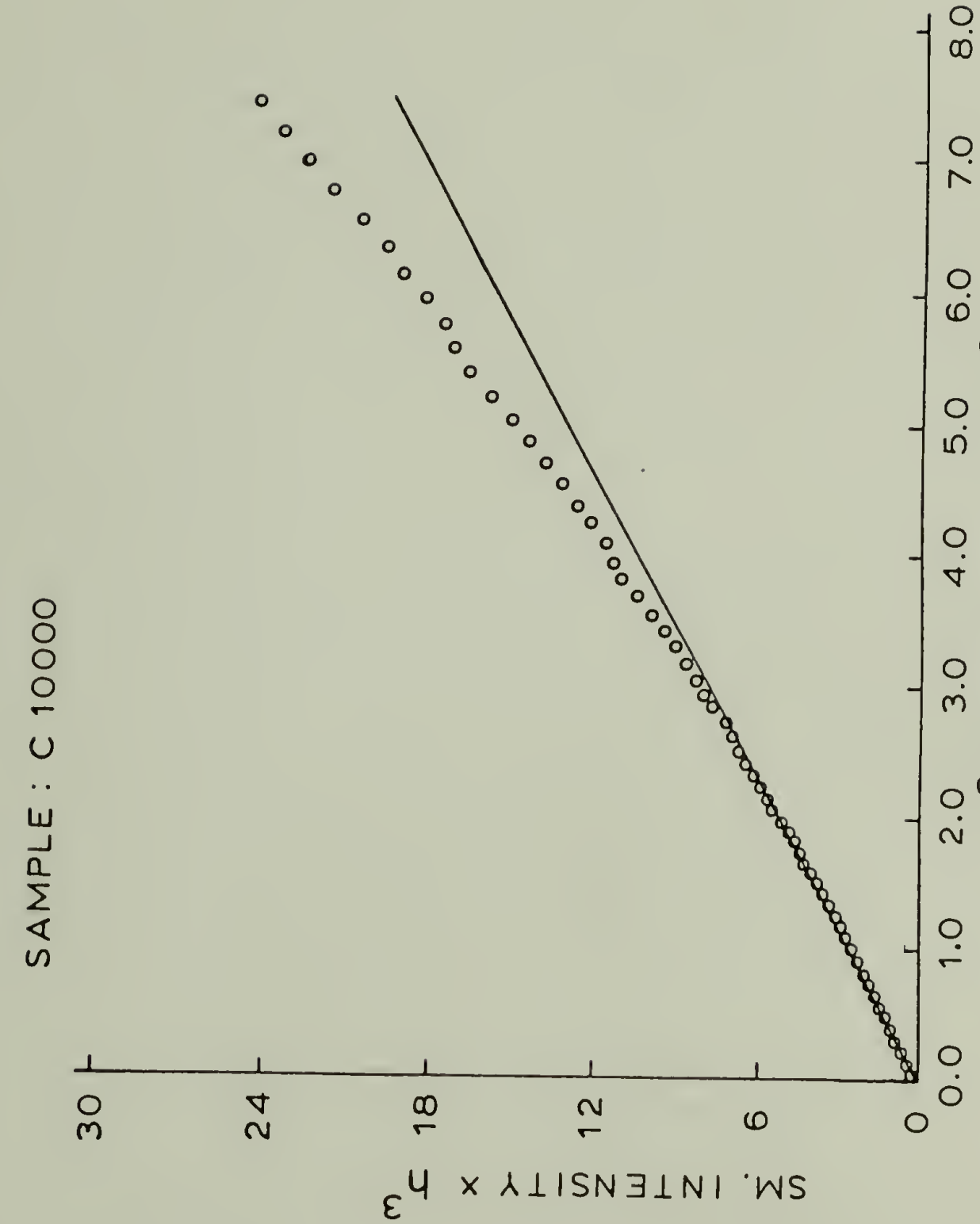

Figure 35. Plot of $J(h)h^3$ vs. h^3 to obtain the background fluctuation for representative sample C10000.

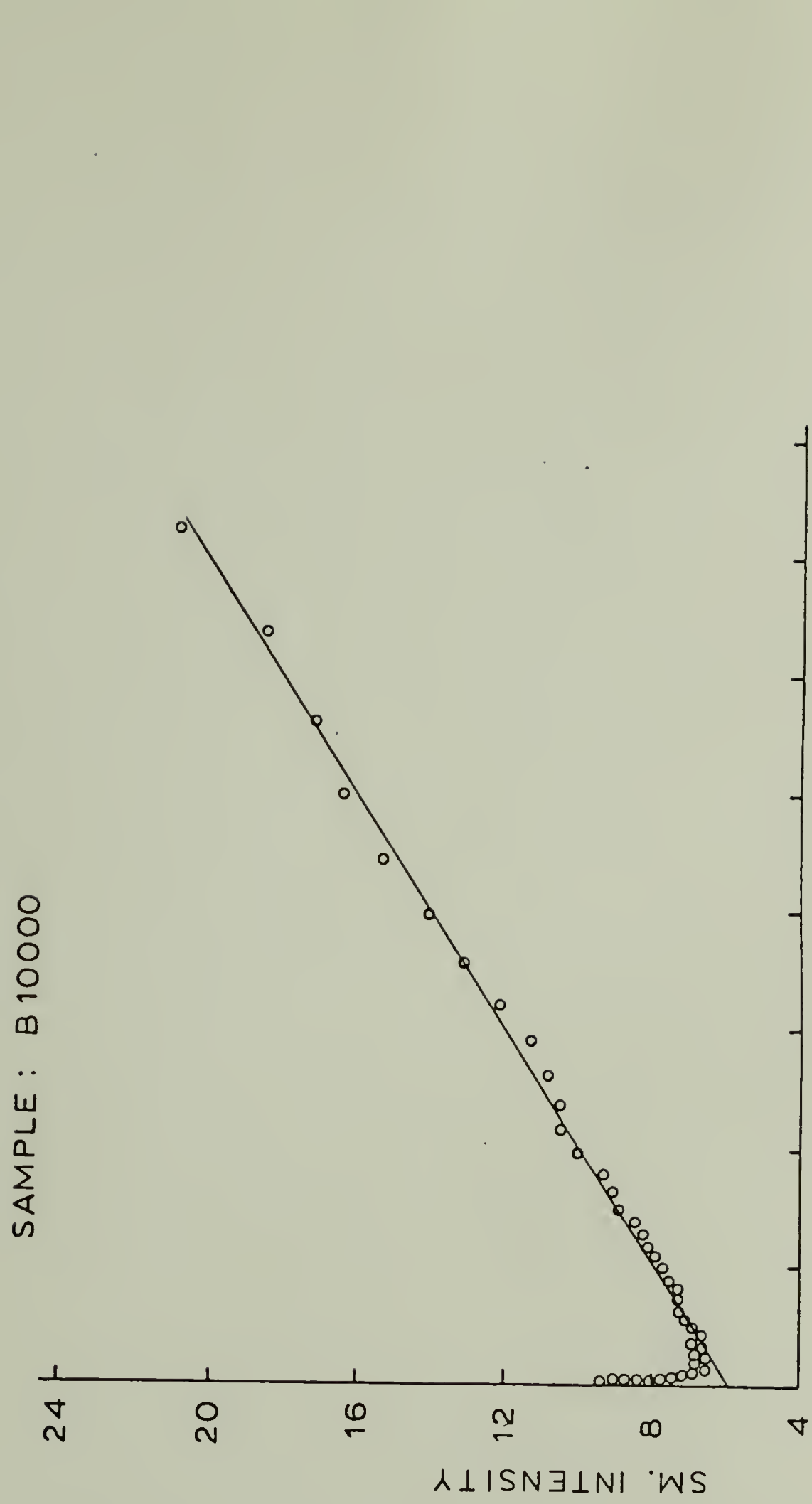

Figure 36. Plot of J(h) vs. $1/h^3$ to obtain background fluctuation for sample B10000. This plot is valid only if plot of Jh^3 vs. h^3 gives a zero intercept.

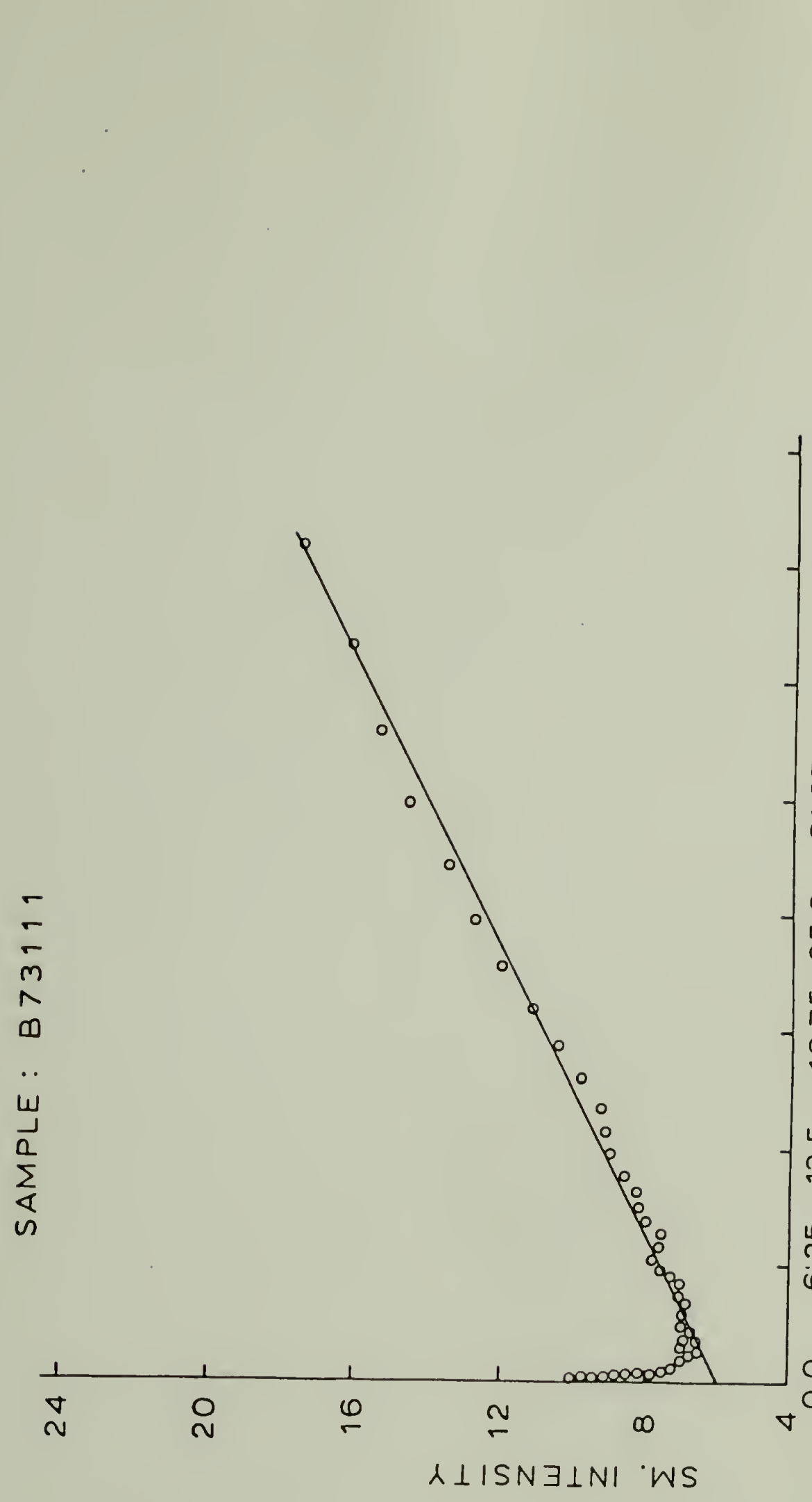

Figure 37. Plot of J(h) vs. $1/h^3$ to obtain background fluctuation for sample B7311. This plot is valid only if plot of Jh^3 vs. h^3 gives a zero intercept.

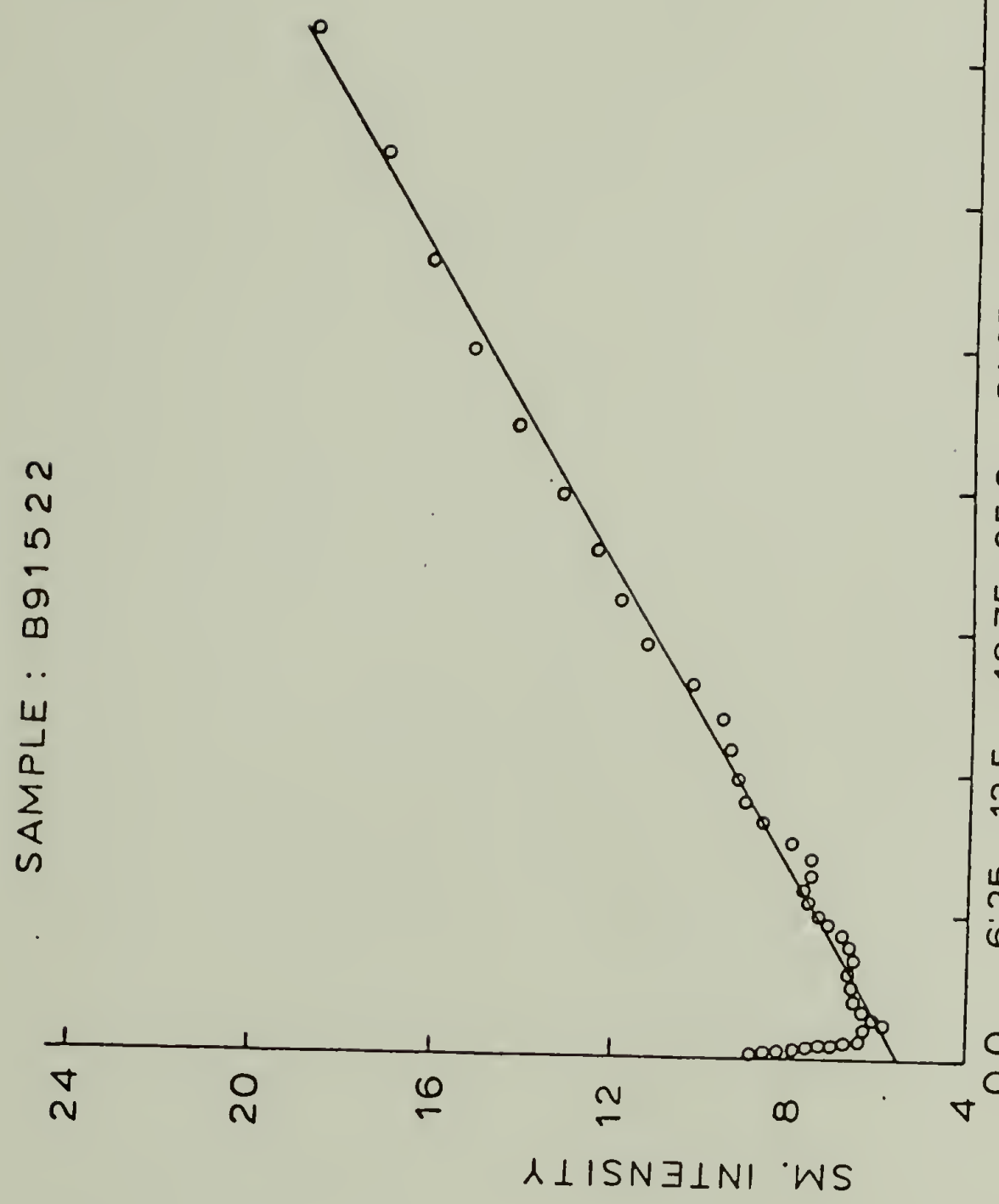

Figure 38. Plot of J(h) vs. h^3 to obtain background fluctuation for sample B19522. This plot is valid only if plot of Jh^3 vs. h^3 gives a zero intercept.

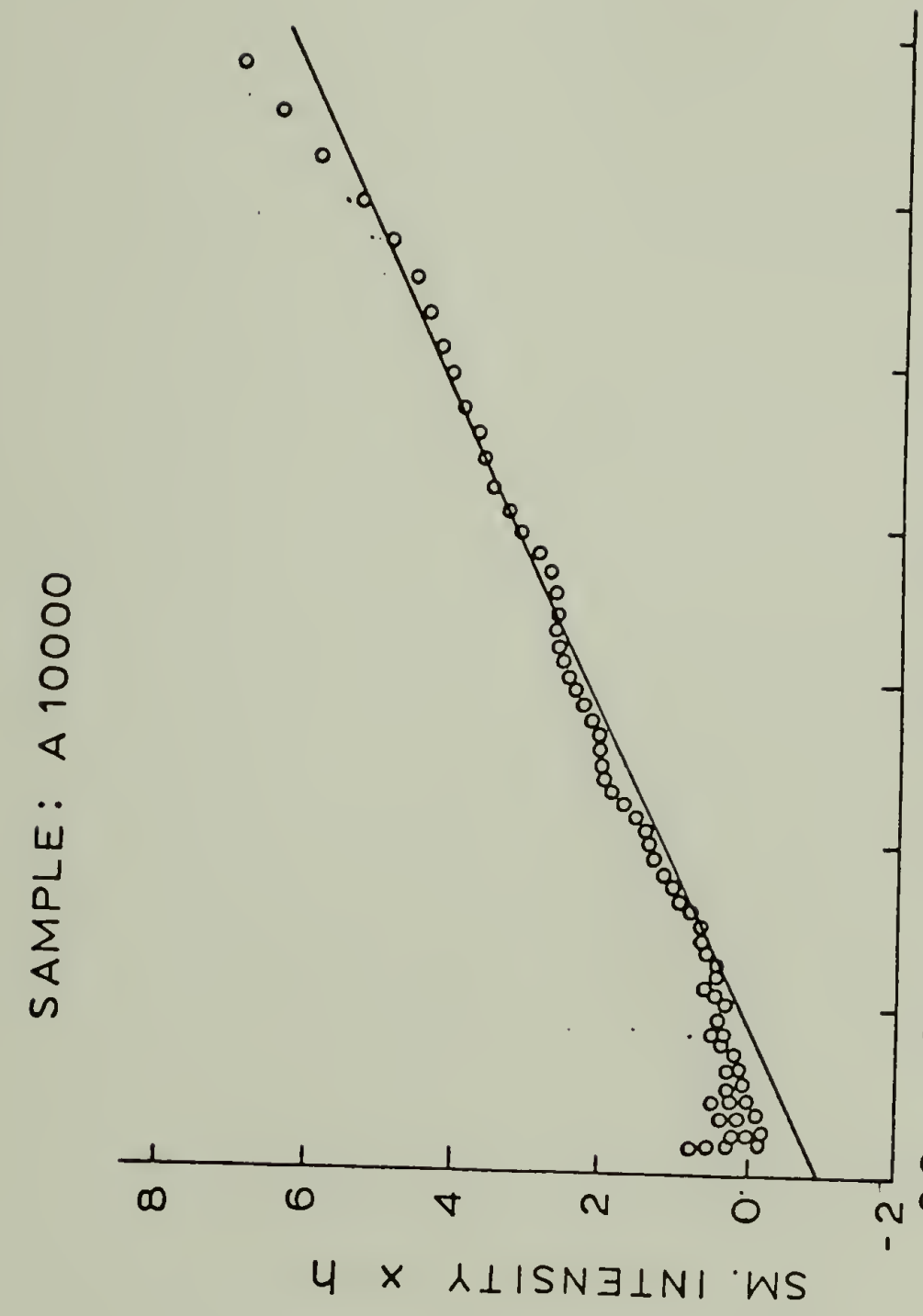

Figure 39. Plot of J(h)h vs. $1/h^2$ to obtain the linear transition zone thickness.

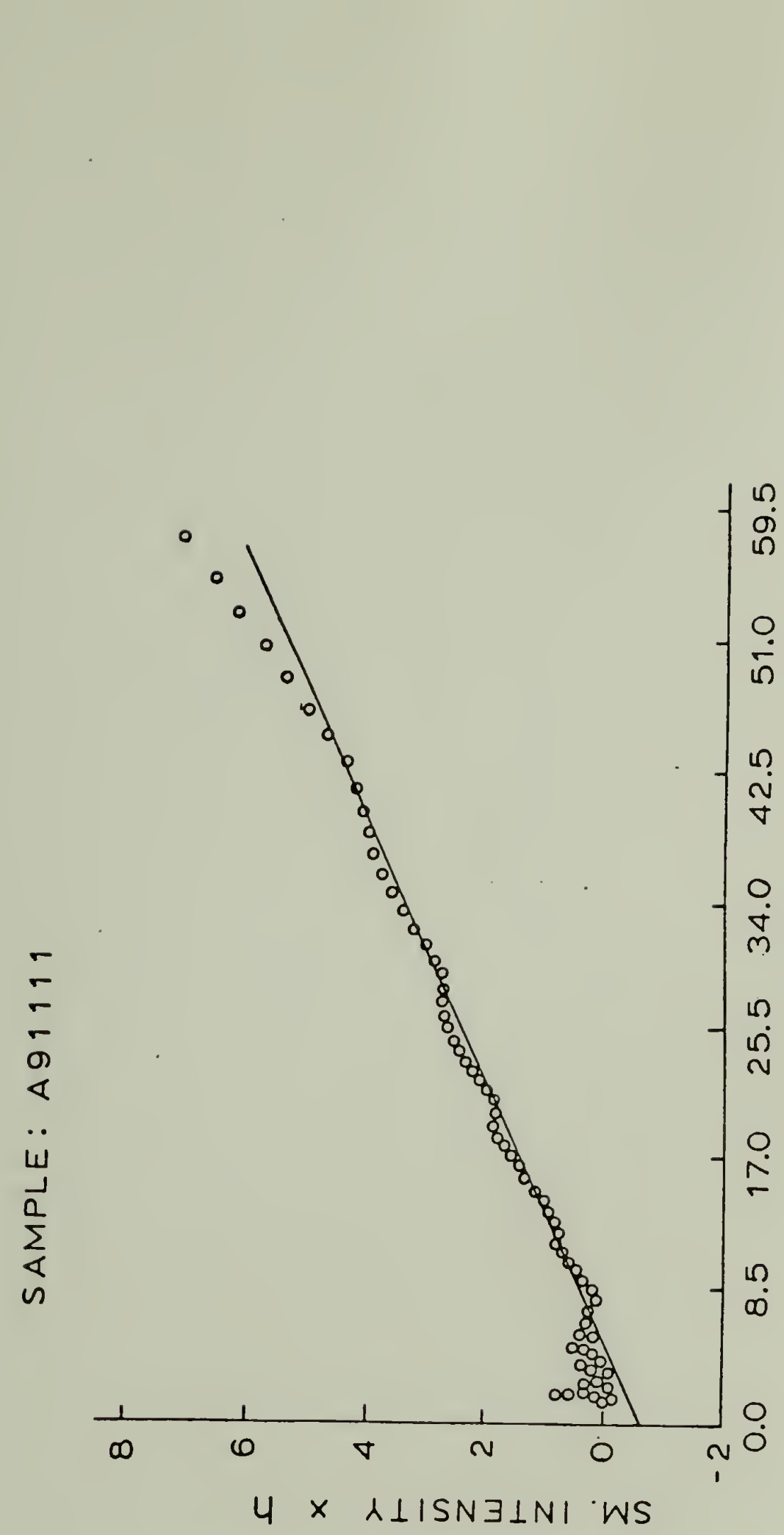

Figure 40. Plot of J(h)h vs. $1/h^2$ to obtain the linear transition zone thickness.

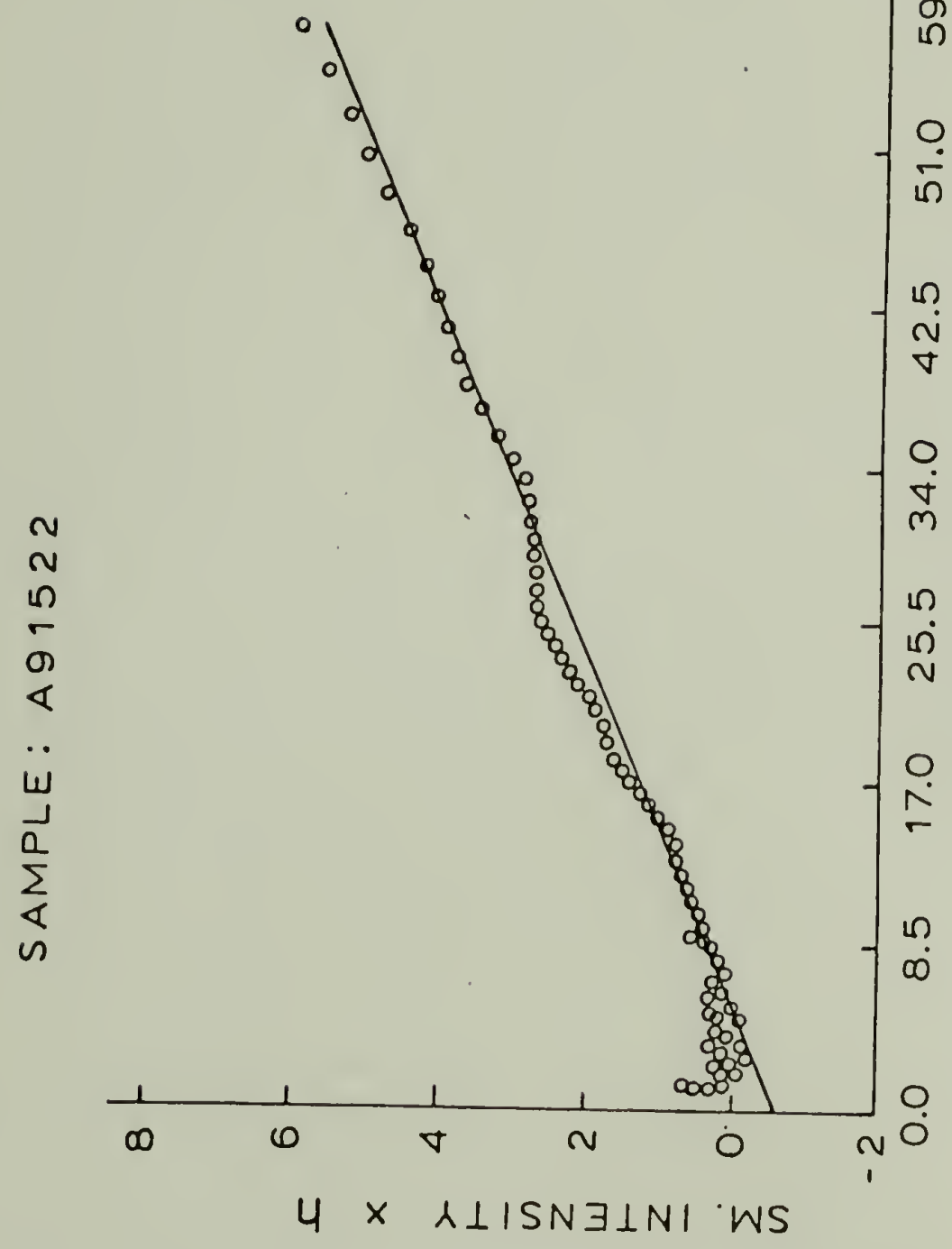

Figure 41. Plot of J(h)h vs. $1/h^2$ to obtain the linear transition zone thickness.

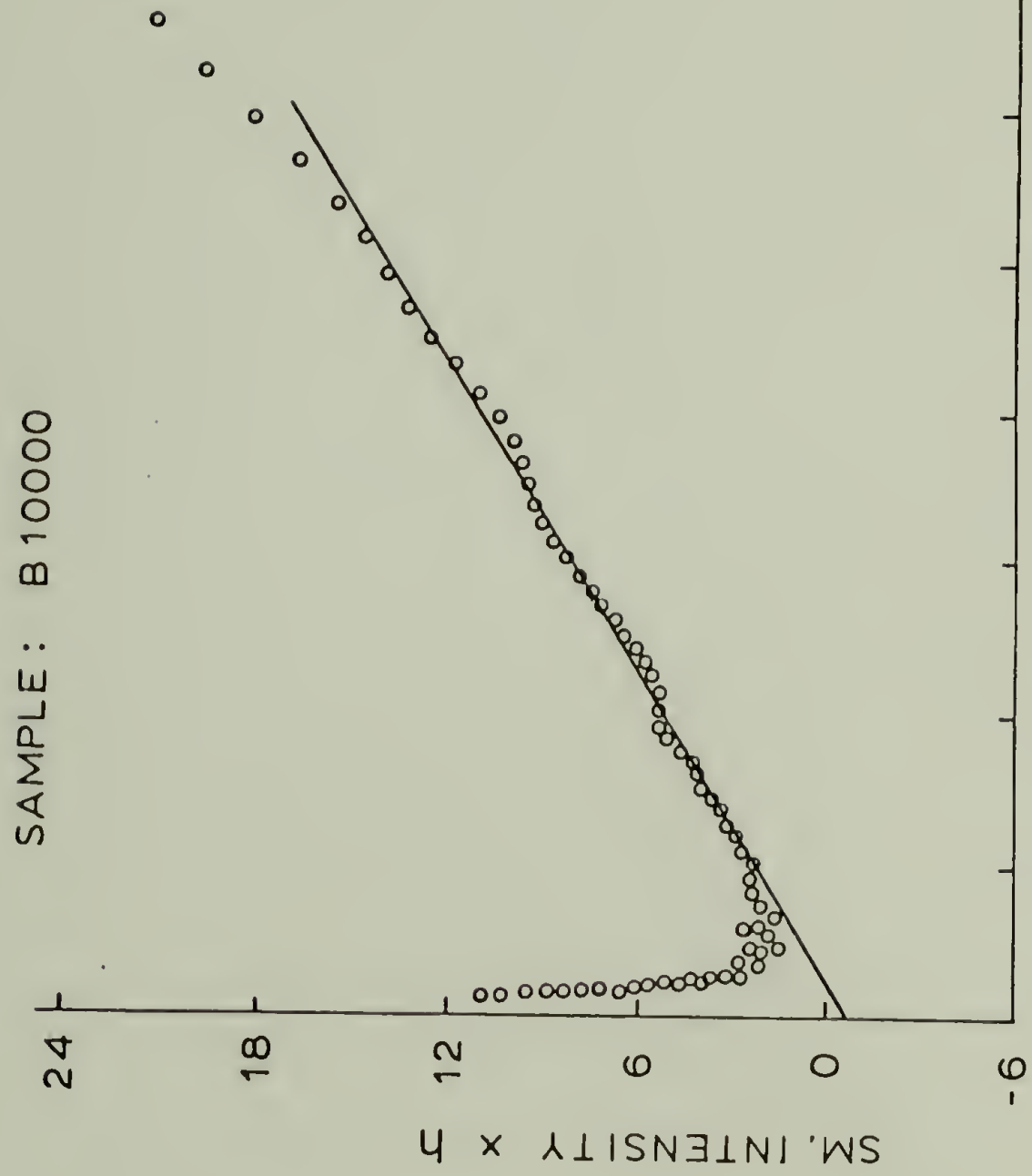

Figure 42. Plot of J(h)h vs. $1/h^2$ to obtain the linear transition zone thickness.

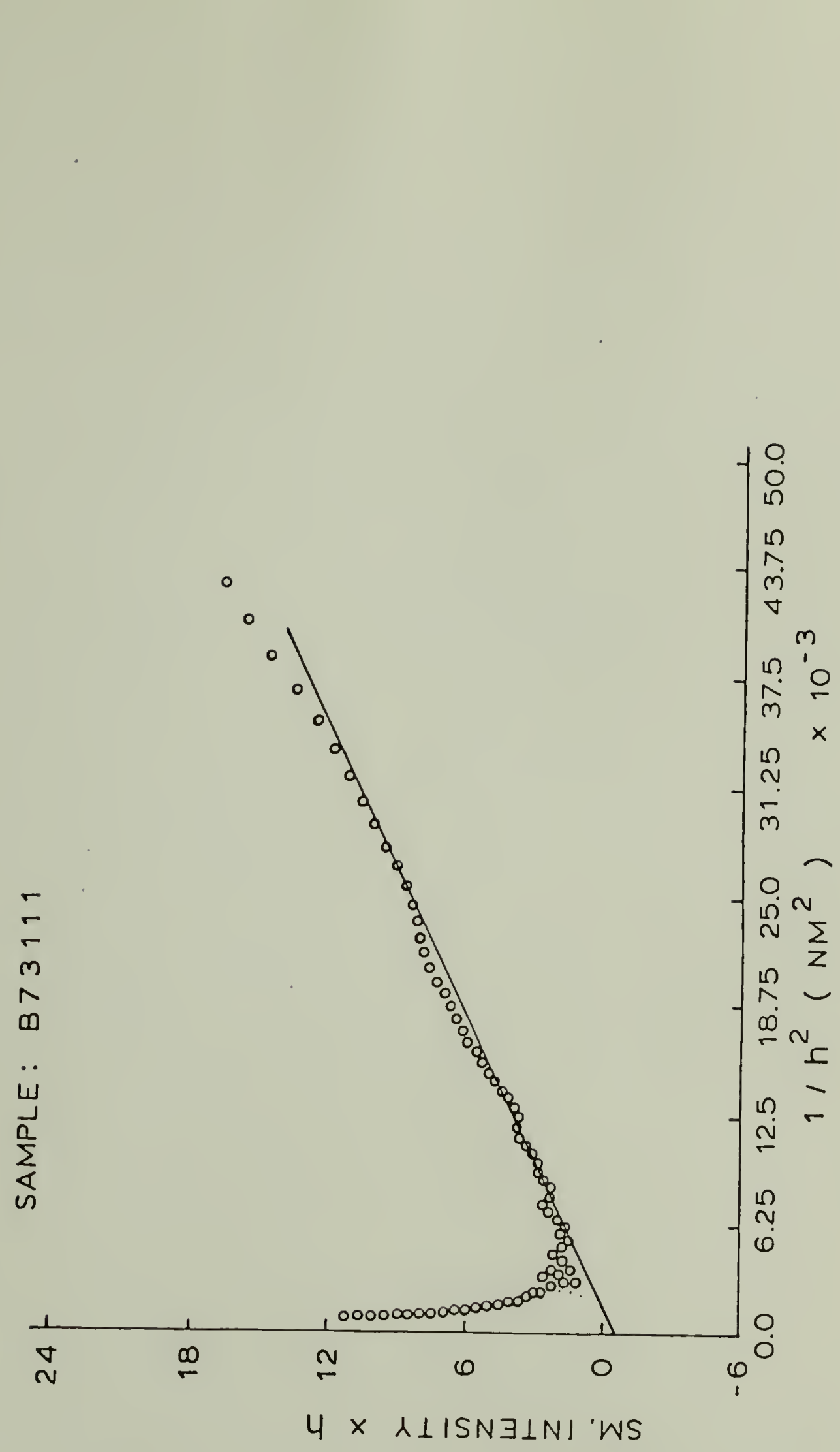

Figure 43. Plot of J(h)h vs. $1/h^2$ to obtain the linear transition zone thickness.

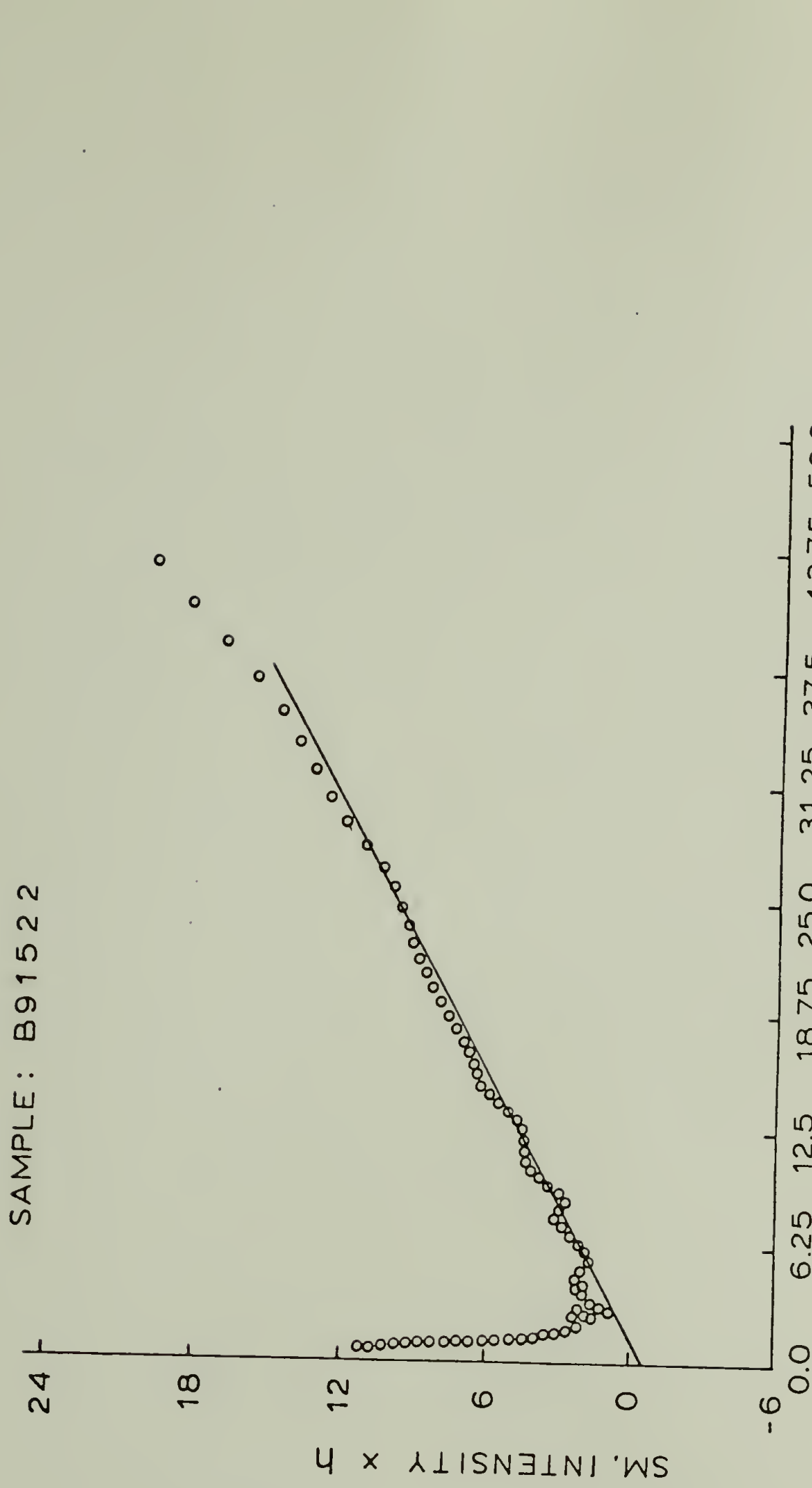

Figure 44. Plot of J(h)h vs. 1/h2 to obtain the linear transition zone thickness.

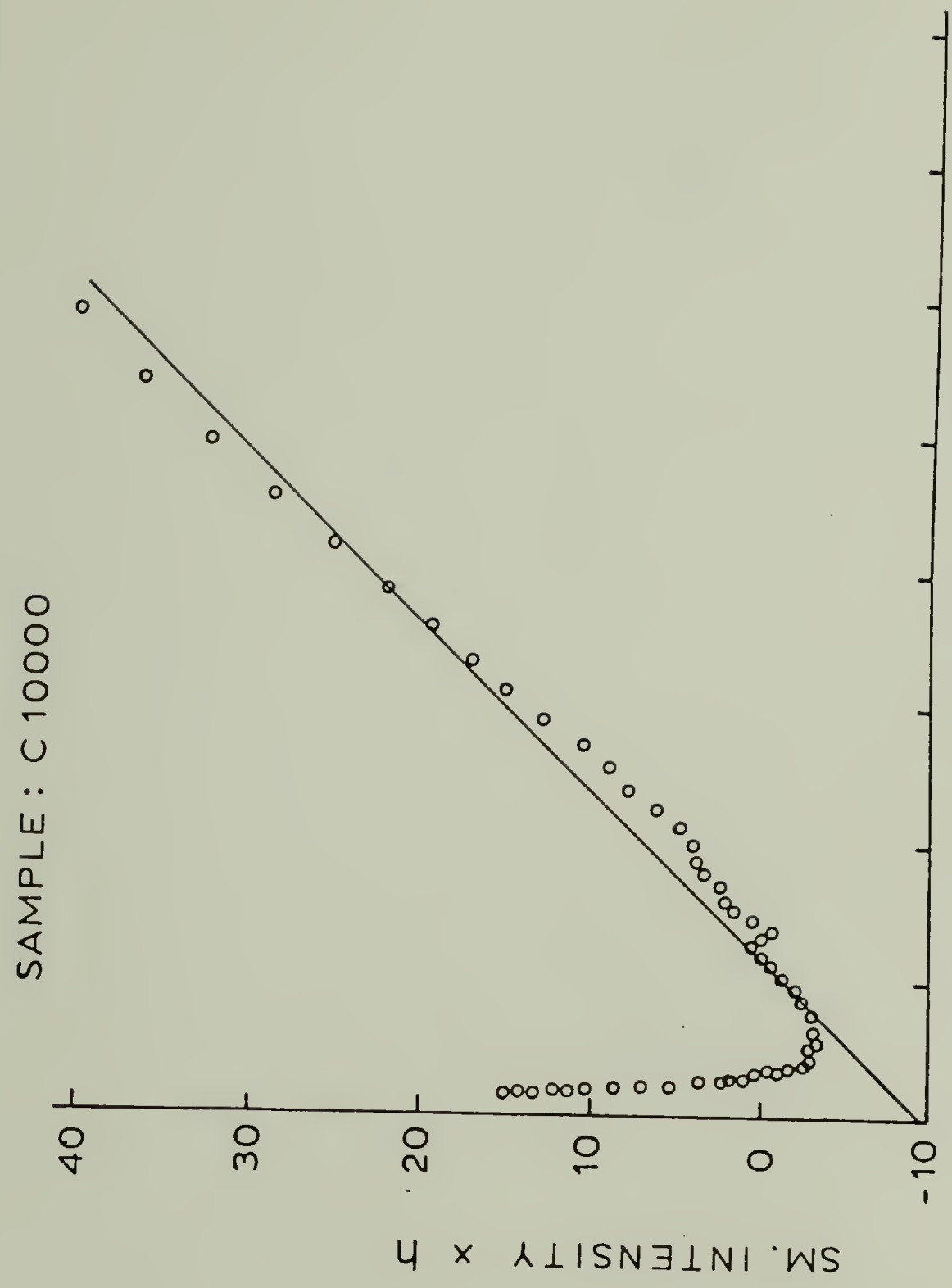

Figure 45. Plot of J(h)h vs. 1/h2 to obtain the linear transition zone thickness.

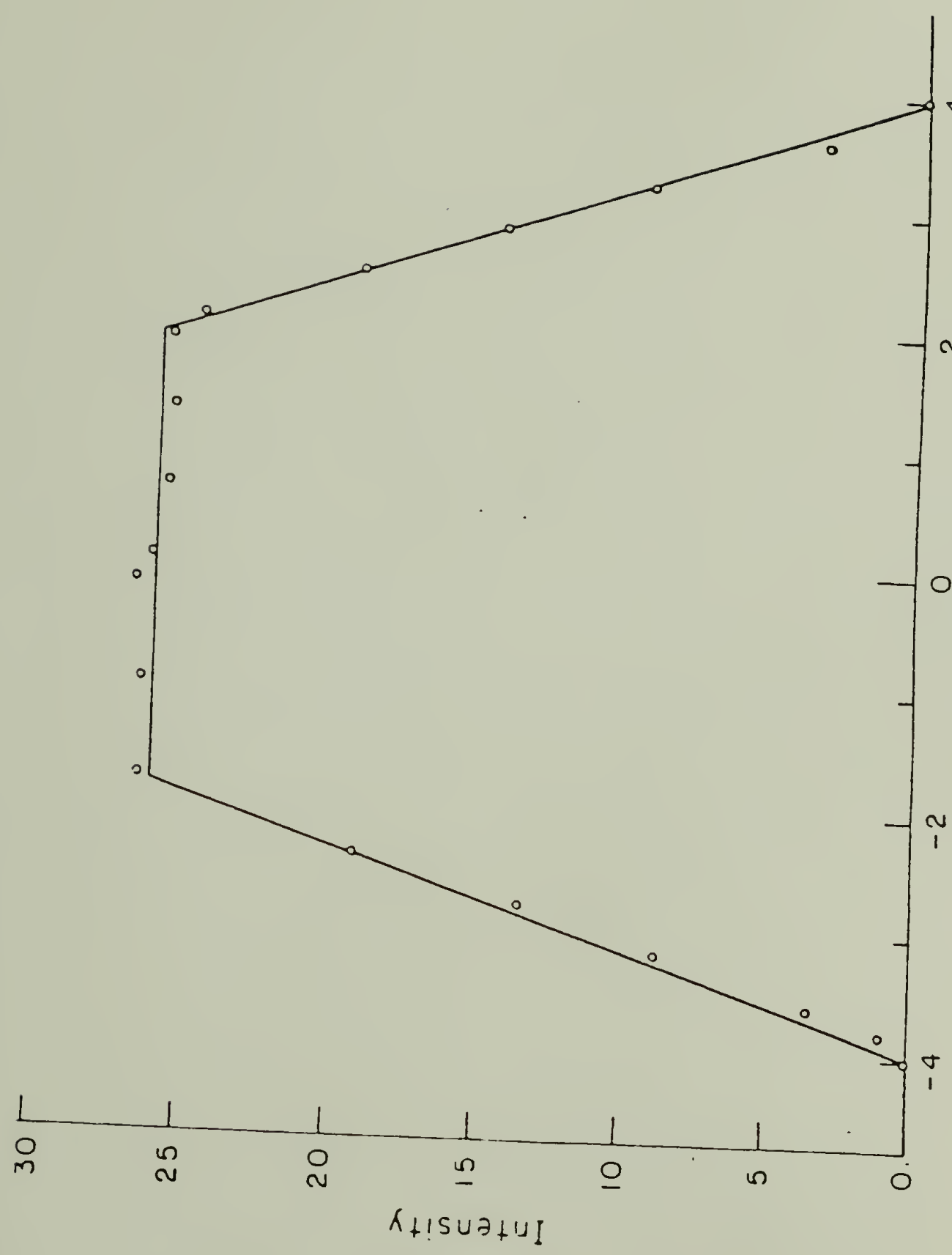

Figure 46. Slit profile of beam at the detector, used for weighting function desmearing.

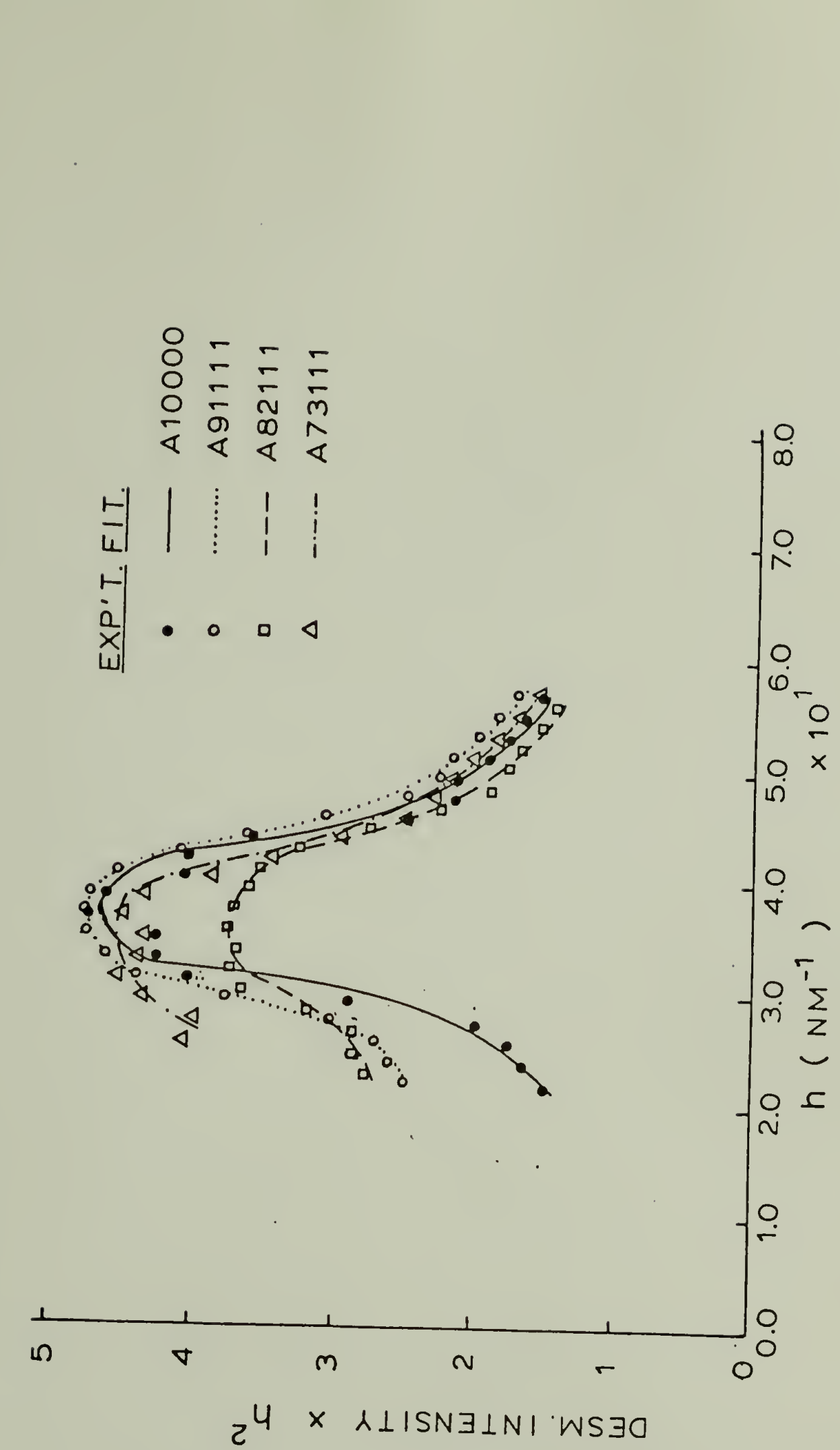

Figure 47. Lorentz corrected intensity. Symbols represent experimental data. Lines represent the best Hosemann fit. Intensity values are on a relative basis.

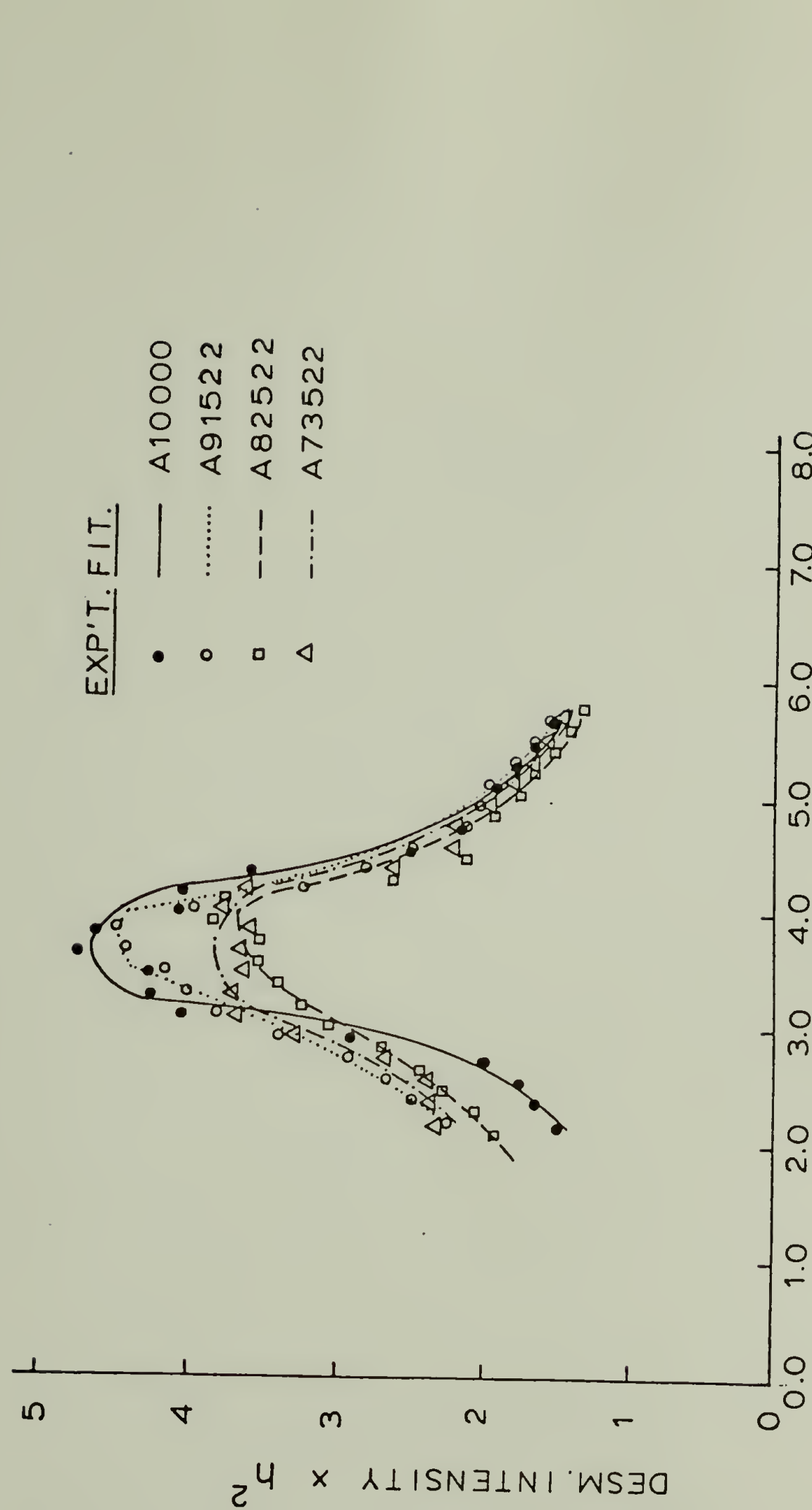

Figure 48. Lorentz corrected intensity. Symbols represent experimental data. Lines represent the best Hosemann fit. Intensity values are on a relative basis.

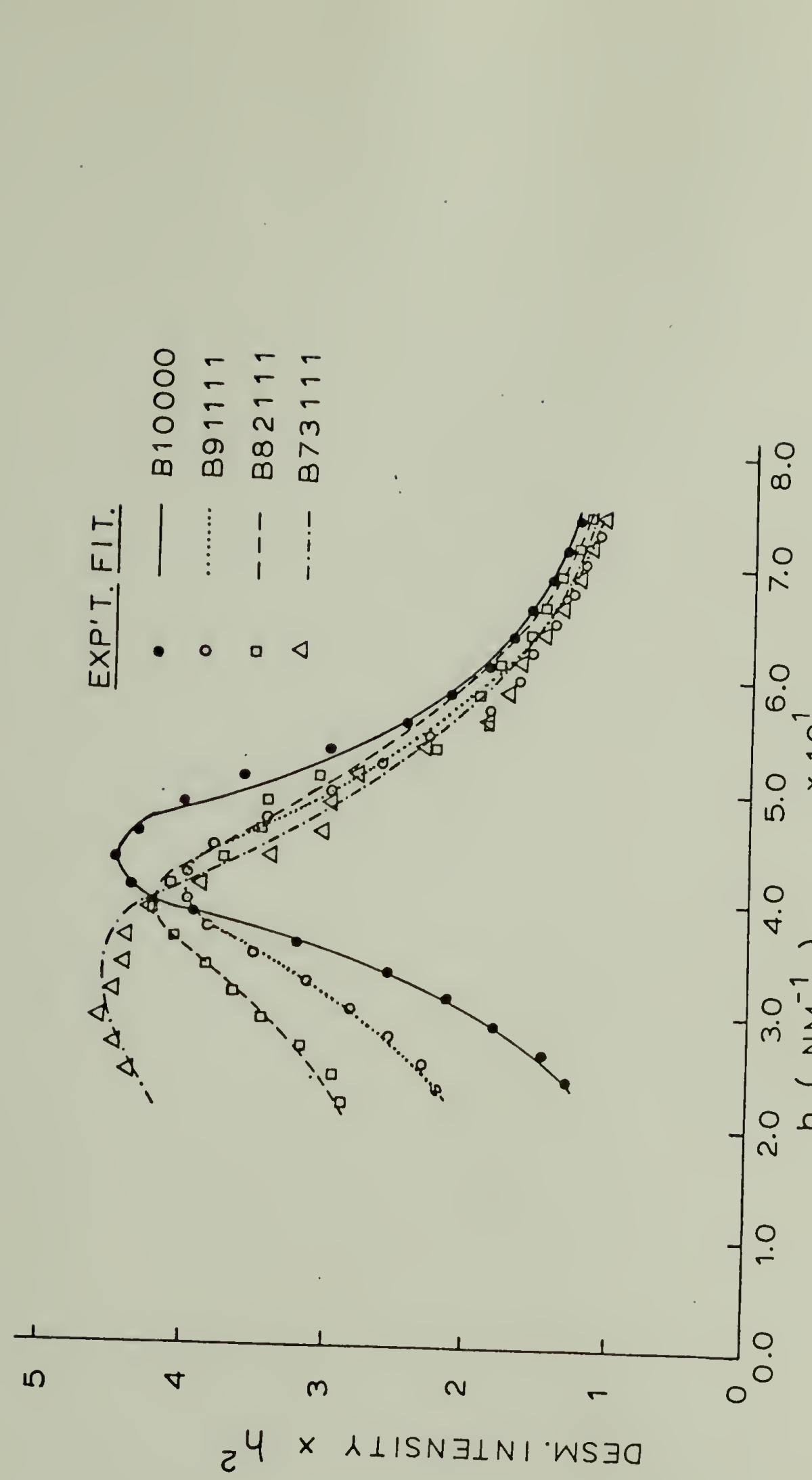

Figure 49. Lorentz corrected intensity. Symbols represent experimental data. Lines represent the best Hosemann fit. Intensity values are on a relative basis.

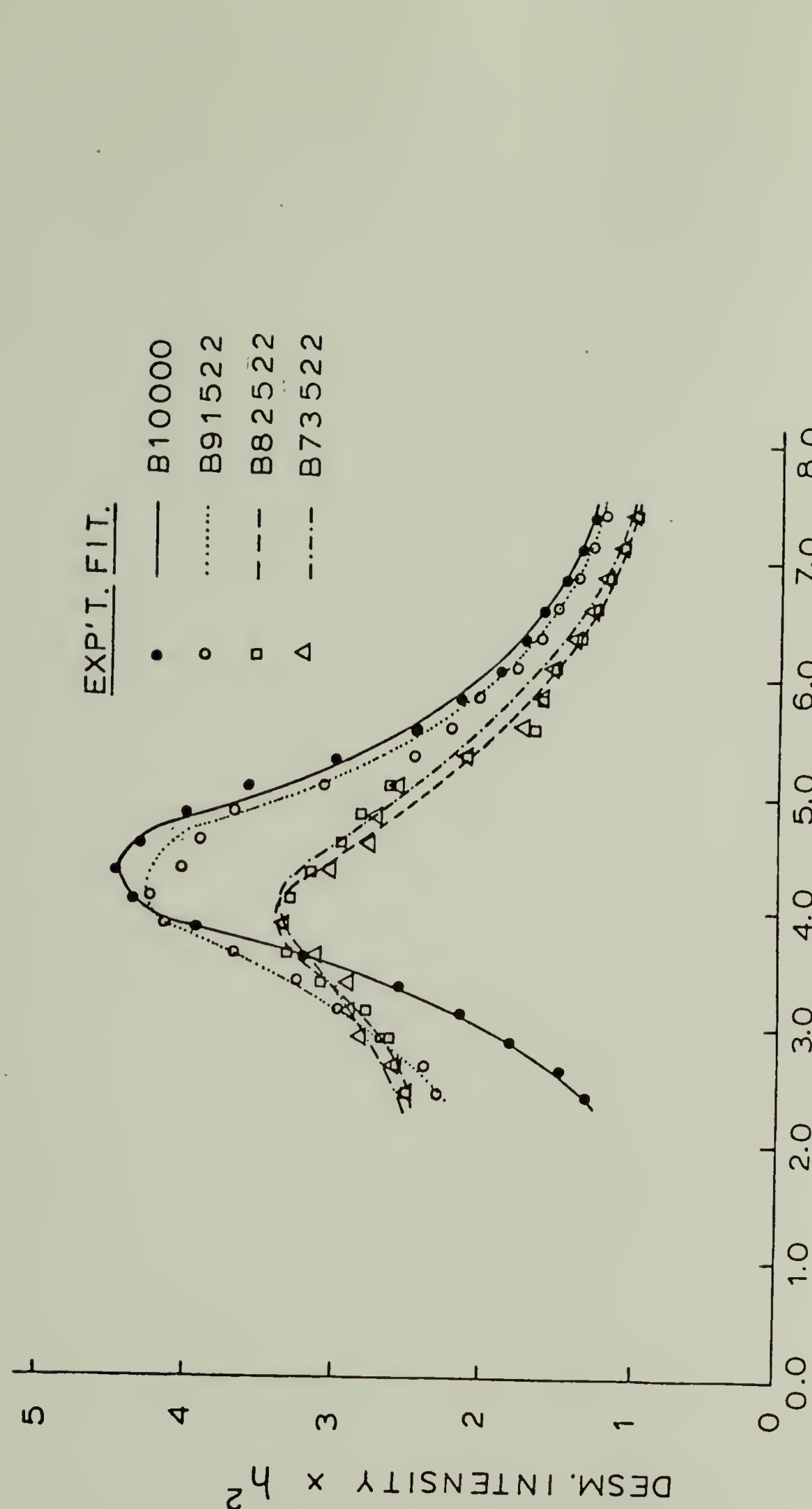

Figure 50. Lorentz corrected intensity. Symbols represent experimental data. Lines represent the best Hosemann fit. Intensity values are on a relative basis.

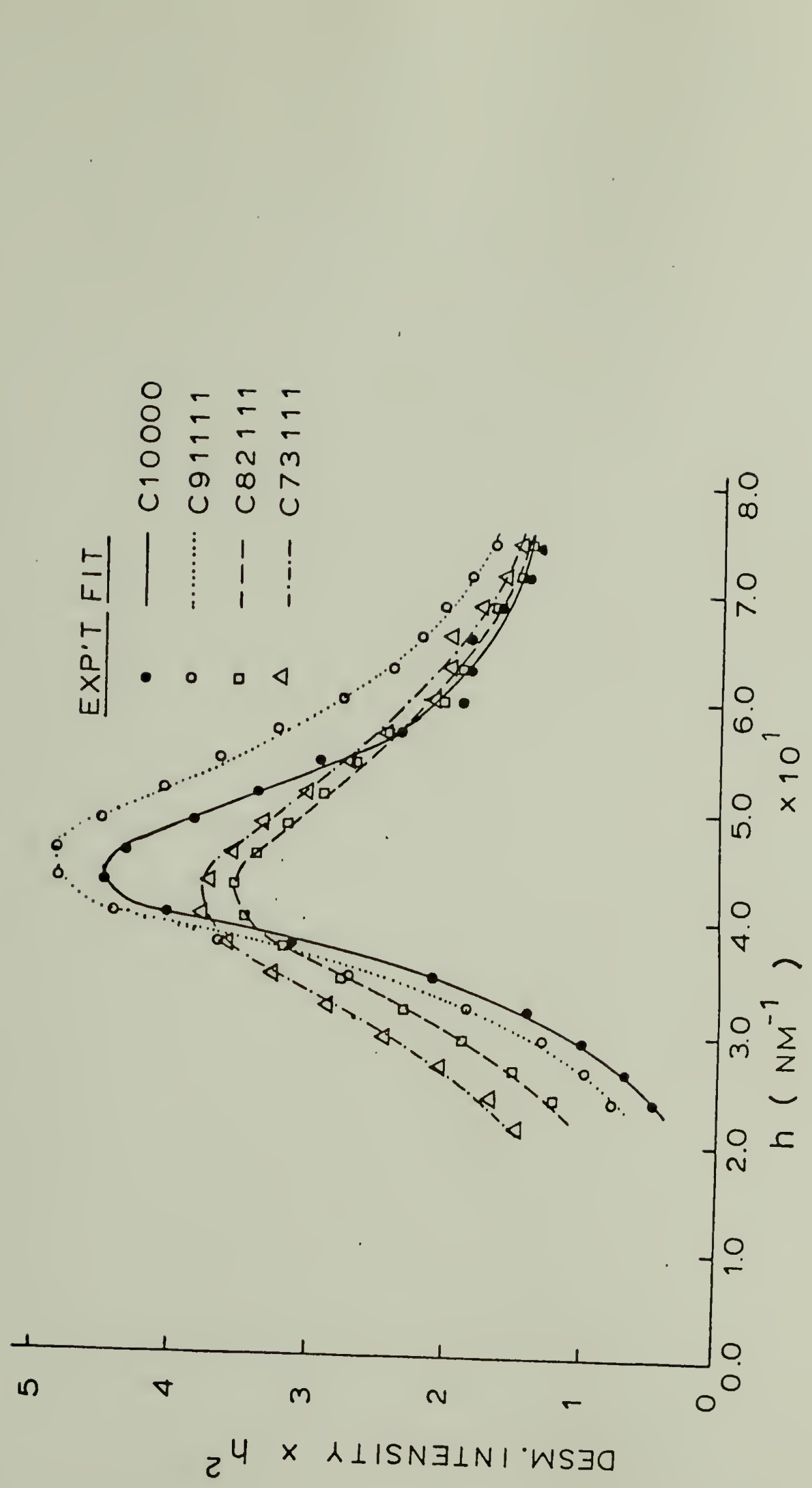

Figure 51. Lorentz corrected intensity. Symbols represent experimental data. Lines represent the best Hosemann fit. Intensity values are on a relative basis.

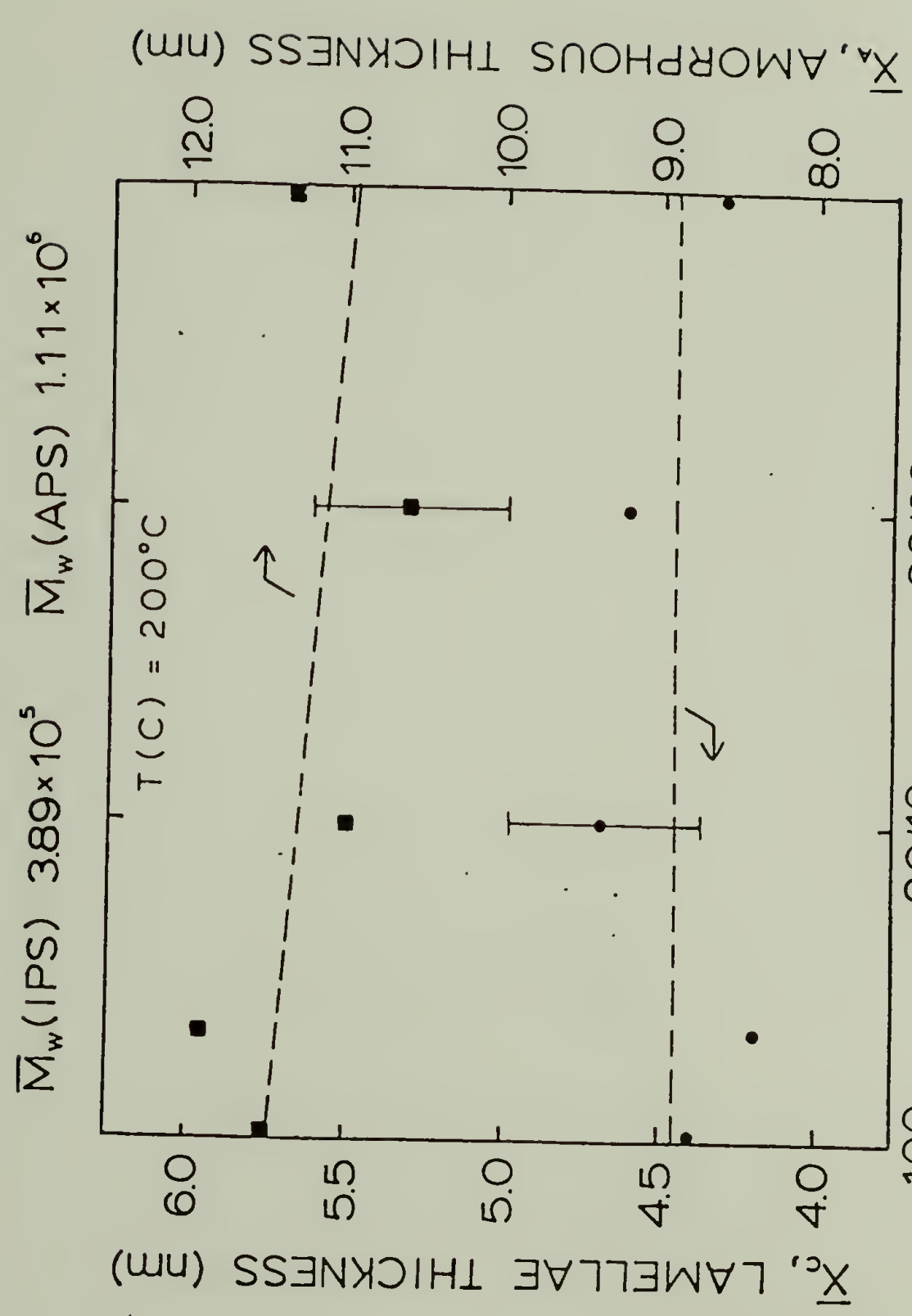

Figure 52. Comparison of best Hosemann fitted values for crystal line and amorphous thickness as a function of composition. Molecular weight of APS and crystallization temperature are indicated.

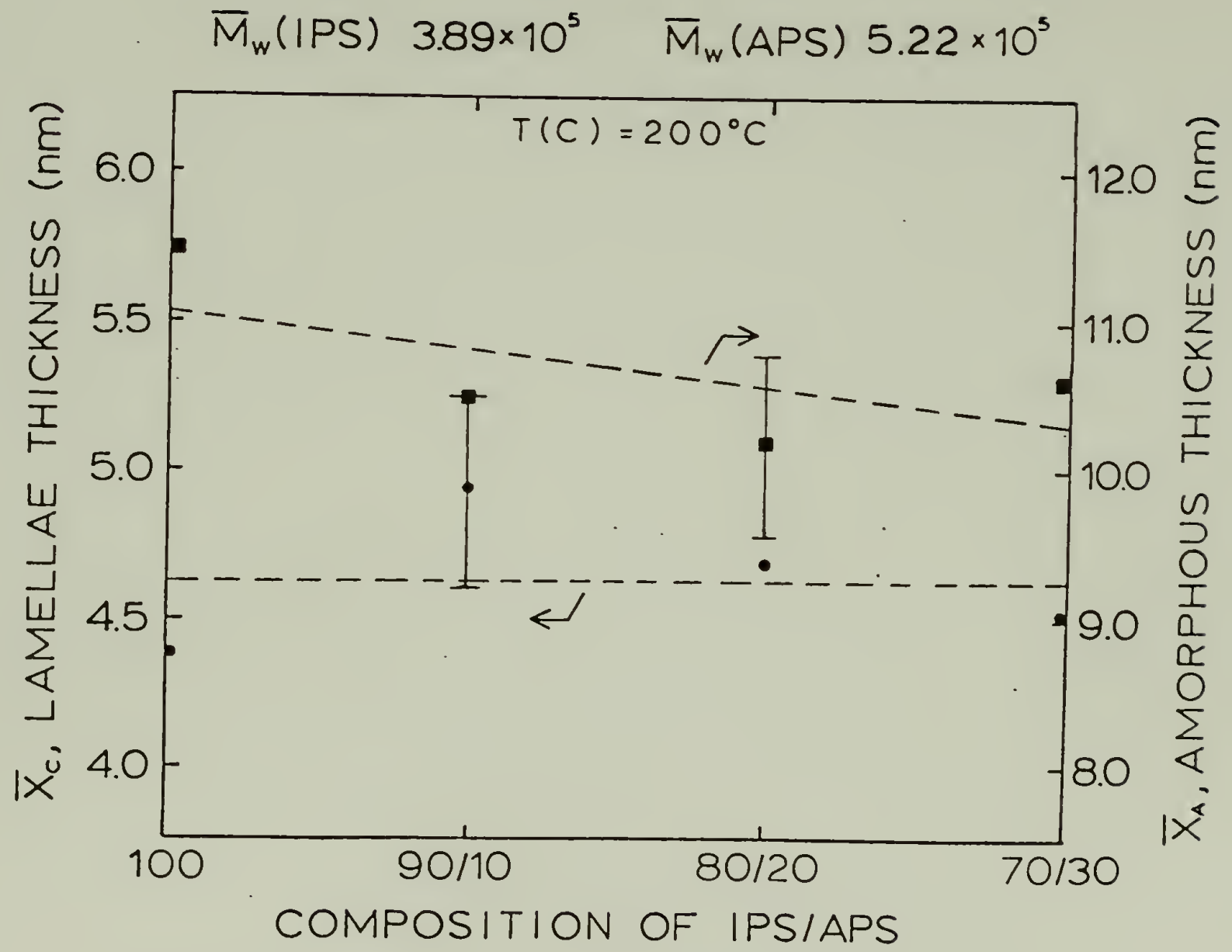

Figure 53. Comparison of best Hosemann fitted values for crystal line and amorphous thickness as a function of composition. Molecular weight of APS and crystallization temperature are indicated.

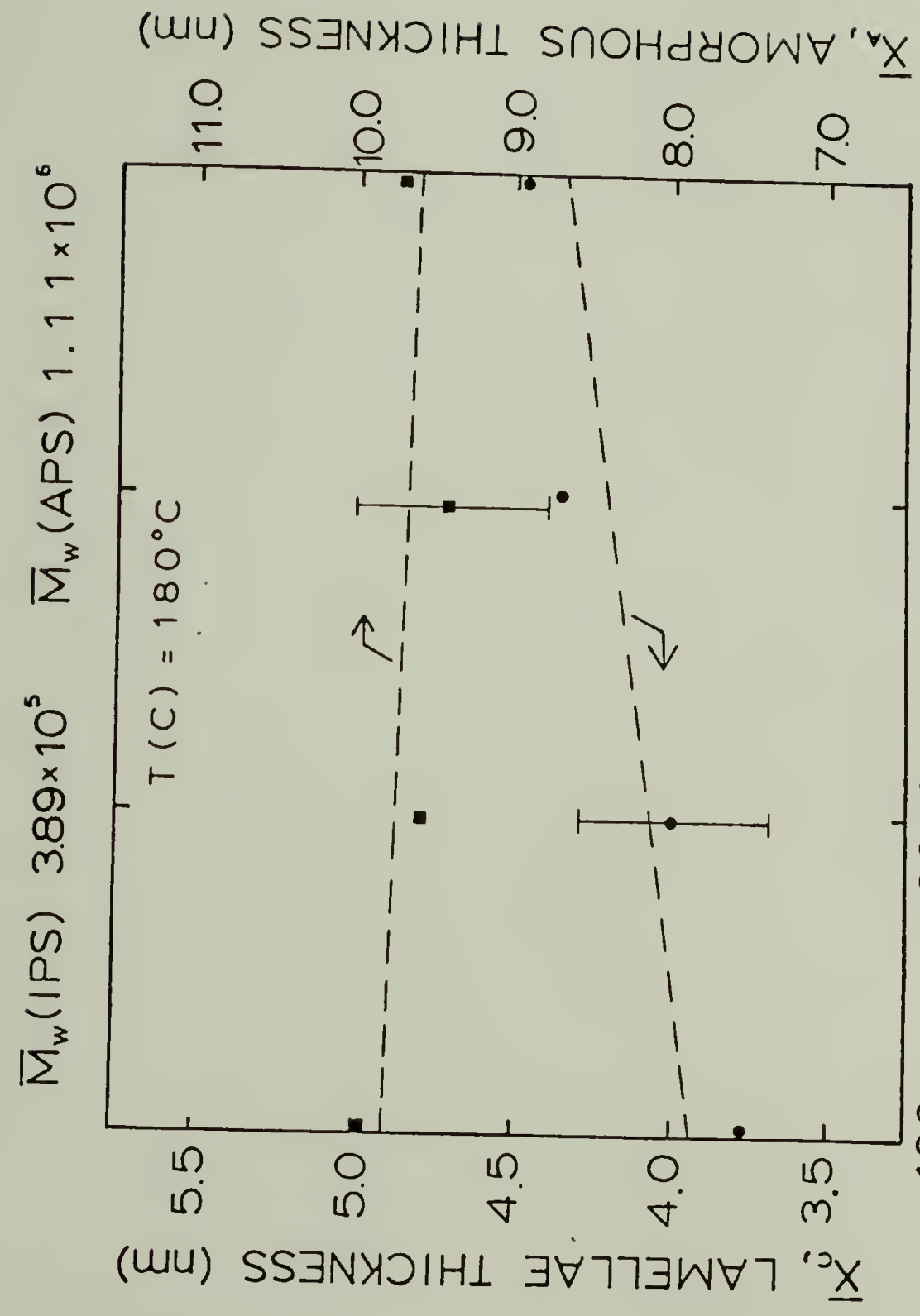

Figure 54. Comparison of best Hosemann fitted values for crystal line and amorphous thickness as a function of composition. Molecular weight of APS and crystallization temperature are indicated.

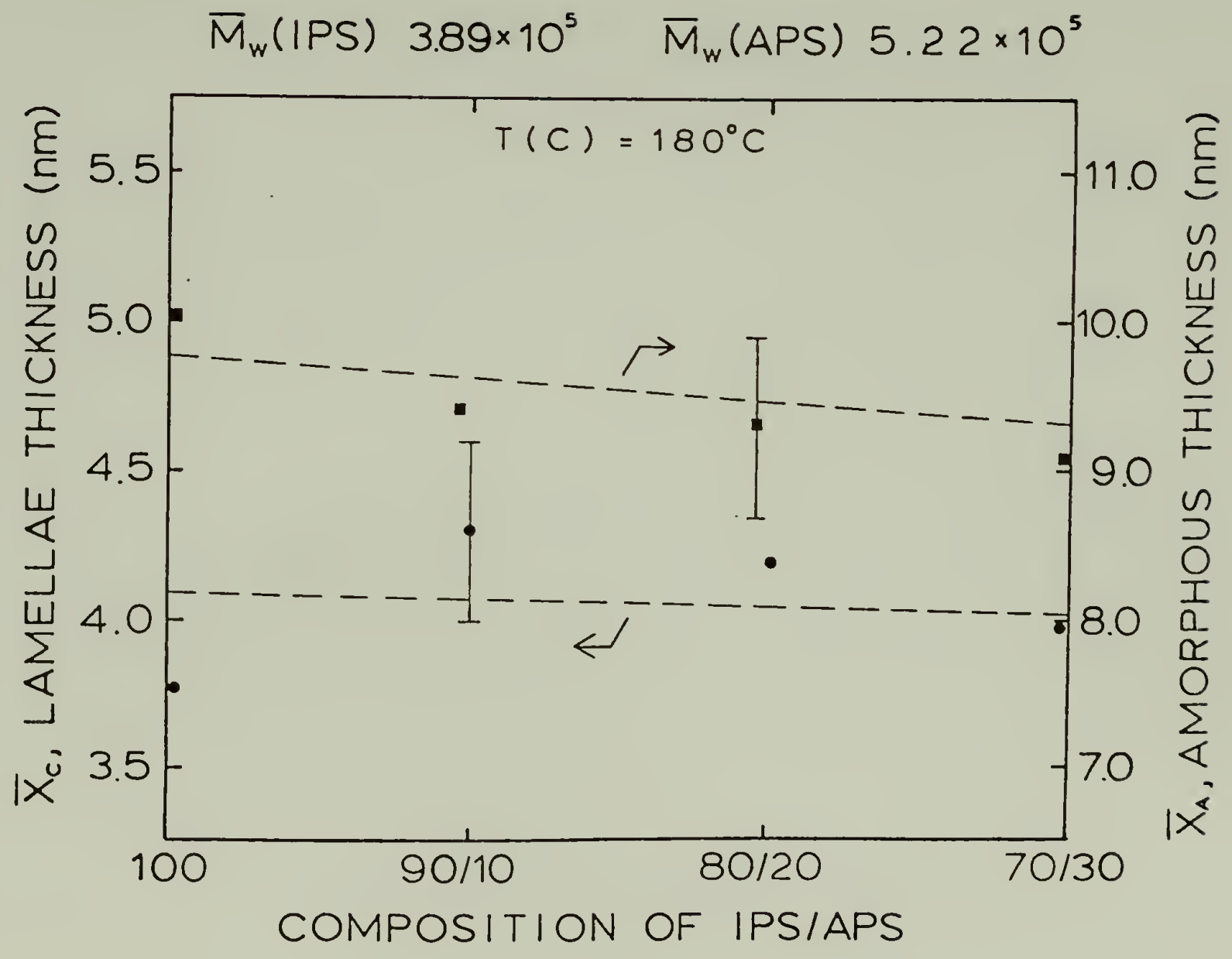

Figure 55. Comparison of best Hosemann fitted values for crystal line and amorphous thickness as a function of composition. Molecular weight of APS and crystallization temperature are indicated.

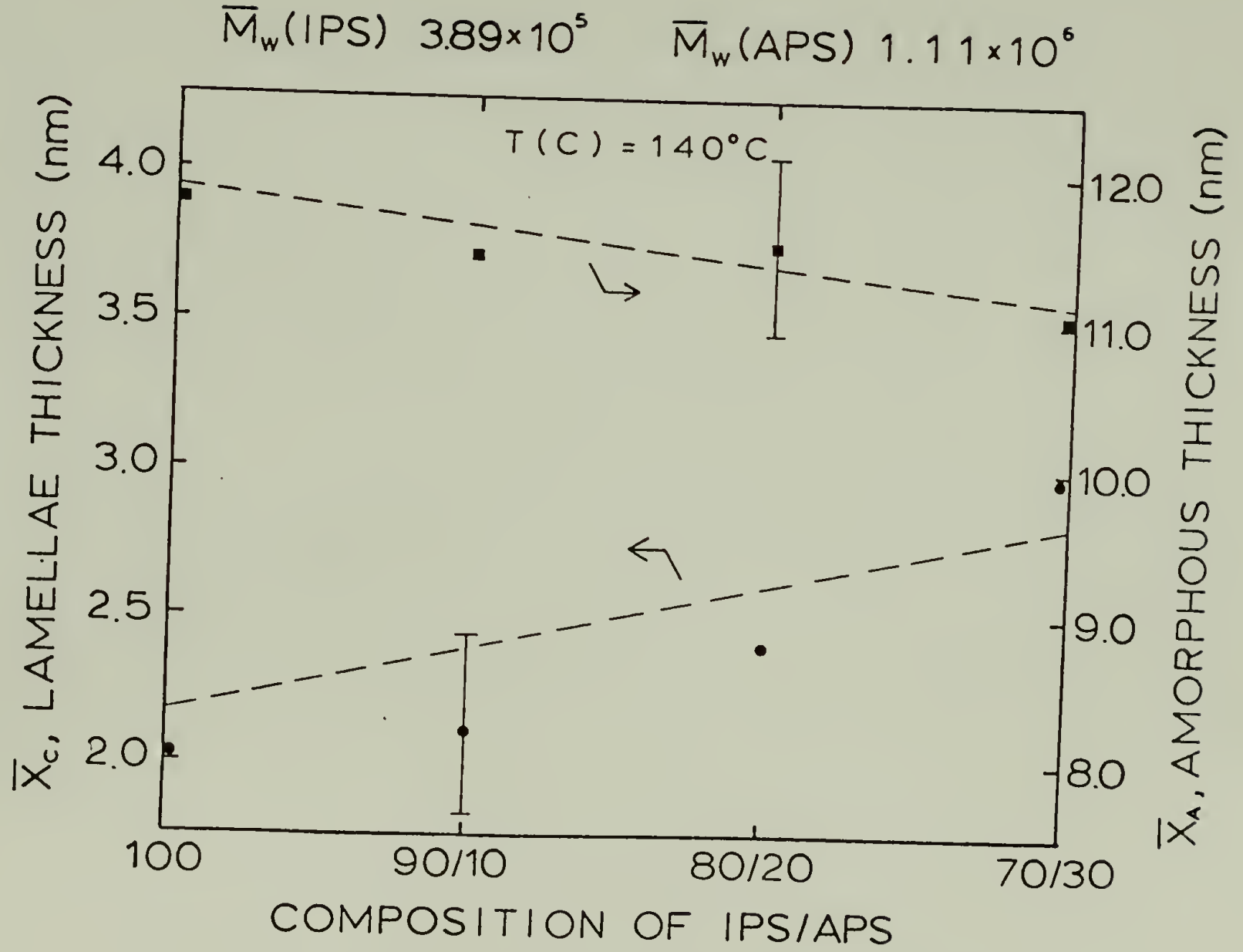

Figure 56. Comparison of best Hosemann fitted values for crystal line and amorphous thickness as a function of composition. Molecular weight of APS and crystallization temperature are indicated.

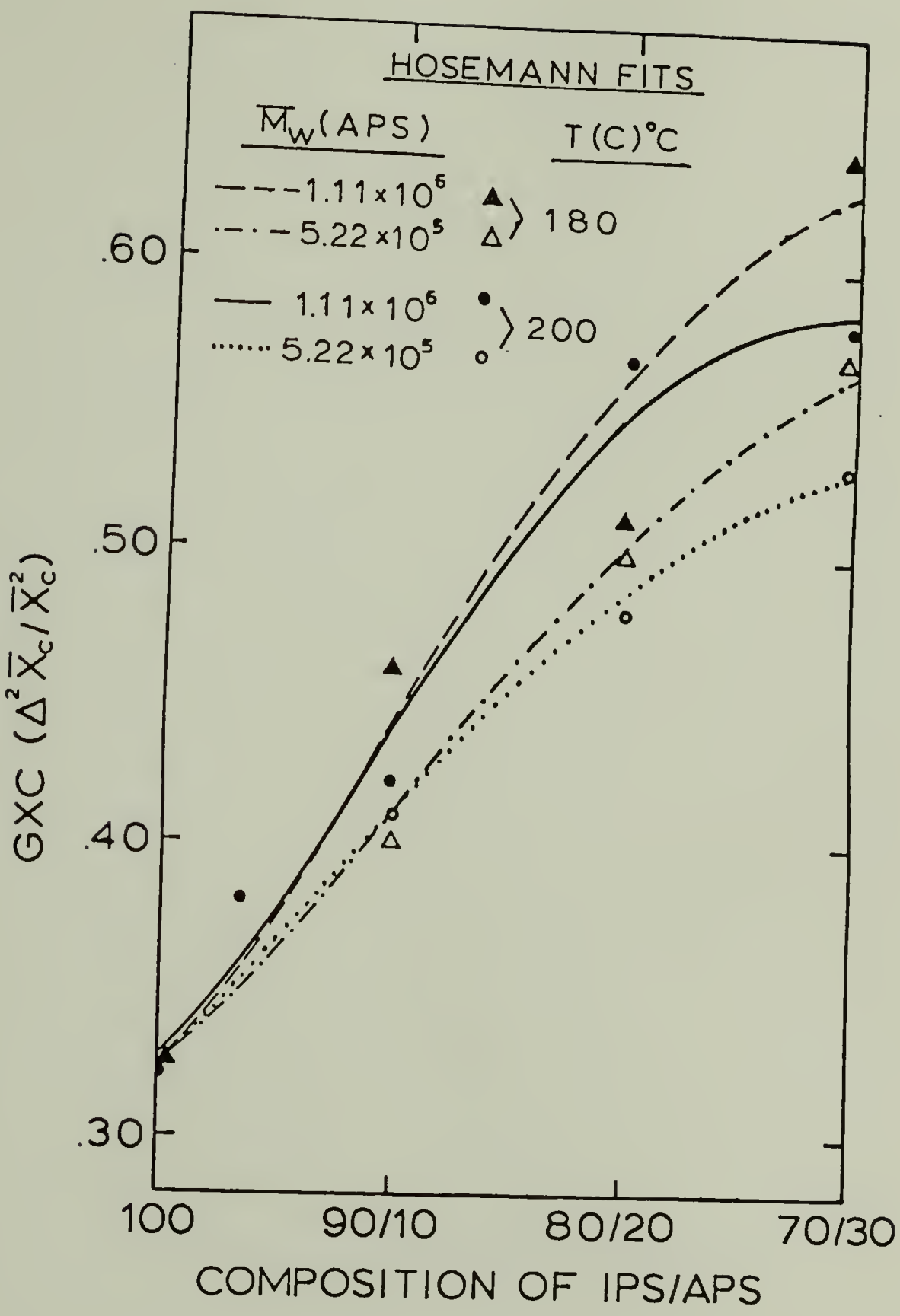

Figure 57. Comparison of best Hosemann fitted values for the crystalline thickness distributions as a function of composition.

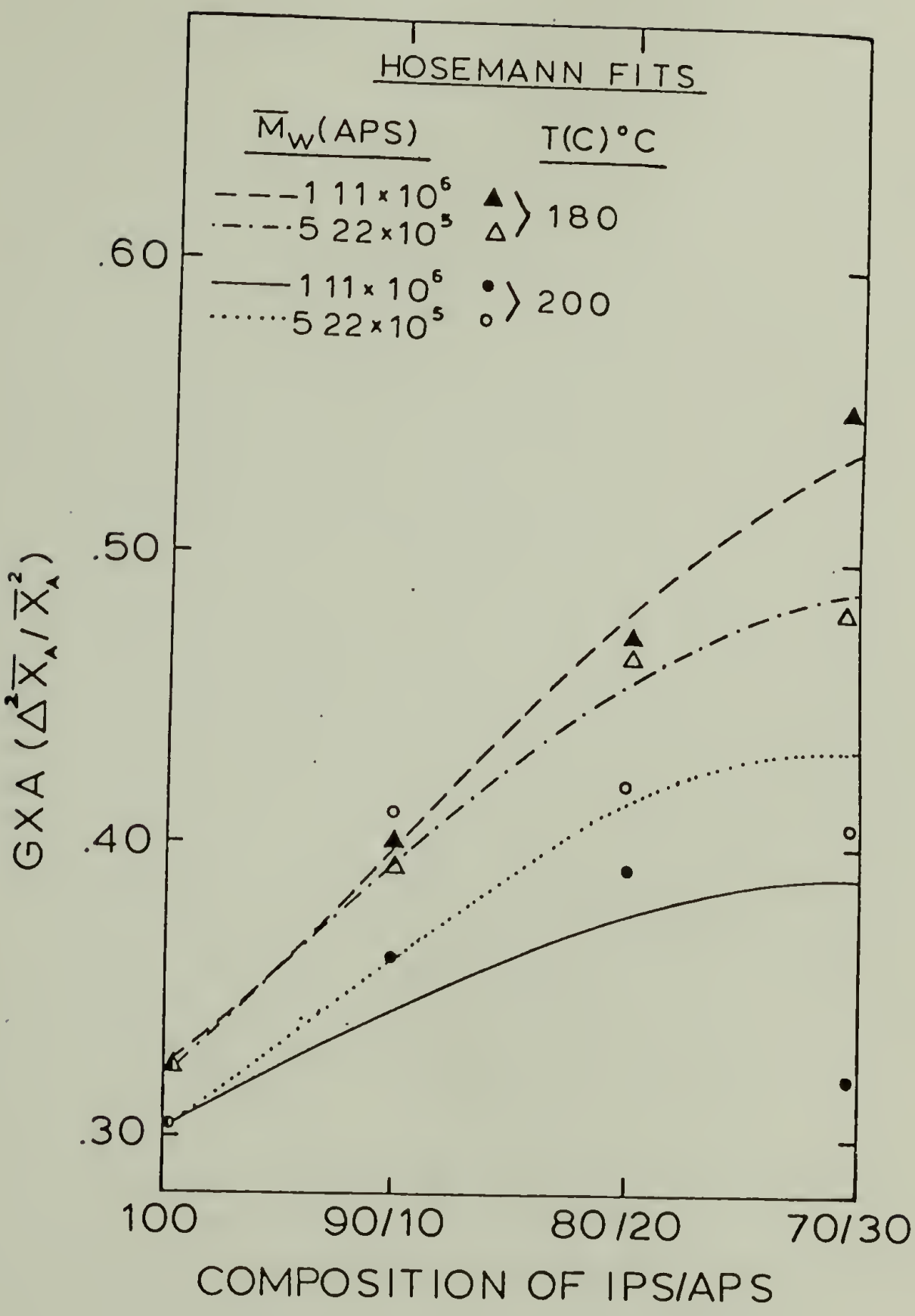

Figure 58. Comparison of best Hosemann fitted values for the amorphous thickness distribution as a function of composition.

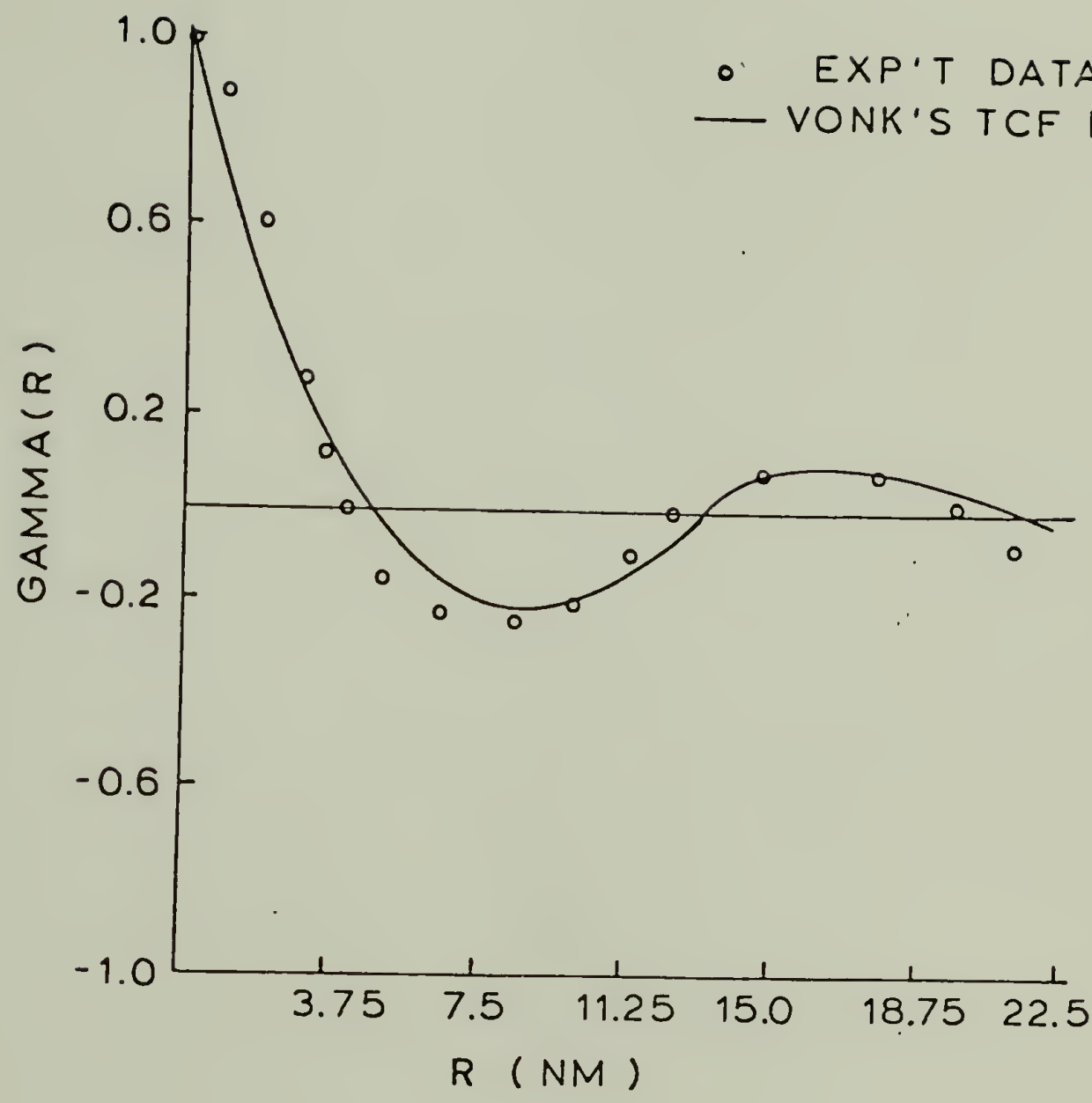

Figure 59. Comparison of experimental correlation function (open circles) and best fitted values for Vonk's theoretical correlation function (TCF) for sample A10000.

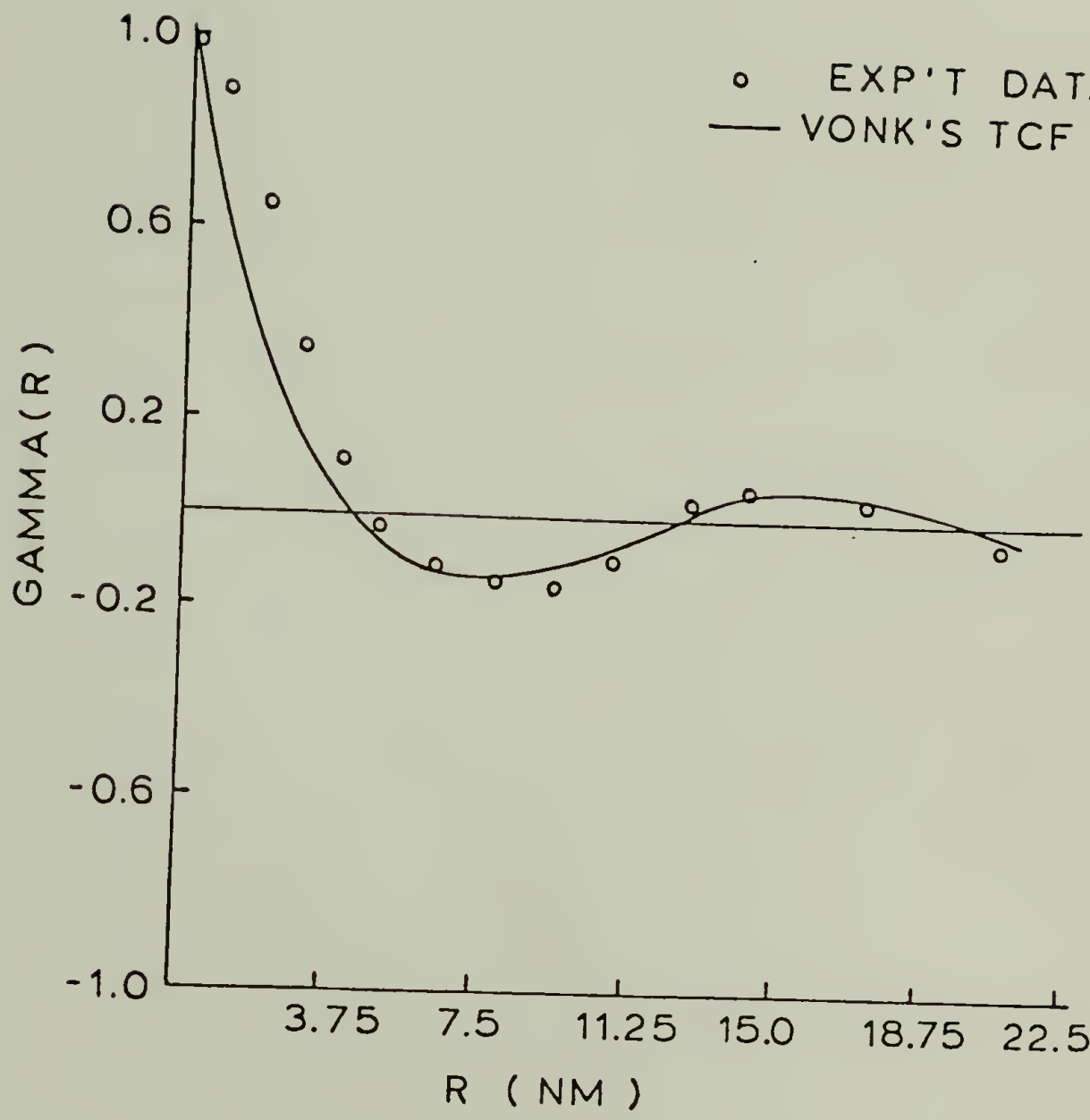

Figure 60. Comparison of experimental correlation function (open circles) and best fitted values for Vonk's theoretical correlation function (TCF) for sample A91111.

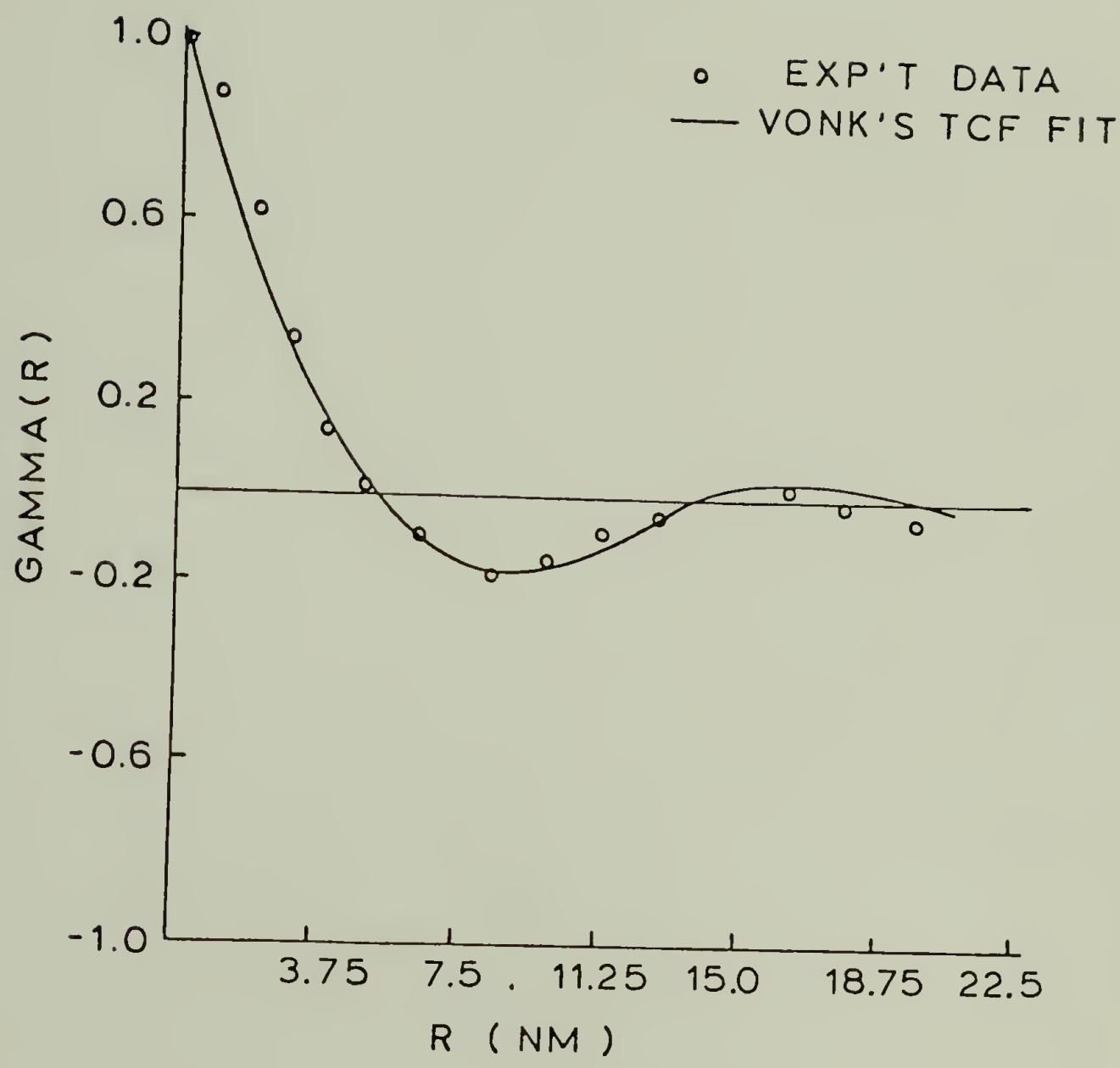

Figure 61. Comparison of experimental correlation function (open circles) and best fitted values for Vonk's theoretical correlation function (TCF) for sample A82111.

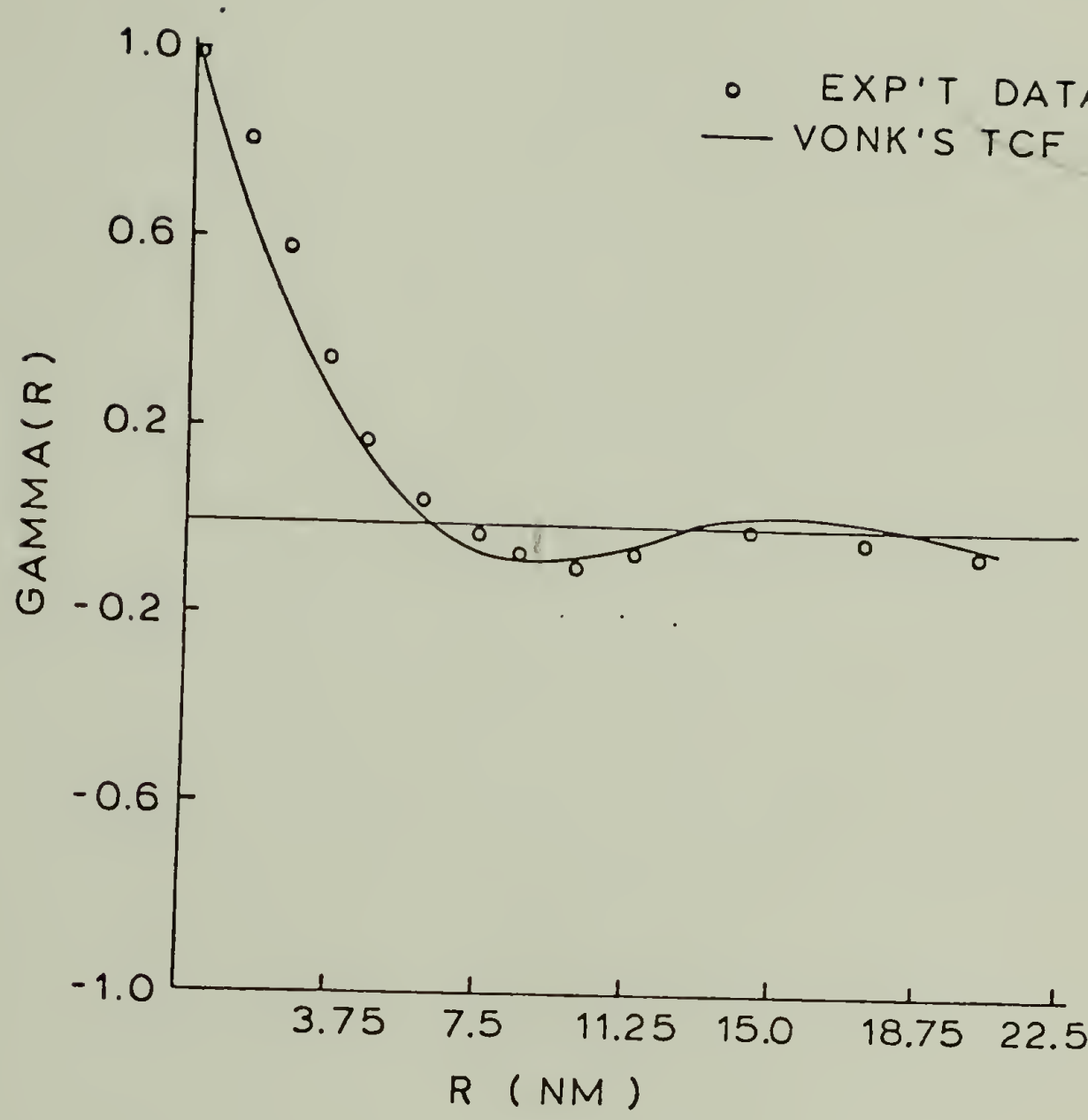

Figure 62. Comparison of experimental correlation function (open circles) and best fitted values for Vonk's theoretical correlation function (TCF) for sample A73111.

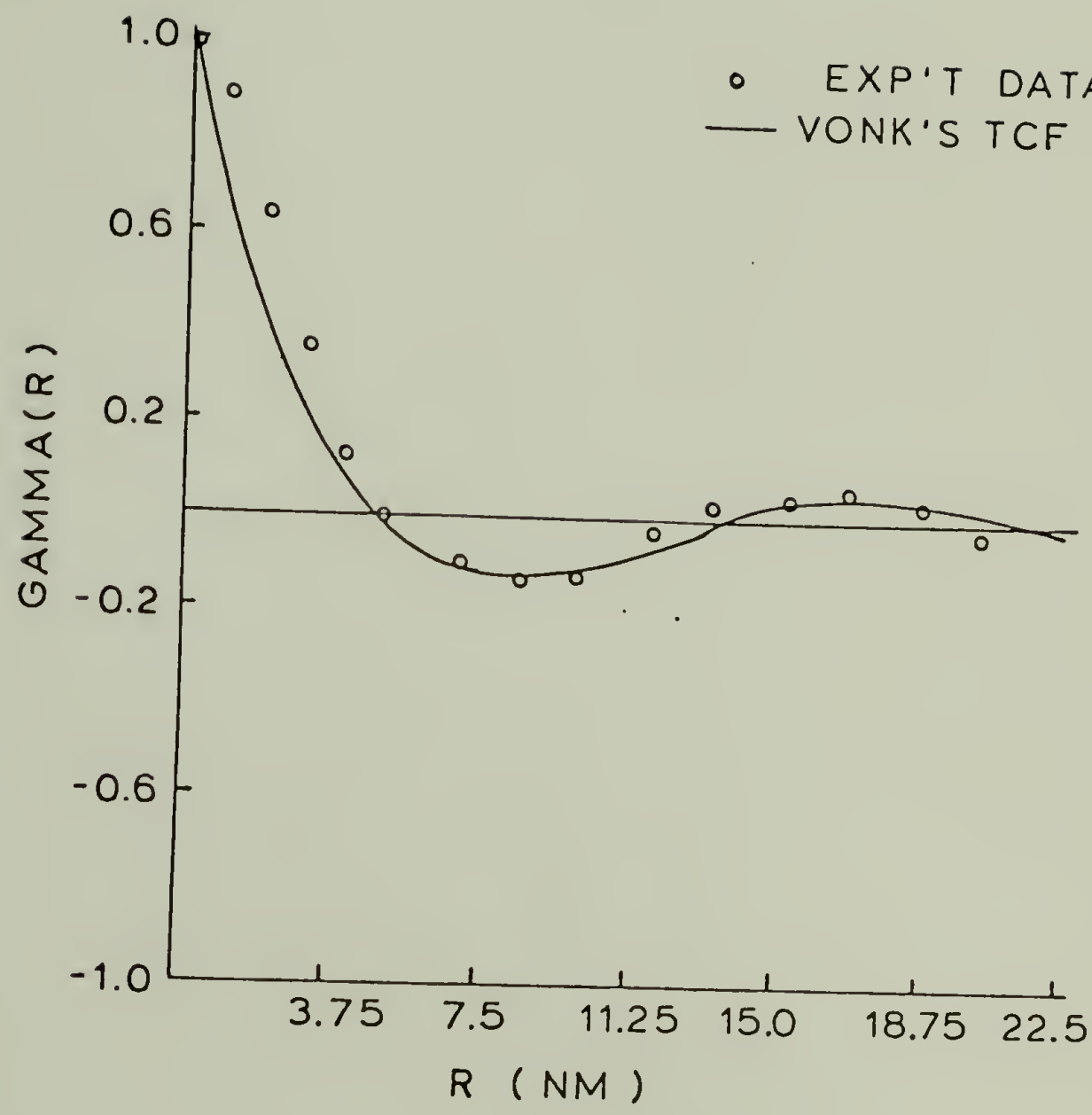

Figure 63. Comparison of experimental correlation function (open circles) and best fitted values for Vonk's theoretical correlation function (TCF) for sample A91522.

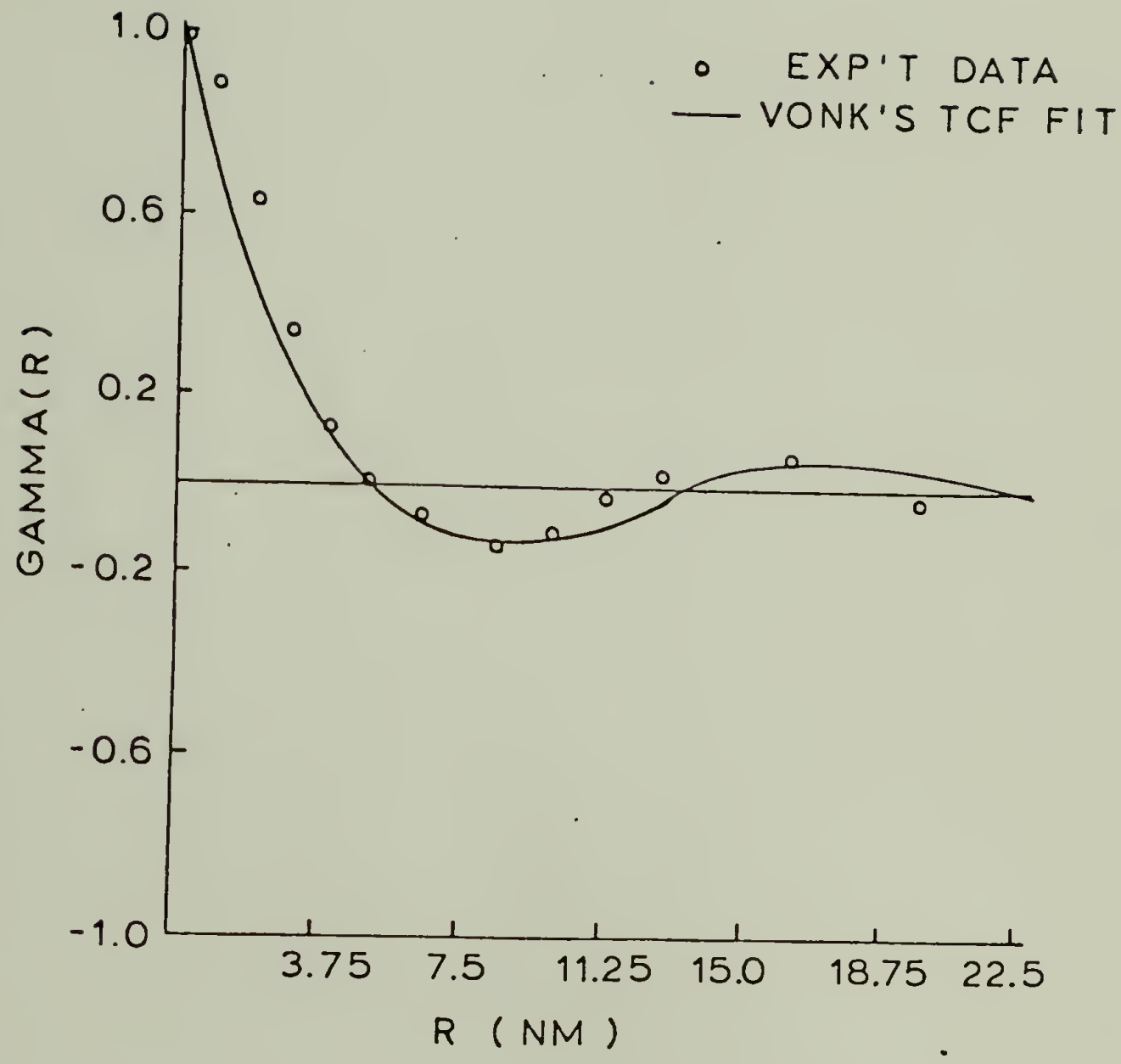

Figure 64. Comparison of experimental correlation function (open circles) and best fitted values for Vonk's theoretical correlation function (TCF) for sample A82522.

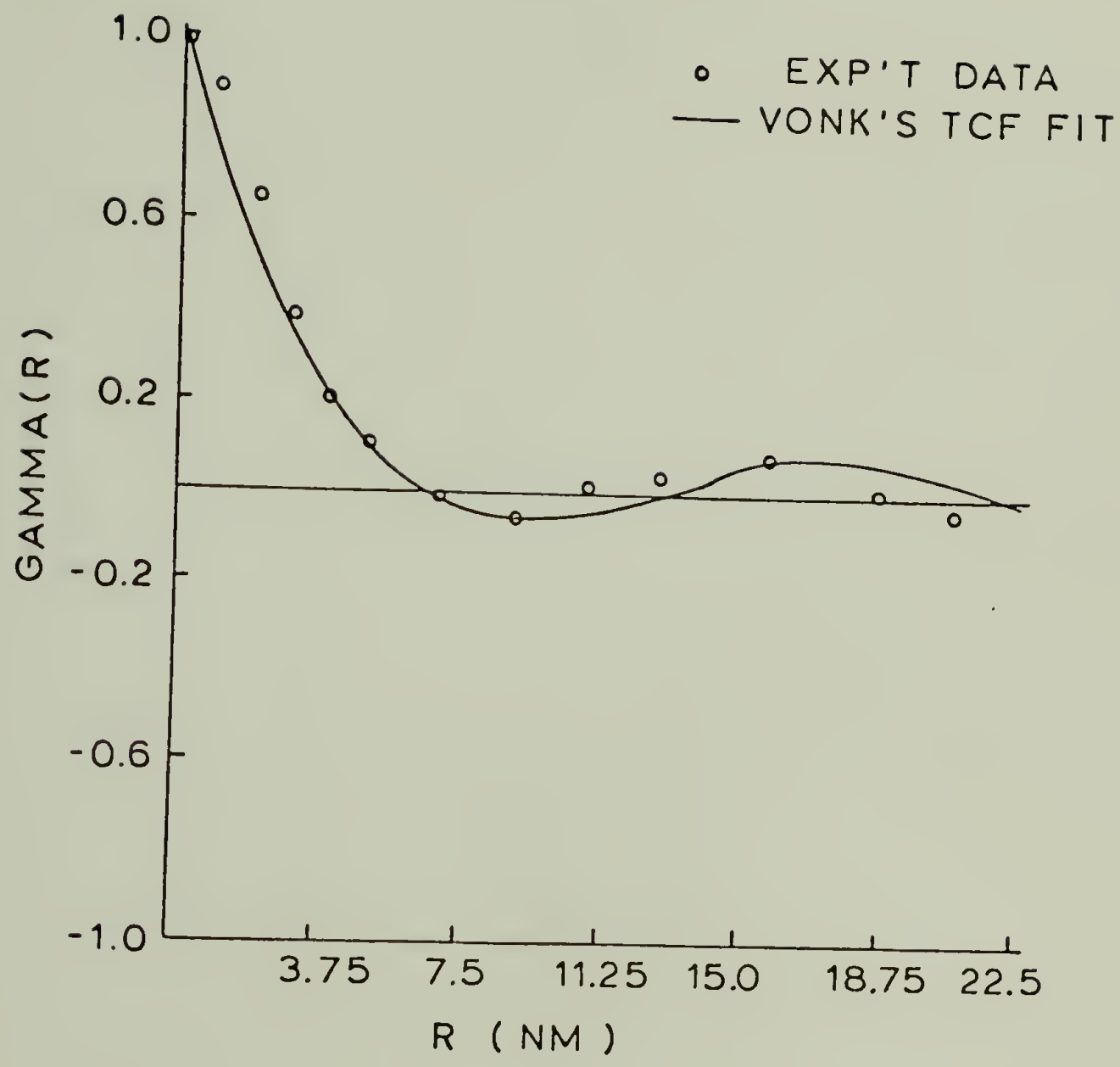

Figure 65. Comparison of experimental correlation function (open circles) and best fitted values for Vonk's theoretical correlation function (TCF) for sample A73522.

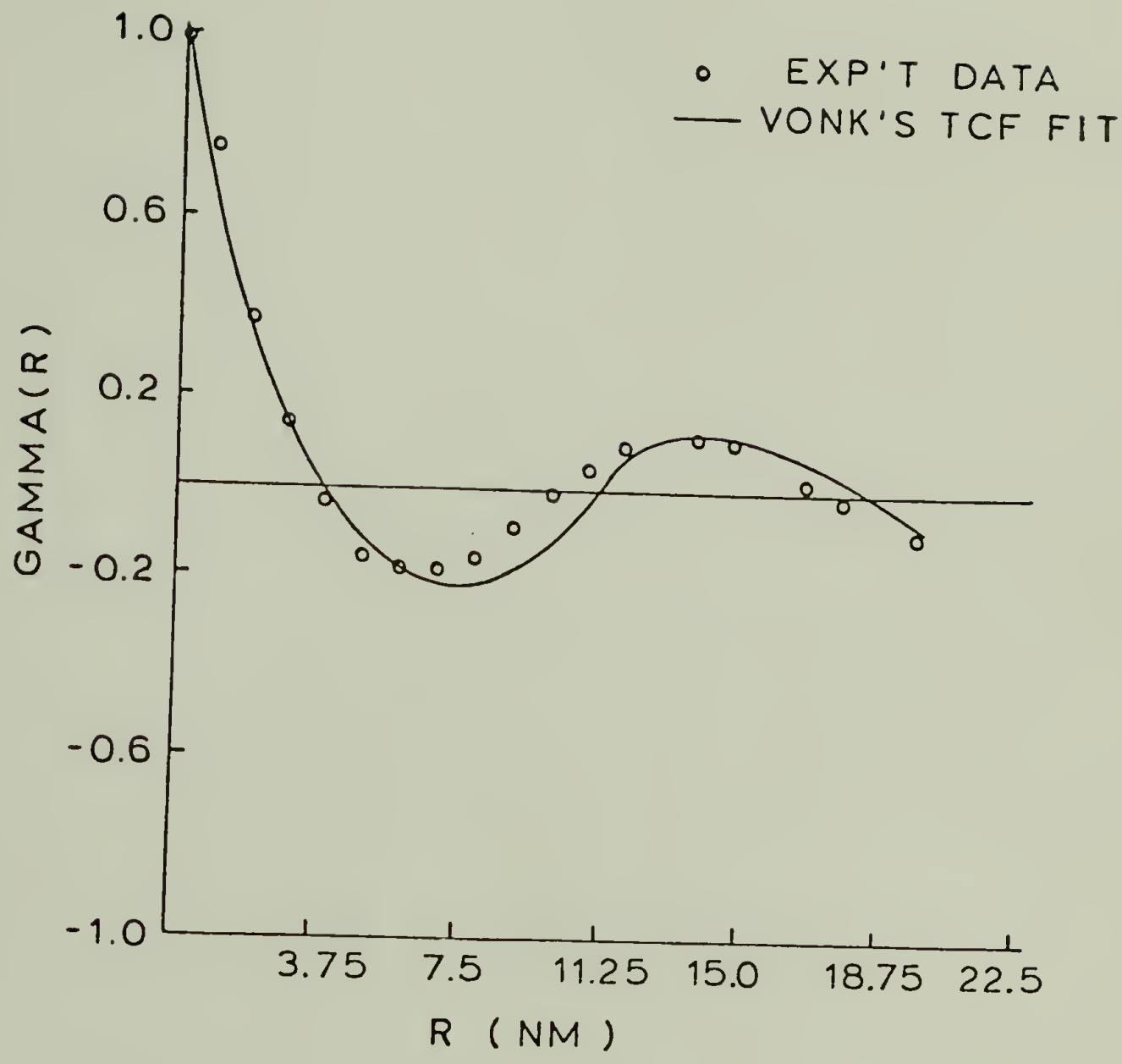

Figure 66. Comparison of experimental correlation function (open circles) and best fitted values for Vonk's theoretical correlation function (TCF) for sample B10000.

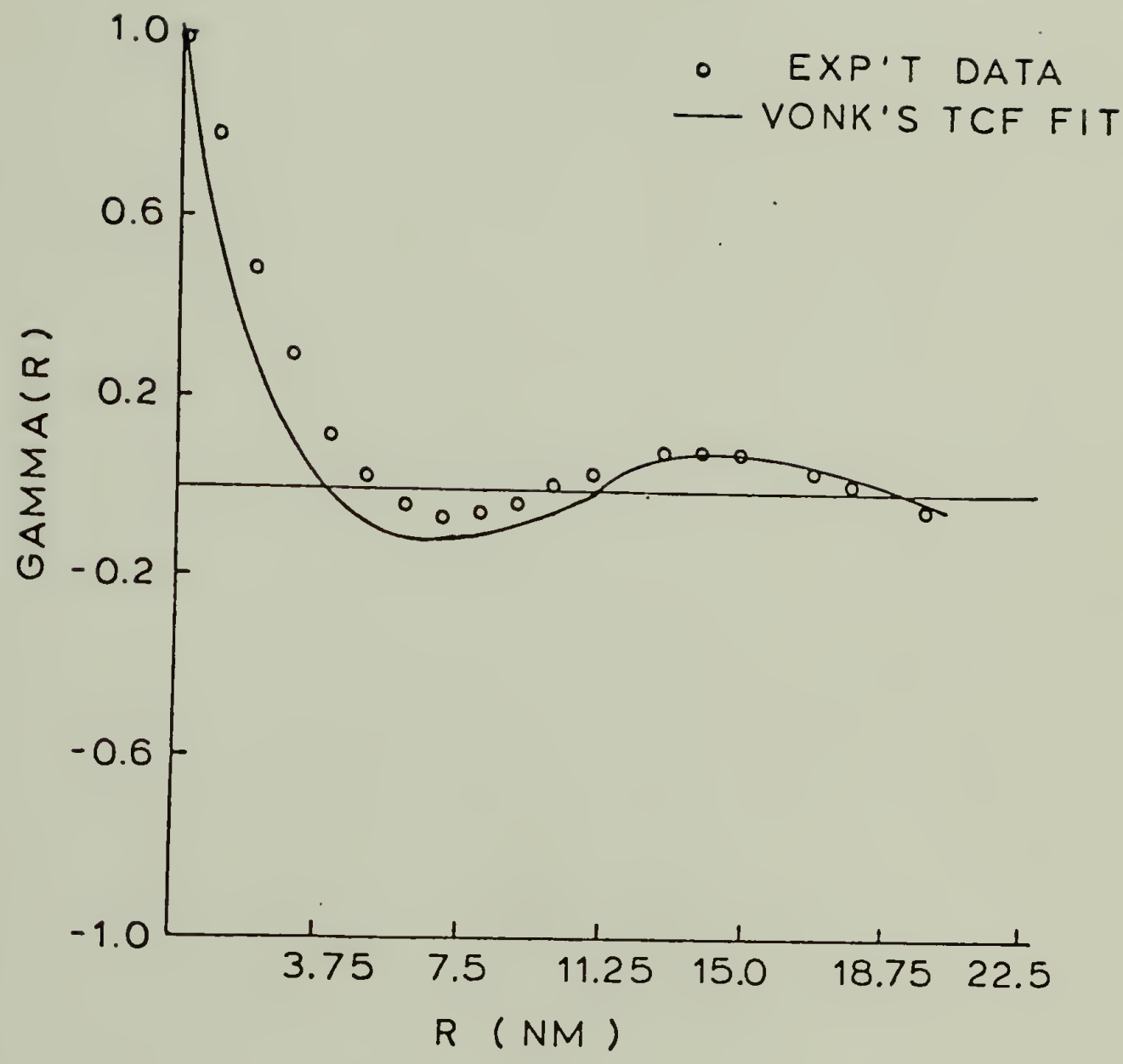

Figure 67. Comparison of experimental correlation function (open circles) and best fitted values for Vonk's theoretical correlation function (TCF) for sample B91111.

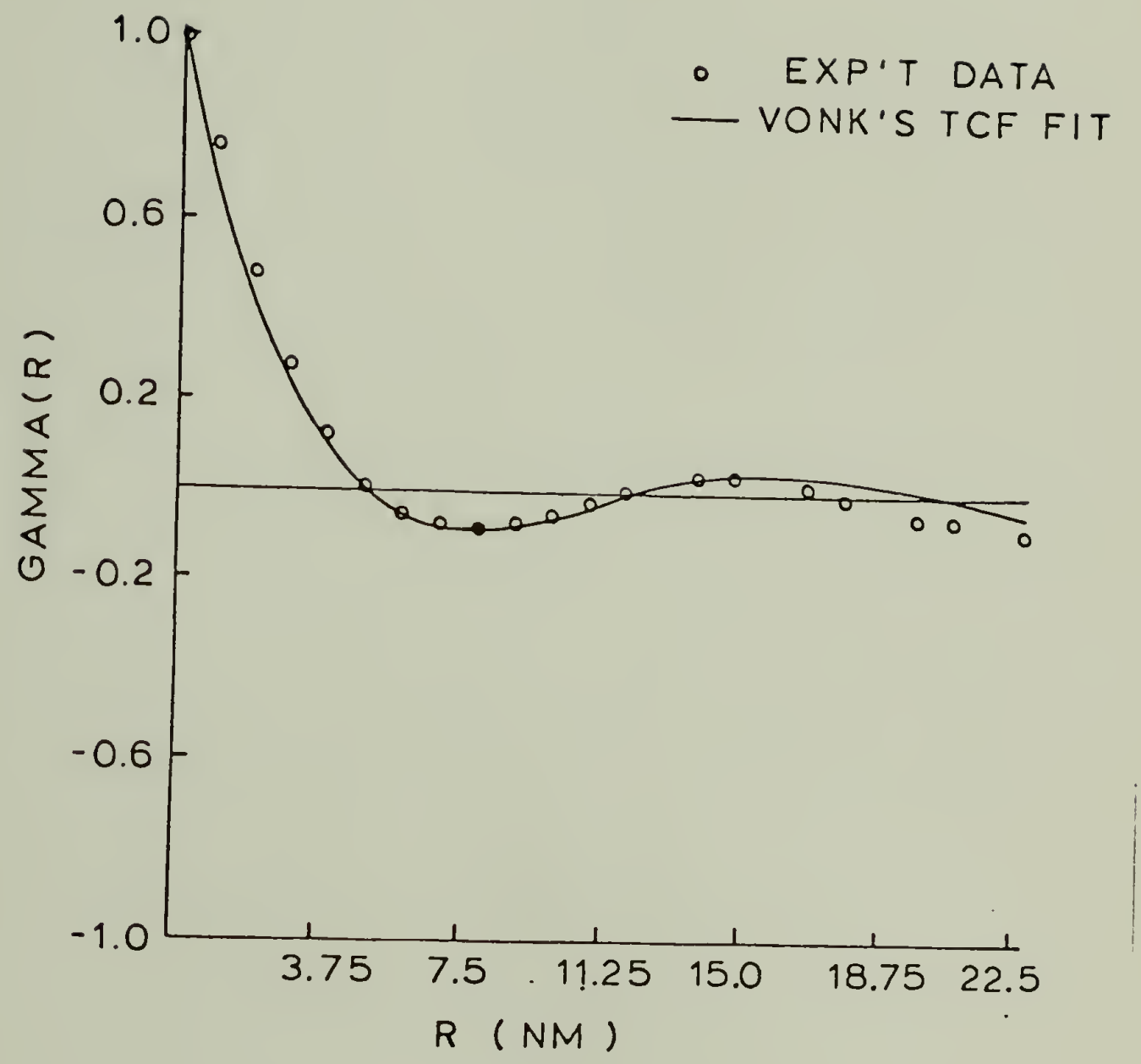

Figure 68. Comparison of experimental correlation function (open circles) and best fitted values for Vonk's theoretical correlation function (TCF) for sample B82111.

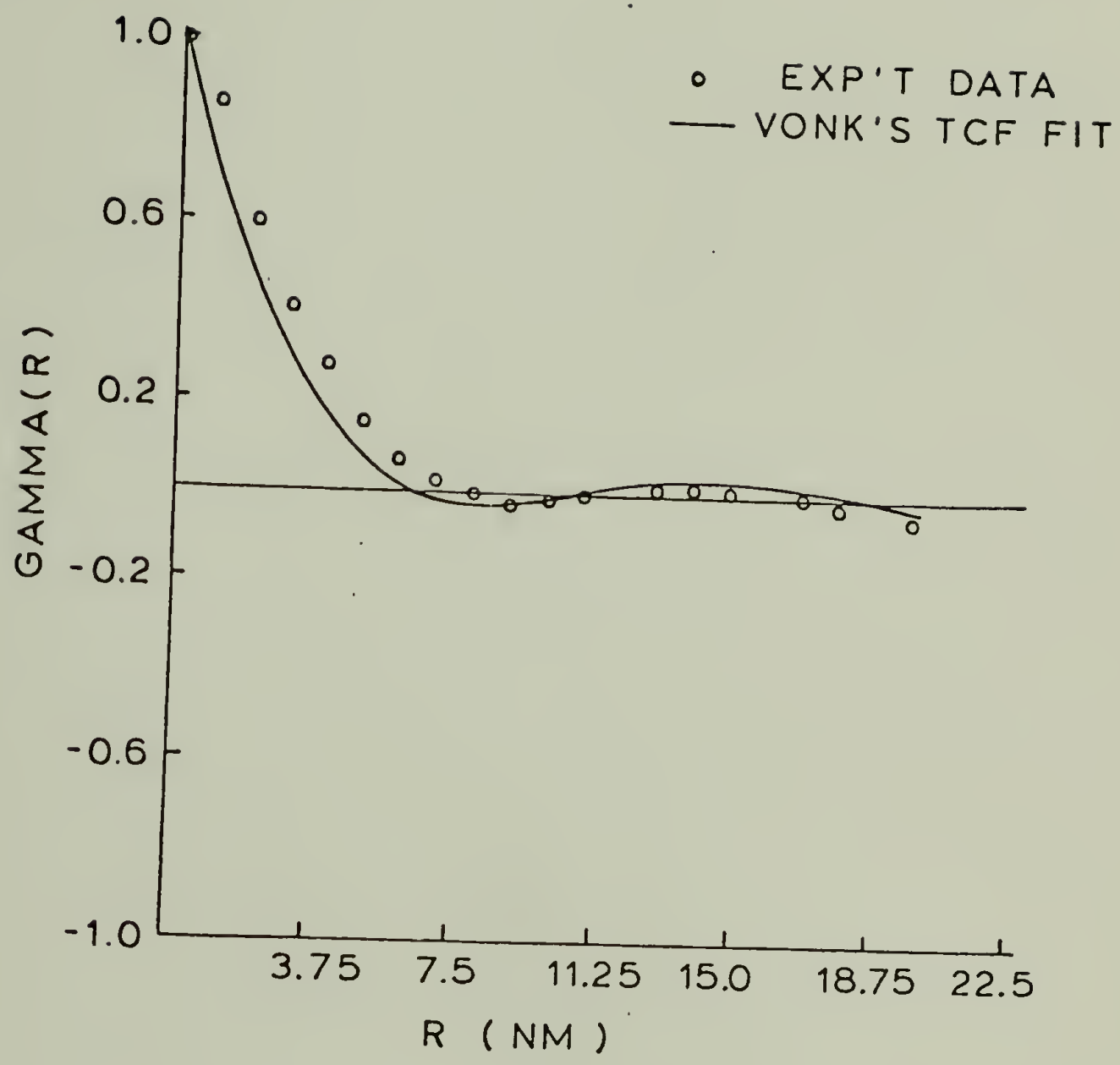

Figure 69. Comparison of experimental correlation function (open circles) and best fitted values for Vonk's theoretical correlation function (TCF) for sample B73111.

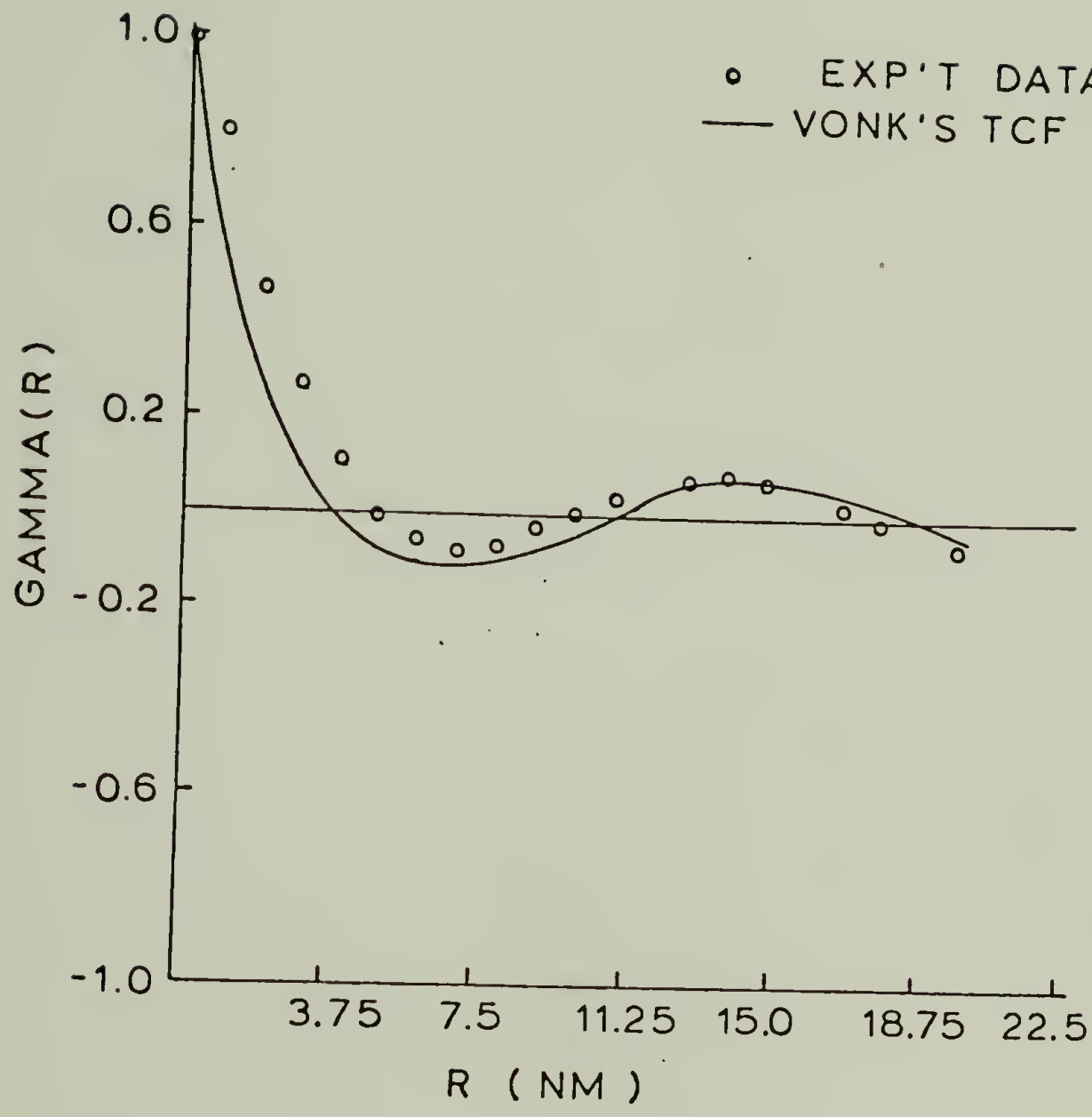

Figure 70. Comparison of experimental correlation function (open circles) and best fitted values for Vonk's theoretical correlation function (TCF) for sample B91522.

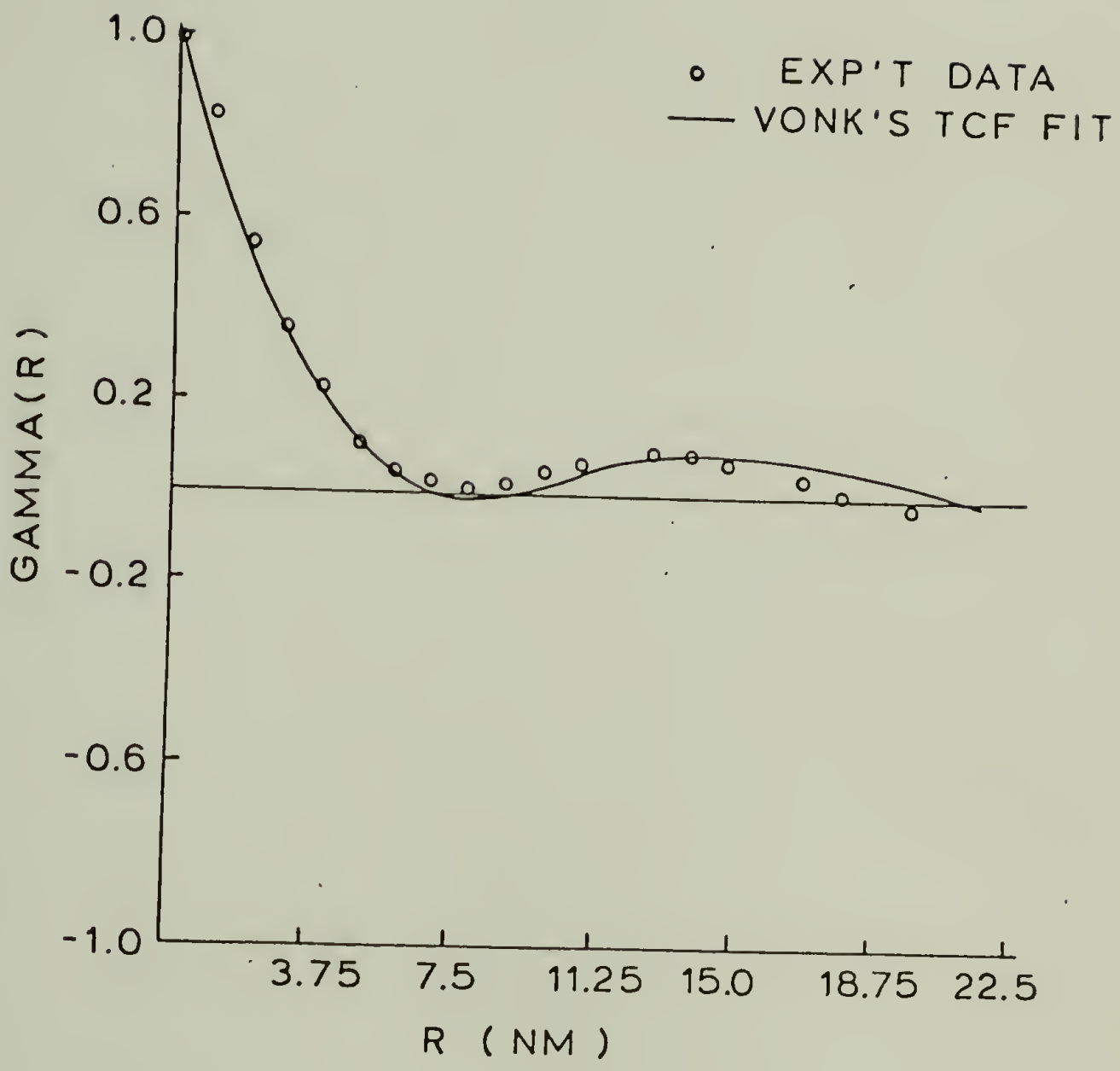

Figure 71. Comparison of experimental correlation function (open circles) and best fitted values for Vonk's theoretical correlation function (TCF) for sample B82522.

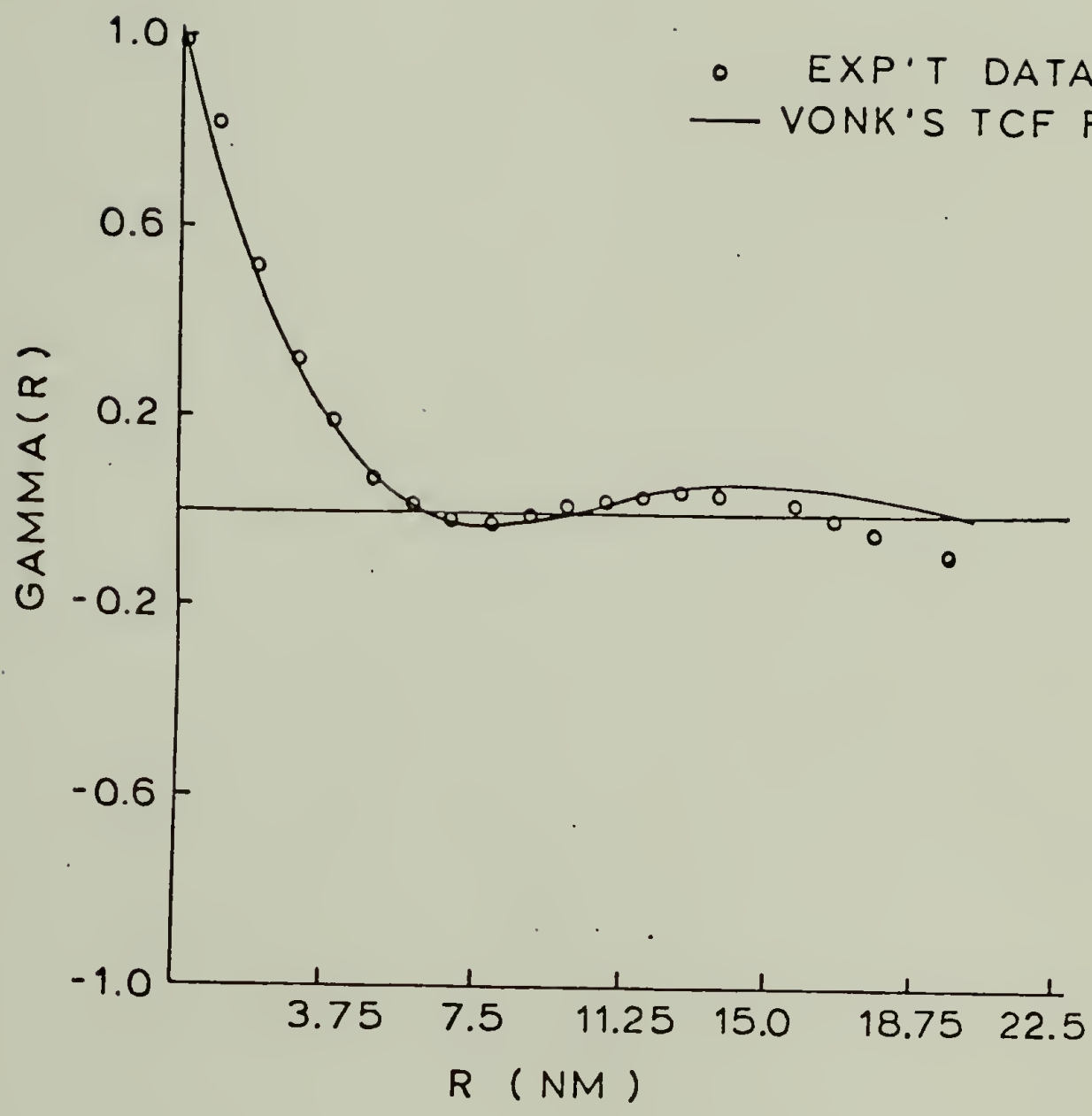

Figure 72. Comparison of experimental correlation function (open circles) and best fitted values for Vonk's theoretical correlation function (TCF) for sample B73522.

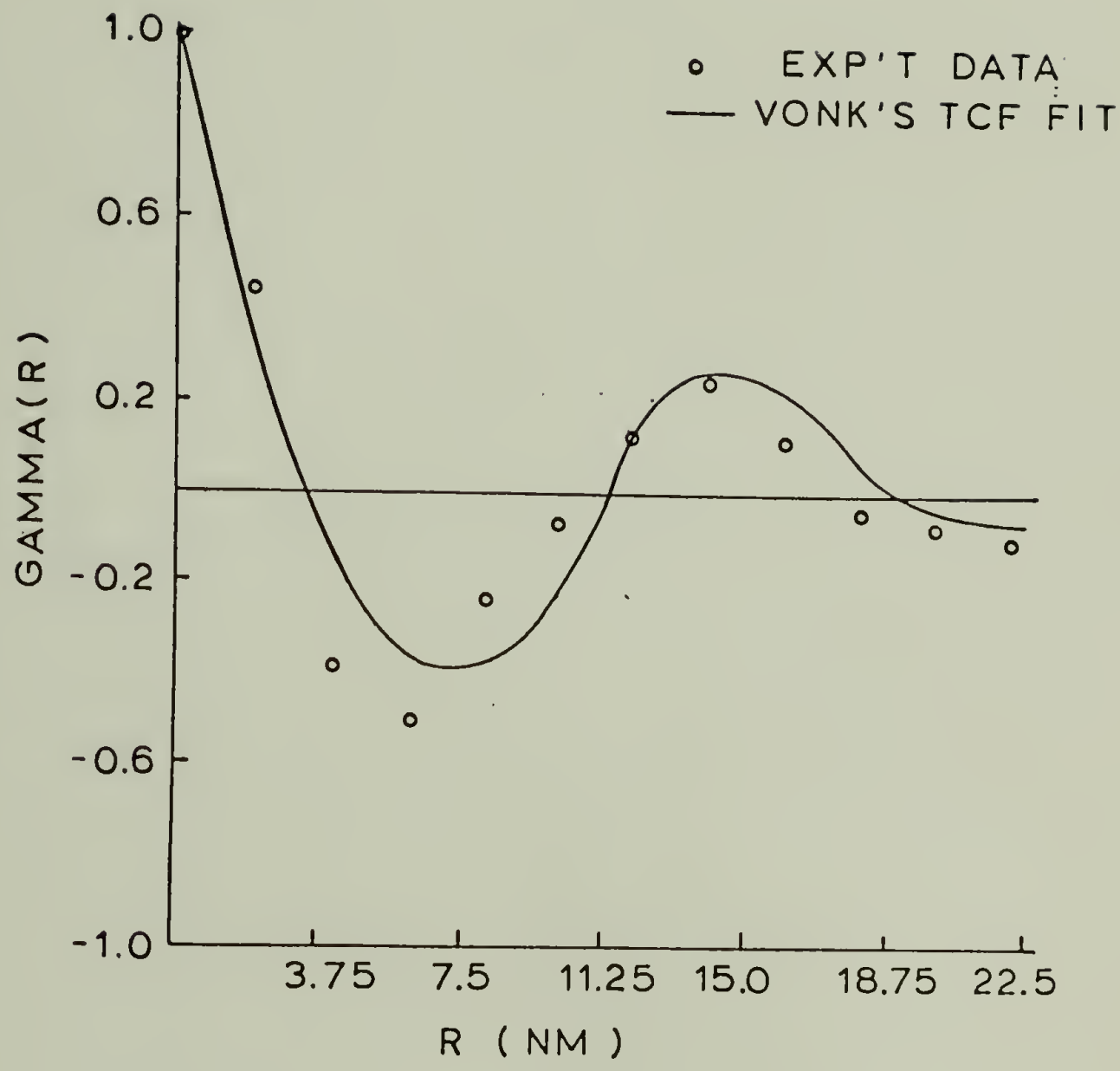

Figure 73. Comparison of experimental correlation function (open circles) and best fitted values for Vonk's theoretical correlation function (TCF) for sample C10000.

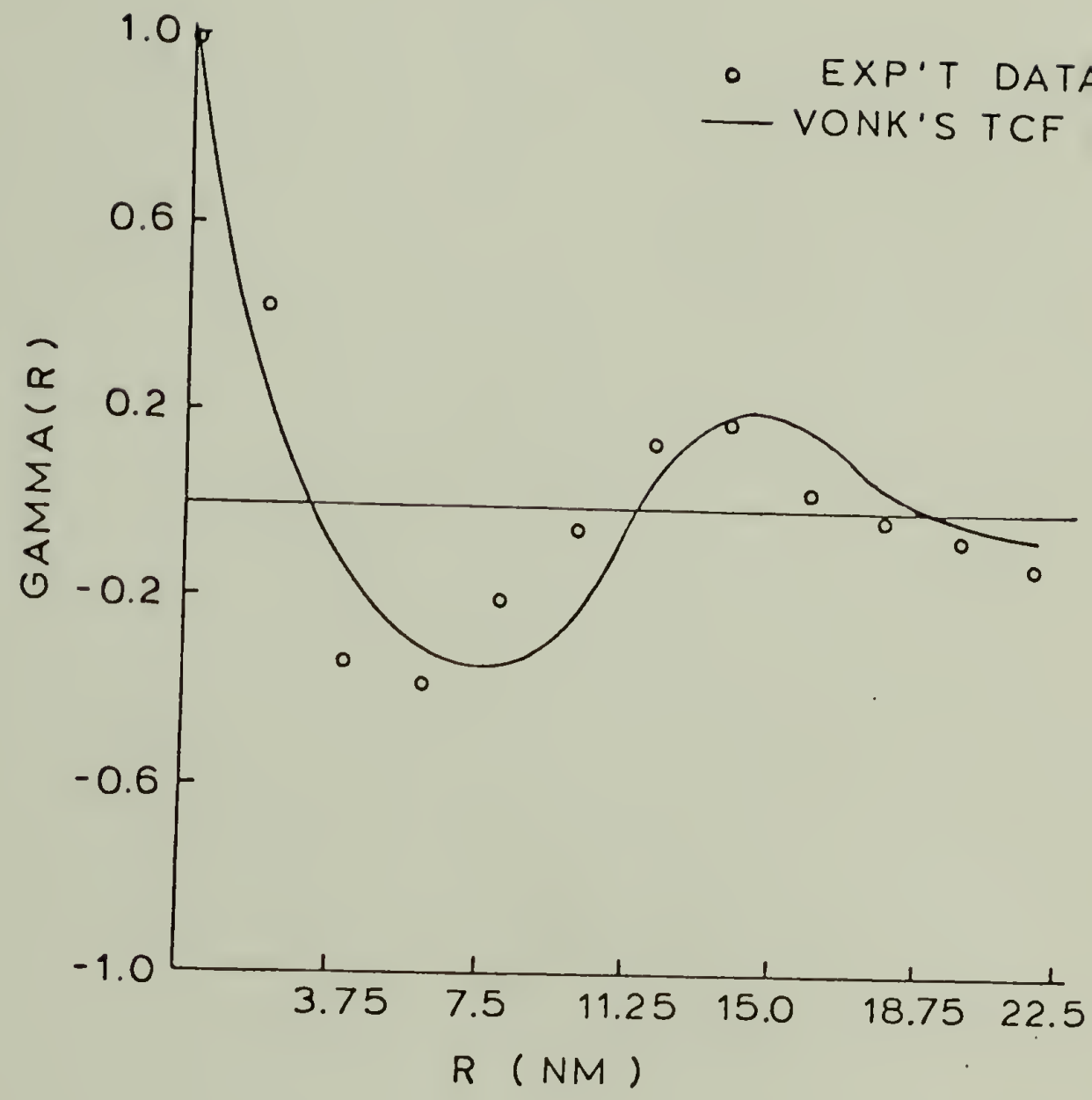

Figure 74. Comparison of experimental correlation function (open circles) and best fitted values for Vonk's theoretical correlation function (TCF) for sample C91111.

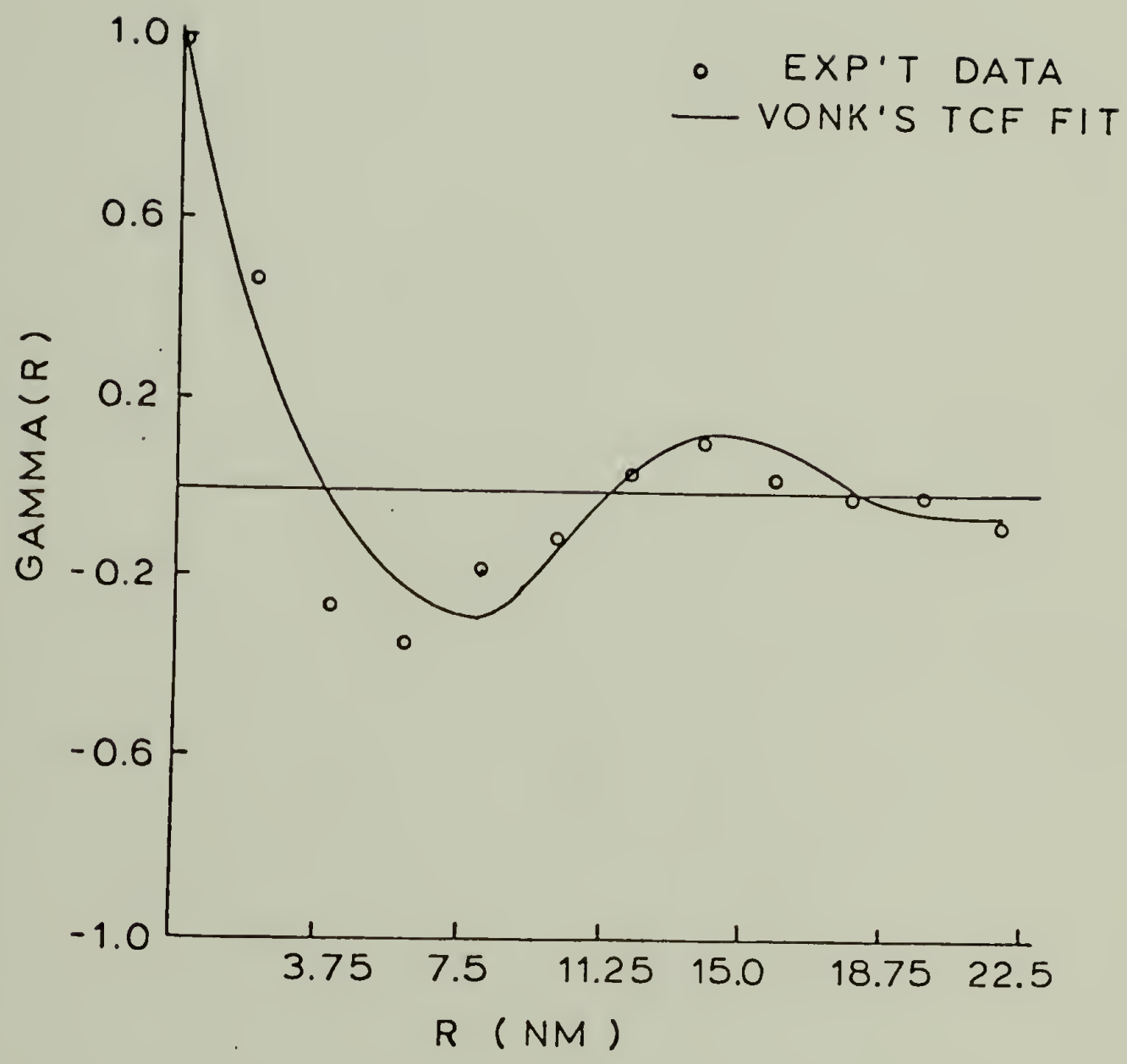

Figure 75. Comparison of experimental correlation function (open circles) and best fitted values for Vonk's theoretical correlation function (TCF) for sample C82111.

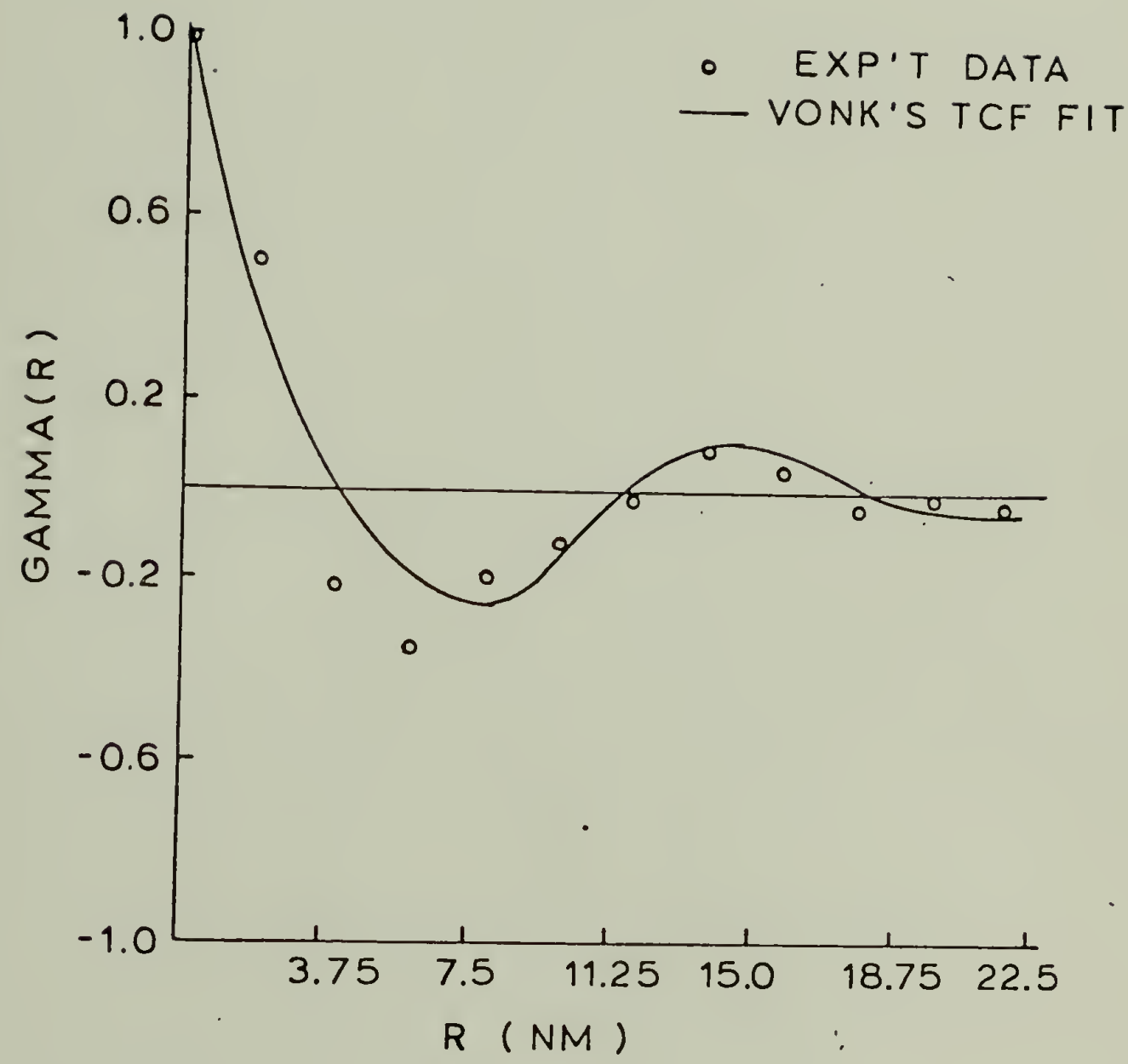

Figure 76. Comparison of experimental correlation function (open circles) and best fitted values for Vonk's theoretical correlation function (TCF) for sample C73111.

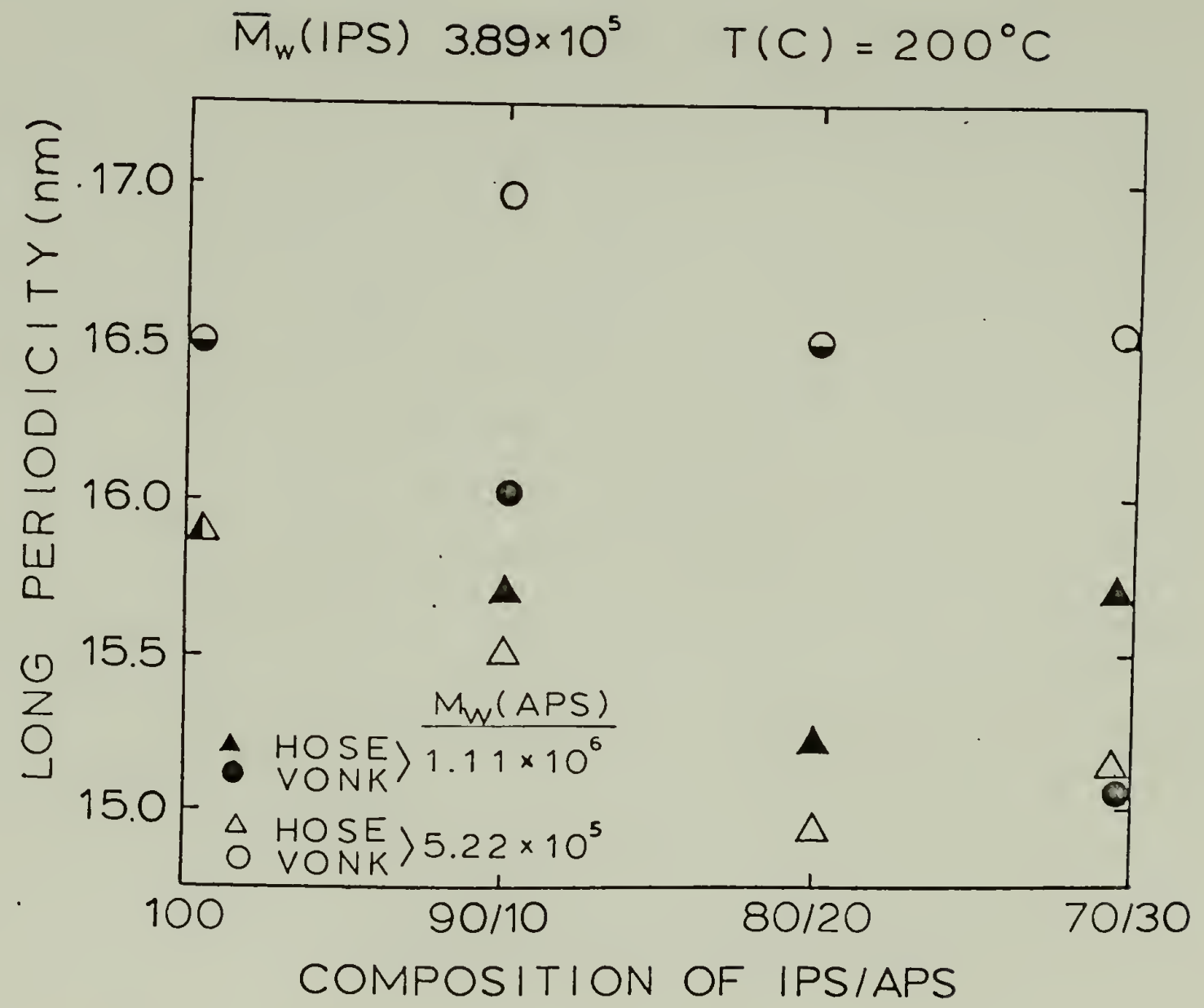

Figure 77. Comparison of values of long periodicity as calculated circles) from best Hosemann's fit and the correlation function.

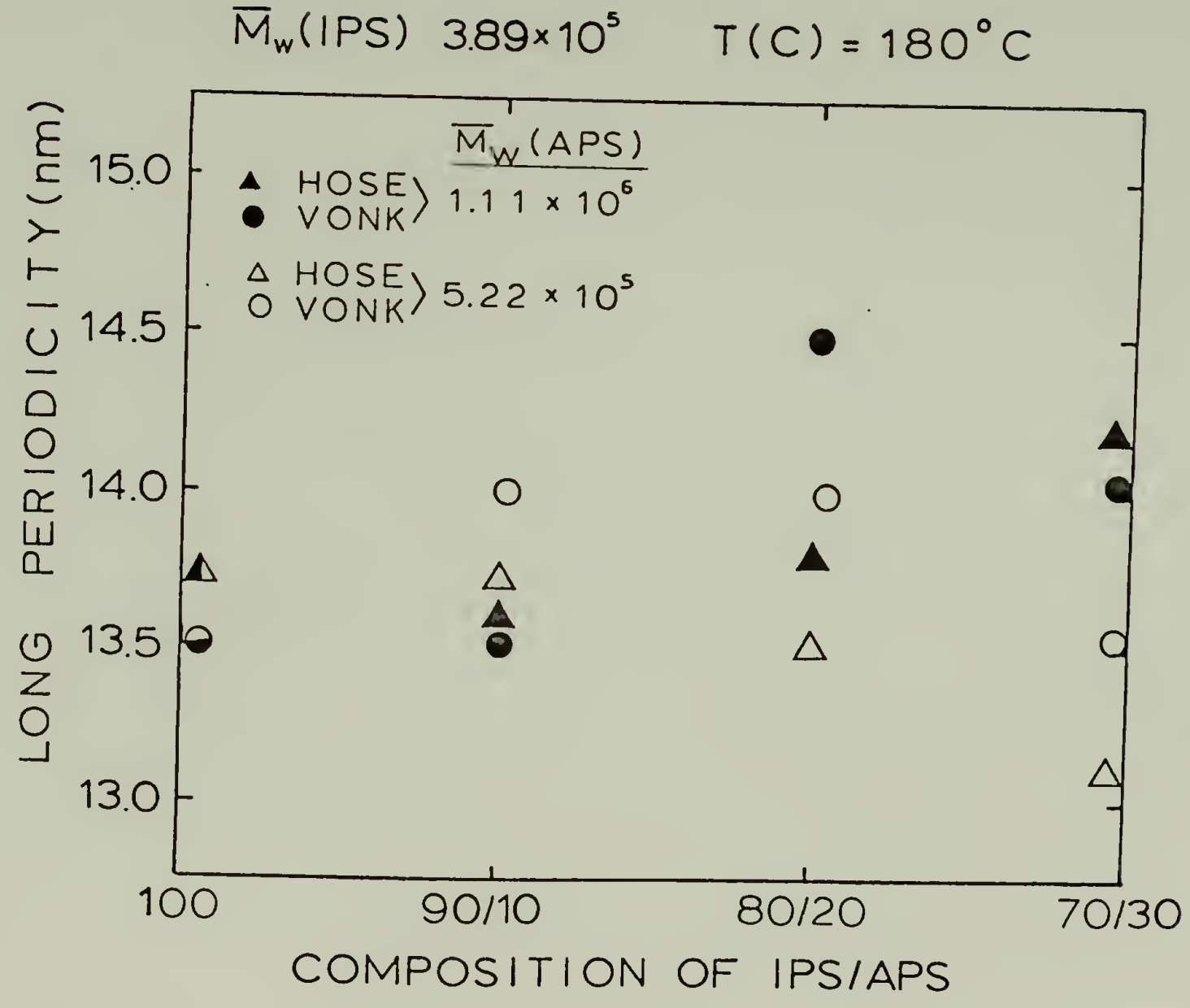

Figure 78. Comparison of values of long periodicity as calculated from best Hosemann's fit and the correlation function.

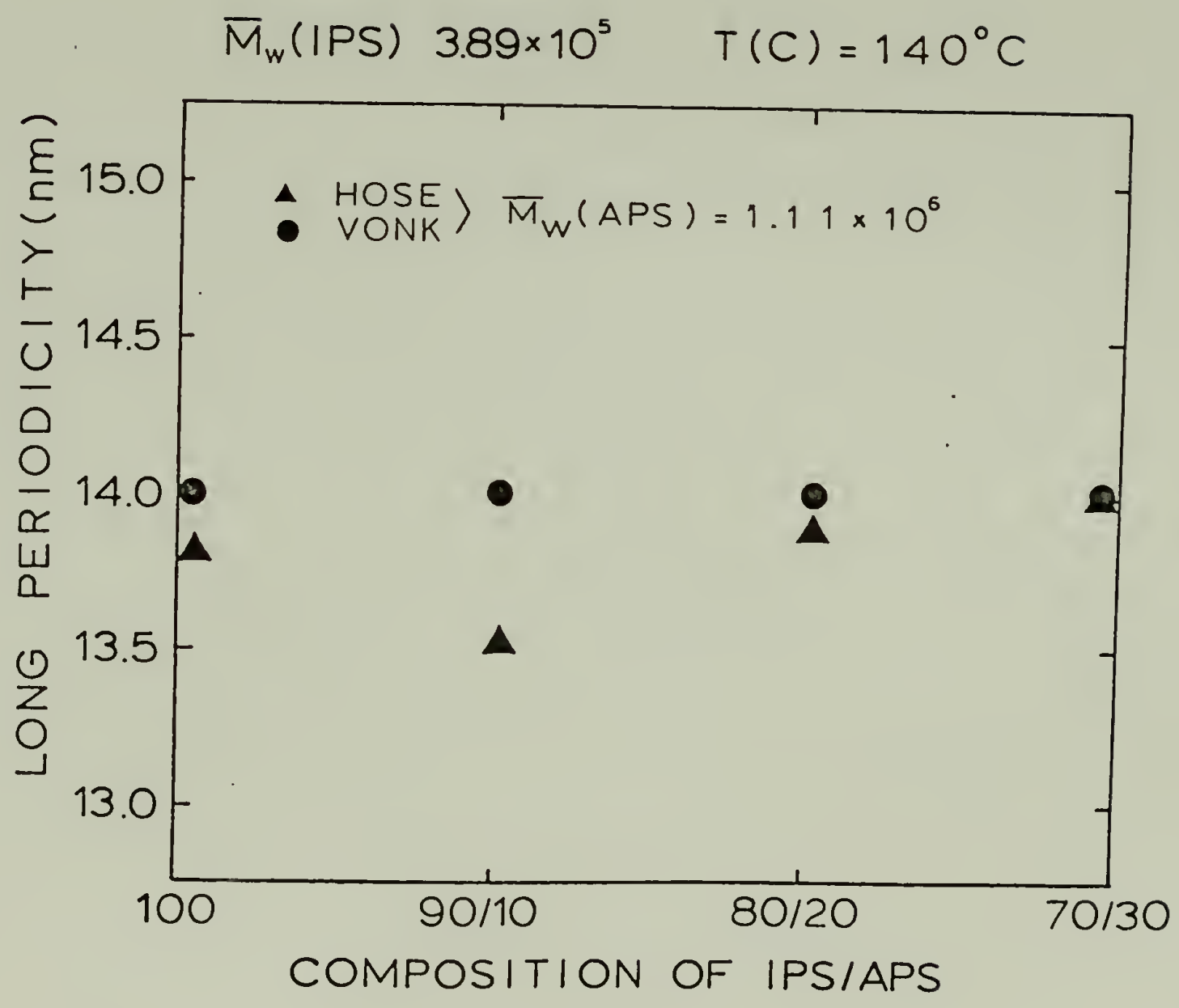

Figure 79. Comparison of values of long periodicity as calculated from best Hosemann's fit and the correlation function.

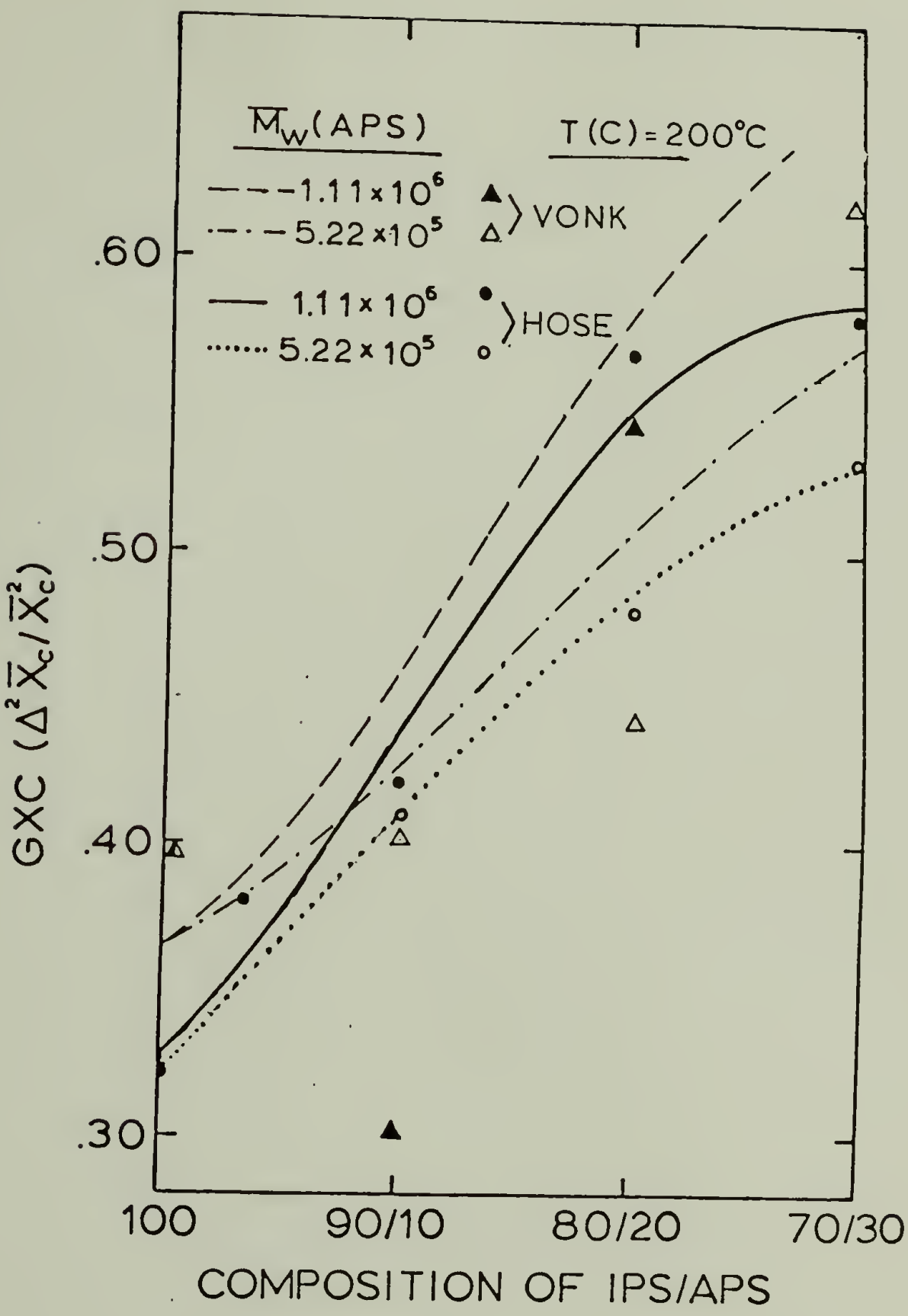

Figure 80. Comparison of Hosemann's and Vonk's model on the values of crystal thicknesses distribution.

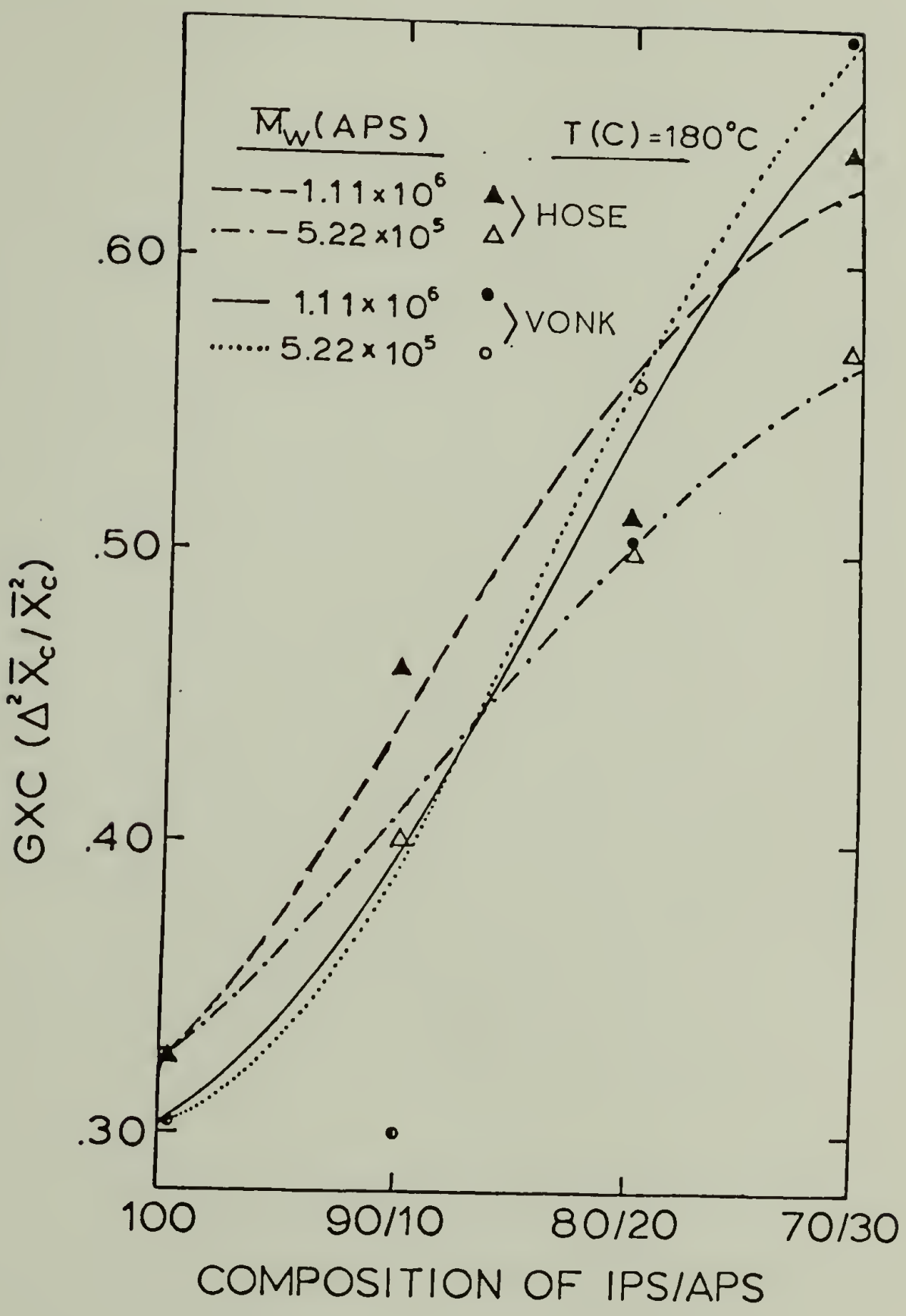

Figure 81. Comparison of Hosemann's and Vonk's model on the values of crystal thicknesses distribution.

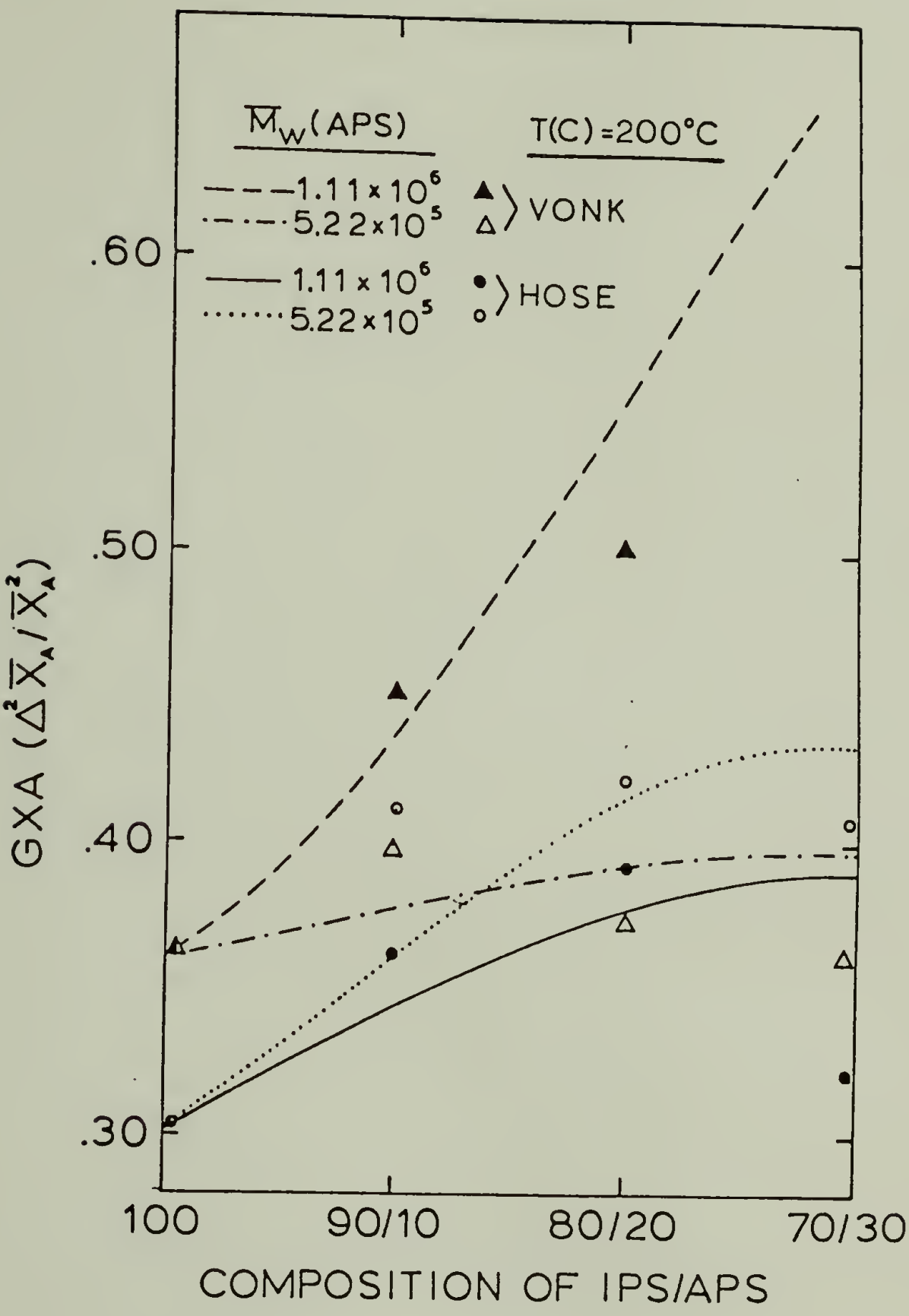

Figure 82. Comparison of Hosemann's and Vonk's model on values of the amorphous thicknesses distribution.

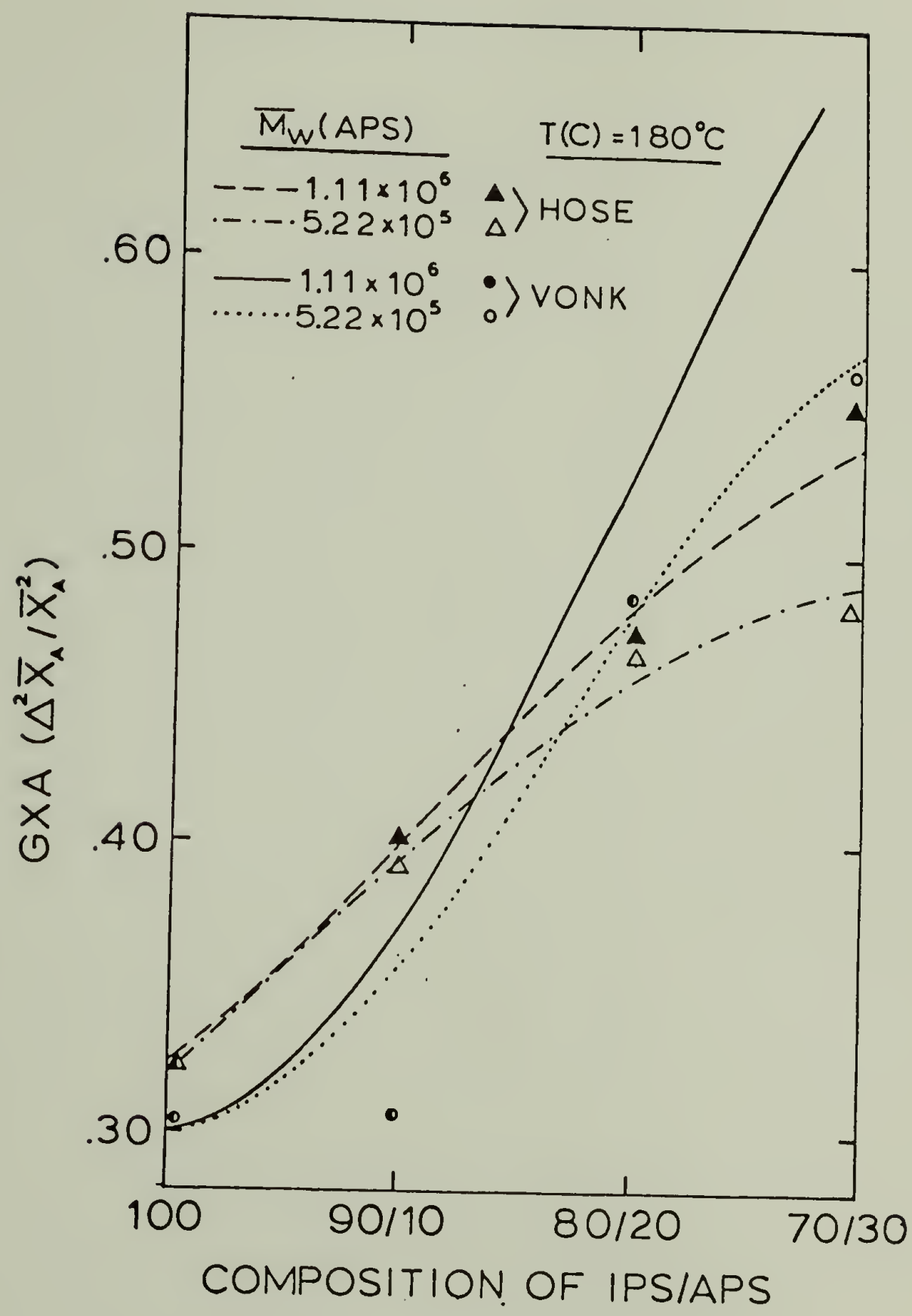

Figure 83. Comparison of Hosemann's and Vonk's model on values of the amorphous thicknesses distribution.

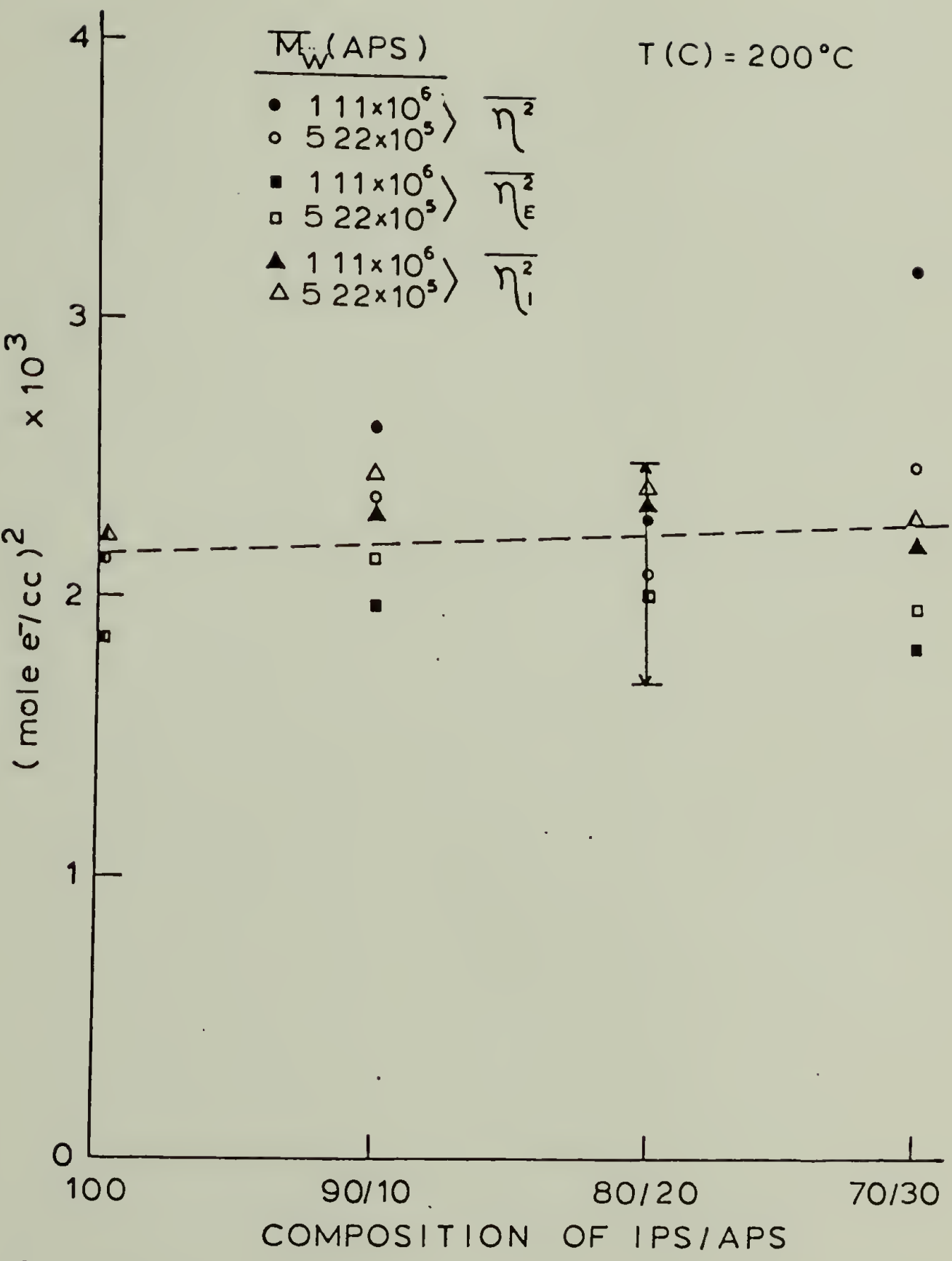

Figure 84. Comparison of the values of the experimental (η) and those calculated assuming a sharp interface (η_I) and a transition zone thickness (η_E).

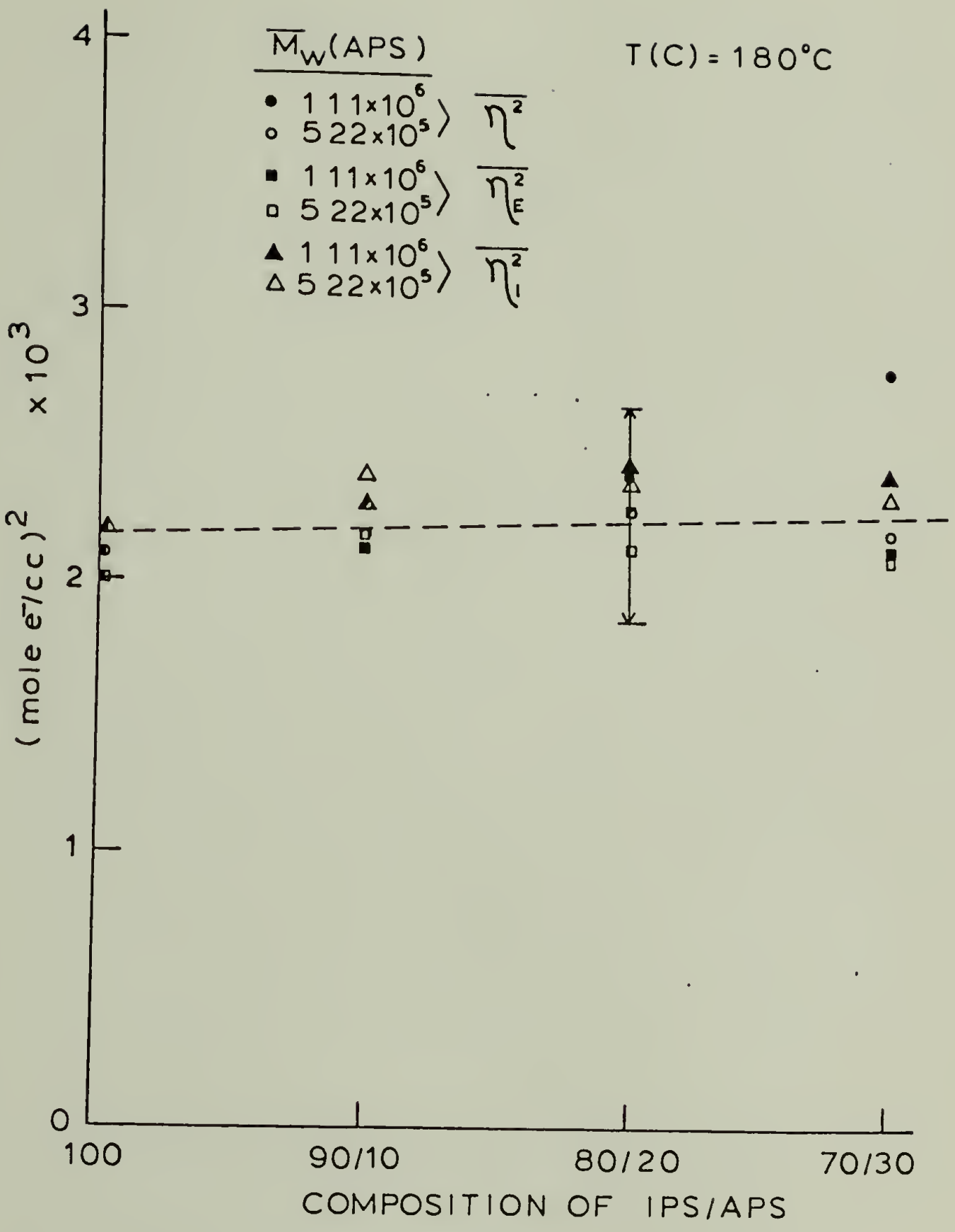

Figure 85. Comparison of the values of the experimental invariant (n) and those calculated assuming a sharp interface (n_I) and a transition zone thickness (n_E).

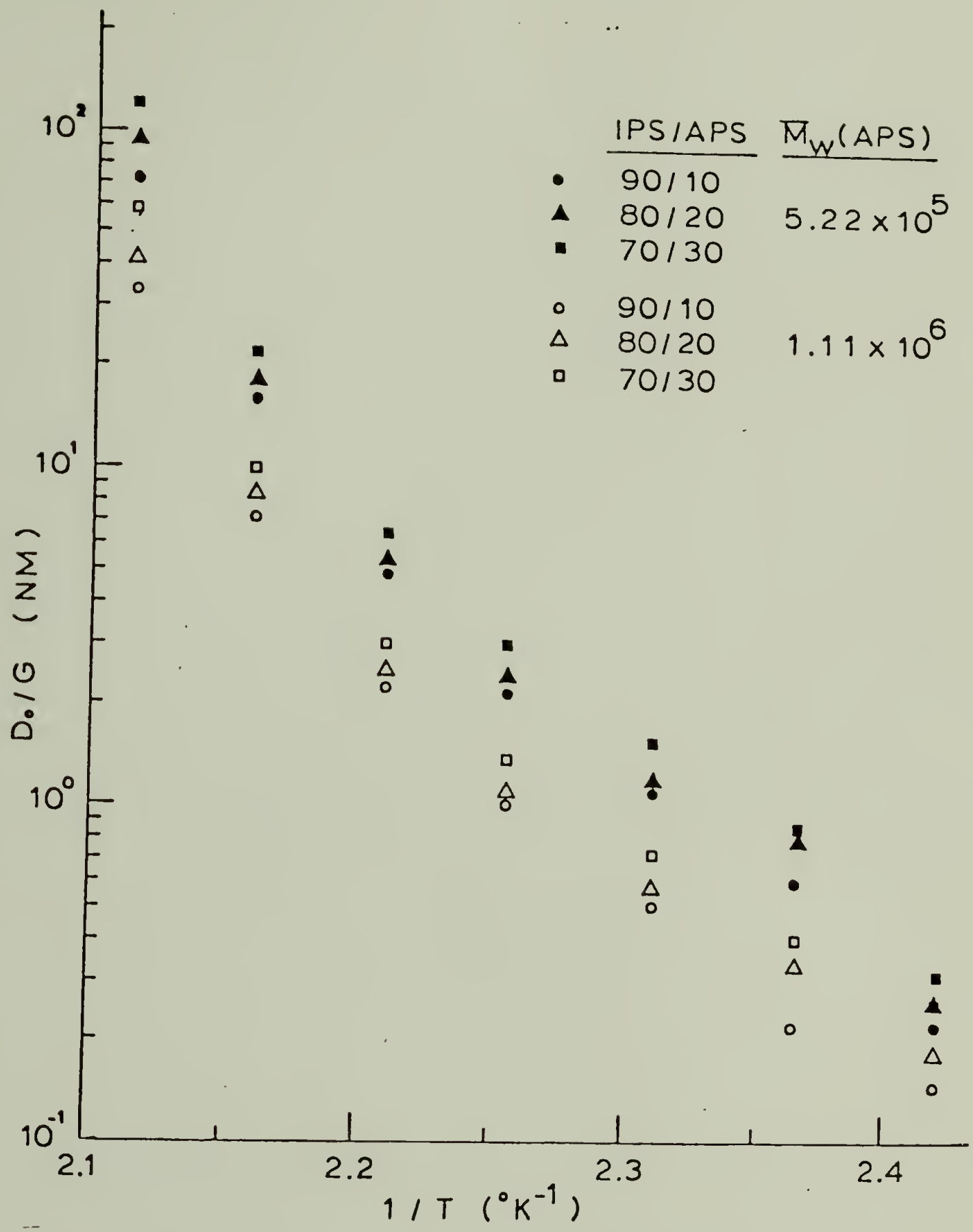

Figure 86. Theoretical values of the rejected specie dimension, as calculated by $\delta = D_o/G$.

SECTION I

REFERENCES

1. B. Wunderlich, Macromolecular Physics, Volume I, II, and III, Academic Press, New York, NY (1973).
2. J.A. Mansen and L.H. Sperling, Polymer Blends and Composites, Plenum Press, New York, NY (1976).
3. R.S. Stein, Polymer Blends, ed. by D.R. Paul and S. Newman, Academic Press, New York, NY (1978).
4. S.L. Cooper and G.M. Estes, ed., Multiphase Polymers (Adv. in Chem. Series No. 176) American Chemical Society, Washington, D.C. (1979).
5. N.A.J. Platzer, ed., Multicomponent Polymer Systems (Adv. in Chem. Series. No. 99) American Chemical Society, Washington, D.C. (1971).
6. N.A.J. Pltzer, ed., Copolymers, Polyblends and Composites (Adv. in Chem. Series No. 142) American Chemical Society, Washington, D.C. (1975).
7. S. Krause, J. Macromol. Sci., Rev. Macromol. Chem., C7, 251 (1972).
8. P.F. Bruins, ed., Polyblends and Composites (J. Appl. Polym. Sci., Appl. Polym. Symp. No. 15), Interscience, NY (1970).
9. A. Noshay and J.E. McGrath, Block Copolymers, Academic Press, NY (1977).
10. R.S. Stein, et al., J. Polym. Sci., Polym. Symp. 63, 313 (1978).
11. C.J. Ong, Ph.D. Thesis, University of Massachusetts, Amherst, MA (1974).

12. C.J. Ong and F.P. Price, J. Polym. Sci., Symp. Ser. 63, (1978).

13. F.B. Khambatta, Ph.D. Thesis, University of Massachusetts, Amherst, MA (1976).

14. F.B. Khambatta, T. Russell, F. Warner, and R.S. Stein, J. Polym. Sci., Polym. Phys. Ed., 14, 1391 (1976).

15. T. Russell, Ph.D. Thesis, University of Massachusetts, Amherst, MA (1979).

16. F.E. Karasz, W.J. MacKnight, and P. Alexandrovich, J. Macromol. Sci.-Phys. Ed., B17, 501 (1980).

17. C. Ryan, Ph.D. Thesis, University of Massachusetts, Amherst, MA (1979).

18. F.E. Karasz, W.J. MacKnight, and J. Stoelting, J. Appl. Phys., 41, 4357 (1970).

19. F.E. Karasz, W.J. MacKnight, and J. Stoelting, Polym. Eng. Sci., 10, 133 (1970).

20. A.R. Schultz and B.M. Gendron, J. Appl. Polym. Sci., 16, 461 (1972).

21. D.J. Meier, J. Polym. Sci., Part C, 26, 81 (1969).

22. G. Holden, E.T. Bishop, and N.R. Legge, J. Polym. Sci., Part C, 26, 37 (1969).

23. T.K. Kwei, T. Nishi and R.F. Roberts, Macromol., 7, 667 (1974).

24. T. Nishi and T.K. Kwei, Polymer, 16, 285 (1975).

25. M. Bank, J. Leffingwell, and C. Thies, Macromol., 4, 43 (1970).

26. B. Morra, Ph.D. Thesis, University of Massachusetts, Amherst, MA (1980).

27. T. Nishi and T.T. Wang, Macromol. 8, 909 (1975).

28. J.H. Wendorff, J. Polym. Sci., Polym. Lett. Ed., 18, 439 (1980).

29. H.D. Keith and F.P. Padden, J. Appl. Phys., 35, 1270 (1964), 1286 (1964).

30. W. Wenig, F.E. Karasz, and W.J. MacKnight, J. Appl. Phys., 46, 4194 (1975).

31. A. Escala, Ph.D. Thesis, University of Massachusetts, Amherst, MA (1978).

32. P. Young and R.S. Stein, in preparation.

33. D.C. Bassett and A.M. Hodge, Proc. Royal Soc. London, A377, 61 (1981).

34. D.C. Bassett and A.M. Hodge, Proc. R. Soc. Lond., A359, 121 (1978).

35. P.V. Papero, E. Kuba, and L. Roldan, J. Text. Res., 37, 823 (1967).

36. L.E. Nielsen, Mechanical Properties of Polymers, Reinhold Pub. Co., New York, NY (1962).

37. J. Boon and J.M. Azcue, J. Polym. Sci., Part A-2, 6, 885 (1968).

38. A.V. Tobolsky, Properties and Structures of Polymers, Wiley, New York, Ny (1960)

39. M. Takayanagi, H. Harima, and Y. Iwata, Mem. Fac. Eng., Kyushi Univ., 23 1 (1963).

40. T. Horino, Y. Ogawa, T. Soen, and H. Kawai, J. Appl. Polym. Sci. 9, 2261 (1965).

41. K.T. Chiang and M.V. Sefton, J. Polym. Sci., Polym. Phys. Ed., 15, 1927 (1977).

42. S. Manabe, R. Murakami, M. Takayanagi, Mem. Fac. Eng., Kyushu Univ., 28, 295 (1969).

43. D.J. Massa, private communication.

44. E.J. Perry, J. Appl. Polym. Sci., 8, 2605 (1964).

45. L.J. Hughes and G.L. Brown, J. Appl. Polym. Sci., 5, 580 (1961).

46. C.W. Frank and M.A. Gashgari, Macromol., 12, 163 (1979).

47. S.N. Semerak and C.W. Frank, Macromol., 14, 443 (1981).

48. R.S. Stein, "Proceedings of China-U.S. Bilateral Symposium on Polymer Chemistry and Physics", L. Hun Ed. Pub., New York, NY (1981).

49. R.S. Stein, G. Hadziioannou, M. Wai, J. Gilmer, F. Herold, and B. Morra, Polymer Preprint, Am. Chem. Soc., August 1981.

50. J.W. Cahn, J. Chem. Phys., 42, 93 (1965).

51. J.W. Cahn and J.E. Hilliard. J. Chem. Phys., 31, 6881 (1959).

52. J.S. Langer, Ann. Phys., 65, 53 (1971).

53. H.E. Cook, Acta. Metall., 18, 297 (1970).

54. G.S.Y. Yeh and S.L. Lambert, J. Polym. Sci. Pt. A-2, 10, 1183 (1972).

55. J. Gilmer and N. Goldstein, private communication.

56. R.S. Stein, T. Russell, and J. Koberstein, J. Polym. Sci., Polym. Phys. Ed., 17, 1719 (1979).

57. J.P. Cotton, D. Decker, H. Benoit, B. Farnoux, J. Higgins, G. Jannink, R. Ober, C. Picot, and J. des Cloizeaux, Macromol., 7, 863 (1974).

58. R.G. Kirste, W.A. Kruze, and J. Schelten, Makromol. Chem., 162, 299 (1972).

59. G.D. Wignall, D.G.H. Ballard, and J. Schelten, Eur. Polym. J., 10, 861 (1974).

60. J.M. Guenet, C. Picot, and H. Benoit, Macromol., 12, 86 (1979).

61. J. Schelten, G.D. Wignall, and D.G.H. Ballard, Polymer, 15, 682 (1974).

62. G. Lieser, E.W. Fisher and K. Ibel, J. Polym. Sci., 13, 39 (1975).

63. J. Schelten, G.D. Wignall, D.G.H. Ballard, G.W. Longman, and W. Schmatz, Polymer, 17, 751 (1976).

64. J. Schelten, G.D. Wignall, D.G.H. Ballard, and G.W. Longman, Polymer, 18, 1111 (1977).

65. M. Dettenmaier, E.W. Fischer, and M. Stamm, Colloid and Polym. Sci., 258, 243 (1980).

66. D.G.H. Ballard, M. Rayner, and J. Schelten, Polymer, 17, 349 (1976).

67. G.D. Wignall, H.R. Child, and F. LiAravena, Polymer, 21, 131 (1980).

68. R.P. Kambour, R.C. Bopp, A. Maconnachie, and W.J. MacKnight, Polymer, 21, 133 (1980).

69. G. Natta, Makromol. Chem., 16, 77 (1955).

70. A.S. Kenyon, R.C. Gross, A.L. Wurstner, J. Polym. Sci., 15, 159 (1959).

71. D. Turnbull and J.C. Fisher, J. Chem. Phys., 17, 71 (1949).

72. B. Burnett and W. McDevit, J. Appl. Phys., 28, 1101 (1957).

73. J. Boon, G. Challa, D.W. VanKrevelen, J. Polym. Sci., Part A-2, 6, 1791 (1968).

74. J.D. Hoffmann and J.J. Weeks, J. Chem. Phys., 37, 1723 (1962).

75. J.J.B.P. Blais and R. St. John Manley, J. Macromol. Sci. Phys., B1 (3), 525 (1967).

76. B.C. Edward and P.J. Phillips, Polymer, 15, 351 (1974).

77. J.N. Hay, J. Polym. Sci., Part A, 3, 433 (1965).

78. J. Boon, G. Challa, D.W. VanKrevelen, J. Polym. Sci., Part A-2, 6, 1835 (1968).

79. P.J. Lemstra, T. Kooistra, G. Challa, J. Polym. Sci., Part A-2, 10, 823 (1968).

80. P.J. Lemstra, A.J. Schouten, G. Challa, J. Polym. Sci.-Polym. Phys. Ed., 12, 1565 (1974).

81. N. Overbergh, H. Berghmans, G. Smets, J. Polym. Sci., Part C, 38, 237 (1972).

82. N. Overbergh, H. Berghmans, H. Raynaers, J. Polym. Sci.-Polym. Phys. Ed., 14, 1177 (1976).

83. J. Petermann and R.M. Gohil, J. Macromol. Sci.-Phys., B16(2), 177 (1979).

84. H.D. Keith and F.P. Padden, J. Appl. Phys., 34, 2409 (1963).

85. F.P. Warner, W.J. MacKnight, and R.S. Stein, J. Polym. Sci.-Polym. Phys. Ed., 15, 2113 (1977).

86. J.M. Guenet, Ph.D. Thesis, Strasbourg, France (1980).

87. L.E. Alexander, X-Ray Diffraction Methods in Polymer Science, Wiley, New York, NY (1969).

88. R. Hosemann and S.N. Bagchi, Direct Analysis of Diffraction by Matter, North-Holland Pub. Co., Amsterdam, Holland, 1962.

89. R.S. Stein, Rubber Chemistry and Technology, 49, 458 (1976).

90. A. Guinier and G. Fournet, Small Angle Scattering of X-Rays, Wiley, New York, NY 1955).

91. R.S. Stein and J.S. Higgins, J. Appl. Cryst., 11, 346 (1978).

92. Lord Rayleigh, Proc. Roy. Soc. London, A90, 219 (1914).

93. G. Fournet, Bull. Sco. France, Mineral, et Crist., 74, 39 (1949).

94. T. Neugebauer, Ann. Physik, 42, 509 (1943).

95. O. Kratky and G. Porod, J. Colloid Sci., 4, 35 (1949).

96. P. Debye, J. Appl. Crystallogr., 15, 338 (1944).

97. P. Debye, H.R. Anderson, and H. Bramberger, J. Appl. Phys., 28, 679 (1957).

98. O. Kratky, Pure and Appl. Chem., 12, 483 (1966).

99. G. Porod, Kolloid Z., 124, 83 (1951); 125, 51 (1952); 125, 108 (1952).

100. D. Buchanan, J. Polym. Sci., Part A-2, 9, 645 (1971).

101. C. Vonk and G. Kortleve, Kolloid Z.Z. Polym., 220, 19 (1967); 224, 124 (1968).

102. B. Crist and N. Morosott, J. Polym. Sci.-Polym. Phys. Ed., 11, 1023 (1973).

103. D. Caulfield and R. Ullman, J. Appl. Phys. 33, 1737 (1962).

104. F.P. Warner, Ph.D. Dissertation, Univ. of Loughborough, England (1975).

105. F.P. Warner, D.S. Brown, R.E. Wetton, Faraday Trans. I., 72, 1064 (1976).

106. D.S. Brown, K.U. Fulcher, R.E. Wetton, Polymer, 1, 379 (1973).

107. S.K. Baczek, Ph.D. Dissertation, University of Massachusetts, Amherst, MA (1977).

108. W. Ruland, Colloid and Polym. Sci., 225, 29 (1977).

109. J.T. Koberstein, B. Morra, and R.S. Stein, J. Appl. Cryst., 13, 34 (1980).

110. W. Ruland, J. Appl. Cryst., 4, 70 (1971).

111. R. Bonart and E.H. Muller, J. Macromol. Sci.-Phys., B10(1), 177 (1974).

112. T. Hashimoto, A. Todo, H. Itoi, and H. Kawai, Macromol., 10, 377 (1977).

113. C.G. Vonk, J. Appl. Cryst., 6, 81 (1973).

114. J. Rathje and W. Ruland, Colloid Polym. Sci., 254, 358 (1976).

115. W. Wiegand and W. Ruland, Prog. Colloid Polym. Sci., 66, 355 (1979).

116. O. Kratky, I. Pilz, and P.J. Schmitz, J. Colloid and Inter. Sci., 21, 24 (1966).

117. I. Pilz and O. Kratky, J. Colloid and Inter. Sci., 24, 211 (1967).

118. O. Kratky, Makromol. Chem., 35A, 12 (1960).

119. R. Hendricks, J. Appl. Cryst., 5, 315 (1972).

120. I. Pilz, J. Colloid and inter. Sci., 30, 141 (1969).

121. R. Hendericks, J. Appl. Cryst., 11, 15 (1978).

122. General Information and Guide for the Neutron and X-Ray Facilities of the National Center for Small Angle Scattering Research, Oak Ridge National Laboratory, Oak Ridge, NY, May 1980.

123. A. Guinier and G. Fournet, J. Phys. Rad., 8, 345 (1947).

124. R. Hendricks and P. Schmidt, Acta. Phys. Austr., 26, 97 (1967).

125. M.G. Buchanan and R.W. Hendricks, J. Appl. Cryst., 4, 176 (1971).

126. R.W. Hendricks and P. Schmidt, Acta. Phys. Austr., 37, 20 (1973).

127. J.A. Lake, Acta. Cryst., 23, 191 (1967).

128. P. Schmidt, Acta. Cryst., 19, 938 (1965).

129. P. Schmidt, J. Appl. Cryst., 3, 137 (1970).

130. M. Deutsch, Comp. Phys. Comm., 17, 337 (1979); 17, 345 (1978); 18, 143 (1979); 18, 149 (1979).

131. O. Glatter and P. Zipper, Acta. Phys. Austr., 43, 347 (1975).

132. O. Glatter, J. Appl. Phys., 7, 147 (1974).

133. C.G. Vonk, J. Appl. Cryst., 4, 340 (1971).

134. C.G. Vonk, J. Appl. Cryst., 8, 340 (1975).

135. L.F. Johnson, F. Heatley and F.A. Bovey, Macromol., 3, 175 (1970).

136. J.M. Guenet, Z. Gallot, C. Picot, and H. Benoit, J. Appl. Polym. Sci., 21, 2181 (1977).

137. GPC apparatus manufactured by Waters Associates, Massachusetts.

138. Y. Kumagai, H. Watanabe, K. Miyasaka, and T. Hata, J. Chem. Engr. Japan, 12, 1 (1979).

139. P.T. Gilmore, R. Falabella, and R.L. Laurence, Macromol, 13, 880 (1980).

140. C.G. Vonk, C.A.F. Tuijnman, G. Kortleve, J. Polym. Sci., Part A-2, 10, 123 (1972).

141. O. Kratky, G. Porod, and Z. Skola, Acta. Phys. Austriaca, 13, 876 (1973).

142. J.H. Wendorff, J. Polym. Sci.-Polym. Lett. Ed., 18, 439 (1980).

143. A. Todo, H. Uno, K. Miyoshi, T. Hashimoto, and H. Kawai, Polym. Engr. Sci., 17, 587 (1977).

144. W. Ruland, Colloid and Polym. Sci., 5, 29 (1977).

145. B. Crist, J. Polym. Sci., Polym. Phys. Ed., 11, 635 (1973).

146. A.J. Carter, C.K.L. Davies, and A.G. Thomas, Joint Polish-Italian Symposium on Polymer Blends, Plenum Press, NY, 1981.

147. J.P. Runt, Macromol., 14, 420 (1981).

148. P.J. Flory, Principles of Polymer Chemistry, Cornell Univ. Press, Ithaca, NY, 1953.

149. R. Neira, Ph.D. Dissertation, University of Massachusetts, Amherst, MA, 1974.

150. P.G. DeGennes, J. Chem. Phys. 72, 4756 (1980).

151. F. Bueche, W.M. Cashin, and P. Debye, J. Chem. Phys., 20, 1956 (1952).

152. F. Bueche, J. Chem. Phys., 48, 1410 (1968).

153. J. Klein and B.J. Briscoe, Proc. Roy. Soc. London, A365, 53 (1979).

154. J. Klein and B.J. Briscoe, Polymer, 17, 481 (1976).

155. H. Sillescu, Makromol. Chem., 178, 2759 (1977).

156. D.E. Koppel, D. Axelrod, J. Schlessinger, E.L. Elson, and W.W. Webb, Biophys. J., 16, 1315 (1976).

157. B.A. Smith, W.R. Clark, and H.M. McConnell, Proc. Nat'l. Acad. Sci. USA, 76, 5641 (1979).

158. L.M. Smith, W. Parce, B.A. Smith, H.M. McConnell, Proc. Nat'l. Acad. Sci. USA, 76, 4177 (1979).

159. P.G. deGennes, J. Chem. Phys., 72, 4756 (1980).

160. P.G. deGennes, Scaling Concepts in Polymer Physics, Cornell Univ. Press, Ithaca, NY, 239 (1979).

161. L. VanHove, Phys. Rev., 95, 1374 (1954).

162. P.G. DeGennes, Ph.D. Dissertation, University of Paris, 1957.

163. J. Jelenic, R.G. Kirste, and B.J. Schmitt, to be published in Makro. Chemie, 183 (1982).

164. D. Van der Hart, private communication.

S E C T I O N I I

MOLECULAR DISPERSION AND THERMODYNAMICS OF ISOTACTIC AND ATACTIC POLYSTYRENE BLEND BY NEUTRON SCATTERING

CHAPTER I

Introduction

The conformations of atactic polystyrene (APS) and isotactic polystyrene (IPS) have been studied in both solution and the bulk state. Benoit et al. [1,15], employing small angle neutron scattering (SANS), did an extensive study on the conformation of deuterium labelled atactic polystyrene (APSD) in both good and poor solvent as well as in the bulk state. Using Zimm's analysis, their results confirmed that APSD retained its Θ conformation in the bulk state, as predicted by Flory [2], and confirmed by numerous experiments on APS in solution [3,4,5].

Krigbaum et al. [6] studied the solution properties of IPS in various solvents and compared them with equivalent parameters of APS. It was shown that the IPS exhibited a slightly larger dimension than equivalent APS under identical conditions.

Recently Guenet et al. [7], used SANS to study the conformation of deuterium labelled isotactic polystyrene (IPSD) in two kinds of matrices, hydrogenous isotactic polystyrene (IPSH) and hydrogenous atatic polystyrene (APSH). Their results indicated that in the melt state, the labelled IPSD retained its unperturbed dimension in both the IPSH and APSH matrix. Furthermore the dimension occupied by the IPSD is the same as that occupied by IPS in ideal solution as observed by Krigbaum [6].

The study of the conformation of chains in a mixed components blend

in the melt state by deuterium labelling of one of the component is the subject of intensive research. Ballard et al. [8] demonstrated that polystyrene and poly (α-methylstyrene) formed a truly compatible mixture. Wignall et al. [9] did SANS measurements on blends of atactic polystyrene and poly (2,6-dimethyl phenylene oxide) (PPO) with labelled atactic polystyrene. Their results indicated there was a slight chain expansion but the experimental determined molecular weight stayed the same within experimental error to that obtained by GPC/osmometry. The variation of molecular weight with concentration indicated a positive second virial coefficient in the range of $1 \times 10^{-5} \leq 2A_2 \leq 1.5 \times 10^{-4}$ cm^3 g^{-2} mol.

Kambour et al. [10] did SANS studies in a three component system of labelled and unlabelled polystyrene with brominated poly(xylenyl ether)(PXE). Zimm analysis on their samples yielded a radius of gyration value for labelled PS that agrees within experimental error to that of the unperturbed dimension. However, they obtained a positive value of the second virial coefficient as 3.7×10^{-4} cm^3 g^{-2} mol. Furthermore, their data suggested that both R_g and A_2 are depended upon the temperature from which the blend is quenched. The positive value of A_2 indicated that there is favorable free energy of mixing for these samples.

Kirste and coworkers did a series of SANS studies on various polymer blends to determine the coil dimensions and thermodynamic parameters. In a blend of poly (dimethyl siloxane)(PDMS) diluted with deuterium labelled PDMS, Kirste and Lehren [11] studied the effect of

molecular weight of the dilute specie in a high molecular weight matrix. They found that if the molecular weight of the labelled specie is low compared to the host molecular weight, there was chain expansion of the labelled specie from its unperturbed dimension and a positive second visual coefficient was obtained. However, if the host and guest molecular weights are comparable, the blend exhibits the characteristics of an ideal mixture, where the radius of gyration remains in the unperturbed state and A_2 goes to zero.

Kirste et al. [12,13] did a study on blends of deuterium labelled poly(methyl methacrylate)(PMMA) blended with poly(styrene/acrylonitrile) (PSAN) and labelled PMMA blended with poly(vinyl chloride) (PVC). In these studies, they calculated the value of the interaction parameter, χ from the second virial coefficient. Since the value of χ was less than zero and the coils are expanded from their unperturbed dimension, their results indicated that both blend systems are compatible in the dilute regime.

More recently, Kirste et al. [14] studied the SANS behavior of polystyrene (PS) and poly(vinyl methyl ether) (PVME) blend as a function of temperature. They calculated a value of χ for each temperature studied. Their result indicated that as the temperature is raised, the value of χ increases from negative to positive. This means that the blend is becoming incompatible as the temperature is raised. Indeed they showed that when χ is above a critical value of χ, χ_c, given by Scott [22] as:

$$\chi_c = \frac{1}{2}\left(\frac{1}{\sqrt{P_1}} + \frac{1}{\sqrt{P_2}}\right)^2 \qquad (1)$$

where P_1 and P_2 are the degree of polymerization of component 1 and 2, respectively, the blend becomes optically opaque.

In this section we report the results of a study on blends of isotactic polystyrene with atactic polystyrene of various compositions. By deuterium labelling of the atactic polystyrene (which does not appreciably change the physiochemical properties of the blend, except its neutron scattering cross sectional area), we have determined the conformation of the labelled atactic chain, its experimental determined molecular weight and the second virial coefficient which is directly related to the interaction parameter χ.

C H A P T E R I I

Theory

In a binary mixture in which at least one component is of low molecular weight, the main contribution to a negative free energy of mixing, ΔG_{mix} is the combinatorial entropy of mixing. If on the other hand both molecular weights (M_1 and M_2) approach infinity, then the combinatorial entropy vanishes and the thermodynamic behavior is governed by the contact energy [16]. A third contribution to ΔG_{mix} results from free volume change, but this contribution is always positive, i.e. unfavorable mixing. However, if there is no volume change upon mixing, then for a polymer blend to exhibit compatibility (at M_1, $M_2 \to \infty$), the contact energy due to "specific" interaction such as hydrogen bond, must be exothermic which can counterbalance the unfavorable entropy of mixing.

The usual method to describe polymer compatibility is the lattice treatment as developed by Flory-Huggin [2]. For a two-component system in the absence of a solvent, is given is by Scott [23] as:

$$\Delta G_{mix} = \Delta H_{mix} - T\Delta S_{mix} \qquad (2a)$$

$$\Delta G_{min} = RT\,[n_1 \ln\phi_1 + n_2 \ln\phi_2 + \chi_{12}\,\phi_1\,\phi_2\,(n_1P_1 + n_2P_2)] \qquad (2b)$$

where ϕ_1 and ϕ_2 denote the volume fractions of the two polymers in the mixture, P_1 and P_2 are the degree of polymerization, and n_1 and n_2

are the number of moles of polymer 1 and 2, respectively. The chemical potential of component 1, μ_1, is then defined as

$$\Delta\mu_1 = \left(\frac{\partial G}{\partial n_1}\right)_{n_2,T,P} \tag{3a}$$

$$\Delta\mu_1 = RT\,[\ln\phi_1 + (1 - P_1/P_2)\,\phi_2 + P_1\,\chi_{12}\phi_2^2] \tag{3b}$$

The degree of polymerization is then defined as:

$$P_1 = \frac{V_1}{V_r} \qquad P_2 = \frac{V_2}{V_r} \tag{4}$$

where V_1 and V_2 are the molar volume of polymer 1 and 2 respectively and V_r is the reference volume of the volume occupied by the monomer unit. Equation (3b) (for small value of ϕ_2) then becomes, as derived by Kriste [11]:

$$-\Delta\mu_1 = RT\,[\,(P_1/P_2)\,\phi_2 + (0.5 - P_1\chi_{12})\,\phi_2^2 + ...] \tag{5a}$$

$$= RT\,[(V_1/M_2)C_2 + A_2\,V_1\,C_2 2 + ...] \tag{5b}$$

where A_2 (second virial coefficient) $= \frac{V_2^2}{V_1 M_2^2}\,(0.5 - P_1\chi_{12})$ (6)

In equation (5), C_2 is the concentration of component 2 which is given as:

$$C_2 = \phi_2/V_2 \tag{7}$$

and M_2 is the molecular weight of component 2. However for a three component system, such as the case of isotactic polystyrene, hydrogenated atactic polystyrene and deuterated atactic polystyrene, we must rewrite equation (2) as a summation over all components:

$$\Delta G_{mix} = RT \left\{ \sum_{i=1}^{3} n_i \ln \phi_i + \sum_{ij=1}^{3\,3} \chi_{ij} \phi_i \phi_j \left(\sum n_i P_i \right) \right\} \qquad (8)$$

Afterward the chemical potential is defined as:

$$\Delta \mu_1 = \left(\frac{\partial G}{\partial n_1} \right)_{n_2,\, n_3,\, T,P} \qquad (9)$$

The calculation of equation (9) is very tedious and cumbersome. Unfortunately, at the time of this writing the exact mathematical solution has not been worked out to obtain the equation for the second virial coefficient. This is the objective of future work.

Yamakawa [17] derived the general expression for scattering based upon the fluctuation theory, for a multicomponent system as:

$$R_\theta = \frac{K}{|\psi|} \left[\sum k^2 c^2 \psi_{ii} - 2 \sum \sum k_i k_j c_i c_j \psi_{ij} \right] \qquad (10)$$

where

R_θ = Rayleigh ratio

K = constant

c_i = concentration of component i

k_i = contrast factor relative to the solvent

$$\psi_{ij} = \frac{c_i c_j}{M_i kT} \left(\frac{\partial \mu_i}{\partial c_j} \right)_{T,P,c_k} = \psi_{ji} \qquad (11)$$

where

μ_i = chemical potential of component i

M_i = molecular weight of component i

The chemical potential is expressed by Yamakawa as:

$$\mu_1 = \mu_1^{\circ} (T,P) + kT \ln \gamma_i c_i \qquad (12)$$

where γ_i is an activity coefficient such that $\gamma_i \to 1$ as $c_i \to 0$. Thus for the case of a dilute solution:

$$\ln \gamma_i = M_i (\Sigma B_{2,ij} c_j + \Sigma \Sigma B_{3,ijk} c_j c_k + \ldots) \qquad (13)$$

where the B's are the apparent second and third virial coefficients, respectively.

Substitution of Ψ into equation (10) and after tedious calculation for a three components system, Yamakawa arrived at:

$$\frac{K'c_2}{R_\theta} = \left[\frac{1}{M_{2,app}} + 2 B_{2,app} c_2 + \ldots\right] \qquad (14)$$

The derivation of equation (14) is valid only at zero scattering angle and dilute concentration of c_2. However, to take into account the effect of intramolecular destructive interference in a system, Yamakawa [17] derived the general formulation for scattering from a multicomponent system, based upon the distribution function as:

$$I(q) = \Sigma k_i^2 M_i P_{1i} (q,c) c_i - 2 \Sigma \Sigma c_i c_j k_i k_j M_i M_j A_{2ij}(c) P_{2ij}(q,c) \qquad (15)$$

where:

k_i, k_j = contrast factor relative to the solvent

q = scattering vector = $(4\pi/\lambda)$ (sin $\theta/2$)

c_i = concentration of component i

$P_1(q,c)$ = single particle scattering function

$P_2(q,c)$ = interparticle scattering function

Equation (15) is valid only at infinite dilution due to the expansion of concentration terms. In the particular case of two components, equation (15) reduces to the Zimm equation in the limit of θ and $c \to 0$.

Both approaches suffer from the fact that the expressions were developed assuming infinite dilution. In a highly concentrated system, the expansion of equation (13) is not valid, and the expansion of concentration to derived equation (15) is not valid. The exact nature of this concentration expression needs to be derived and remains the objective of future studies.

Nevertheless, for a three component system consisting of only deuterated and hydrogenated specie, we can define:

Polymer 1	Hydrogenous	Concentration C_H
Polymer 1	Deuterated	Concentration C_D
Polymer 2	Hydrogenous	Concentration $1-(CH+C_D)$

Thus, we can write:

$$k_1 = (a_H - a_S) = B_H \qquad (16a)$$

$$k_2 = (a_D - a_S) = B_D \qquad (16b)$$

where a's are the scattering cross section of the hydrogenated, deuterated, and solvent species.

Now assuming that:

a) deuteration of the hydrogenous molecule has negligible effect on the monomer-monomer interactions, we can write very generally:

$$A_{2HD} = A_{2HH} = A_{2DD} = A_2 \tag{17}$$

b) Both the deuterated and hydrogenerated specie have the same molecular weights with narrow polydispersity. In this case the interparticle scattering functions would be the same, so we can write very generally:

$$M_1 = M_2 = M$$

$$P_{2HD} = P_{2HH} = P_{2DD} = P_2 \tag{18}$$

Thus equation (15) becomes:

$$I(q) = (C_H B_H^2 + C_D B_D^2)\, M\, P_1(q,c) \tag{19}$$
$$- 2\,(C_H B_H + C_D B_D)^2\, M^2\, A_2(c)\, P_2(q,c)$$

Now keeping the blend concentration constant, i.e. $C_D + C_H = C$, we can envisage a number of experiments:

a) Measure the scattering from a blend with $C_D = 0$

$$I(q)\Big|_{C_D=0} = CB_H^2\, MP_1(q,c) - 2C^2\, B_H^2\, M^2\, A_2\,(C)\, P_2\,(c) \tag{20}$$

Thus if we subtract equation (20) from equation (19), the excess intensity is therefore:

$$I(q) = C_D(B_D^2 - B_H^2)\, MP_1(q,c)$$
$$-2\,[C_D^2(B_D - B_H)^2 + 2\,C_HC_D(B_D-B_H)]M^2\,A_2\,(c)\,P_2\,(q,c) \qquad (21)$$

The equation for the two component system is developed by Zimm [18] as:

$$\frac{I(q)}{B_D^2} = MC_DP_1(q,c) - 2A_2M^2\,C_D^2\,P_2\,(q,c) \qquad (22)$$

In a conventional Zimm plot, the extrapolation of C_D to zero yields the single chain scattering function, extrapolation of q to zero yields the value of A_2 and double extrapolation of q and c to zero yields the value of the molecular weight. In equation (21), we can extrapolate q to zero to yield a value of A_2 but its coefficient is different from that of a two component system. However, we cannot extrapolate $c \to 0$ due to the dependence of C_D in the second term of the equation. However if MA_2 or $(B_H/(B_H + B_D)) \ll 1$, then we can do the extrapolation for concentration only as an approximation. Another way is to obtain P_1 separately. This can be done by several methods:

a) Do two experiments with different concentrations of the deuterated specie (C_D) weighted by the coefficient of P_2 to obtain P_1.

b) Look for a null system where $C_D = \dfrac{-2C_HB_H}{B_D - B_H}$

c) Use a different background subtraction. Consider a system where polymer 1 is a random copoymer where the H/D ratio = C_H/C_D. In such a case:

$$B_{cop} = (C_DB_D + C_HB_H)/C \qquad (23)$$

$$I_{cop}(q) = \frac{1}{C} (C_D B_D + C_H B_H)^2 \, M P_1 (q,c) - 2(C_D B_D + C_H B_H)^2 \, M^2 \, A_2 (c) \, P_2 (q,c) \quad (24)$$

Now, subtraction of equation (24) from equation (19) to remove the P_2 (q,c) terms completely gives:

$$I(q) = \frac{C_D C_H}{C} (B_D - B_H)^2 \, M \, P_1(q,c) \quad (25)$$

This development is similar to that of Summerfield et al. [23,24]. This third method is employed in this study to measure the single chain scattering function. In the Guinier range, (i.e. $q\bar{R}_g << 1$, where $\bar{R}_g$ is the mean radius of gyration), P_1 (q,c) can be written as:

$$P_1(c) = 1 - \frac{q^2 \overline{R_g^2}}{3} \quad (26)$$

Equation (19) was derived upon the basis that the labelled and unlabelled molecules are of similar molecular weight. King, et al. [25] had shown that this equation is valid up to a molecular weight ratio $\bar{M}w(PSD)/\bar{M}w(PSH)$ of 3.0. Equation (19) deteriorates very rapidly when the ratio is greater than 3.0 because of the concentration dependence on the scattering function.

In this study the molecular weight of the labelled and unlabelled polystyrene are very nearly identical, so there not be the problem of mismatched molecular weights to effect the concentration dependence on the scattering function.

C H A P T E R I I I

Experimental

Sample Preparation. Both isotactic and atactic polystyrene were obtained from Polymer Laboratories of Shrewsbury, England. The weight averaged molecular weight ($\bar{M}w$) of IPS was 389,000 with a polydispersity less than 3.2 and the $\bar{M}w$ of APSH were 522,000 and 456,000 with a polydispersity less than 1.1 and and 1.05, respectively. Deuterated atactic polystyrene (APSD) was also obtained from Polymer Laboratories with a $\bar{M}w$ of 547,000 and a polydispersity of less than 1.12.

All blends were prepared in identical fashion. The isotactic polystyrene was purified according to the procedure used by Warner et al. [27]. Pre-weighed amounts of IPSH and APSH were prepared first to obtain the host matrix composition. Each host matrix was then blended with 1, 3, 5 and 7% by weight of labelled atactic polystyrene, by dissolving in benzene to make a 1% solution and then freeze-dried. The resulting blend was then pressed under vacuum into disc-shaped pellets, 0.13 cm thick. The pellets were molded at 260°C under vacuum to avoid oxydative degradation and to eliminate microvoids. To reach the relaxed state of the macromolecule, a molding time of 25 minutes was used. The system was then quenched in room temperature water to freeze the conformation. All the characteristics of these blends (molecular weight, composition, and concentration) are listed in Table 17.

SANS Measurement. All measurements were done at room temperature.

Table 17

Samples for SANS Experiments

Matrix Composition APS/IPS	$\bar{M}w$(IPS)[a]	$\bar{M}w$(APS)[a]
Pure IPS	3.89×10^5[b]	———
25/75	"	5.22×10^5[c]
50/50	"	"
75/25	"	4.56×10^5[c]

Each composition blended with 1, 3, 5 and 7 wt% deuterated polystyrene (PSD_8)

$\bar{M}w(PSD_8)$[a] = 5.47×10^5

$\bar{M}w/\bar{M}n < 1.12$

a) Molecular weights as determined by GPC

b) $\bar{M}w/\bar{M}n < 3.2$

c) $\bar{M}w/\bar{M}n < 1.1$

The measurements were carried out at the National Center for Small Angle Scattering Reserach (Oak Ridge National Laboratory) (NCSASR) on the 30 meter SANS facility. Description of the apparatus is given in references 19 and 28. For this investigation, the incident beam was 4.74 Å ($\Delta\lambda/\lambda$ = 6%) and the sample to detector distance was 14.8 meters. This gives a transfer momentum value of $q = 1.0 \times 10^{-3}$ Å^{-1} where $q = \frac{4\pi}{\lambda} \sin \frac{\theta}{2}$, where θ is the angle between the scattered and incident beam.

CHAPTER IV

Results

In this study, it was felt that in the melt state, the only difference between the isotactic and atactic polystyrene chains is due to tacticity. Thus the scattering is very similar to that of a two component system of a labelled specie in a host matrix. By making this assumption we can use equations (5b) and (22) to do a Zimm analysis to obtain the molecular weight and the second virial coefficient A_2.

In this investigation, a reference sample was used to calculate the molecular weight of the labelled specie in the blends. The reference sample that was employed was a 5% APSD in a host APSH matrix of the same molecular weight. The molecular weight of the reference sample was identical to the labelled species used in the blend. Since the single chain scattering function is identical for all specie and the experimental conditions being identical for both the reference and sample, we can rearrange equation (25) to give:

$$\bar{M}_S = \frac{I_{sample}(q)}{I_{reference}(q)} \cdot \frac{C_{ref}(1-C_{ref})}{C_{sam}(1-C_{sam})} \bar{M}_R \qquad (20)$$

where C_{ref} and C_{sam} are the concentrations of the labelled specie in the reference and sample, respectively. $\bar{M}_S$ and $\bar{M}_R$ are the weight-averaged molecular weight of the sample and reference, respectively.

For each blend series, a blank sample (i.e. with no deuteration) of the appropriate ratio of isotactic to atactic polystyrene was

prepared. The scattering from these samples give us the incoherent scattering level.

All of the sample scattering intensity values were corrected for detector's sensitivity and parasatic scattering. The incoherent scattering values for each blend series were then subtracted from the sample scattering of the appropriate blend composition. A plot of the net scattered intensity values is shown in figure 87 for a typical sample.

For each blend series a Zimm analysis was done to measure the radius of gyration, molecular weight and the second virial coefficient. Zimm plots of all blends series are given in figures 88 to 91. The mean z-averaged radius of gyration was measured by extrapolation of $c = 0$. The second virial coefficient (A_2) was measured by extrapolation of $q = 0$. The mean weight averaged molecular weight was measured by double extrapolations of $c = 0$ and $q = 0$.

The mean z-averaged radius of gyration was corrected by method of Schultz [26] to obtain the mean weight averaged radius of gyration. A summary of the results are given in Tables 18 and 19.

Table 18

Zimm Analyzed Results for IPS/APS Blends

Composition APS/IPS	$(\bar{R}_g)_w$, NM	$\bar{M}w \times 10^{-5}$
Pure IPS	23.6 ± 4.3	4.59 ± 0.71
25/75	17.5 ± 1.4	5.14 ± 2.96
50/50	22.9 ± 2.7	7.61 ± 2.09
75/25	20.1 ± 1.9	6.09 ± 1.09

*Unperturbed $(\bar{R}_g)_w$ for PSD_8 ($\bar{M}w = 5.47 \times 10^5$) in Θ solvent is 20.3 nm (Reference 19).

**True $\bar{M}w$ of PSD_8 as determined by GPC is 5.47×10^5

Table 19

Values of A_2 and χ

Sample	$A_2 \times 10^4$ ($cm^3 \times g^{-2} \times mol.$)	$\chi \times 10^{-4}$ [a]
100% IPS	- 2.78 ± 0.69	3.8 ± 1.0
75% IPS	3.98 ± 2.00	- 3.0 ± 1.5
50% IPS	- 1.03 ± 0.56	2.0 ± 1.1
25% IPS	- 1.48 ± 0.83	2.5 ± 1.4

[a] $\chi_c = 4.0 \times 10^{-4}$

Values of χ from equation (6)

C H A P T E R V

Discussion

Radii of Gyration. The most important result to notice is that there is no significant deviation of the labelled APS from the unperturbed dimension. The unperturbed dimension remains quite close to that obtained by various other workers on atactic polystyrene in the bulk state [1,19]. These results indicate that in the melt state, the isotactic polystyrene has no significant interaction with the atactic chain in all concentration ranges studied. However, as shown by Russell [20], the unperturbed dimension does not neccessarily mean non-segregation since for a polymer-polymer system, if there is no significant interaction between chains. However, the experimental molecular weight is much more sensitive to segregation effects.

Molecular Weight. The experimental values of the molecular weight of the labelled polystyrene calculated for each blend series agreed within experimental error to that of the true molecular weight. The true molecular weight was calculated from gel permeation chromatography (GPC). However, on some samples, the error range is about 40%. This is not unexpected since Schelten et al. [21] have shown that deviation from a statistical distribution involving less than one monomer unit in a thousand would cause the experimental determined molecular weight to exceed the true molecular weight by a factor of a hundred.

Second Virial Coefficient. For all blend compositions studied,

the value of the second virial coefficient A_2, was very close to zero, as given in Table 19. For a polymer-polymer system A_2 is related to χ_{12} by equation (6):

$$A_2 = \left(\frac{V_2^2}{V_1 M_2^2}\right)(0.5 - P_1\chi_{12}) \qquad (6)$$

The value of χ_{12} was calculated from equation (6) and is given with the value of A_2 in Table 19. The critical value of χ can be predicted for a polymer-polymer system. As was shown by equation (1):

$$\chi_c = \frac{1}{2}\left(\frac{1}{\sqrt{P_1}} + \frac{1}{\sqrt{P_2}}\right)^2 \qquad (1)$$

The value of χ_c for this system was calculated to be 0.0004. Kirste et al. [14] have shown that if $\chi > \chi_c$, there is phase segregation of the components. If $\chi = 0$, then the mixture is defined as ideal and if $\chi < 0$, then the system is compatible.

The value of χ for this IPS/APS blend system was less then χ_c for all blend series. This indicates that the components are not segregated. Since there was no indication of chain expansion from their unperturbed dimension and the molecular weights are comparable to the true molecular weights, it may be concluded that the IPS and APS blend systems behave in an ideal fashion.

Figure 87. Representative plot of a sample scattering after correction for detector's sensitivity, parasatic scattering and incoherent scattering. [$q=4\pi/\lambda)\sin\theta/2$ when θ = scattering angle and λ = wavelength.]

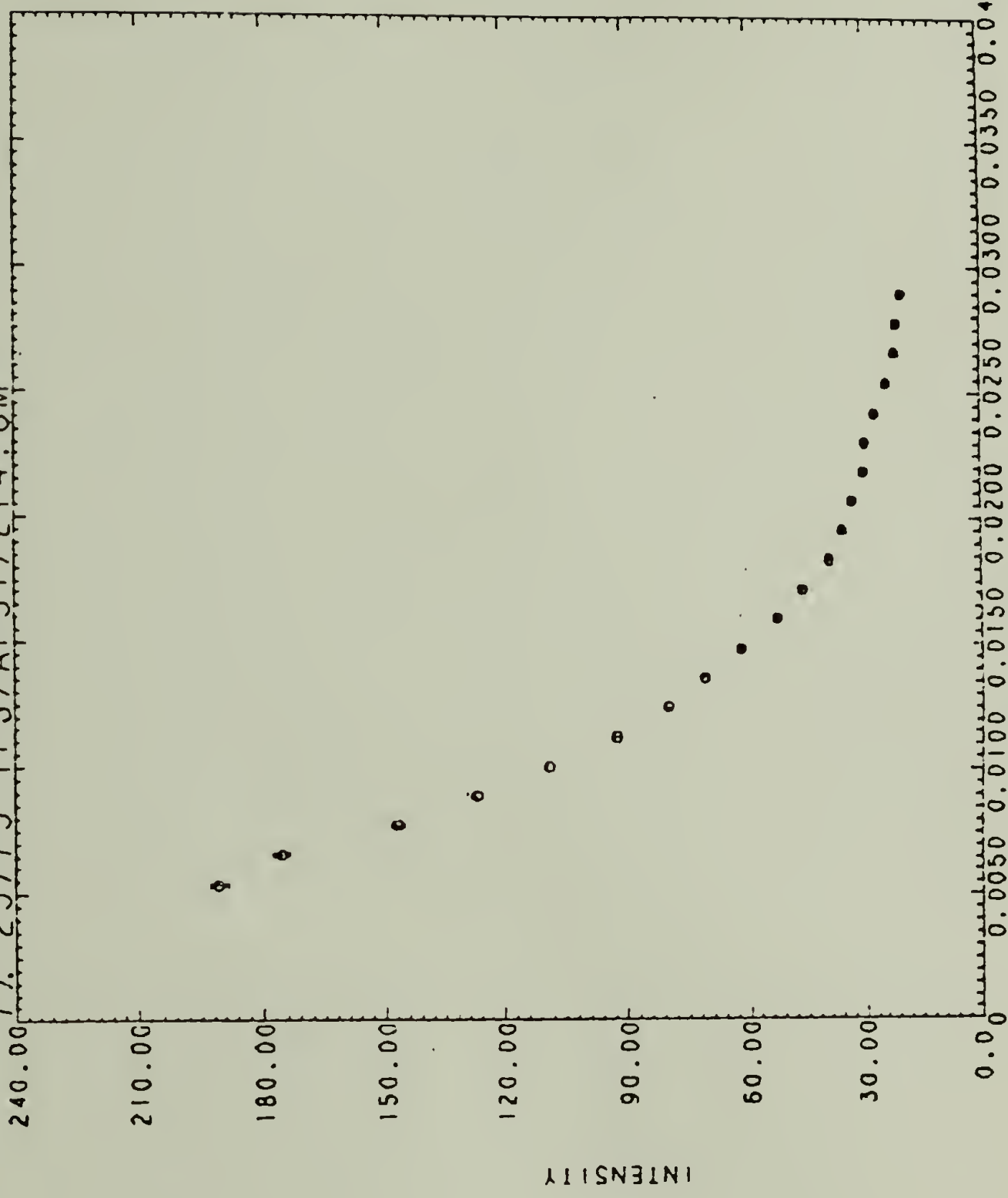
7% 25/75 IPS/APS1/214.8M
INTENSITY
240.00
210.00
180.00
150.00
120.00
90.00
60.00
30.00
0.0
0.0050
0.0100
0.0150
0.0200
0.0250
0.0300
0.0350
0.0400
Q (ANG^{-1})

Figure 88. Zimm plot for perdeuteropolystyrene in 100% isotactic polystyrene matrix. C is concentration in g/cm^3.

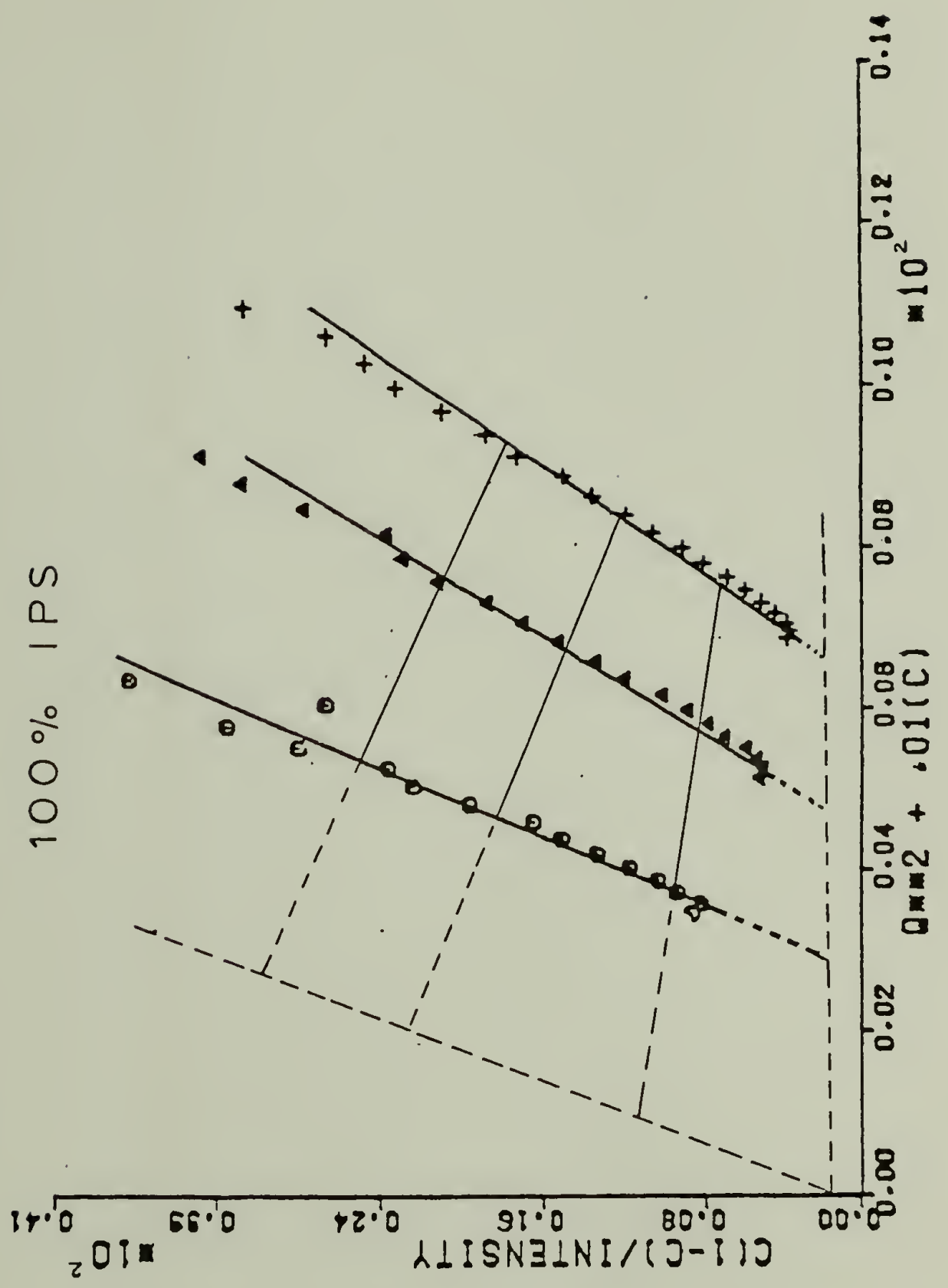
100% IPS
C(1-C)/INTENSITY
×10²
0.00
0.08
0.16
0.24
0.33
0.41
Q=2 + .01(C)
0.00
0.02
0.04
0.08
0.10
0.12
0.14
×10²

Figure 89. Zimm plot for perdeuteropolystyrene in 75/25 IPS/APS blend mixtures. C is concentration in g/cm^3.

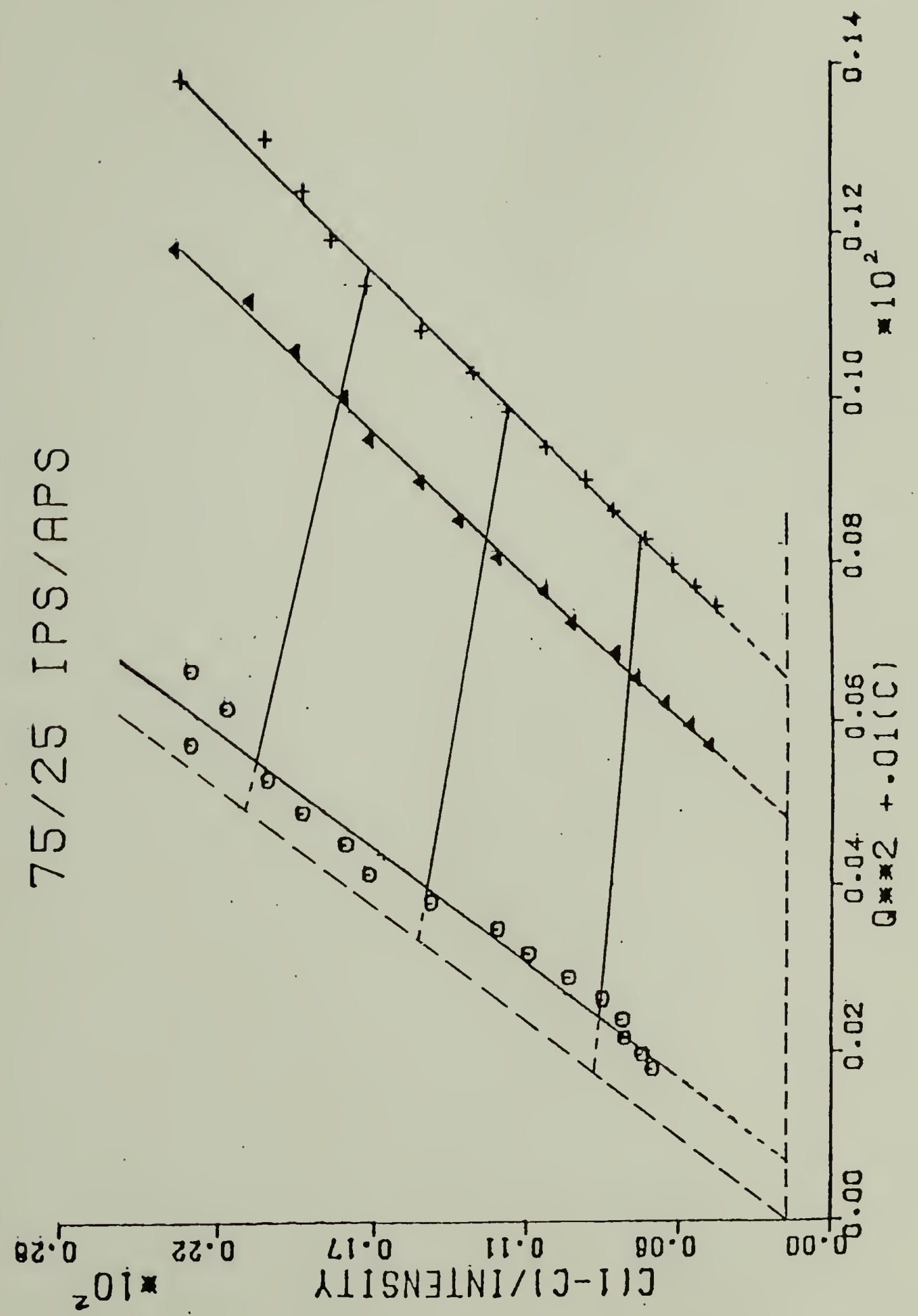
75/25 IPS/APS
CI1-CI/INTENSITY
*10²
0.00
0.06
0.11
0.17
0.22
0.28
Q**2 +-.01(C)
0.00
0.02
0.04
0.06
0.08
0.10
0.12
0.14
*10²

Figure 90. Zimm plot for perdeuteropolystyrene in 50/50 IPS/APS blend mixtures. C is concentration in g/cm^3.

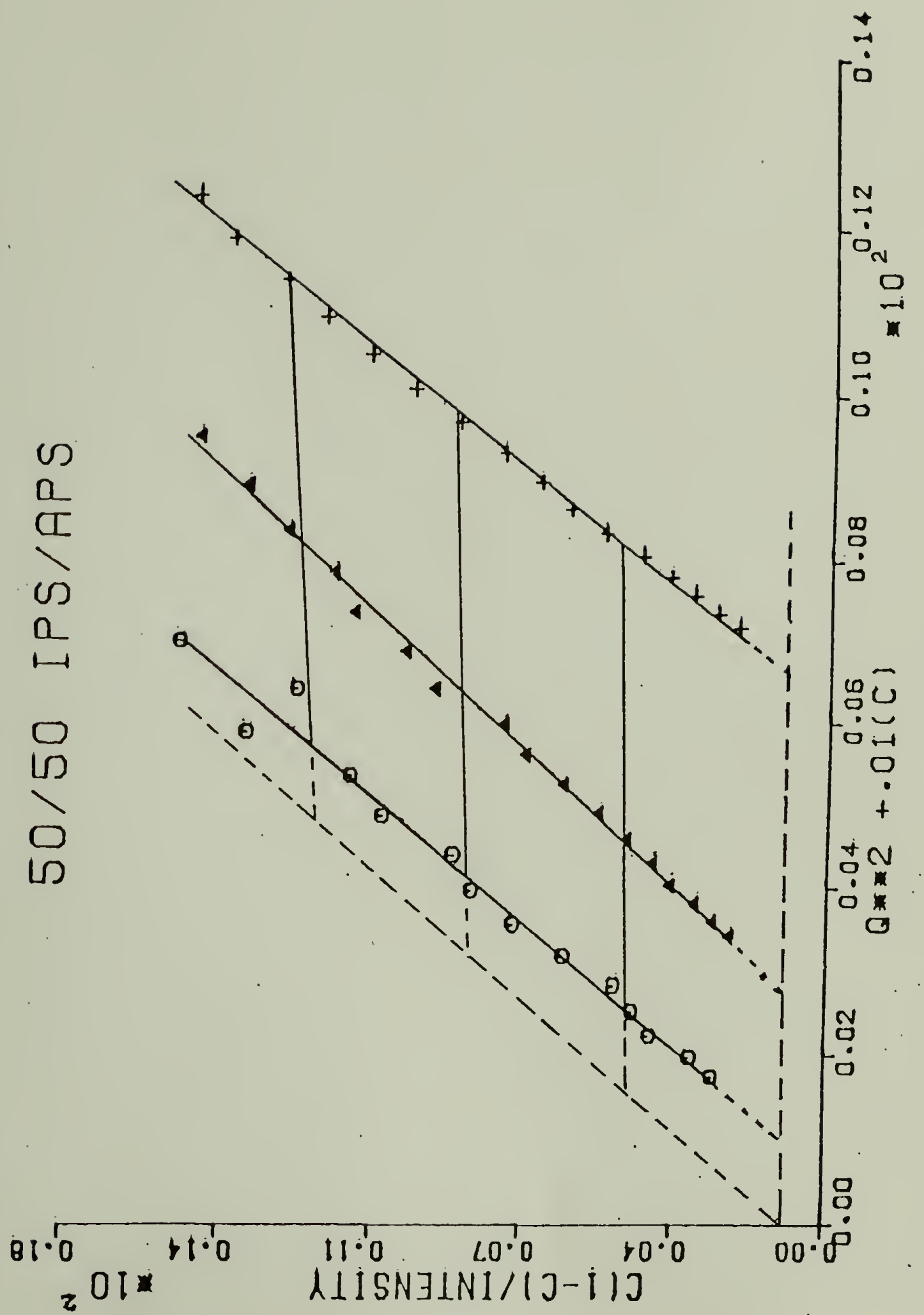
50/50 IPS/APS
CI-C)/INTENSITY
*10 2
0.00
0.04
0.07
0.11
0.14
0.18
0.00
0.02
0.04
0.06
Q**2 +.01(C)
0.08
0.10
*10 2
0.12
0.14

Figure 91. Zimm plot for perdeuteropolystyrene in 25/75 IPS/APS blend mixtures. C. is concentration in g/cm^3.

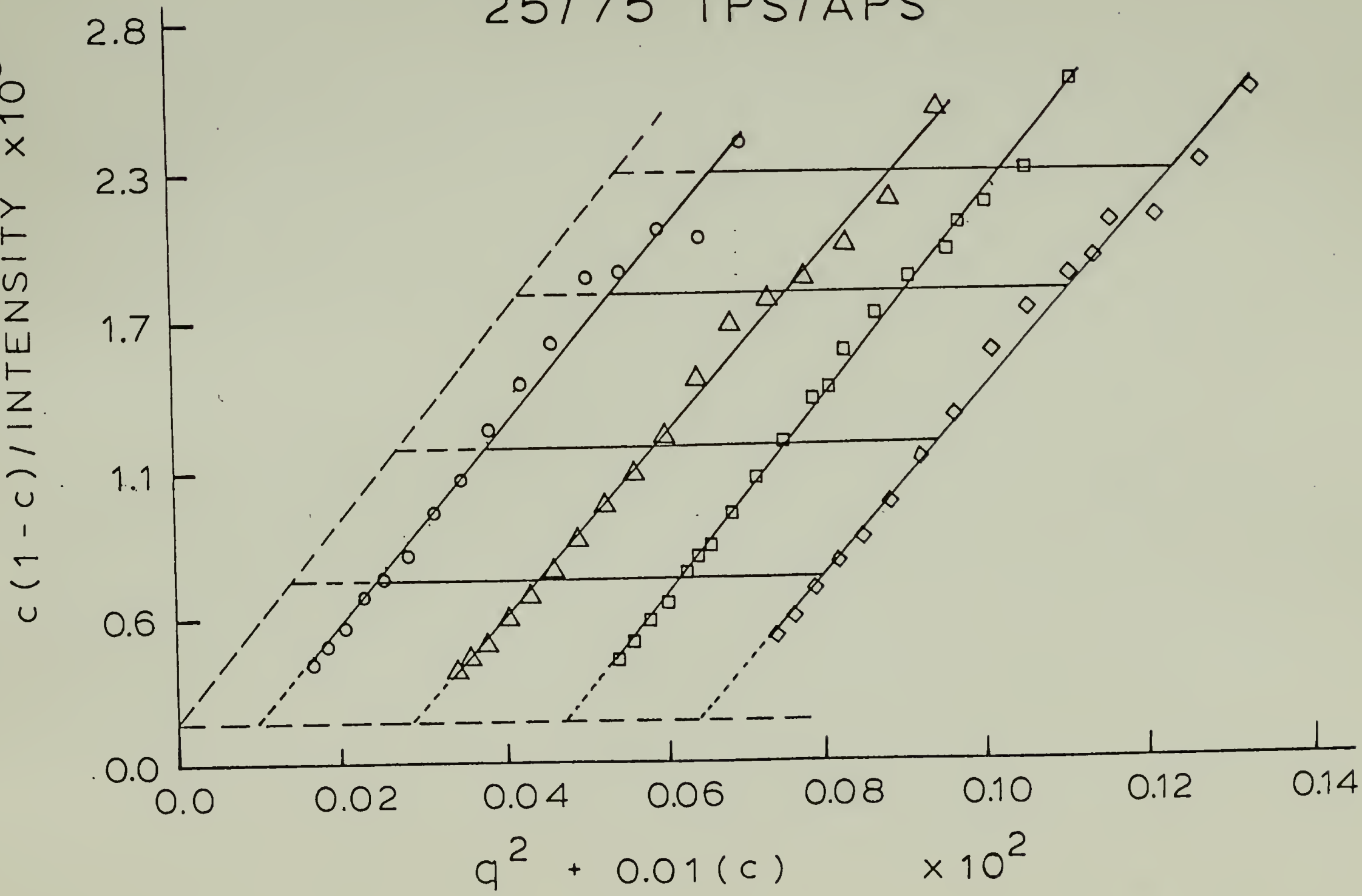
25/75 IPS/APS
c(1-c)/INTENSITY x10^3
2.8
2.3
1.7
1.1
0.6
0.0
0.0
0.02
0.04
0.06
0.08
0.10
0.12
0.14
q^2 + 0.01(c) x 10^2

SECTION II

REFERENCES

1. J.P. Cotton, D. Decker, H. Benoit, B. Farnoux, J. Higgins, G. Jannink, R. Ober, C. Picot, and J. des Cloizeaux, Macromol., 7, 863 (1974).
2. P.J. Flory, Principles of Polymer Chemistry, Cornell Univ. Press, Ithaca, NY, 1953.
3. P. Outer, C.I. Carr, and G.H. Zimm, J. Chem. Phys., 18, 830 (1950).
4. W.R. Krigbaum and D.K. Carpenter, J. Chem. Phys., 59, 1166 (1955).
5. L. Utracki and R. Simha, J. Chem. Phys. 67, 1052 (1962).
6. W.R. Krigbaum, D.K. Carpenter, and S. Newman, J. Chem. Phys., 62, 1586 (1958).
7. J.M. Guenet, C. Picot, and H. Benoit, Macromol., 12, 86 (1979).
8. D.G.H. Ballard, M. Rayner, and J. Schelten, Polymer, 21, 131 (1980).
9. G.D. Wignall, H.R. CHild, and F. LiAravena, Polymer, 21, 131 (1980).
10. R.P. Kambour, R.C. Bopp, A. Maconnachie, and W.J. MacKnight, Polymer, 21, 133 (1980).
11. R.G. Kirste and B.R. Lehnan, Makromol. Chem., 177, 1137 (1976).
12. W.A. Kruse, R.G. Kirste, J. Haas, B.J. Schmitt, and D.J. Stein, Makromol. Chem. 177, 1145 (1976).

13. J. Jelenic, R.G. Kirste, B.J. Schmitt, and S. Schmitt-Strecker, Makromol. Chem. 180, 2057 (1979).

14. J. Jelenic, R.G. Kirste, and B.J. Schmitt, to be published in Makromol. Chem. 183 (1982).

15. H. Benoit, J.P. Cotton, D.Decker, B. Farnoux, J.S. Higgins, G. Jannink, R. Ober, C. Picot, Nature Phys. Sci., 245, 13 (1973).

16. D. Patterson and A. Robard, Macromol., 11, 690 (1978).

17. H. Yamakawa, Modern Theory of Polymer Solutions, Harper and Row, New York, NY (1971) p. 211.

18. B. Zimm, J. Chem. Phys., 16, 1093, 1099 (1948).

19. G.D. Wignall, R.W. Hendricks, W.C. Koehler, J.S. Lin, M.P. Wai, E.L. Thomas, and R.S. Stein, Polymer 22, 886 (1981).

20. T. Russell, Ph.D. Dissertation, University of Massachusetts, Amherst, MA (1979).

21. J. Schelten, D.G.H. Ballard, G.D. Wignall, G. Longman, and W. Schmatz, Polymer, 17, 751 (1976).

22. R.S. Scott, J. Chem. Phys., 17, 279 (1949).

23. A.F. Ackasu, G.C. Summerfield, S.N. Jahshan, C.C. Han, C.Y. Kim, H. Yu, J. Polym. Sci.-Polym. Phys. Ed., 18, 863 (1980).

24. G.C. Summerfield and S.N. Jahshan, J. Polym. Sci.-Polym. Lett. Ed., 10, 859 (1980).

25. C. Tangari, J.S. King, and G.C. Summerfield, Bulletin of the American Physical Society Meeting, Phoenix (1981).

26. K. Altgelt, and G.V. Schultz, Makromol. Chem., 36, 209 (1960).

27. F.P. Warner, W.J. MacKnight, and R.S. Stein, J. Polym. Sci. Polym. Phys. Ed., 15, 2113 (1977).

28. R.W. Hendricks and W.C. Koehler, J. Appl. Cryst., to be published.

APPENDIX I

ONE DIMENSIONAL POSITION SENSITIVE DETECTOR

IN THE DEPARTMENT OF POLYMER SCIENCE AND ENGINEERING

APPENDIX I

DESCRIPTION AND ALIGNMENT OF THE UNIVERSITY OF MASSACHUSETTS ONE DIMENSIONAL POSITION SENSITIVE DETECTOR IN THE DEPARTMENT OF POLYMER SCIENCE AND ENGINEERING

Introduction

The one dimensional position sensitive detection (1DPSD) in the Department of Polymer Science and Engineering is mounted on a Kratky small angle x-ray camera. This project was initiated by Thomas P. Russell [1] and subsequently completed by this author.

The Kratky collimation geometry is one of several SAXS geometries noted for both high angular resolution and very low parasatic scattering [2,3]. Russell [4,5] did an extensive study in the modification of the Kratky to use a 1DPSD and the reader is encouraged to read his report to gain better background understanding of the application of the 1DPSD. For a more detailed understanding of the electronic operation and theory of signal-timing, the pioneering works of Kopp [6,7,8] should be read.

Components

A. Detector. During the course of this study, two types of 1DPSD's were brought from commercial sources. The first type was a flow-gas detector manufactured by Tennelec and marketed as Tennelec PSD 1100. This type of detector uses a P10 gas (90% argon, 10% methane) with a

carbon coated quartz wire for detection of x-ray. The second type of detector used was a sealed detector manufactured by Technology for Energy Corporation (TEC) and marketed as TEC Model 210. This type of detector has a xenon/methane atmosphere with a stainless steel wire for detection of x-ray. Although these two types of detector are of different construction, they are basically resistance-capacitance (RC)line encoding-decoding analysis. The advantages and disadvantages of these two types of detector will be discussed later in this appendix.

B. Electronic. RC-line position encoding and decoding by pulse shape analysis and crossover timing was basically the same one used by Russell [5] and by Schelten and Hendricks [9]. The schematic of the UMASS 1DPSD electronic is given in figure 100. An important aspect to notice is that the preamplifier is included in the detector to minimize the electronic noise. The electronic for the UMASS 1DPSD system was manufactured by ORTEC, a picture of which is shown in figure 101. The multichannel analyzer was manufactured by INO-TECH and marketed as INOTECH 5200.

Modification of the Kratky Collumination System

The unique feature of a Kratky collimnation system is the use of a U-block and a bridge [10,11] to define an asymmetrical beam. These components ultimately define the main beam profile, amount of parasatic scattering and the angular resolution. The usual Kratky camera comes equipped with a step-scanning device mounted on an evacuated

flight path to record the scattering. However, the 1PDSD acquires the entire scattering profile simultaneously and thus a vacuum tank utilizing the PSD must be geometrically similar to a film camera. The extent of modification depends upon the spatial resolution of the detector and the desired angular resolution. In our case the spatial resolution of the commerically-obtained detector was approximately 200 microns point to point resolution. For a 0.4 mradian (~ 3800 Å) angular resolution would require a sample to detector distance of one-half meter.

In the modified camera (Fig. 92), the normal flight path was replaced by a new vacuum chamber. The new vacuum chamber is essentially a trapezoidal box made of aluminium with 1/16" lead lining on the inside. All of the dimensions of the flight chamber are large enough so that there is no chance of the main beam striking the inner wall no matter what entrance slits and beam limiters are employed. The lead lining serves two purposes: to minimize stray radiation from hitting the detector due to any small reflections or diffration effects from the alumnimium walls, thus cutting down the parasatic scattering, and to help stabilize the vacuum chamber and ultimately the alignment. The front section of the flight path was mounted onto a steel dove-tail flange that was compatibile with the initial section of the flight path of the original camera. In this way, the tilting mechanisms of the original camera could be retained. Mylar film covered the entrance slit of the vacuum chamber. A schematic of the system with a 1DPSD is shown in Figure 93.

The rear of the vacuum chamber was designed in an interlocking fashion. They are shown in figures 94 and 95. A slot was cut on one piece and was sealed with a sheet of 0.05 cm thick beryllium as shown in figure 94. On the other side of this piece a slit was cut perpendicular to the slot so that a tungsten beam stop (polish by a diamond tip miller) was held across this slot by a pin. The use of tungsten was necessary to stop the main beam from hitting the detector.* This piece was polished to very low tolerence to ensure that the parasatic scattering be as low as possible. The detector is mounted onto this piece is by way of a dovetail. The dovetail mount is parallel to both the slot of the rear flange and the entrance slit of the detector. A fine tread screw mechanism, equipped with a dial micrometer is attached to the dovetail mount so that there is freedom in the up-down direction for the detector only. The whole vacuum chamber and detector is then mounted on the original step scanning screw mechanism so there is freedom of up-down movement for the vacuum chamber pivoted about the tilting mechanism (this serves to raise or lower the tungsten beam stop).

---

*As pointed out by Russell [5], it is essential to mount the tungsten beam stop in the internal face of the flange so that the incident x-ray beam does not impringe upon the beryllium window. Strong diffraction maximum can be seen if the beam stop is placed after the beryllium window [9].

Alignment of the Kratky Camera with a 1DPSD

The alignment procedure is essentially consisted of three major parts: rail alignment, detector's alignment with the vacuum chamber, and electronic alignment of the detector. This alignment procedure was intially developed by Russell [1] and modified by this author. The use of the extended flight path placed severe limitations on using the normal procedure of alignment since it had to remain attached to the camera during fine adjustments. However, Russell [5] found that if the camera was finely adjusted without the flight path using the normal adjustment procedures, then when the flight path was mounted, the alignment was disturbed simply due to its size and mass.

A. Initial Rail Alignment. This is done without the vacuum chamber nor the sample chamber in place. It is necessary to use a proportional counter to record the intensity at each particular location. The nomenclature used follows that of Anderegg et al. [12].

During the course of assembling Kratky small angle x-ray goniometer an attempt at alignment was made using the manual supplied. This produced very unsatisfactory results and consequently the procedures outlined here was developed. The alignment procedure consists of a series of steps beginning with the intial alignment of the optical bench rail. It should be noted that any alignment should begin here since small maladjustments of movements of the rail can cause rather complicated and, perhaps, unsolvable problems at a step further on. Unless an experimenter can rule out misalignment of the rail then it

is strongly advised that the rail be stripped of its various components and the alignment begin from step one.

Throughout the course of the alignment one crucial assumption must be made. That is, that the track of the horizontal scanning device (HSD) is in a plane parallel to the plane containing the surface of the optical bench rail. The reason this assumption is crucial is not really associated with the alignment itself since one can produce a collimated system oriented in whatever fashion one desires. However, if the track of the HSD, and consequently the line of x-rays, is not parallel to the rail then one can not use the detection equipment supplied with the system. A scattering profile must be collected in a direction strictly perpendicular to the beam in order to correctly apply the various dismearing routines. If the condition mentioned above is not fulfilled then scattering profile can not legitimately be obtained.

As is evident the procedure consists of a series of steps labelled with an appropriate number. This does not necessitate that the order be unchanged. For example the order of steps 1, 2, 3 can be rearranged to 2, 3, 1 if desired. The sequencing listed here was the preference of the authors but can be modified if one desires.

Rail Alignment Procedure

Before entering into a detailed alignment procedure an overview of the strategy used in alignment requires that the focal spot be parallel to both the entrance slit and receiving slit and that all

three are symmetric about a center line in the camera. Consequently, the camera was divided into three sections: the rail, entrance slit collimation and the receiving slit geometry. Sections involving the rail alignment address the problem of symmetry whereas the entrance and receiving slit sections are concerned predominantly with the homogeneity of the beam. Via this approach, a systematic and rigorous alignment of the apparatus can be achieved.

Step 1: Initial Alignment of Optical Bench. Before any sort of quantitative aligning can be done the optical bench must be roughly aligned by eye. This can easily be accomplished by placing the low resolution bridge system at the front of the bench and raising it so that the bridge system is approximately the same height as the aperture on the x-ray tower. Bring the entrance slit to the midpoint of the x-ray port will accomplish this. Now, looking down the optical bench from the end furthest from the tower (referred to as rear of the optical bench) the bridge system is squared visually with the x-ray tower mount. It was found that the low resolution bridge system is best suited for this purpose.

Step 2 A. Vertical Beam Scan with V_1. With the appropriate bridge system on the optical bench a vertical scan of the beam is made. This is done by observing the intensity as a function of dial setting on the front leg, V_1. These data are plotted and the vertical position that is least sensitive to slight fluctuations is chosen. By selecting this position the stability of the beam intensity is maximized

so that drastic fluctuations in the incident beam intensity are not observed.

The data for a 19 micron slit is given below:

Vertical Position, V_1	Intensity
32	2262
33	13438
34	35879
35	66221
36	72159
37	59396
38	47239
39	41714
40	38314
41	36971
42	36557
43	37370
44	38933
45	42360
46	49450
47	62863
48	83783
49	81884
50	52404
51	23429
52	6419
53	2809

The plot for these data are shown in Figure 96. Indicated also is the position selected for the best vertical positioning.

The irregularity of the focal spot profile is due to the shape of the filament and/or current variations along the filament in the x-ray tube used to produce the electrons. Since the filament is a coil, the beam of electrons impinging on the copper target will not be homogeneous and will contain irregularities. Consequently, the x-ray intensity across the target will not be homogeneous.

Step II B. Vertical Scan With V_2. After the optimum position, i.e. the least sensitive position, of V_1 has been determined the front leg is raised or lowered to this position and locked in. Using V_2 a similar scan was performed by adjusting the rear of the optical bench. Again an insensitive position in the profile (not shown) is determined and V_2 is set and locked in place.

Step II A is repeated and the previous setting is compared to the newly obtained setting. If there is a wide discrepancy V_1 is set and locked at the new setting and Step II B is repeated. A comparison to the old setting is made. These steps are repeated until reproducible settings with V_1 and V_2 are found. When satisfactory reproducibility is obtained the rail should be at a 6° take-off angle and in a position that is not sensitive to small vibrations of fluctuations in the focal spot.

A convenient check on the take-off angle can be made from the profile of the focal spot with V_1. The width of the vertical beam profile is directly related to the size of the focal spot, the width of

the entrance slit, and the distance between the focal spot and the entrance slit. The geometry is shown in Figure 97 and the calculations are straightforward.

Step III. Tilt Adjustment of the Bridge System. Using the horizontal scanning device (referred to as HSD) and the detector equipped with a pinhole mounted flush to its face, the beam intensity if observed in the zero position of the HSD. This ensures the experimenter that contributions from both sides of the slit will be collected with equal weighting. In order to perform the remaining part of the tilt experiment it is mandatory that there be two workers present or that there be a rate meter visible to the worker while adjustments are made. The procedure is as follows: By vertical variation of the front leg the entrance slit is brought out of the main beam until the count rate is virtually nil. By reversing the direction, the slit is brought into the main beam to an arbitrarily selected count rate. This is strictly an arbitrary selection and 1 x (10^3) counts per second proved to be adequate. The slit is then moved through the main beam until the same count rate is found on the opposite side of the beam. The two readings of the vertical position are recorded along with the difference and the tilt angle. The tilt angle is then changed and the procedure is repeated with the distance traversed through the beam being determined as a function of tilt angle. These data are then plotted (path length vs. tilt angle) as shown in Figure 98.

Lower Height	Upper Height	Path Difference	Tilt Angle
30.7	55.3	24.6	3.6
30.9	55.55	24.65	3.7
31.0	55.25	24.25	3.8
31.05	55.15	24.12	3.9
31.15	55.2	24.05	4.0
31.2	55.3	24.10	4.1
31.1	55.3	24.20	4.2
31.0	55.35	24.32	4.3

The minimum in the curve is selected as the best tilt angle since when the slit is parrallel to the main beam, the distance traversed through the beam is at the minimum.

Since the scale on V_1 is not calibrated to the tenths position one can question the accuracy of these results. However, the results were found to be reproducible and the subsequent homogeneity run bore this out.

Alternatively, Anderegg et al. [12] describe an alternate technique which may be substituted for the above procedure. The slit which those experimenters employed was not supplied with the camera, thus a suitable piece is needed to be constructed in this laboratory in order to conduct the tilt experiment as they prescribe.

Step IV A. Beam Homogeneity. The height and tilt determined in sections II and III are set by tightening of the adjustment screws. The beam is then scanned horizontally to determine the width of the beam

and its homogeneity. If the intensity of the beam is not constant across the width of the beam then the tilt was not done properly and Step III should be repeated.

Step IV B: Beam Symmetry. Once homogeneity is obtained the symmetry of the beam about the zero point on the HSD is determined. If the beam is not symmetric then the front leg needs adjustment or the back leg needs adjustment in the horizontal plane. This is accomplished by adjusting H_1 and H_2. It is rather difficult to determine whether H_1 or H_2 require adjustment due to their peculiar pivot points. Trial and error, although tedious was the choice of attack. It will be found that accurate eyeing of the rail (Step I) will yield fairly good results.

Once satisfactory symmetry is obtained in this position ($\pm$ 5%) the detector is placed ~ 40 cm down the rail and the symmetry is again determined ($\pm$ 5%). Adjustment of legs with the detector in this position until symmetry is obtained should be minimal. Once symmetry of the beam along the rail is found, then the set screws for the horizontal positions are tightened. The results of this section are shown in Figure 99.

Step V: Placement of the Bridge Beam Limiters. The beam limiters positioned just before the final bridge collimator serve two important functions. First of all they restrict the size of the beam to eliminate parasitic scattering arising from the walls of the vacuum flight path. Secondly, coupled with the actual size of the focal spot the

limiters define the beam in the length (horizontal) direction. The size of the limiters used in the apparatus will determine whether or not an "infinite height" beam assumption can be used for desmearing procedure.

Alignment with the Vacuum Chamber

We will assume that the electronics of the detector are set to detect CuKα radiation. The vacuum chamber is now placed very carefully onto the rail so as not to disturb the rail's alignment. The detector is then lowered onto the rear flange such that its wire is below the tungsten beam stop and in the beam itself. It is now necessary to raise the whole vacuum chamber with the attached detector by the use of the original step scanning mechanism. Now using the attenuated main beam, the chamber is slowly lowered until the incident x-ray start hitting the detector's wire. In order to determine when the tungsten beam stop is set perpendicular to the incident beam, the total number of background counts were collected versus the tilt of the vacuum chamber. When the tungsten edge is perpendicular to the incident beam, the total counts will be minimized. Alternatively, the tilt can also be set using the duck tendon scattering (to be discussed shortly) as a function of the tilt of the vacuum chamber. The correct tile occurs when there is maximum resolution of the duck tendon scattered profile.

Electronic Alignment

The factory calibration of the detector is included in the operating manual of the detector. The theory of the electronic circuit of the systems are given in the articles published by Kopp [6,7,8] and Hendricks [13] gave excellent review articles on the effect of gas pressure (only applicable in the Tennelec detector) on the resolution of the detector.

The schematic block diagram of the UMASS 1DPSD, using a Time to Amplitude Convertor (TAC) is given in Figure 100 and is pictured in Figure 101. In Figure 100 the wavy curve between each component is the shape of the electronic pulse that is being outputted from its proceeding component and that is being inputted into its following component. The Tennelec flow gas detector outputs a negative pulse, while the TEC sealed detector outputs a positive pulse.

The basic underlying logic behind the operation of a position sensitive detector is that an x-ray source, either from sample scattering or main beam, is energized once it hits the detector. Then a pulse is generated and travels along the detector's wire in both directions. The two small electronic pulses in each direction are amplified first by its preamplifier in the detector to create a fast negative or positive pulse (< 1 volt) along its direction. Arbitrary, it is designated that one way be the start channel and the other way be the stop channel. Right here is the basic logic of position resolution. The x-ray that generate a pulse at a particular location in the wire travels in both directions of the wire. The time that each pulse

reaches the preamplifier is different depending on which part of the wire it is coming from. Thus the timing difference of the two identical pulses that reach the preamplifier is different depending on the location of the wire. It is this timing difference that one is measuring. Since the timing difference is on the order of nanosecond (10^{-9} second), it is essential that the start and stop circuit be completely identical since any difference in one circuit will affect the electronic resolution.

The fast negative or positive pulse that is being outputted along the start and stop channel's preamplifier is then amplified by its amplifier and each amplifier outputs a bipolar pulse, which is then fed into the timing single channel analyzer (or single channel analyzer) (TSCA). This timing analyzer only picks off where the bipolar pulse crosses the base line. The timing SCA then generates a fast negative pulse that is being fed into the TAC. The TAC serves two functions: it collects the fast negative pulse from each start and stop channel and resolves its timing difference and generate an amplitude voltage (hence the name time to amplitude converter), that corresponds to a timing difference, that can be converted by a multichannel analyzer (MCA) to resolve the position on the detector wire as a function of channel. However, before the TAC will output an amplitude voltage, the timing difference must be within a timing gate for which it is valid and be in the correct energy spectrum (to be discussed shortly). Thus we can see at this point why all the components of the circuits must be in proper operation condition, the

amplifier must be of very low noise and drift-free, the TSCA be precise enough to pick off the crossover point, and the TAC being able to resolve very fine timing differences.

The middle circuit of Figure 100 is the energy discrimination and the timing gate circuit. This circuit serves two major functions: first it sets a voltage range for the appropriate energy (i.e. Cukα, Mnkα, etc.). This is done by the energy discriminator in the same manner as a pulse height analyzer in a proportional counter. The other function of the ciruit is to set the timing gate for the TAC to use. The timing gate incorporates all of the timing differences between the start and stop channels for the position resolution of the detector that one wishes to analyze.

In the following section, a step by step procedure is given for aligning the electronic of the UMASS 1DPSD. However, before proceeding with this procedure, it is essential that the mechanical alignment of the Kratky camera is done first. For this alignment procedure, one will need the following items:

a. A uniform radioactive source (usually Fe 55).

b. A lead mask with sixteen or so slots (< 1 mm) cut into it, shown in Figure 102 and hereafter referred to as lead mask.

c. An osscilloscope capable of resolving in the nanosecond range.

d. A pulse generator.

Before starting, it is essential that each electronic component is operating properly as specified by the owner's operating manual that comes with each component.

Step I: Correct Energy Pulse for the Electronic. Set the correct operating voltage and polarity for the detector as specified in the owner's operating manual. Higher voltage setting will increase the spatial resolution but decreasing the lifetime of the wire. DO NOT exceed the maximum voltage allowed. Now set the detector on the Kratky camera with its vacuum chamber and the main beam stop (tungsten) above the main beam. Connect the oscilloscope to the bipolar output of the main amplifier (either start or stop channel) with a 100 Ω termination. Now put a sample in the sample chamber and open the x-ray window. Look at the bipolar pulse on the scope and adjust the gain on the amplifier to obtain the maximum voltage output without oversaturation. Note the gain (both the coarse and fine) setting and set the identical gain setting on the other timing amplifier. The shaping time is set as specified by the detector's manual, generally less than 2 μses, depending on the detector used.

Step II: Walk Adjustment. Now disengage the detector wire input to the main amplifiers and connect one of the main amplifiers to a pulse generator, on the attenuated output. Adjust the rise time of the pulse generator to minimum (corresponding to fast rise time) and the pulse height and normalizer until a maximum of 10 volts is registered on the scope. DO NOT ADJUST the gain setting of the amplifier. Disconnect the output of the amplifier to the scope and connect it into the input of the TSCA. Set the TSCA to bipolar pickoff and set the window completely open (i.e. lower level discriminator (LLD) at 0 volt and upper level discriminator (ULD) at 10 volts). We do not use

the discriminator on the start and stop circuit. Connect the negative output of the TSCA into the scope and the direct output of the pulse generator to the external trigger of the scope. Triggering off the direct output pulse, adjust the trigger level until a negative pulse appears on the scope (set the time division to about 5 μsec/div). Remember to have a 100 Ω terminator. Now use the delay triggering and set the delay time division to 1 μsec/div. or less. Adjust the time interval until the negative pulse reappears on the scope. Now increase the sensitivity of the delay time division (i.e. towards the nanosecond/div range). Now attenuate the pulse at the pulse generator to 2X, look at the negative pulse at the scope. There should NOT be any shift in its position. If there is, adjust the WALK screw on the timing SCA until there is no shift when switching back and forth on 2X on the pulse generator. Repeat for 4X, 10X, etc. until 100X, if possible. As one increases the attenuation factor, there will be increasing distribution of the pulse's position due to decrease in the signal to noise.

Now reconnect the wires to the detector.

STEP III. SETTING THE TIMING GATE

Let the detector face the Fe 55 radioactive source. Connect the output of the summing amplifier to the scope and adjust the gain to give maximum pulse amplification without oversaturation. Shaping time is the same as that of the timing amplifiers. The bipolar pulse one sees on the scope is the summation of all pulses from the detector. Notice the scale of the voltages. The LLD and ULD of the energy

discriminator is set to incorporate these pulses only. For example, consider the diagram below of a set of pulses one sees on the scope:

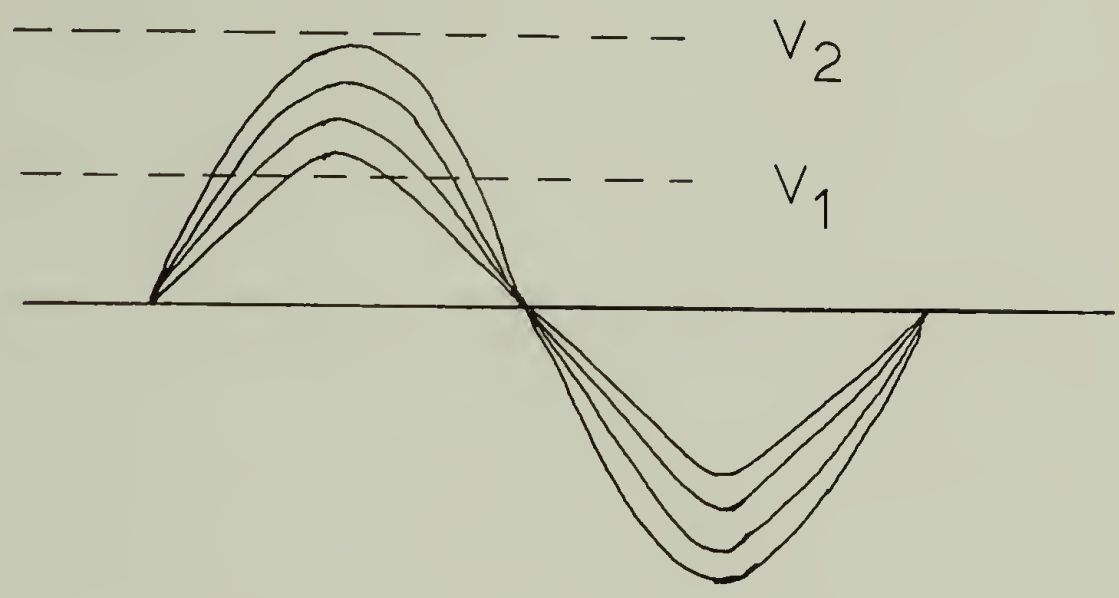

The discrimination is set at V_1 for the LLD and V_2 for the ULD. This setting of the discriminator is different depending on the radiation source.

At this moment the discriminator is set for Fe 55. Later on, one needs to reset the LLD and ULD for CuKα in a similar fashion.

Connect the output of the TAC to the multichannel analyzer. Set the gate wide open on the gate and delay generator. Set the timing delay on the start channel (the end that is towards the zero angle) to minimum and the timing delay of the stop channel to maximum. Adjust the TAC range until the whole detector wire is on the MCA. This can be checked by placing the lead mask in front of the detector and count the number of spikes that are shown. They should correspond to one another. Remove the lead mask and adjust both the timing delay of the start and stop channels until they just start affecting the homogeneity of the wire. Now recollect the data of the Fe 55 radiation source. The intensity spectrum should be constant across the whole

wire unless there is deterioration on the wire. Russell et al. [5] gave alternative ways to test the homogeneity of the detector's wire.

The linearity of the detector is determined according to the manner of Russell [5] based upon the manner of Schelten and Hendrick [9]. The lead mask is placed in front of the detector and a profile is obtained as shown in Figure 103. The position of the maxima were determined as a function of channel number and plotted versus their real-space separation. This plot should give a straight line. If not, then the walk adjustment off, provided every component is in operating condition as specified in the manual. As alternative way of determining the linearity of a very small length of wire is by way of the duck tendon scattering. This will be discussed later.

Now determine the length of the wire that is needed for measuring the scattering. This is deterined geometrically as to the maximum angle that one needs to measure. Adjust the TAC range to the wire length that is needed. Now readjust the start and stop delay to be within the TAC range. Adjust the delay and the timing gate of the discrinimator and gate generator to be also within the TAC range.

STEP IV: ADJUSTING FOR CuKα AND ZERO ANGLE SCATTERING

A. ADJUSTING FOR CuKα

Reposition the detector on the vacuum chamber and lower the detector until the wire is sensitive to the parasatic scattering off the tungsten beam stop. Now connect the output of the summing amplifier to the scope and adjust the gain to give maximum pulse amplification without oversaturation. Readjust the LLD and ULD of

the discriminator accordingly.

B. ZERO ANGLE DETERMINATION

One characteristic of a Kratky collimation system is the asymmetric profile of the incident x-ray beam. Because of this the center of gravity of the beam (i.e. the zero of angle) must be determined experimentally. Using standard step-scanning equipment this can be done easily by scanning through the beam with subsequent integration and determination of the first moment of the profile. However, this could not be done with a 1DPSD because of two reasons:

1. There is no easy method available for obtaining a beam profile without disturbing the system due to the position of the tungsten beam stop.

2. There are less than 10 channels available in the MCA to obtain the attenuated beam profile, which only permits a coarse integration of the profile.

Thus an alternate method was given by Russell [5] based upon the works of Stinson et al. [14]. This method employs a sample scattering. The sample selected was a dry, uranyl-acetate stained duck tendon specimen. Stinson et al. have shown that up to seven orders of diffraction maxima were clearly visible in the low angle region. A scattered profile obtained on the same specimen with the apparatus used is shown in Figure 104. For this case 9 orders are clearly visible. Employing Bragg's law ($n\lambda = 2d \sin 2\theta/2$), where $d = 640$ Å the repeat distance of the duck tendon, we can determine the

angle as function of channel number. Thus with this procedure, two major elements are seen:

1. The relationship of the channel number to the angular position of the wire can be determined, thus serving as a standard for angular calibration.

2. Not only the zero angle can be obtained by extrapolation but also the linearity of the detector in the low angle region can be obtained. Plot of the position of each scattered maximum versus the channel number will be a straight line. Such a plot is shown in Figure 105. As can be seen, this gives excellent angular resolution and linearity.

STEP V: NOISE LEVEL AND PARASATIC

The system's performance was characterized in three different ways:

1. The apparatus should have low noise level.
2. A minimal of parasatic scattering which is characteristic of a Kratky geometry.
3. The apparatus should be able to resolve both weakly scattered intensities and high angular resolution.

The 1DPSD has a very low noise level because the electronic noise is distributed over the entire angular range, even though the 1DPSD has approximately the same electronic noise per unit time as a proportional counter. Therefore, if 100 channels were being used on the MCA the electronic noise and background would be 100 times less per angular reading on the 1DPSD than with a proportion counter. This apparatus was found to have an average total backgound (electronic noise)

level of less than 1 count per channel over a collection time of 5 hours.

When the camera is properly aligned, the parasatic scattering will drop off very fast in both intensity and angular position. This was found to be the case.

The third performance test was done on the angular resolution. This was previously shown for the case of the duck tendon scattering where one can easily see a spacing of 400 Å while employing a relatively wide entrance slit. Morra [15] employed the 1DPSD to analyze the scattering from a semi-crystalline blend and was able to resolve easily a periodicity greater than 350 Å.

STEP VI: SUMARY AND COMMENTS

Thus the basic elements of the alignment procedure are given. It should be said at this time that one should not be intimidated by all the buttons and switches of the electronic components. Practice first with the Fe 55 radioactive source and the lead mask. Once you have mastered the resolution of the slots on the lead mask then all there is to do is to adjust to the region one wishes to see.

Russell [5] gave an excellent summary on the effect of fill gas (for the Tennelec's detector), detectors wire and comparison to other systems. The use of a 1DPSD is a very powerful instrument to collect SAXS data. Rather than waiting 24 hours or more to collect a scan, a 1DPSD can collect SAXS data in less than 5 hours with good S/N. If the sample scattering is weak, then a longer collection time is necessary. Furthermore, since one is able to see the scattering

profile, it can be immediately qualitatively deduced whether the data collected is correct or not, or for a series of sample, any kind of trend is noted or not.

For this study, both types of detectors were used. If it was found that there was no significant differences between the detectors as far an angular resolution and linearity goes. However the TEC detector does have one major advantage in that the resistance does not change when there is deterioration of the wire, unlike the quartz wire. This is especially so when one is dealing with strong scattering. Nevertheless, when both are properly aligned electronically, the homogeneity and linearity of the wires are indistinguishable.

Figure 92. Photograph of the 1DSPS mounted on the Kratky camera.

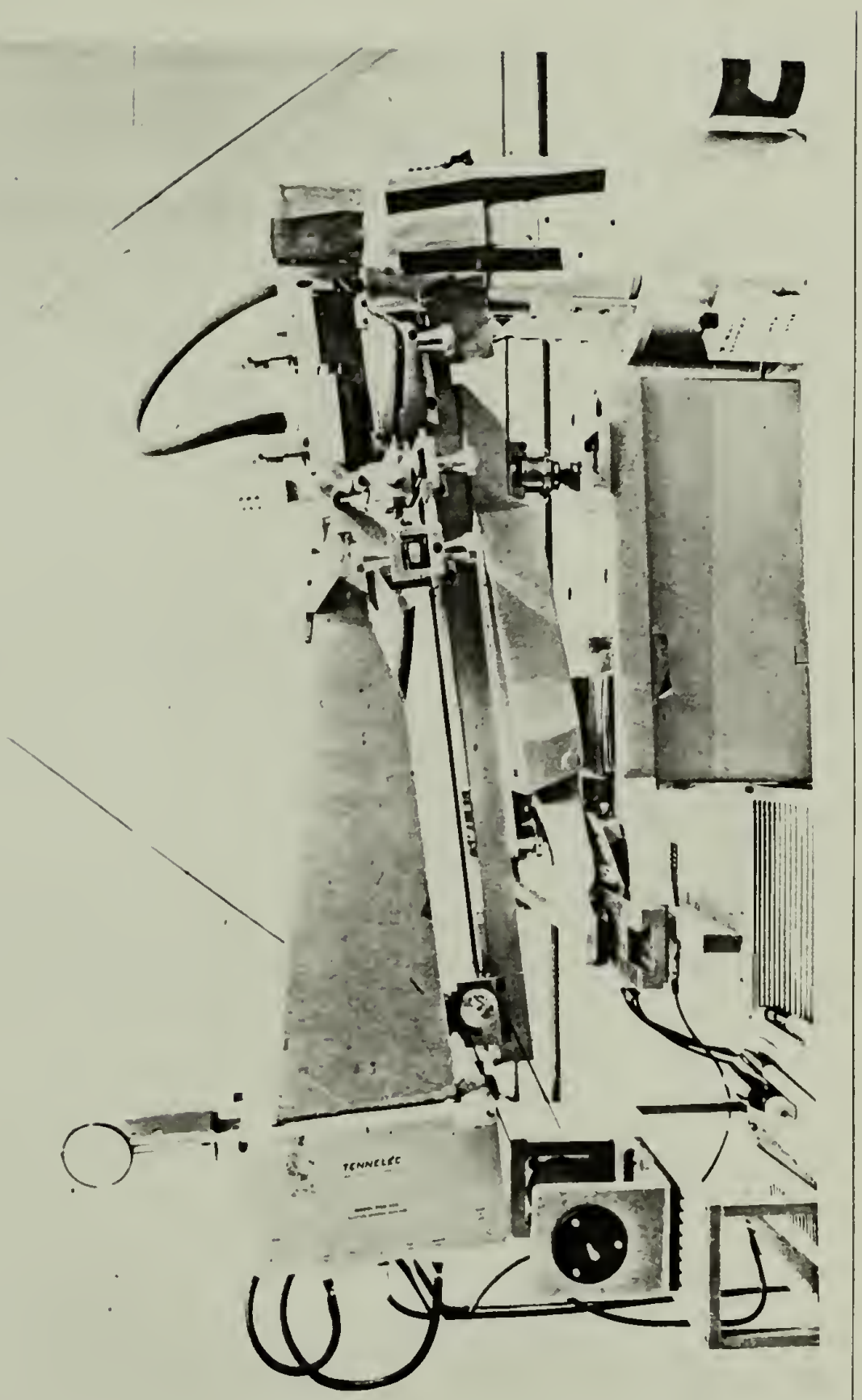
TENNELEC

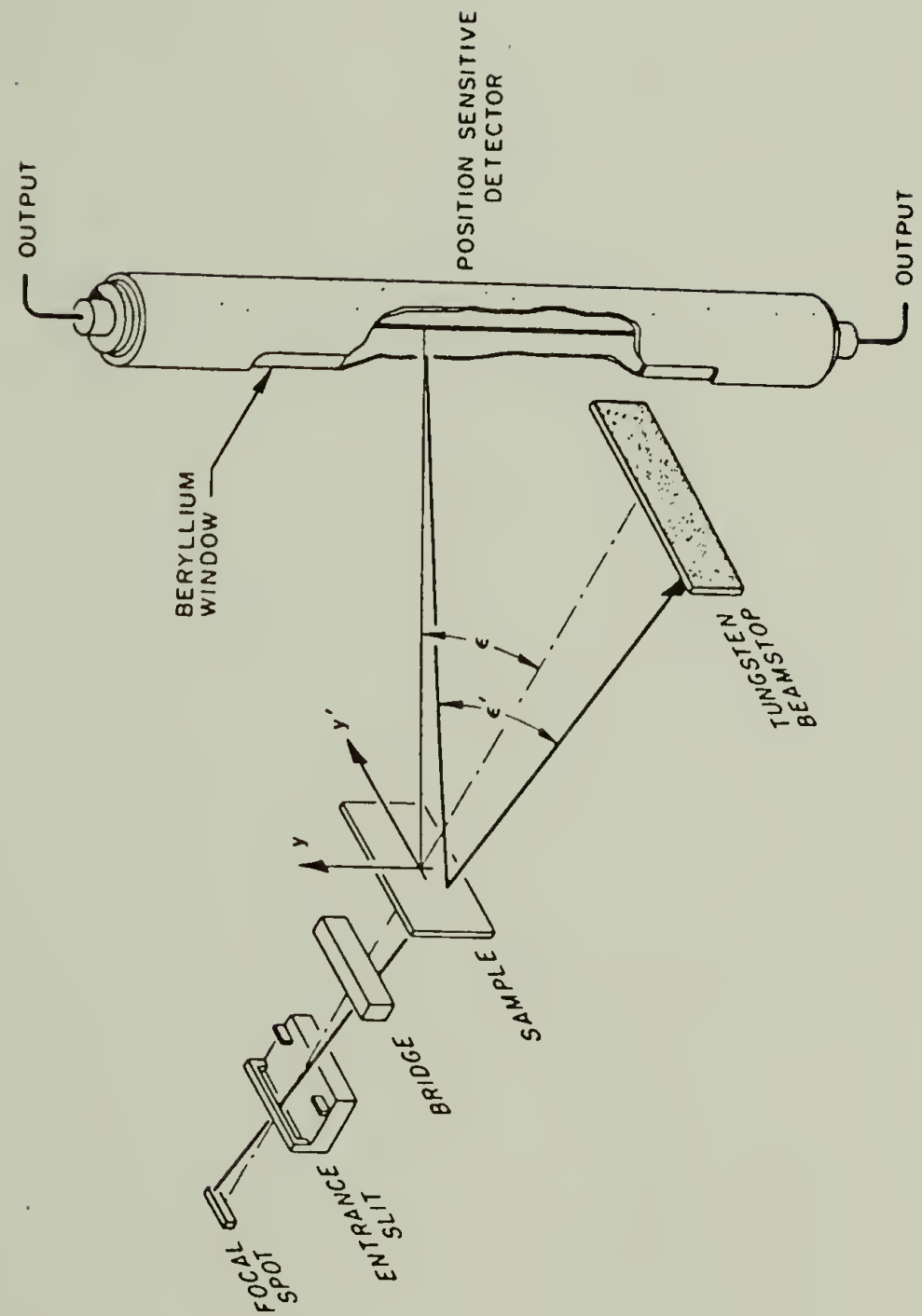

Figure 93. Schematic of system with 1DPSD (reference 5).

Figure 94. Exterior view of the rear flange showing the beryllium window and the dovetail mount for the detector.

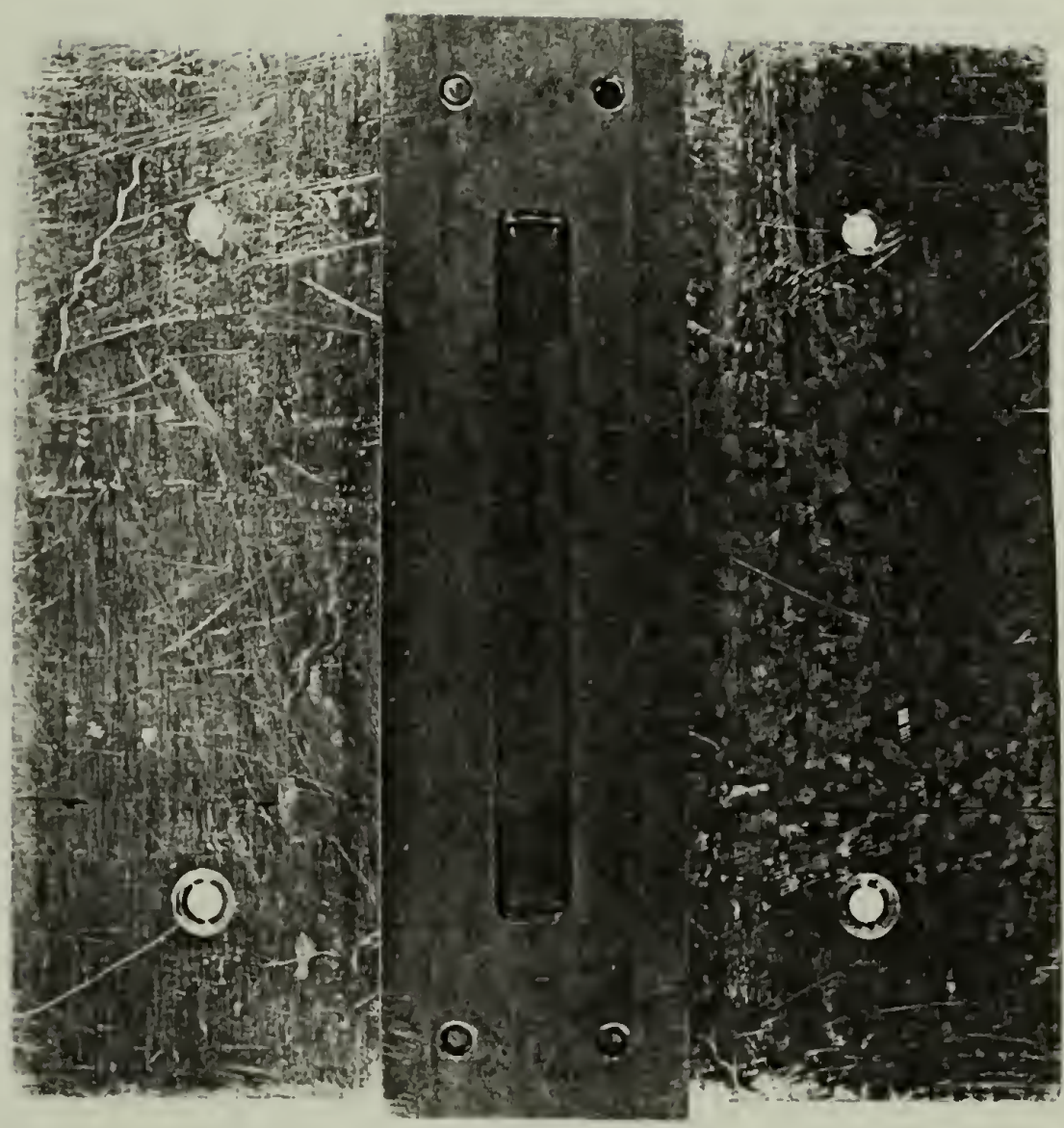

Figure 95. Interior view of the rear flange showing the pin for holding the polished tungsten main beam stop.

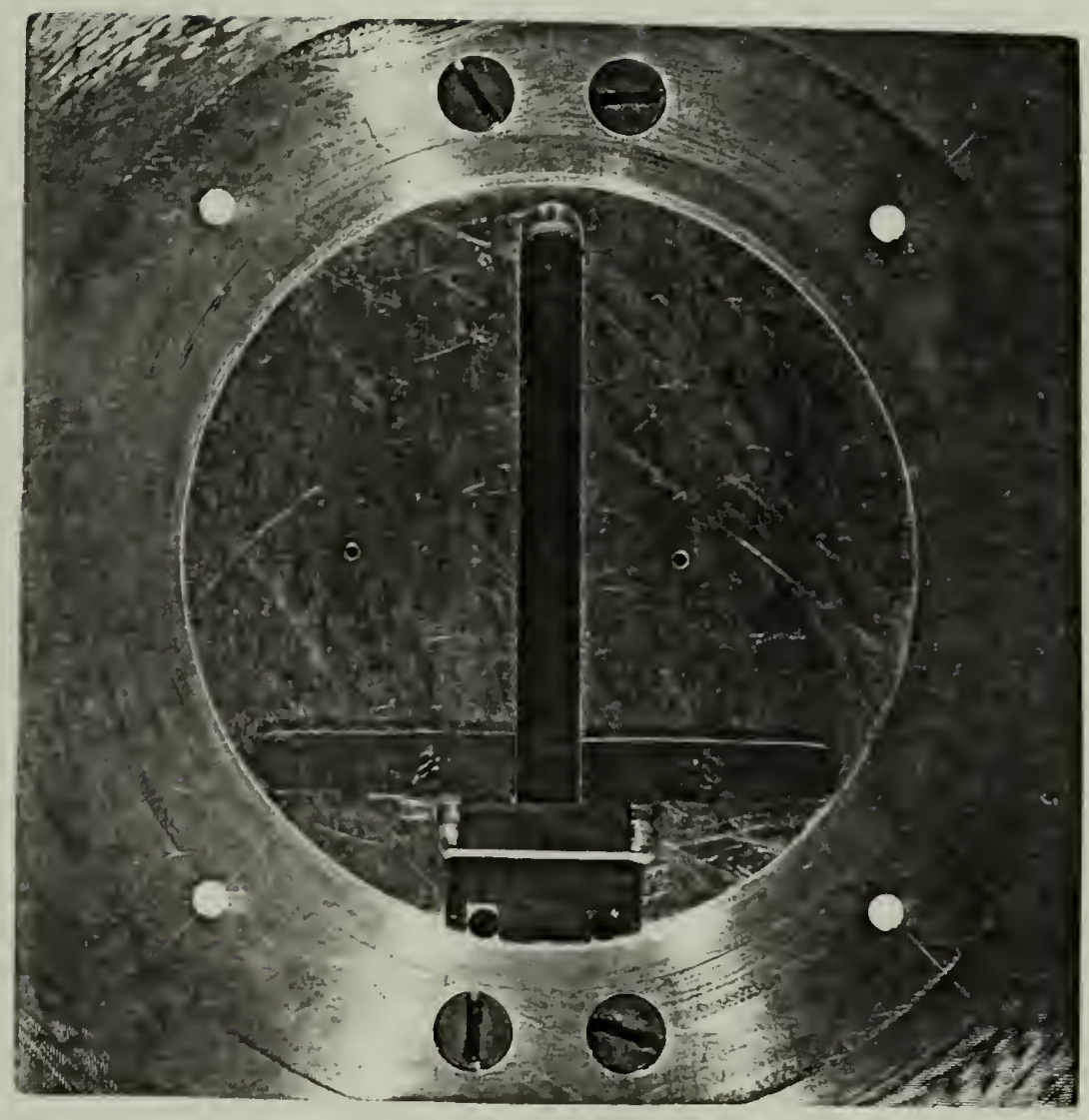

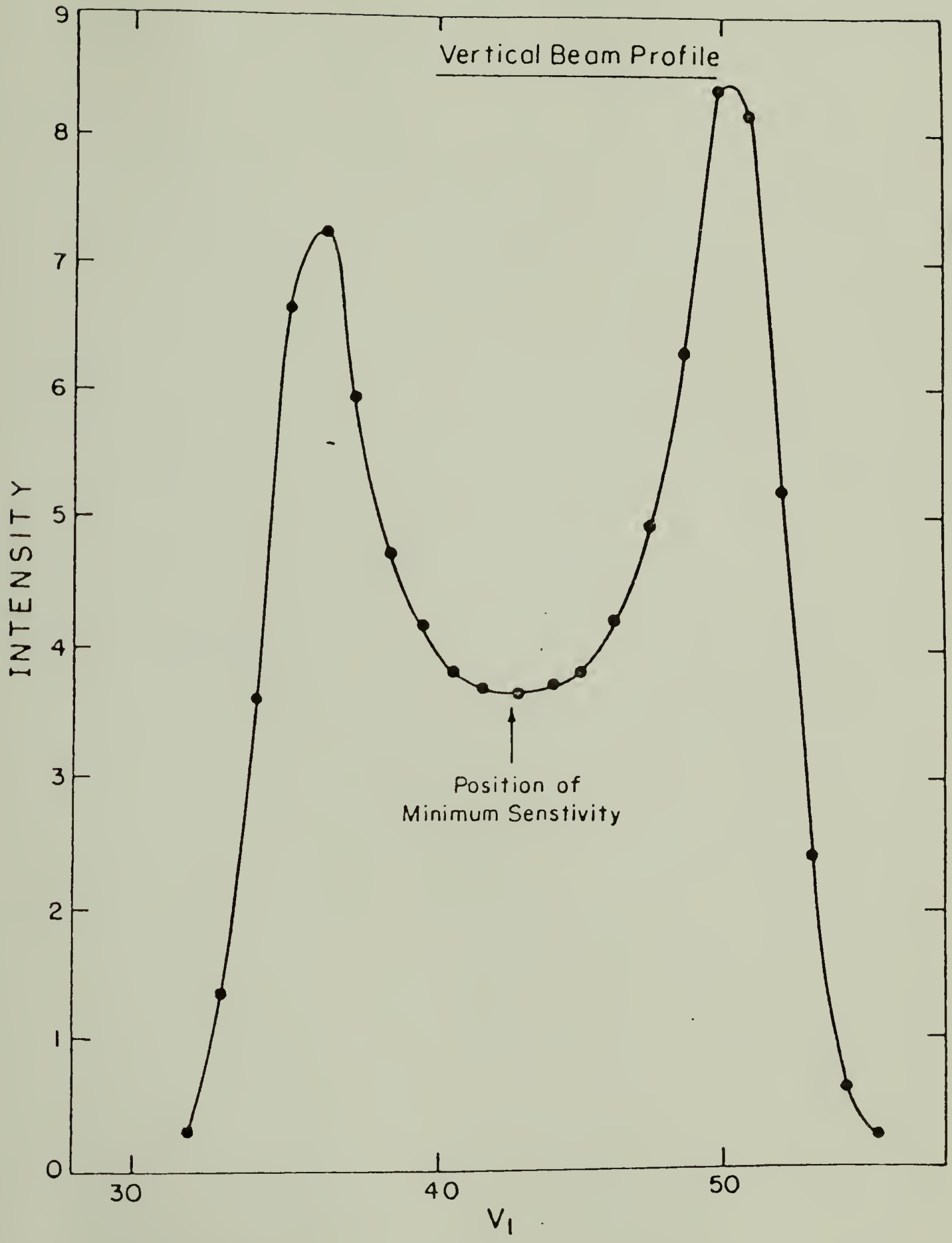

Figure 96. Vertical main beam profile.

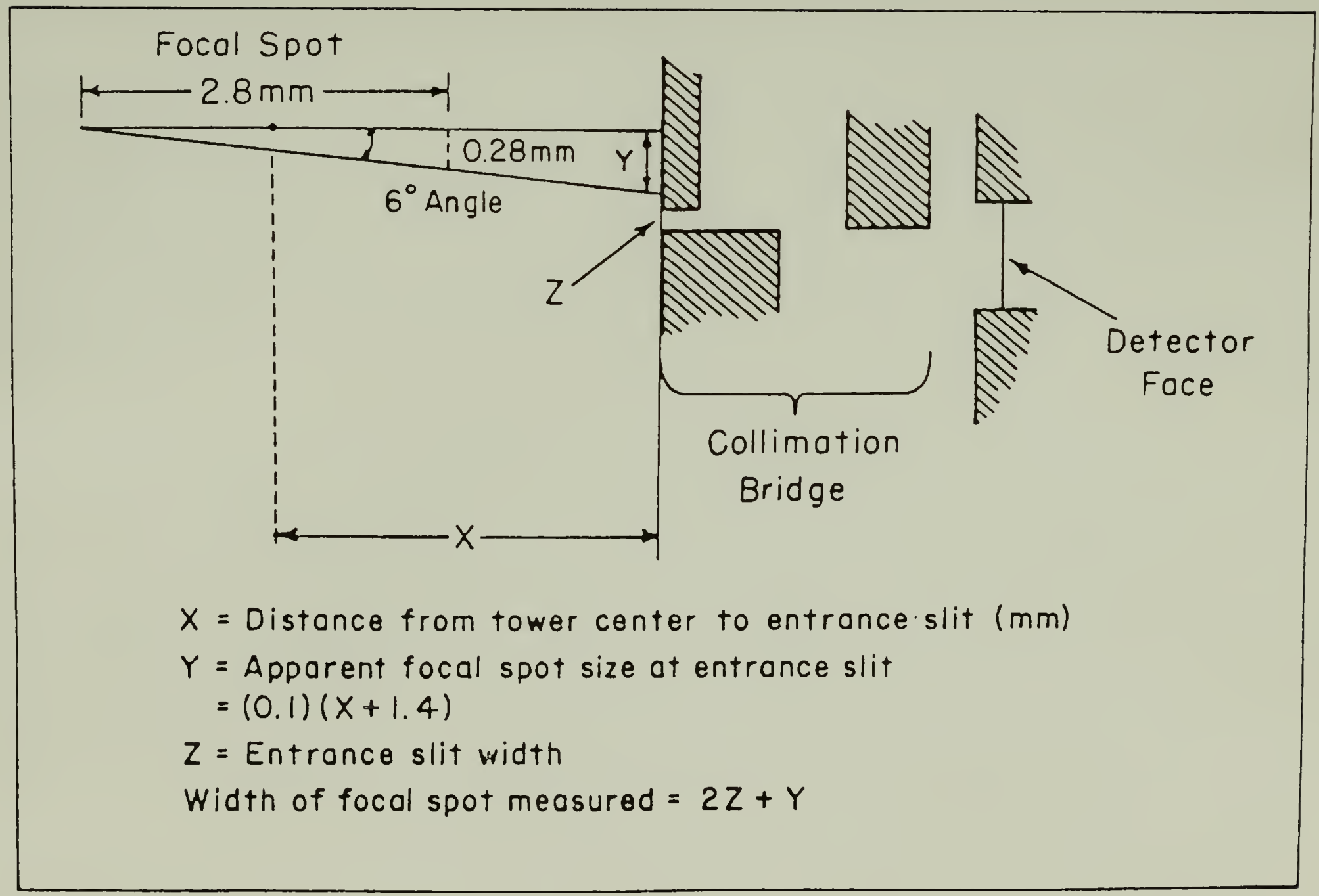

Figure 97. Apparent focal spot size.

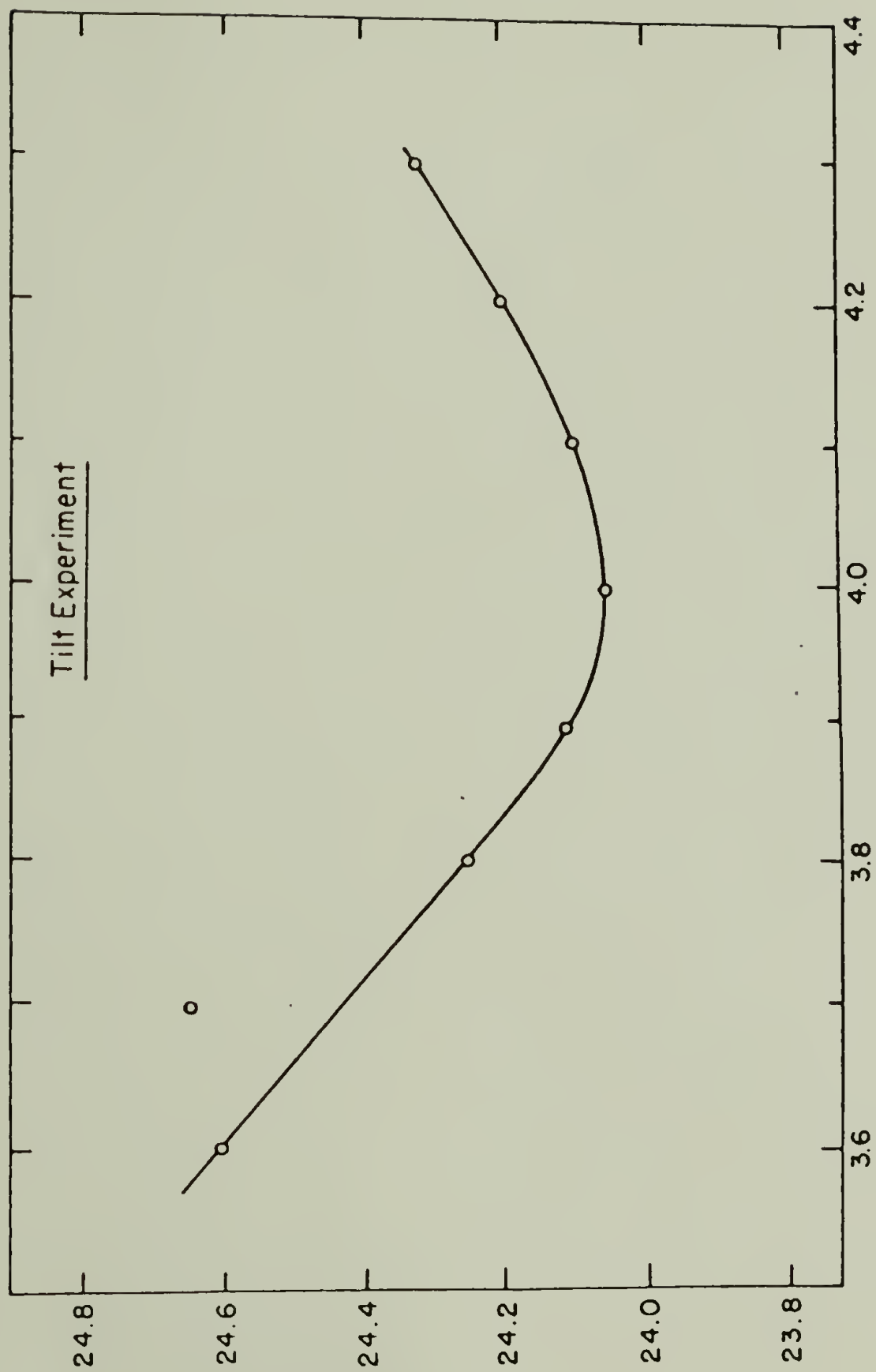

Figure 98. Tilt experiment to determine the correct tilt angle, which is the minimum of the curve.

Figure 99. Horizontal beam profile of the Kratky camera taken at a distance of 33.5 and 62.5 cm from the focal spot.

Horizontal Beam Profiles

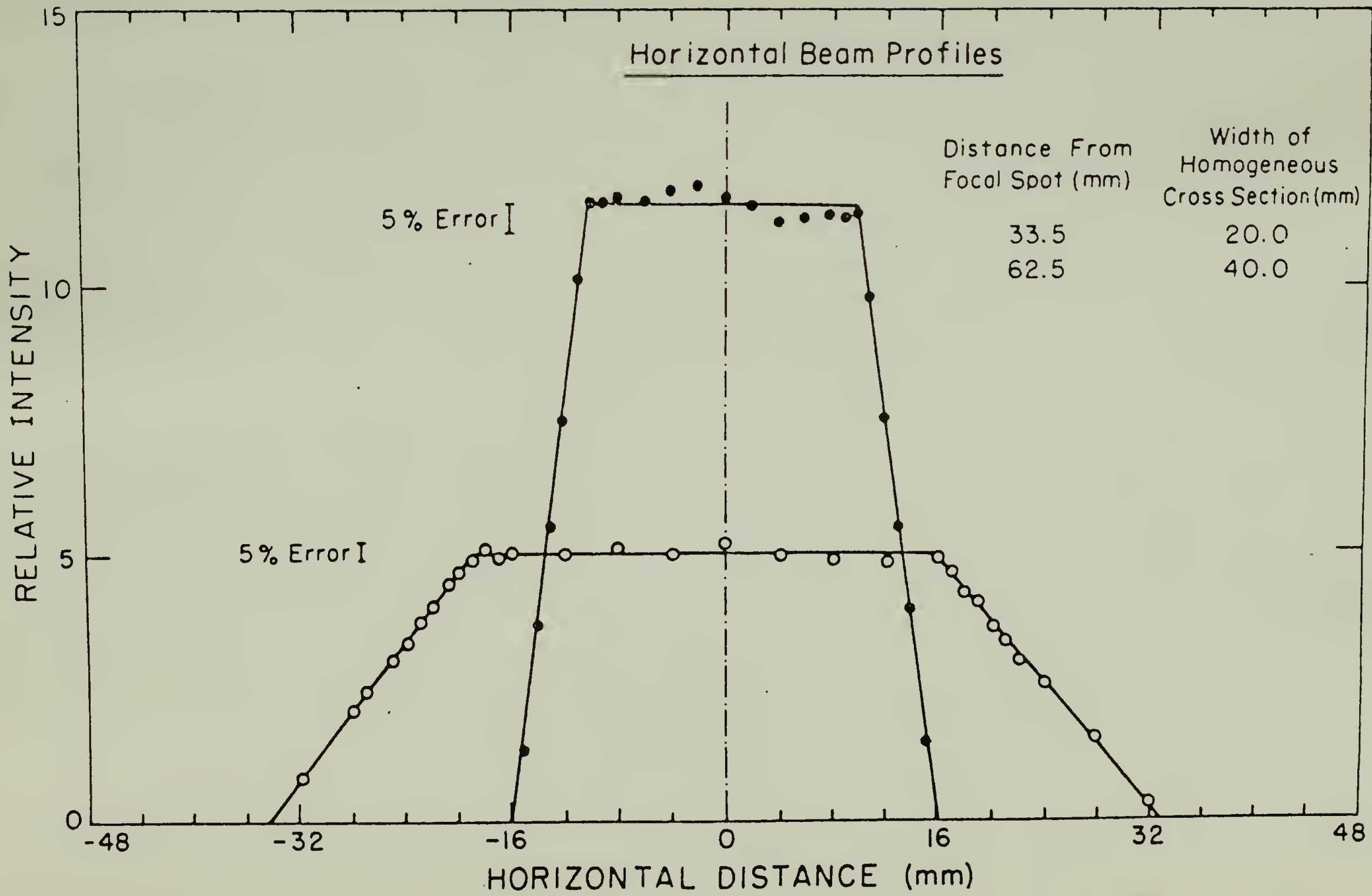

Distance From Focal Spot (mm)	Width of Homogeneous Cross Section (mm)
33.5	20.0
62.5	40.0

Figure 100. Analog signal processing electronics for the detector.

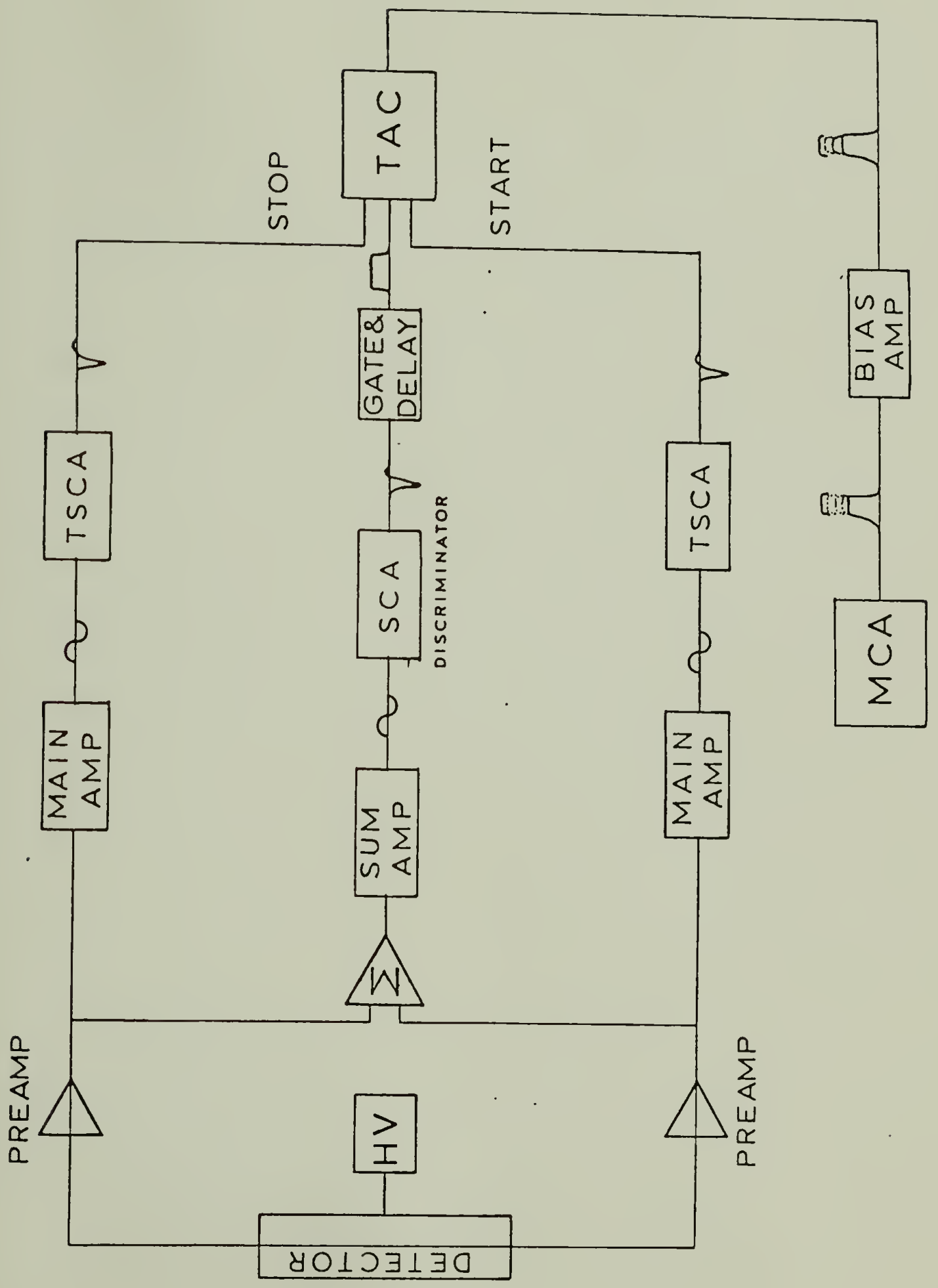
TAC
STOP
START
GATE&
DELAY
SCA
DISCRIMINATOR
TSCA
TSCA
BIAS
AMP
MCA
MAIN
AMP
MAIN
AMP
SUM
AMP
PREAMP
PREAMP
HV
DETECTOR

Figure 101. Photograph of the electronic set-up for the 1DPSD.

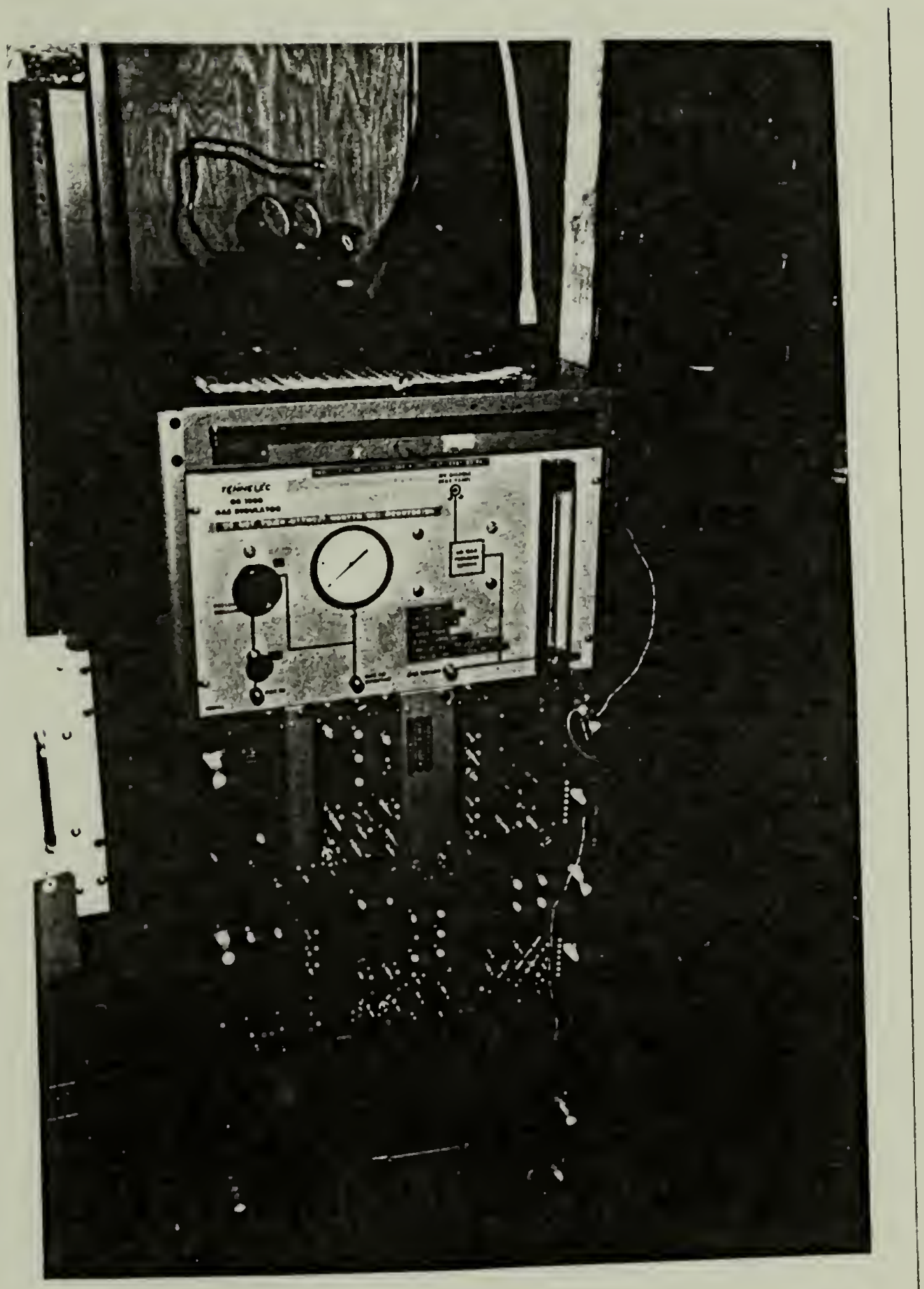

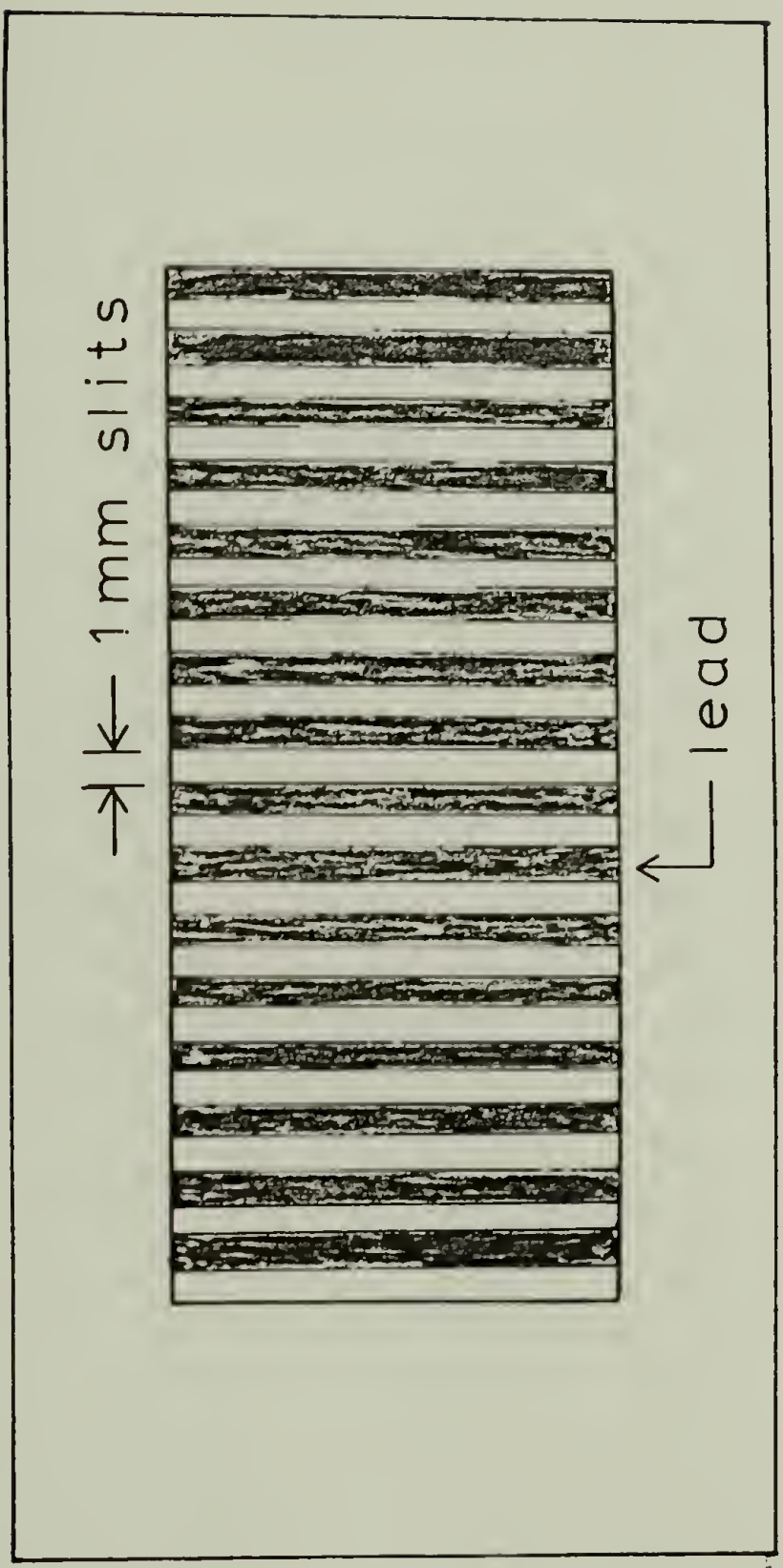

Figure 102. Schematic of a lead mask used for determining the linearity of the detector's wire.

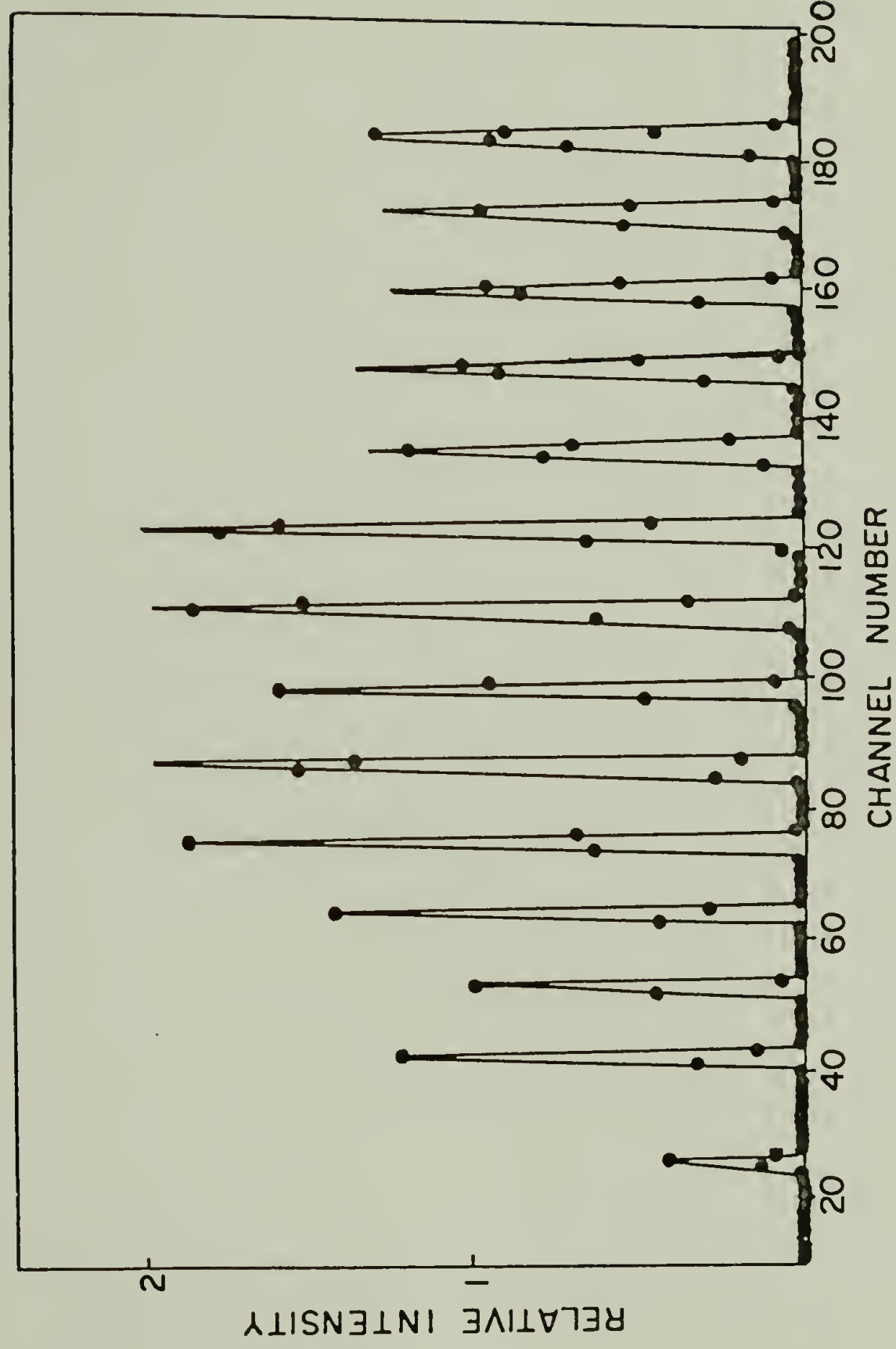

Figure 103. Linearity test as determined by recording a Fe55 spectrum with a mask consisting of 15 narrow (1 mm) slits normal to the detector length in front of the detector (from reference 5).

Figure 104. Photograph of the uranyl acatate stained duck tendon. This is used to determine the linearity of the wire at small angles and to determine the channel of the zero order scattering.

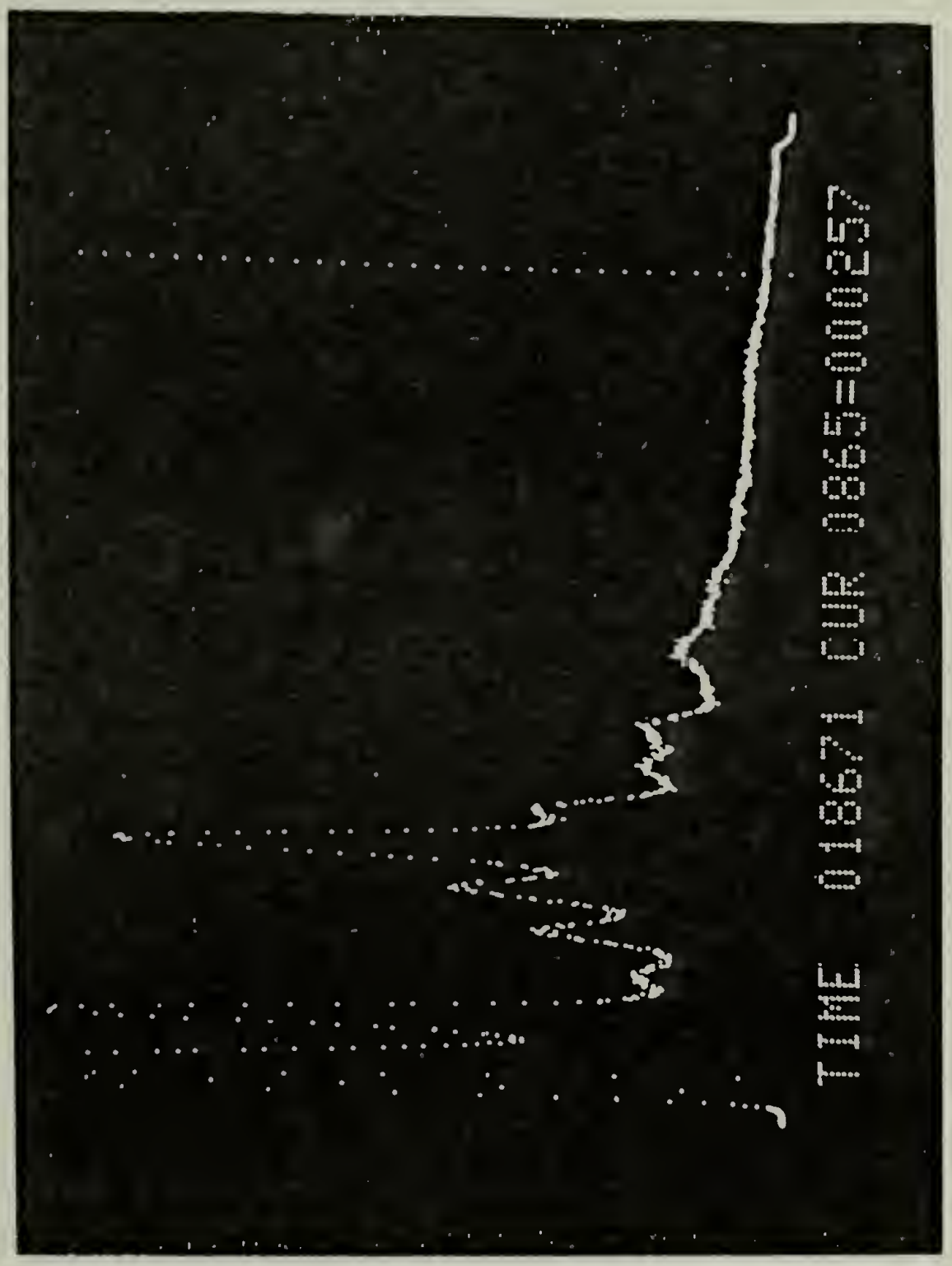
CUR 06:05:05
1.00
1.50

Figure 105. Plot of the scattering angles (as determined from Bragg's law diffraction for the uranyl acetate stained duck tendon) vs. channel number. The linear regression fit is represented by the drawn line.

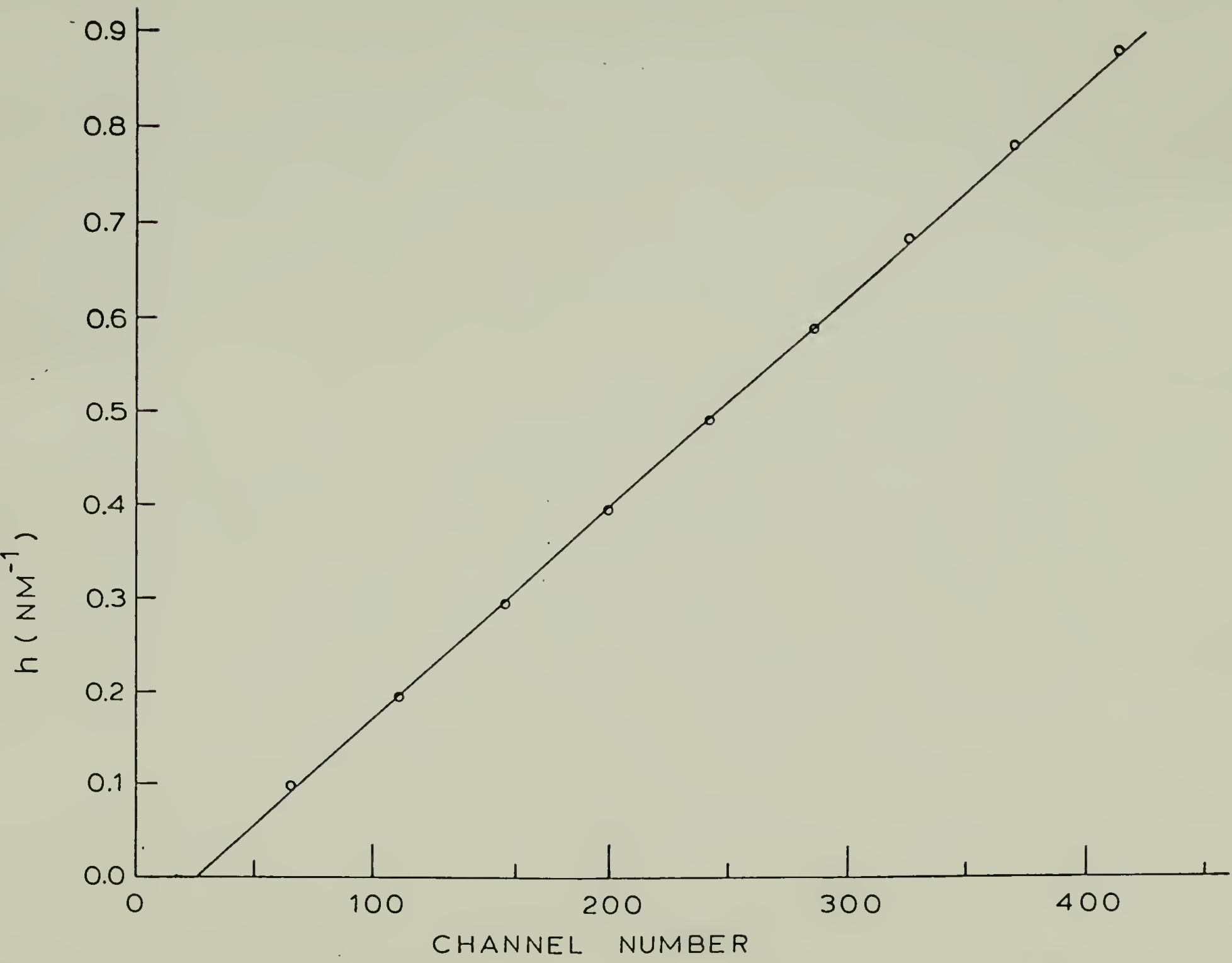
0.9
0.8
0.7
0.6
0.5
0.4
0.3
0.2
0.1
0.0
h (NM^{-1})
0
100
200
300
400
CHANNEL NUMBER

APPENDIX II

REFERENCES

1. T.P. Russell, private communication.
2. Specification Sheet for Kratky Camera, Anton-Parr, Austria.
3. L.B. Schatter, R.W. Hendricks, Opt. of Kratky SAXS Coll. Sys. Para., Oak Ridge Nat'l. Lab Rep. ORNL-TM-4278 (1973).
4. T.P. Russell, Ph.D. Dissertation, Univ. of Massachusetts, 19 .
5. T.P. Russell, R.S. Stein, M.K. Kapp, R.E. Zedler, R.W. Hendricks, J.S. Lin, The Application of a One-Dimensional Position-Sensitive Detector to a Kratky Small Angle X-Ray Camera, Oak Ridge National Laboratory Report ORNL/TM-6678 (1979).
6. C.J. Borkowski and M.K. Kopp, Rev. Sci. Instrum. 39, 1515 (1968).
7. C.J. Borkowski and M.K. Kopp, IEEE Trans. Nucl. Sci. NS17, 340 (1970).
8. C.J. Borkowski and M.K. Kopp, IEEE Trans. Nucl. Sci. NS19, 161 (1972).
9. J. Schelten and R.W. Hendricks, J. Appl. Cryst. 8, 421 (1975).
10. O. Kratky, Z. Electrochem., Ber. Bunsegnes. Physik Chem. 58, 49 (1954); 62, 66 (1958).
11. O. Kratky, in Small Angle X-Ray Scattering (H. Brumberger, ed.), Proceeding of Conference held at Syracuse Univ., June 1965, Gordon and Breach, New York (1966).

12. J.W Anderegg, P.G. Mardon, and R.W. Hendericks, An Alignment Procedure for the Kratky Small Angle X-Ray Camera, Oak Ridge National Laboratory, Oak Ridge National Laboratory Report ORNL-4476 (1970).

13. R.W. Hendricks, Nuc. Inst. and Methods, 102, 309 (1972).

14. R.H. Stinson, M.W. Bartlett, T. Kung, P.R. Sweaney and R.W. Hendricks, Biophysical J., 26, 209 (1979).

15. B.S. Morra, Ph.D. Dissertation, Univ. of Massachusetts (1980).

APPENDIX II

SINGLE CHAIN SCATTERING FACTORS FROM HIGHLY CONCENTRATED BLENDS

Measurements of single chain form factors by small-angle neutron scattering from polystyrene blends containing high concentrations of labelled molecules†

G. D. Wignall, R. W. Hendricks**, W. C. Koehler and J. S. Lin
Oak Ridge National Laboratory, Oak Ridge, Tennessee 37830, *USA*

and M. P. Wai, E. L. Thomas and R. S. Stein
Polymer Research Institute, University of Massachusetts, Amherst, Massachusetts 01002, *USA*
(*Received* 21 *November* 1980, *revised* 30 *December* 1980)

A series of small angle neutron scattering measurements on blends of normal polystyrene (PSH) and labelled (deuterated) polystyrene (PSD) have been made with concentrations of PSD from 5 to 50 mol %. It is shown that the single chain form factor of the polymer in bulk can be obtained from a single concentration measurement for any concentration of labelled molecules, providing the molecular weights of the parent and labelled molecules are the same and the molecular weight distributions are narrow.

INTRODUCTION

Small-angle neutron scattering (SANS) measurements on samples made up of a host polymer matrix in which a proportion of isotopically labelled molecules are dispersed have been used in a wide variety of studies of amorphous[1-4] and crystalline[5-8] polymers. These measurements have conventionally been performed with small relative concentrations of labelled molecules and have involved an extrapolation to zero concentration in order to eliminate interchain interference effects. The intensity of the scattering signal is limited by the small number of labelled chains, and this has restricted the SANS measurements to strongly scattering systems in order to achieve a reasonable signal-to-noise ratio.

Recent developments in scattering theory have indicated that it is possible to extract both the single-chain and interchain (interference) functions by performing measurements at high relative concentrations of labelled polymer, and Williams *et al.*[9] first reported SANS experiments on concentrated solutions of polyelectrolytes. They obtained the single chain form factor by extrapolation of the scattered intensity per labelled monomer to zero content of labelled chains at constant total solution concentration, and the interchain factor from the slope of the extrapolation line. Akcasu *et al.*[10] generalized the technique of Williams *et al.*[9] noting that a concentration extrapolation procedure was not necessary, and measured the radius of gyration of polyisoprene in the bulk by extracting the intrachain signal using scattering data from two different concentrations (6.9 and 14.5 wt %) of labelled molecules. In this paper we show, with well-defined polystyrenes, that the single chain form factor of the polymer in bulk may be obtained from a single concentration measurement for any concentration of labelled molecules, provided the molecular weights of the parent and labelled molecules are the same and the molecular weight distributions are narrow.

THEORY

The intensity $I(K)$ of coherent elastic neutron scattering from a pure unlabelled system consisting of one component (type 1) can be written as

$$I(K) = Na_1^2 P_1(K) + N^2 a_1^2 Q_{11}(K) \qquad (1)$$

where $K = 4\pi/\lambda \sin\theta$ is the neutron scattering vector, λ is the wavelength of the neutron, 2θ is the angle of scatter, a_1 is the scattering length of a monomer of component 1, N is the number of molecules per unit volume, $P_1(K)$ is the intrachain signal which originates from the scattering of the monomer pairs belonging to the same polymer chain and $Q_{11}(K)$ is the interchain signal which originates from the scattering by intermolecular monomer pairs. For a pure single component which contains no residual voids or heterogeneities (catalyst residues, impurities, stabilizers, etc.), the scattering is due simply to density fluctuations. For amorphous polymers the density fluctuation scattering is small[11,12] and, neglecting this component, we may write, following Benoit[13]:

† Research sponsored by the Division of Materials Sciences, U.S. Department of Energy under contract W-7405-eng-26 with the Union Carbide Corporation, by the National Science Foundation under grants DMR-77-24458 to the Oak Ridge National Laboratory and DMR-80-12724 (ELT) and DMR 78-05925 (RSS) to the University of Massachusetts, and by the Materials Research Laboratory of the University of Massachusetts.
** Present address: Technology for Energy Corporation, 10770 Dutchtown Road, Knoxville, Tennessee 37922

0032-3861/81/070886-04$02.00

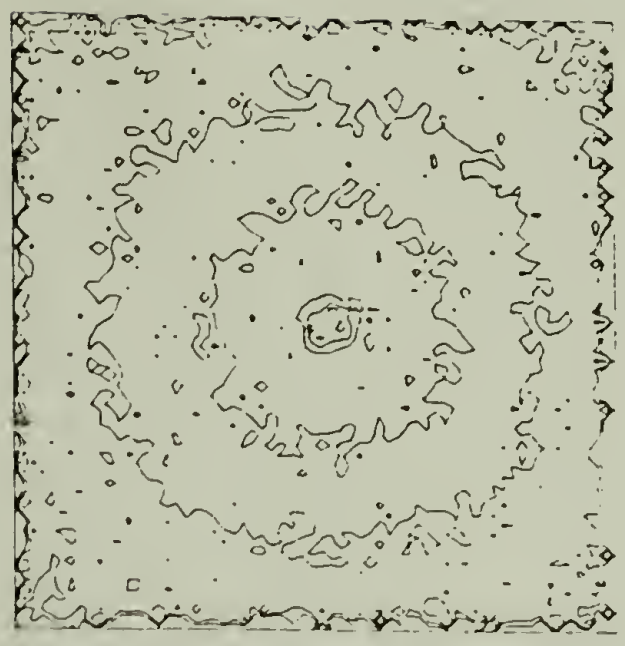

Figure 1 Two-dimensional scattering from 10.4% PSD molecules (M_w = 77 400) in PSH matrix (M_w = 75000)

$$P_1(K) + N Q_{11}(K) = 0 \tag{2}$$

and similar equations may be written for a system consisting of a pure unlabelled component 2 with only a change of subscripts. If two polymers are blended together in such a fashion that X_1 equals the mole fraction of component 1, X_2 is the mole fraction of component 2 and N is the total number of molecules per unit volume, the resulting scattering is now given by:

$$\begin{aligned} I(K) = {} & X_1 N a_1^2 P_1(K) + X_1^2 a_1^2 N^2 Q_{11}(K) + \\ & X_2 N a_2^2 P_2(K) + X_2^2 a_2^2 N^2 Q_{22}(K) + \\ & 2 X_1 X_2 N^2 a_1 a_2 Q_{12}(K) \end{aligned} \tag{3}$$

In general the intrachain functions $P_i(K)$ and interchain functions $Q_{ij}(K)$ in equation (3) are different for a blend of dissimilar components. However, in the case where the components of the blend differ only in that the molecules of one component are isotopically labelled, we may simplify equation (3) as follows. Assuming that deuteration of the hydrogenous molecule has a negligible effect on the monomer–monomer interaction, the average configuration of a labelled molecule does not differ from that of an unlabelled molecule and hence we may write:

$$P_1(K) = P_2(K) = P(K) \tag{4}$$

and

$$Q_{11}(K) = Q_{22}(K) = Q_{12}(K) = Q(K) \tag{5}$$

Since both labelled and unlabelled molecules have the same molecular weight, equation (2) is valid independent of the subscript:

$$Q(K) = -P(K)/N \tag{6}$$

Substituting equation (6) into equation (3) and simplifying yields the final result for the scattering

$$I(K) = X_1 X_2 (a_1 - a_2)^2 N P(K) \tag{7}$$

This shows that the form of the scattering curve in this case is governed only by the single chain form factor $P(K)$. The mole fraction of each component will modulate the scattered intensity with the maximum coherent scattering of the blend occurring at a 50–50 mixture of the two components. The analogy between this result and the Laue monatonic scattering from binary alloys is apparent.

Our result differs from that of Akcasu *et al.*[10] in that we have assumed at the outset that density fluctuation scattering is small and hence the scattering from a fully labelled sample is negligible compared with that from a blend of labelled and unlabelled molecules. While this assumption has been verified for amorphous polystyrene (see below), it does not hold for semicrystalline polymers or phase segregated blends where significant scattering from the two phase structure occurs. For these systems, a correction must be made by subtracting a term proportional to the coherent scattering from a fully labelled blend as pointed out by Akcasu *et al.*[10].

EXPERIMENTAL

Hydrogenated and deuterated atactic polystyrene were obtained from Polymer Laboratories of Shrewsbury, England. The molecular weight, M_w, of the hydrogenated and deuterated samples were 75000 and 77400, respectively, with polydispersities of 1.03 and 1.09, respectively. Samples were prepared by dissolving each component in boiling chlorobenzene and reprecipitating into excess methanol. The polymer was vacuum dried and pressed into a disc-shaped pellet, 0.13 cm thick. Samples containing 5, 10, 20, 30, 40, and 50 mol % deuteropolystyrene (PSD) in hydrogenated polystyrene (PSH) were prepared in addition to pure PSH and PSD blanks.

The neutron experiments were performed on the new 30 m SANS facility[14,15] at the National Center for Small Angle Scattering Research (Oak Ridge National Laboratory). The incident beam, of wavelength $\lambda = 4.74$ Å ($\Delta\lambda/\lambda = 6\%$), was collimated by a source slit (1.8 × 1.8 cm) and a sample slit (0.9 cm diameter) separated by a distance of 10 m. The area detector (64 × 64 cm^2), with 1 cm^2 element size, mounted on rails inside a 20 m vacuum flight path, was positioned at a distance of 10 m from the sample. The samples were typically measured for 2700 s and after correcting for instrumental backgrounds, incoherent scattering, and sample transmission, the scattered intensities were normalized to a constant sample thickness. Samples of both pure PSD and PSH were also measured to check that no voids or scattering heterogeneities were present and to provide a basis for subtracting incoherent scattering, arising principally from ^{1}H nuclei. A typical two-dimensional contour plot of a blend is shown in *Figure 1*.

RESULTS AND DISCUSSION

Debye[16,17] has shown that the single chain scattering function for a Gaussian random coil is given as:

$$P(K) = \frac{2}{u^2}(e^{-u} - 1 + u) \tag{8}$$

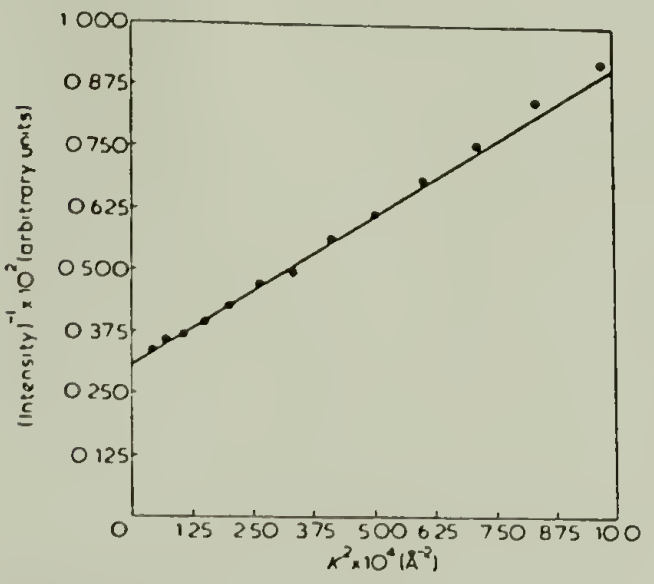

Figure 2 $I^{-1}(K)$ vs. K^2 for PSD molecules in sample containing 10.4 wt % PSD in PSH

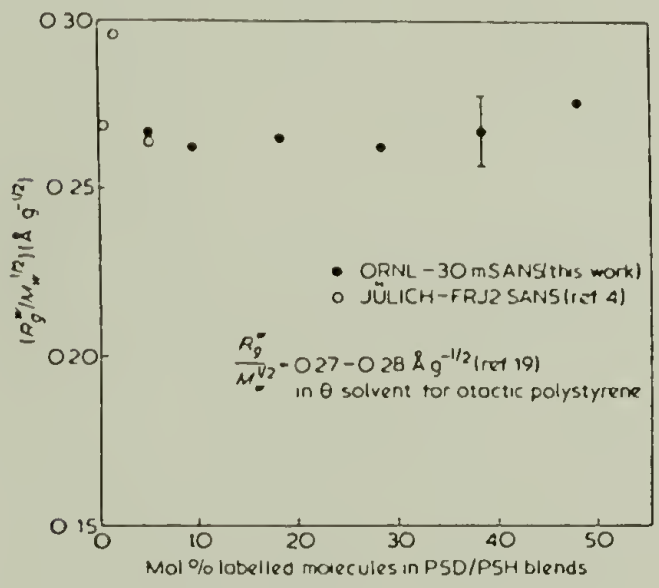

Figure 3 Variation of $R_g^w/M_w^{1/2}$ with concentration of labelled molecules for PSD/PSH blends

where $u = K^2\langle R_g^2\rangle$ and $\langle R_g^2\rangle$ is the mean square radius of gyration. For $K^2\langle R_g^2\rangle \ll 1$, the radius of gyration can be obtained from the slope of the plot of $I(K)^{-1}$ vs. K^2.

Figure 2 shows a typical plot of $I(K)^{-1}$ vs. K^2 from which (z-averaged) values of the radius of gyration were obtained. Small polydispersity corrections[18] were applied to give weight-averaged radii, R_g^w.

Figure 3 shows the plot of $R_g^w/M_w^{1/2}$ vs concentration of the tagged chain. The average value of 0.266 Å g$^{-1/2}$ is in excellent agreement with previous measurements made at low concentrations[2-4] and with the value for polystyrene in a θ-solvent[19]. No concentration dependence was observed.

Figure 4 shows the normalized forward scattering (extrapolated to $2\theta = 0$), vs concentration of the labelled chains. A straight line could be drawn through all the points, indicating that the intensity of the scattering is simply dependent on the mole fraction of the labelled chains (see equation 7). Extensive studies of labelled polystyrene blends[2-4] have shown that these systems do not exhibit anomalous forward scattering associated with segregation of the labelled species[5-8], and for this reason accurate absolute calibration of the intensity was not attempted. However, an approximate internal calibration, performed with respect to the ^{1}H incoherent scattering from the PSH blank, demonstrated that the molecular weights calculated from the forward scattering are of the correct order of magnitude, as expected for statistically distributed labelled molecules.

These results indicate that provided the molecular weight of the parent and labelled molecules are the same and their distributions are narrow, the single chain form factor of the polymer in bulk may be obtained from a scattering measurement at a single concentration for any concentration of labelled molecules. The theory given above has therefore been confirmed for well-defined polystyrenes over the range of concentration of 5–50 mol% deuterated polystyrene. For the special case of matched parent and labelled molecules, the radius of gyration is independent of the concentration of labelled molecules and there is no need to restrict SANS measurements to dilute concentrations of labelled molecules or to extrapolate to zero concentration, thus permitting a significant gain of scattering intensity for weakly scattering systems*. While the maximum coherent scattering occurs at a 50:50 mixture of the two components, it may be advisable to work at a somewhat lower ratio of PSH in PSD to maximize the ratio of coherent to incoherent scattering.

* During the course of this work we have become aware of complementary high concentration SANS work on polystyrene by C. Tangan *et al.* (University of Michigan) and F. Boue *et al.* (Laboratoire Leon Brillouin, Saclay). Similar conclusions were reached on methods to extract single chain form factors at high concentrations of labelled polymer.

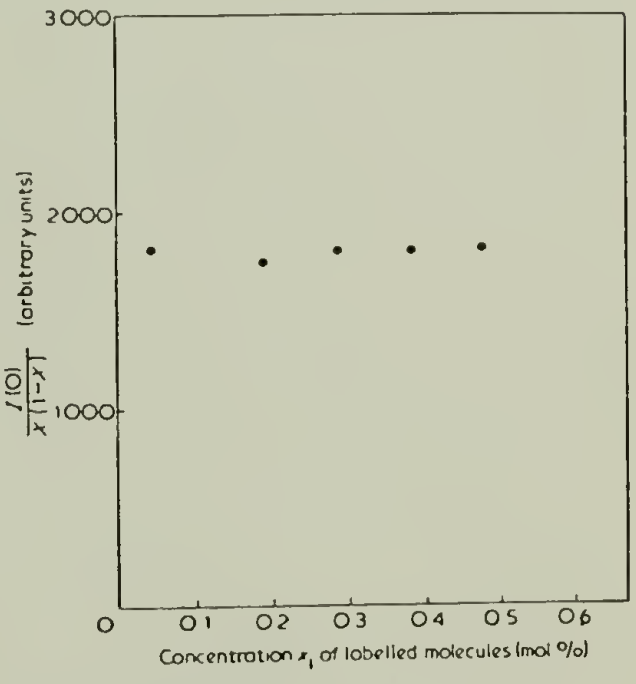

Figure 4 Variation of $I(0)$ with concentration of labelled molecules in PSD/PSH blends

ACKNOWLEDGEMENTS

We are grateful to Professor H. Benoit for initiating the theoretical development and for valuable discussions

Research sponsored by the Division of Materials Science US Department of Energy under contract W-7405-eng-26 with the Union Carbide Corporation, by the National Science Foundation under grants DMR-77-24458 to the Oak Ridge National Laboratory and DMR-80-12724 (ELT) and DMR-78-05925 (RSS) to the University of Massachusetts, and by the Materials Research Laboratory of the University of Massachusetts

REFERENCES

1 Kirste, R. G., Kruse, W. A. and Schelten, J. *Makromol. Chem.* 1972, 162, 299
2 Ballard, D. G. H., Wignall, G. D. and Schelten, J. *Eur. Polym. J.* 1973, 9, 965
3 Benoit, H., Cotton, J. P., Decker, D., Farnoux, B., Higgins, J. S., Jannink, G., Ober, R. and Picot, C. *Nature* 1973, 245, 13
4 Wignall, G. D., Ballard, D. G. H. and Schelten, J. *Eur. Polym. J.* 1974, 10, 861
5 Schelten, J., Wignall, G. D. and Ballard, G. D. H. *Polymer* 1974, 15, 682
6 Lieser, G., Fisher, E. W. and Ibel, K. *J. Polym. Sci.* 1975, 13, 39
7 Schelten, J., Ballard, D. G. H., Wignall, G. D., Longman, G. and Schmatz, W. *Polymer* 1976, 17, 751
8 Schelten, J., Wignall, G. D., Ballard, D. G. H. and Longman, G. W. *Polymer* 1977, 18, 1111
9 Williams, et al., *J. Polym. Sci. (Polym. Lett. Edn.)* 1979, 17, 379
10 Akcasu, A. Z., Summerfield, G. C., Jahshan, S. N., Han, C. C., Kim, C. Y. and Yu, H. *J. Polym. Sci.* 1980, 18, 865
11 Fischer, E. W., Wendorff, J. H., Dettenmaier, M., Lieser, G. and Voigt-Martin, 'Physical Structure of the Amorphous State', Marcel Dekker, 1977, p 41
12 Ullman, D., Renninger, A. L., Kritchevsky, G. and Vander Sander, 'Physical Structure of the Amorphous State', Marcel Dekker, 1977, p 153
13 Benoit, H. Personal communication
14 Koehler, W. C. and Hendricks, R. W. *J. Appl. Phys.* 1979, 50, 1951
15 Hendricks, R. W. and Koehler, W. C. *J. Appl. Crystallogr.* in be published
16 Debye, P. *J. Appl. Crystallogr.* 1944, 15, 338
17 Debye, P. *J. Phys. Colloid. Chem.* 1944, 51, 18
18 Altgelt, K. and Schultz, G. V. *Makromol. Chem.* 1960, 36, 209
19 Brandrup, J. and Immergut, E. H. 'Polymer Handbook' Interscience, New York, 1965, IV